Comptes Rendus
de l'Académie des sciences

1878-1543 (electronic)

Chimie

Volume 25, Special Issue S2, 2022

Special issue / *Numéro thématique*

Sustainable Biomass Resources for Environmental, Agronomic, Biomaterials and Energy Applications 3 / *Ressources de biomasse durables pour des applications environnementales, agronomiques, de biomatériaux et énergétiques 3*

Guest editors / *Rédacteurs en chef invités*

Mejdi Jeguirim, Salah Jellali, Besma Khiari

Académie des sciences — Paris

INSTITUT DE FRANCE
Académie des sciences

CENTRE MERSENNE

Comptes Rendus

Chimie

Objective of the journal

Comptes Rendus Chimie is a peer-reviewed electronic journal of international standing, covering all areas of the discipline. It publishes mainly thematic issues, but also original research articles, preliminary announcements, review articles, historical perspectives, pedagogical texts or conference proceedings, without length limit, in English or in French. Comptes Rendus Chimie is published according to a virtuous policy of diamond open access, free for authors (no publication fees) as well as for readers (immediate and permanent open access).

About the journal

All journal's information, including the text of published articles, which is fully open access, is available from the journal website at https://comptes-rendus.academie-sciences.fr/chimie/.

Author enquiries

For enquiries relating to the submission of articles, please visit this journal's homepage at https://comptes-rendus.academie-sciences.fr/chimie/.

Contact

Académie des sciences
23, quai de Conti, 75006 Paris, France
Tel: (+33) (0)1 44 41 43 72
CR-Chimie@academie-sciences.fr

Comptes Rendus
Chimie
2022, 25, nº S2

Contents / *Sommaire*

Comptes Rendus
Chimie
2022, Vol. 25, Special Issue S2, p. 1-5
https://doi.org/10.5802/crchim.190

Foreword: Recent Advances in Sustainable Biomass Valorization

Avant-propos : Récentes Avancées dans la Valorisation Durable de la Biomasse

Mejdi Jeguirim*, [a], Salah Jellali [b] and Besma Khiari [c]

[a] Institut de Science des Matériaux de Mulhouse, Université de Haute Alsace, Université de Strasbourg, France

[b] Centre for Environmental Studies and Research, Sultan Qaboos University, Oman

[c] Wastewaters and Environment Laboratory, Water Research and Technologies Centre, Tunisia

E-mails: mejdi.jeguirim@uha.fr (M. Jegurim), s.jelali@squ.edu.om (S. Jellali), besmakhiari@yahoo.com (B. Khiari)

Published online: 4 August 2022

Huge amounts of biomasses are annually generated in the world by several sectors including agriculture, industry, tourism etc. The sustainable management of these organic wastes has been pointed out as an urgent challenge to be urgently taken into consideration in order to avoid any negative effects onto human health and environment and to dispose of a supplementary resource that can be valorized in several domains. Indeed, some biomasses have high volatile matter contents allowing them to be used as a source for renewable energy extraction. Other biomasses contain high contents of valuable nutrients that can be used as low cost and eco-friendly biofertilizers in agriculture instead of synthetic fertilizers. Besides, some treated biomasses could exhibit promising properties permitting them to act as efficient adsorbents for pollutants removal from aqueous and gaseous effluents. Finally, some specific biomasses have interesting physical, chemical and biological properties allowing them to be precious source of various biomaterials.

In this context, the current special issue entitled: "**Sustainable Biomass Resources for Environmental, Agronomic, Biomaterials and Energy Applications 3**" aims to collect the most recent scientific works related to biomasses sustainable management and valorization in the domain of energy, agriculture, environment and biotechnology. This special issue aims to contribute to the international efforts deployed in order to make progress in the achievement of several related worldwide initiatives such as: "2030 United Nations Sustainable Development Goals" (UN-SDGs), the "4 per 1000" aiming to boost

* Corresponding author.

the annual carbon storage in agricultural soils by 0.4%, the "Greenhouse Gas Emissions reduction" as recommended by the Intergovernmental Panel on Climate Change (IPCC).

This special issue contains 10 peer-reviewed papers dealing with the valorization of several types of biomasses in various domains including energy, environment, and biotechnology.

The first paper is entitled: "*Pharmaceutical pollutants adsorption onto activated carbon: isotherm, kinetic investigations and DFT modeling approaches*" [1]. In this work, the removal of pharmaceutical pollutants, i.e., oxytetracycline (OTC) was studied through adsorption onto activated carbon (ACT) produced from households or agricultural wastes under various experimental conditions. The physicochemical properties of the produced carbon were investigated using multiple techniques. The characterization analysis highlighted an essential concentration of surface functional groups and a very developed porous structure. The adsorption process onto activated carbon occurs with a high yield at a large range of pH values varying between 4 and 8 at an optimum contact time of 2 h. It was established that the pseudo-second-order kinetic model fitted well OTC adsorption onto ACT. Moreover, the adsorption isotherm data showed that the pollutant removal process followed the Langmuir model with high regression coefficients (R^2) values and important adsorption efficiency of 80% for 100 mg·L^{-1} of OTC. Consequently, the use of ACT could be considered an efficient, sustainable, and low-cost alternative for pharmaceuticals-loaded wastewater treatment.

The second paper is entitled: "*Competitive biosorption of basic dyes onto petiole palm tree wastes in single and binary systems*" [2]. This work aimed to study petiole palm tree wastes (PTW) efficiency in removing two basic dyes: Rhodamine B (RB) and Victoria blue B (VBB) from aqueous solutions in single and binary systems under various experimental conditions including the effect of contact time, pH, initial concentration, and temperature. The PTW characterization shows that the PTW is a lingo-cellulosic material. The experimental results indicate that the removal of both dyes was relatively fast, spontaneous, exothermic and occurred on monolayers. Moreover, the adsorption competition between these two dyes on the adsorbent particles surface was important since the Langmuir's adsorption capacities were evaluated to 260.1; 440.1; 168.0; and 417.4 mg/g for RB and VBB in single and binary systems, respectively. These adsorption capacities, even in binary systems, are interesting compared to other raw materials and prove that this abundant agricultural waste can be considered as a promising material for an efficient dyes removal from aqueous effluents.

The third paper is entitled: "*Industrial dye removal from tannery wastewater by using biochar produced from tannery fleshing waste: a road to circular economy*" [3]. In this study, the capacity of biochars, derived from the pyrolysis of tannery fleshing waste (TFW) at 400 °C; 500 °C and 600 °C, in removal of red dye Sella Fast Red (SFR) from aqueous solutions and tannery wastewater was investigated under various experimental conditions in batch mode. Results show that for all applied biochars, the removed kinetics data were well fitted by the pseudo-second-order model, and the equilibrium state was obtained after 240 min of contact time. For an aqueous pH of 6 and a red dye concentration of 75 mg·L^{-1}, the removed amounts increased from 26 mg·g^{-1} to 39.86 mg·g^{-1} when the used pyrolysis temperature was increased from 400 °C to 600 °C. Moreover, SFR adsorption data at equilibrium were well fitted by Langmuir model suggesting a probable monolayer adsorption process with a maximal removal capacity of 62.7 mg·g^{-1} for BTFW-600 °C. The thermodynamic study demonstrated that SFR adsorption was endothermic for the three tested biochars. Desorption experiments with distilled water proved that SFR was significantly desorbed from the tested biochars, which offers possible reusability. On the other hand, BTFW-600 °C has demonstrated an important ability in removing SFR from real wastewater since only one dosage of 15 g·L^{-1} was enough to ensure more than 97% of dye removal. According to pHZC and FTIR analysis, the possible mechanism toward SFR dye removal was attributed to electrostatic interactions that occurred between biochar and functional groups of SFR. This work could provide guidance for the value-added utilization of tannery solid waste and a practical way to remove dyes from tannery wastewater.

The fourth paper is entitled: "*Cationic dye removal using Pergularia Tomentosa L. fruit: kinetics and isotherm characteristics using classical and advanced models*" [4]. In this study, different techniques

were used to characterize the powdered *pergularia tomentosa* fruit. After that, the biomaterial was exploited to investigate the adsorption of methylene blue in batch mode. The effects of initial pH, contact time, dye concentration, biosorbent dose, and temperature on the biosorption capacity have been performed. The fit of the adsorption isotherms was performed by means of several classical models and advanced models derived from statistical physics. The two-energy monolayer model proves to be the more suitable. It appears that two functional groups of the biosorbent are involved in the dye biosorption. The adsorption energy ranges from 14 to 18 kJ·mol^{-1} which indicates a physiosorption mechanism. The maximum adsorption capacity is 152 mg·g^{-1}. *Pergularia tomentosa* fruit proves to be attractive for the efficient removal of cationic dyes from polluted water.

The fifth paper is entitled: "*Investigations on potential Tunisian biomasses energetic valorization: thermogravimetric characterization and kinetic degradation analysis*" [5]. During this work, six Tunisian local biomasses, namely ziziphus wood (ZW), almond shells (AS), olive stones (OS), vine stems (VS) and date palm leaflets (DPL) and trunks (DPT) were slowly pyrolyzed under inert atmosphere at a heating rate of 5 °C/min through thermogravimetric (TG) analyses. The thermal degradation of samples involves the interaction in a porous media of heat, mass and momentum transfer with chemical reactions. Heat is transported by conduction, convection and radiation and, mass transfer is driven by pressure and concentration gradients. Thermal degradation curves have been studied with minute details for each degradation step. The Coats–Redfern model was used to extract the kinetic parameters from the TG data, then the kinetic parameters such as the activation energy, the pre-exponential factor and the order of the reaction were calculated. Results showed that the total mass losses amounts and kinetics are dependent on the type of the used biomass. Moreover, the devolatilization could be described by the first order model, while the char formation stage was better described by the second and third order reactions model. The physicochemical characteristics of these samples were also determined. The volatile matter (VM) content varies considerably, with values ranging from 67.19% for AS to 77.4% for ZW. The maximum values were obtained for ZW and VS with values of 77.4% and 71.9%, respectively. The lowest value (67.19%) was determined for AS. In addition, the ash contents vary between 0.8% for OS and 5.66% for DPT. The ashes vary significantly from one sample to another, with the values being even lower than 1% for OS, whereas the higher values in the DPT is 5.66%. Further, activation energies corresponding to main devolatilization regions were 59.5, 47.0, 55.8, 41.1, 89.1, 45.2 kJ/mol for ZW, AS, OS, VS, DPL, and DPT respectively. Among all the tested biomasses, the ZW and VS appear to have an important potential to be used for energy production.

The sixth paper is entitled: "*D-optimal design optimization of unsaturated palm fatty acid distillate and trimethylolpropane esterification for biolubricant production*" [6]. In this work, polyol ester of green biolubricant base oil was synthesized through the esterification of unsaturated palm fatty acid distillate (USFA-PFAD) with polyhydric alcohol, trimethylolpropane (TMP) in the occurrence of sulphuric acid catalyst. The optimization process was conducted by using D-optimal design of the response surface methodology (RSM). The results showed that the highest yield percentage of resultant polyol ester, USFA-TMP ester was obtained at 96.0 ± 0.5% with 99.9 ± 0.9% of tri-ester selectivity. These were obtained at the esterification optimal condition at reaction temperature of 150 °C for 6 h with 5% H_2SO_4. The polyol ester chemical structure was characterized by using spectroscopy analysis techniques of infrared (FTIR), proton (^{1}H) and carbon (^{13}C) nuclear magnetic resonance (NMR). The resultant USFA-TMP ester recorded viscosity index of 163, pour points at −45 °C, flash points at 298 °C, and thermal oxidative stability temperatures at 215 °C. It was found that the ester product as a Newtonian fluid with viscosity grade lubricant ISO VG 46. In overall, the resultant polyol ester has shown good lubrication properties that make it conceivable to be used for many industrial green biolubricant applications.

The seventh paper is entitled: "*CFD multiphase combustion modelling of oleic by-products pellets in a counter-current fixed bed combustor*" [7]. In this research work, a transient two-dimensional multiphase model was built to study the combustion of pellets of oleic by-products (Olive Pits (OPi)) in a cylindrical counter-current 40 kW fixed bed combus-

tor. The fixed bed is modelled as a porous medium, which is randomly packed with spherical particles of equal size. A $\kappa - \varepsilon$ model for low Reynolds number flows was used for turbulence Modelling. Primary and secondary air injections were supplied at the bed (solid phase combustion) and at the freeboard zone (gas phase combustion), respectively. The mass loss history, the temperature distribution at different heights inside the reactor and the gas emissions of CO, CO_2, O_2, H_2, CH_4 and C_{org} were computed. Key parameters related to the reaction front velocity, the mass conversion rate and the progress of ignition were also computed. We show that computational results are in good agreement with experimental measurements obtained using a similar reactor fed with the same pellet types. These results also motivate the implementation of the present formulation and its extension to industrial scale furnaces, having established the results for the comparison with pilot-scale experiments.

The eighth paper is entitled: "*Biohydrogen production by Thermotoga maritima from a simplified medium exclusively composed of onion and natural seawater*" [8]. In this work, biohydrogen production by the anaerobic hyperthermophilic and halophilic bacterium, Thermotoga maritima (TM) was conducted using a mixture of Onion Waste Juice (OWJ) and seawater (SW). The highest production of biohydrogen (H_2) with OWJ, as the exclusive source of carbon and energy, was obtained for an optimum volume of 50% (v/v), with the highest overall productivity of biohydrogen (15.6 mM/h) and a maximum yield of 2.6 ($molH_2/molH_{exose}$). This was mainly due to the presence of organosulfur compounds and the natural presence of ammonium contained in OWJ. The addition of inorganic nitrogen and iron sources in the mixture of SW and OWJ has improved biohydrogen production, achieving productivity yield (23.0 mM/h for 3.2 $molH_2/molH_{exose}$) close to the maximum obtained for TM. Above 600 mL, the high concentration of substrate (>30 g COD/L) led the metabolism to deviate towards lactate production at the expense of H_2 production. A fed-batch culture with the sequential addition of concentrated OWJ mixed with only sea salt was investigated for the prevention of substrate-associated growth inhibition by controlling the nutrient supply. The total cumulative biohydrogen produced was about 300 mM after 30 h of incubation.

The ninth paper is entitled: "*Enhanced transesterification of rapeseed oil to biodiesel catalyzed by KCl/CaO*" [9]. In this work, a series of supported solid based catalysts were prepared by impregnation of chloride salts over CaO. The catalytic activity of the prepared catalysts was tested for the transesterification reaction of biodiesel from rapeseed oil and methanol. The KCl/CaO catalyst containing 15% KCl exhibited the highest catalytic activity after calcination at 600 °C for 6 h. A reaction optimization study was carried out using KCl/CaO as catalyst leading to operation conditions for achieving a 98.3% yield of fatty acid methyl ester (FAME) at 2.5 h and 65 °C, a catalyst amount of 10%, and a mole ratio of methanol to rapeseed oil of 15:1. It was found that the highest FAME yield at 2.5 h was faster than that at 6 h for commercial CaO catalysts under the same reaction conditions. The characterization results showed that the pore size of CaO particles was greatly improved by the addition of KCl, which facilitated better access of the reactive molecules to the active sites of the catalyst.

The last paper is entitled: "*H_2-rich syngas production by sorption enhanced steam gasification of palm empty fruit bunch Catalytic*" [10]. In this work, hydrogen-rich syngas from palm empty fruit bunch has been produced in the presence of CaO and bentonite as absorbent and catalyst, respectively. The gasification process is carried out at 550–750 °C at atmospheric pressure in a fixed bed gasifier with steam to biomass ratio (S/B) of 0–2.5 and Ca/C ratio of 0–2. The results showed that CaO only acts as CO_2 absorber during the process. Increasing the ratio of Ca/C and S/B have increased the concentration of H_2 and absorption of CO_2 in the syngas. The addition of CaO did not significantly increase the production of CH_4 and CO in the syngas. The H_2 concentration reaches about 78.16 vol% at 700 °C and Ca/C ratio of 2.

Guest Editors of this special issue are grateful to all the authors for their valuable contribution and to the reviewers for their comments that contributed to the quality improvement of the above-cited accepted papers. Many thanks to the Editor-in-Chief of Comptes Rendus Chimie, Professor Pierre Braunstein for renewing his confidence and support. Special thanks to the entire production team of the journal for their constructive collaboration.

Mejdi Jeguirim
Co-Guest Editor
Institut de Science des Matériaux de Mulhouse
France
mejdi.jeguirim@uha.fr

Salah Jellali
Co-Guest Editor
Sultan Qaboos University
Oman
s.jellali@squ.edu.om

Besma Khiari
Co-Guest Editor
Water Research and Technologies Centre
Tunisia
besmakhiari@yahoo.com

References

[1] M. Kebir, R. Bourzami, N. Nasrallah, S. E. I. Lebouachera, F. Dergal, R. Ladji, M. Trari, H. Ben Harharah, A. El Jery, A. A. Azzaz, L. Khezami, *C. R. Chim.*, 2022, **25**, no. S2, Online first.
[2] S. Jmai, S. Guiza, S. Jellali, M. Bagane, M. Jeguirim, *C. R. Chim.*, 2022, **25**, no. S2, Online first.
[3] K. Haddad, A. Hantous, R. Chagtmi, H. Khedhira, C. Chaden, A. B. H. Trabelsi, *C. R. Chim.*, 2022, **25**, no. S2, Online first.
[4] H. Belmabrouk, M. Selmi, T. Alshahrani, Z. Raddaoui, A. Bajahzar, M. Jabli, T. Alharbi, H. Kerras, N. Outili, K. Loubar, A. H. Meniai, *C. R. Chim.*, 2022, **25**, no. S2, Online first.
[5] J. Mabrouki, M. A. Abbassi, B. Khiari, S. Jellali, M. Jeguirim, *C. R. Chim.*, 2022, **25**, no. S2, Online first.
[6] M. A. Jumaah, N. Salih, J. Salimon, *C. R. Chim.*, 2022, **25**, no. S2, Online first.
[7] M. A. Mami, M. Lajili, T. Echekki, *C. R. Chim.*, 2022, **25**, no. S2, Online first.
[8] L. Ben Gaida, H. Gannoun, L. Casalot, S. Davidson, P. P. Liebgott, *C. R. Chim.*, 2022, **25**, no. S2, Online first.
[9] S. Tao, L. Zhang, F. Qin, S. Chen, R. Zhou, Y. Tang, *C. R. Chim.*, 2022, **25**, no. S2, Online first.
[10] N. Aprianti, M. Faizal, M. Said, S. Nasir, *C. R. Chim.*, 2022, **25**, no. S2, Online first.

Comptes Rendus
Chimie
2022, Vol. 25, Special Issue S2, p. 7-8
https://doi.org/10.5802/crchim.213

Sustainable Biomass Resources for Environmental, Agronomic, Biomaterials and Energy Applications 3

Guest editors

Not yet published

Dr. Mejdi Jeguirim, is a Professor at the University of Haute Alsace (France) in the field of energy, process engineering and kinetics modelling. He dedicates most of his career to the biomass valorization through thermochemical conversion and the chars elaboration for the treatment of aqueous and gaseous effluents. These research topics were performed in the frame of several international collaborations (Tunisia, Germany, Belgium, Algeria, Lebanon, Greece, Cyprus, Spain, Lithuania, the Netherlands…) and industrial contracts. He acted as PhD advisor for 10 students and he has co-authored more than 150 referred international journal papers in his research field. He is member of the editorial board of international journals (Energy, Energies, Energy for Sustainable Development, Biofuels) and scientific committee of several international congresses. He is involved as a scientific expert for more than 40 international scientific journals as well as for several national and international research programs. He has received the French National Research Excellence Award for researcher with high level scientific activity for the 2009-2012, 2013-2016 and 2017-2020 periods.

Le Dr Mejdi Jeguirim est professeur à l'Université de Haute Alsace (France) dans le domaine de l'énergie, du génie des procédés et de la modélisation cinétique. Il consacre l'essentiel de sa carrière à la valorisation de la biomasse par conversion thermochimique et à l'élaboration de charbons de synthèse pour le traitement des effluents aqueux et gazeux. Ces recherches ont été menées dans le cadre de plusieurs collaborations internationales (Tunisie, Allemagne, Belgique, Algérie, Liban, Grèce, Chypre, Espagne, Lituanie, Pays-Bas...) et de contrats industriels. Il a été directeur de thèse pour 10 étudiants et a co-écrit plus de 150 articles de journaux internationaux référencés dans son domaine de recherche. Il est membre du comité éditorial de revues internationales (Energy, Energies, Energy for Sustainable Development, Biofuels) et du comité scientifique de plusieurs congrès internationaux. Il est impliqué en tant qu'expert scientifique pour plus de 40 revues scientifiques internationales ainsi que pour plusieurs programmes de recherche nationaux et internationaux. Il a reçu le Prix national d'excellence de la recherche française pour les chercheurs ayant une activité scientifique de haut niveau pour les périodes 2009-2012, 2013-2016 et 2017-2020.

Dr. Salah Jellali is serving as senior researcher at the Centre for Environmental Studies & Research, Sultan Qaboos University, Sultanate of Oman. His research interests include wastewaters treatment by low cost materials, nutrients recovery from wastewaters and reuse in agriculture, local water management and groundwater flow and pollutants transport modelling for a sustainable management. He was involved in various national and international projects regarding the above-cited topics. He has co-authored more than 80 referred international journal papers in his research field. He was involved in the management of several international conferences and special issues of scientific journals related to wastes/wastewaters sustainable management. He acted as a national and international expert for the evaluation of research projects related to the domain of water/wastes management. He was the holder of the ministerial award of rural engineering diploma in 1994 and the presidential award for the best national supervised PhD thesis in 2018.

Le Dr Salah Jellali est chercheur principal au Centre d'études et de recherches environnementales de l'Université Sultan Qaboos, au Sultanat d'Oman. Ses recherches portent sur le traitement des eaux usées par des matériaux à faible coût, la récupération des nutriments des eaux usées et leur réutilisation en agriculture, la gestion locale de l'eau et la modélisation de l'écoulement des eaux souterraines et du transport des polluants pour une gestion durable. Il a participé à divers projets nationaux et internationaux concernant les sujets susmentionnés. Il a co-écrit plus de 80 articles de journaux internationaux référencés dans son domaine de recherche. Il a participé à la gestion de plusieurs conférences internationales et de numéros spéciaux de journaux scientifiques liés à la gestion durable des déchets et des eaux usées. Il a agi en tant qu'expert national et international pour l'évaluation de projets de recherche liés au domaine de la gestion de l'eau et des déchets. Il a reçu le prix ministériel du diplôme de génie rural en 1994 et le prix présidentiel de la meilleure thèse de doctorat supervisée au niveau national en 2018.

Dr. Besma Khiari is a Professor at the University of Carthage (Tunisia) in the field of energy and environment processes, applied mainly to wastes. Recovery from urban, agricultural and industrial wastes is the main objective of the different papers, books, academic supervisions and industrial projects she took part in. Her expertise in the area best met the needs and expectations of professionals such as engineering companies, design offices, health services, environmental businesses and units, farmers, etc.

La Dr Besma Khiari est professeur à l'Université de Carthage (Tunisie) dans le domaine des procédés énergétiques et environnementaux, appliqués principalement aux déchets. La valorisation des déchets urbains, agricoles et industriels est l'objectif principal des différents articles, livres, supervisions académiques et projets industriels, auxquels elle a participé. Son expertise dans le domaine répondait le mieux aux besoins et aux attentes des professionnels tels que les sociétés d'ingénierie, les bureaux d'études, les services de santé, les entreprises et les unités environnementales, les agriculteurs, etc.

Comptes Rendus
Chimie
2022, Vol. 25, Special Issue S2, p. 9-25
https://doi.org/10.5802/crchim.161

Sustainable Biomass Resources for Environmental, Agronomic, Biomaterials and Energy Applications 3 / *Ressources de biomasse durables pour des applications environnementales, agronomiques, de biomatériaux et énergétiques 3*

Pharmaceutical pollutants adsorption onto activated carbon: isotherm, kinetic investigations and DFT modeling approaches

Mohammed Kebir *, [a], **Riadh Bourzami** [b], **Noureddine Nasrallah** [c], **Seif El Islam Lebouachera** [d], **Fayçal Dergal** [e], **Riad Ladji** [a], **Mohamed Trari** [f], **Hamed Ben Harharah** [g], **Atef el Jery** [g], **Ahmed Amine Azzaz** [h] and **Lotfi Khezami** *, [i]

[a] Research Unit on Analysis and Technological Development in Environment (URADTE/CRAPC), BP 384 Bou-Ismail Tipaza, Algeria

[b] Emergent Materials Unit, Université Ferhat Abbas Sétif 1, 19000 Sétif, Algeria

[c] Laboratory of Reaction Engineering, USTHB, 32 Algiers, BP, Algeria

[d] Université de Pau et des Pays de l'Adour, E2S UPPA, CNRS, Total Energies, Allée du Parc Montaury, 64600 Anglet, France

[e] Centre de Recherche Scientifique et Technique en Analyses Physico Chimiques, (C.R.A.P.C), Bou-Ismail, Tipaza, Algeria

[f] Laboratory of Storage and Valorization of Renewable Energies, Faculty of Chemistry, USTHB, BP 32 Algiers, Algeria

[g] Department of Chemical Engineering, College of Engineering, King Khalid University, Abha 61411, Saudi Arabia

[h] Environnements Dynamiques et Territoires de la Montagne, Université Savoie Mont-Blanc, EDYTEM, 5 Boulevard de la Mer Caspienne, 73370 Le Bourget-du-Lac, France

[i] Department of Chemistry, Al Imam Mohammad Ibn Saud Islamic University (IMISIU), P.O. Box 5701, Riyadh 11432, Saudi Arabia

E-mails: medkebir@yahoo.fr (M. Kebir), riadh_bourzami@hotmail.com (R. Bourzami), nas_nour@yahoo.fr (N. Nasrallah), s.lebouachera@univ-pau.fr (S. E. I. Lebouachera), dergalf@yahoo.fr (F. Dergal), rladji@hotmail.com (R. Ladji), Solarchemisrty@gmail.com (M. Trari), hhharharah@kku.edu.sa (H. Ben Harharah), ajery@kku.edu.sa (A. el Jery), ahmed-amine.azzaz@univ-smb.fr (A. A. Azzaz), lkhezami@gmail.com (L. Khezami)

Abstract. In this work, significant interest has been focused on removing pharmaceutical pollutants, i.e., oxytetracycline (OTC), which was studied through adsorption onto activated carbon (ACT)

* Corresponding authors.

produced from households or agricultural wastes under various experimental conditions. The physicochemical properties of the produced carbon were investigated using multiple techniques. The characterization analysis highlighted an essential concentration of surface functional groups and a very developed porous structure. The adsorption process onto activated carbon occurs with a high yield at a large range of pH values varying between 4 and 8 at an optimum contact time of 2 h. It was established that the pseudo-second-order kinetic model fitted well OTC adsorption onto ACT. Moreover, the adsorption isotherm data showed that the pollutant removal process followed the Langmuir model with high regression coefficients (R^2) values and important adsorption efficiency of 80% for 100 mg·L^{-1} of OTC. The displayed results consequently, the use of ACT as an adsorbent could be considered an efficient, sustainable, and low-cost alternative for pharmaceuticals-loaded wastewater treatment.

Keywords. Adsorption, Activated carbon, OTC, Physico-chemical characterization, Kinetics, Isotherm.

Published online: 15 March 2022

1. Introduction

The development of pharmaceutical industries led to an increase in the consumption of antibiotics by humans for multiple medical purposes. Unfortunately, their excessive application led to their displacement at large quantities in the environment, which affected the ecosystem equilibrium and the native fauna, flora, waters, and soils, thus reducing their assimilative capacity towards other organic and inorganic pollution. Furthermore, of these organic contaminants in the natural soils became a source of antibiotic-resistant bacteria, leading to serious mass contaminations and pandemics [1]. It is worth mentioning that detecting pharmaceuticals in water as a new barrier to access for clean water has interested scientists in focusing their research activities on their sources and occurrences in the environment witnessing.

Recently, pharmaceutical compounds can be introduced in the environment differently as parent compounds or by-products issued from human/animal metabolic activities or by disposal of unused or expired drugs and accidental spills in nature [2]. Therefore, the existance of antibiotics in the environment at low concentrations ranging from 1 μg·L^{-1} to ng·L^{-1} is detected thanks to the advanced analytical methods [3]. Oxytetracycline (OTC) belongs to the tetracyclines antibiotic family and is widely used in veterinary chemicals, with a stable naphthol ring as the main structure to the microorganism in wastewater [4]. The occurrence of OTC in the environment may lead to the development of antibiotic-resistant strains in microorganisms, which can be transferred to humans and animals through food and drinking water [5].

Numerous treatment approaches for the removal of antibiotics have been considered in recent studies, including reverse osmosis, biodegradation, membrane filtration, photocatalysis, photo Fenton reaction, ozonation, and peroxidation [6]. Despite their confirmed treatment performances, these techniques are unfortunately limited at some levels that might hamper their overall economic feasibility, especially for pollutants at trace levels or relatively high concentrations [7,8]. The adsorption onto activated carbon could be considered an efficient approach and presents a practical alternative for removing pollution [9,10]. There is, therefore, a growing interest in novel and low-cost adsorbents. It is to be stressed that obtaining carbon from biomass waste as a biological material derived from plant residues is comparatively cheap. This is because of their large availability, low cost, the ability to be converted easily into highly porous carbon as well as the possibility of regeneration for multiple uses.

Artichoke, a commonly consumed vegetable in the Mediterranean food style, represents a significant share of household bio-organic wastes. It is part of a circular economy and sustainable development concepts. The disposal of these lingo-cellulosic materials in nature might result in serious environmental issues, including the fungi development and the disruption of N, P, and K of the surrounding environment [11]. Moreover, it would be interesting to maximize the physicochemical properties of these wastes into largely-employed added-value materials for multiple environmental purposes. Hence, the artichoke waste conversion into an effective adsorbent for water purification at multiple cycles offers the possibility for water recovery to reduce the risk of hydric pollution [9,12].

This study aims to properly manage artichoke

residues as an example of households and abundant agricultural waste as a precursor for activated carbon production. Moreover, this research describes the preparation of activated carbon from artichoke bio-waste by H_3PO_4 activation to report the kinetic of batch adsorption of OTC molecules used in veterinary activities. This investigation will be achieved by examining the effect of the pH, adsorbent dose, initial OTC concentration, and temperature on the kinetics in a combined manner and the applicability of lumped kinetic models to describe the adsorption process. Equilibrium data are also included to support the kinetic findings. In addition, computational modeling using density functional theory (DFT) is considered a complementary tool to understand the adsorption behavior and their nature better and explain the interactions energies between adsorbent/adsorbate systems, which contribute to OTC removal from aqueous solution. Furthermore, the results obtained here make them suitable and valuable for other environmental applications, including water treatment processes such as filtration and gas purification.

2. Materials and methods

All chemicals and reagents were of analytical grade, and supplied from standard sources. Orthophosphoric acid (H_3PO_4, Sigma-Aldrich, 86%), hydrochloric acid (HCl, Biochem, 37%), sodium hydroxide (NaOH, Merck, Oxytetracycline (OTC, $C_{22}H_{24}N_2O_9$, MW = 460.43 g·mol^{-1}) were acquired from Sigma Aldrich (China; 95–102%). The structural formula of OTC is illustrated in Supplementary Figure S1. The OTC stock solution was prepared at a concentration of 1000 mg·L^{-1}, and the appropriate volume was diluted to the distilled water to obtain the desired OTC concentration. The pH was measured by a HI 2210 pH meter (Hanna instruments, Rhode Islands, USA). The removal efficiency of OTC was determined by measuring the residual concentration in the filtrate spectrophotometrically using a UV–visible spectrophotometer (Shimadzu 1800, Tokyo, Japan) at a maximum wavelength of 354 nm.

2.1. *Adsorption experiment*

The adsorption experiments were carried out in a 1000 mL double welled Pyrex reactor, in which OTC solution and a known amount of adsorbent were mixed at room temperature (25 °C). The pH was adjusted by adding HCl or NaOH using a pH meter (HANA 2210). To study the optimal conditions such as the contact time, the initial pH of the solution (1–11), the amount of adsorbent (0.1–2 g), the initial OTC concentration (50–200 mg·L^{-1}), and the temperature (20–50 °C).

The aliquots were withdrawn at regular times and separated by centrifugation. The experimental protocol was investigated by changing only one parameter once for a given test, while the others were kept constant. All experiments, including blank tests, were performed in triplicate.

2.2. *Preparation and characterization of the adsorbent*

The biomass agriculture waste precursor, i.e., Artichoke (origin west north Algeria), is thoroughly washed with distilled water, dried in an oven at 80 °C until the obtention of constant weight, then mechanically ground into powder. Afterward, the precursor is impregnated with H_3PO_4 solution with a ratio solid to the volume of 1:1 using a stirring reactor for 12 h. The mixture was then filtered, recovered, and dried at 100 °C.

The activated precursor was subsequently carbonized at 500 °C in a thermally controlled furnace (Nabertherm, Germany) with a linear rise of 5 °C·min^{-1} for 1 h. The obtained product is washed with hot distilled water to leach the ash from carbon and remove the acid trace until getting a neutral pH. Finally, the black residue is dried at 100 °C for 24 h, after which it was ground again, sieved, and denoted ACT until obtaining a powder with an average particles size of about 200 μm. The produced activated carbon was then stored in an airtight glass container for subsequent use.

Physical and chemical characterizations of the ACT are investigated to characterize better the morphological structure and the chemical composition of the adsorbent surface, which are helpful to make hypotheses on the adsorption process mechanisms.

2.2.1. *Physical characterization*

The surface area and the pore size distribution of the samples were determined by N_2 adsorption/desorption at −77 K using a Micromeritics

Tristar 3100. Before gas adsorption analysis, the sample was outgassed at 573 K for 4 h, porosity. The micropore surface area and micropore volume were obtained via t-plot analysis. Pore size distribution (PSD) was estimated by a Non-Local Density Functional Theory (NLDFT) method using nitrogen adsorption data and assuming a slit pore model. The textural properties and morphologies were studied through scanning electron microscope SEM (FEI Quanta 200, SEM) and X-ray diffraction (XRD) Xpro Philips.

2.2.2. *Chemical characterization*

The prepared activated carbon was characterized using various techniques. These techniques are its zero-point charge as cited previously [13–16], chemical elemental composition analysis by X-ray fluorescence spectrometry (XRF), Rijuka Zsxpriness II, and Fourier Transform Infrared Spectroscopy (ATR-FTIR) using a spectrometer Brucker Alpha one.

2.3. *Theoretical study*

The adsorption energy is regarded as a critical parameter to understand the behavior and nature of the adsorption mechanism. This parameter distinguishes the physical or chemical adsorption process mechanism of OTC onto ACT. As reported in the literature, strong adsorption can be related to the higher negative energy [10,17–21]. Frequently, the E_{ads} values determine the physisorption or chemisorption interaction nature [13]. The following formula can give the OTC adsorption energy (E_{ads}) onto ACT [14]:

$$E_{ads} = E(AB) - (E(A) + E(B)), \quad (1)$$

where $E(A)$ is the adsorbates total energy, $E(B)$ is the total energy of the substrate, and $E(AB)$ is the total energy of the adsorbent/adsorbate system at equilibrium. All the calculations were performed through the computational approach based on the Monte Carlo calculations, which are used to estimate the interaction energies between ACT and OTC molecules using the adsorption locator modulus in Biovia Materials studio software (Accelrys, San Diego, USA). ACT geometry was optimized in vacuum media employing the Gaussian program package. The dimension stable molecular structure of OTC is 1.26161 × 0.8240 × 0.5320 (nm) [15], in focus to compare the geometries of this last before and after the adsorption process. In which 202 Å is the topological surface area of ACT. In this study, based on the XRD analysis, the cellulose and cellulose-H_2PO_3 were considered as a model (30 Å × 15 Å × 25 Å) box dimension. For the activated carbon surface properties [16].

For the reaction mechanism occurring between the OTC surface functional groups and the different functional groups existing on the adsorbent surface such as COOH, OH, C=C, C=O, C–H, P–O–OH, P–O–C, and P–O–P, a schematic diagram and the obtained cluster models of the ACT, are established according to the DFT calculation.

3. Results and discussion

3.1. *Adsorbent characterization*

3.1.1. *FTIR analysis*

The FTIR analysis provides information about the nature of surface functional groups and the efficiency of the activation process with the H_3PO_4 chemical agent. The IR spectra of raw artichoke biomass and activated carbon ACT measured within the range of 400–4000 cm^{-1} are presented in Figures 1(a) and (b).

The FTIR spectrum shows a fingerprint region of 1630–400 cm^{-1} for the source identification of biomass raw Artichoke in Figure 1(a) shows the most complicated and apparent spectrum. The FTIR spectra are displayed in Figures 1(a) and (b). Before activation (Figure 1(a)), the broadband at 3380 cm^{-1} corresponds to the O–H groups. The band that appeared at 2924 cm^{-1} can be assigned to C–H stretching related to alkanes (CH_2) deformation and alkyl groups C–O–C stretching.

A strong conjugated C=C peak was also observed around 1630 cm^{-1}; the transmittance at 1418 cm^{-1} could be assigned to the bending OH vibration of hydroxyl groups.

774 cm^{-1} was identical to C–H in (CH_3) deformation and $(CH_2)_n$ groups, respectively, while the carboxylic group was shifted to 1055 cm^{-1}. The band at 531 cm^{-1} was related to –C–C stretching of cellulose and hemicellulose.

Figure 1(b) corresponds to the activated carbon ACT displays an absorption band around 3553–3263 cm^{-1} can be attributed to –OH associated with the stretching vibration of water, phenols, and alcoholic groups. The strong bands of OH stretching vibrations are observed after activation [22]. The peak

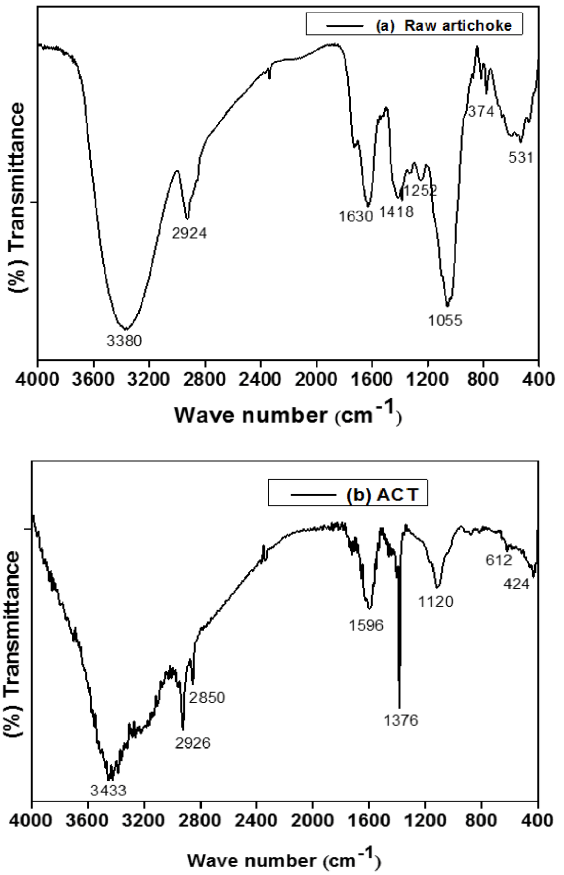

Figure 1. FTIR spectra of the raw artichoke (a) and ACT (b) adsorbents.

at 2926 cm^{-1} is assigned to the C–H bonds stretching vibrations of aromatic rings groups. The distinct bands at 2850 cm^{-1} belong to C–H symmetric bond stretching vibration in the group CH_2. The spectra show a pronounced band at 1696 cm^{-1} assigned to the aromatic carbon, or carboxyl groups, C=C stretching vibration in aromatic rings or stretch of C=O in –COOH group of the structure of activated carbon [23].

However, the band at 1658 cm^{-1} corresponds to the C=O elongation vibrations in the plane of the aromatic rings. A low peak at 1376 cm^{-1} corresponds to the C–H bond in the CH_3 group. Nevertheless, it is also characteristic of the phosphorus, and phosphorus–carbon compounds in H_3PO_4 activated carbon. The peak at 1120 cm^{-1} can be attributed to the elongation mode of the hydrogen-bond POOH groups of the phosphates or polyphosphates

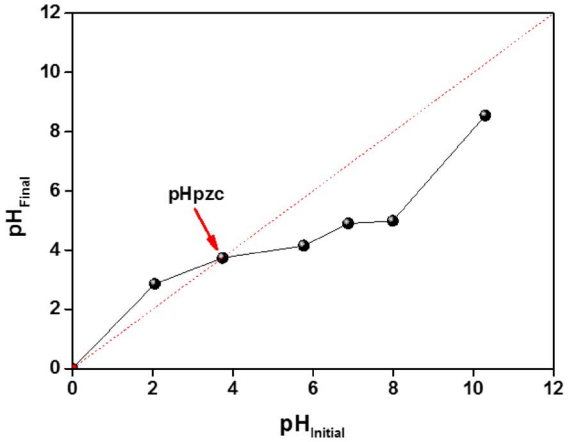

Figure 2. Determination of the pH_{pzc} of the ACT.

to the elongation vibration of the O–C in the P–O–C (aromatic rings) bond [19]. A low peak at 424 cm^{-1} corresponds to the phosphoric element or aromatic structure of ACT. In addition, as a significant effect, the activation with H_3PO_4 increases the amount of oxygen in different functional groups such as carboxylic, phosphate groups, hydroxyl, and phenolic hydroxyl on the activated carbon surface.

3.1.2. *Determination of pH_{pzc}*

These properties are essential because the interactions between the functional groups of the ACT surface and the ions in the solution strongly depend on the superficial charge. 25 mL of 0.01 M NaCl was placed in different closed Erlenmeyer flasks and added 0.1 M of NaOH or 0.1 M of HCl solutions for adjusting the pH value from 2 to 10 for each flask. Then 0.25 g of ACT was added and stirred for 24 h to reach equilibrium at ambient temperature.

The plot to determine the point of zero charges for ACT is represented in Figure 2. The pH_{pzc} corresponds to the intersection point of the pH_{ini}, and the pH_{fin} plot demonstrated a zero charge of the material. It was found to be equal to 3.7, close to pH_{pzc} values found by many investigators preparing activated carbon by H_2SO_4 [20,21].

The pH_{pzc} value suggests that ACT is acidic; this indicates that the concentration of active sites is greater than that of the basic one of the ACT surfaces. After oxidation, a large number of O–C=O groups

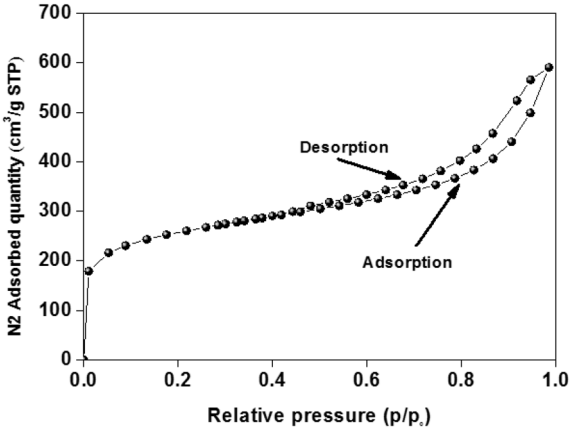

Figure 3. Adsorption and desorption isotherms of N_2 at 77 K for ACT.

Table 1. Characteristics of activated carbon

Physical properties	Values
DFT pore size (nm)	20.35
Surface external (m^2/g)	475.05
Surface interne (m^2/g)	429.79
Surface BET (m^2/g)	904.8

were introduced in the material, which increased the surface acidity significantly.

At low pH 3.7, the adsorbent material presents a positive surface charge and a negative charge for pH > pHzc, since OTC is linked to the ACT structure, and the functional groups were strongly protonated.

3.1.3. *Surface area and pore characteristics*

The characteristic of ACT material, such as the specific surface area, the pore size, and distribution, were determined from nitrogen adsorption-desorption isotherm at 77 K using the BET method and the Non-Local Density Functional Theory (NLDFT) software for analysis. Table 1 summarizes the textural properties of produced ACT.

Figure 3 exhibits the isotherm adsorption–desorption of nitrogen for ACT prepared by chemical activation. As observed, the adsorption isotherm of N_2 onto ACT corresponds to a type I or IV isotherm according to the IUPAC classification with an H3 hysteresis loop, typical of character.

The plateau of the isotherm at high relative pressures (P/P_o) results from the presence of the mesoporous structure. For the obtained material, the percentage of the surface area attributed to mesopores and micropores to the total surface area are 52.5 and 47.74%, respectively. More specifically, the isotherms of ACT display a relatively large hysteresis loop, suggesting the existence of larger size pores and high specific surface area. As a result, the BET-specific surface area (S_{BET}) for the ACT can be determined as 904.848 $m^2 \cdot g^{-1}$.

The S_{BET} of ACT compared to various activated carbon materials prepared by chemical activation with H_3PO_4. It was unearthed that ACT has a suitable surface area, making it a promising adsorbent for OTC and other pollutants such as dyes and metals [24–26].

In addition, compared to those data found in the literature, this study shows that the phosphoric acid activation process is an exciting approach for activated carbon production. This result could be due to the phosphoric acid action that moves impurities from precursors' materials [27,28].

Therefore, it can be inferred that the excellent S_{BET} and the development of large mesoporous structure 52.5% with a portion of micropores created by the chemical activation leading to the high adsorption of OTC molecules.

Table 2. XRF analysis of ACT

Element	Wt (%)
C	88.90
O	09.18
Na	00.18
Al	00.08
P	00.99
S	00.09
Cu	00.33
Zn	00.24

3.1.4. *Chemical composition analysis*

The XRF analysis involves the determination of element composition.

The analysis results depicted in Table 2 indicated that C and P are the major abundant cotenant and Na, Mg, Al, Si, S, Ca, Fe, Ni, Cu, and Zn at trace level. The high carbon yields are due to the original composition of raw biomass of cellulose, phenolic, and

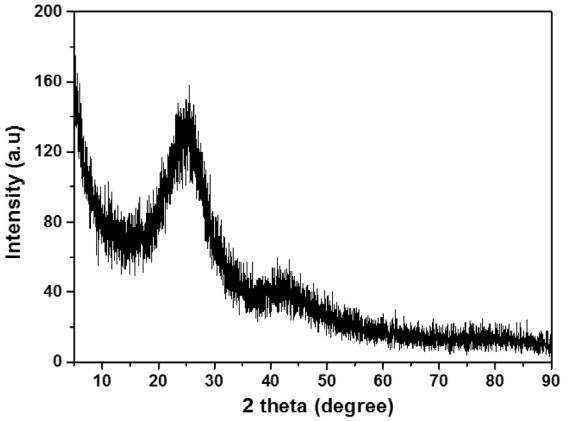

Figure 4. XRD diffractogram of the ACT.

lignin, while the P content is original chemical activation agent.

3.1.5. *X-ray diffraction (XRD) analysis*

The XRD analysis result of the ACT adsorbent is shown in Figure 4. The activated carbon is amorphous and composed of microcrystalline carbon fragments randomly. It has graphite-like microcrystalline, single reticular plane carbon, and non-organized parts. Figure 4 illustrates the XRD pattern of ACT activated with H_3PO_4 at 500 °C shows characteristic peaks at $2\theta = 28°$ and can be indexed to (002) and (100) diffraction for typical graphite carbons [29]. Furthermore, the broad peak detected at $2\theta = 28°$ indicates amorphous ACT.

3.1.6. *SEM analysis*

The scanning electron microscopy (SEM) was adopted to visualize the sample morphology of the prepared ACT using the SEM model (FEI Quanta 200) operating at 15 kV acceleration voltage and the analysis is portrayed in the photographs Figure 5(a,b).

It can be observed that the surface of raw biomass, as displayed in Figure 5(a), was heterogeneous form, highly packed, poreless, and had smaller cavities. These characteristics suggest that the raw Artichoke biomass comprises lignin, cellulose, and hemicellulose.

Figure 5(b), shows that the activation at 500 °C with H_3PO_4 resulted in the creation of a considerable number of pores due to the removal of volatiles matter. These findings have been approved by the

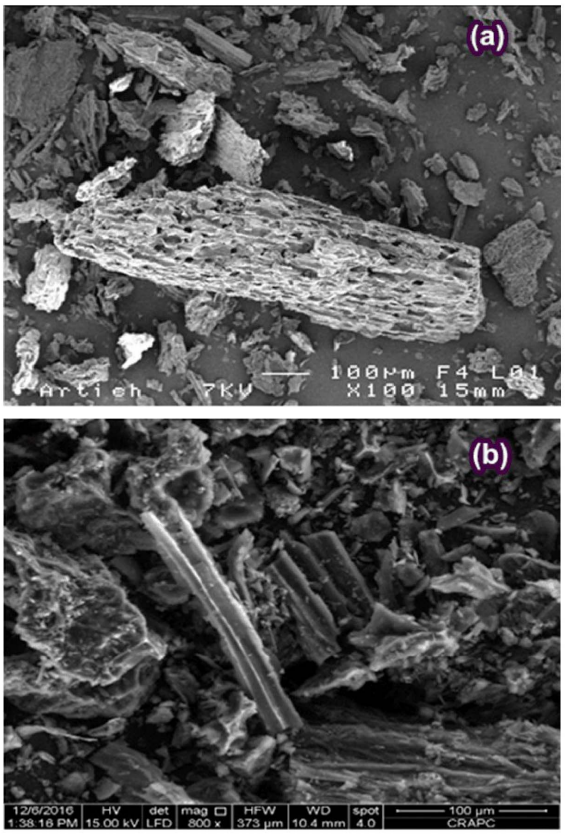

Figure 5. SEM analysis of raw artichoke biomass (a) and ACT (b).

well-developed pores observed on the surface of the ACT (Figure 5(b)). Pore development in the ACT during the activation process was also signeficant. This phenomenon would enhance the ACT surface area and pore volume under the diffusion of H_3PO_4 molecules into the pores, thereby increasing the $H_3PO_4^-$ carbon reaction via acid hydrolysis processes creating more pores and crosslink [30]. Khezami and Capart [31] have stated comparable effects of the acidic activating agents on the pin wood structural characteristics.

3.2. *Adsorption study*

3.2.1. *Effect of the initial pH*

The pH variation is considered to simulate and highlight the real conditions concerning the interpretation of the functional groups' manifestation that

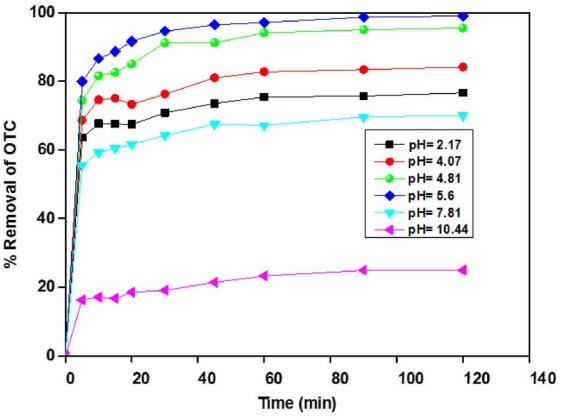

Figure 6. Effect of pH on the adsorption of OTC onto ACT, ACT dose = 1 g·L^{-1}, [OTC] = 50 mg·L^{-1}.

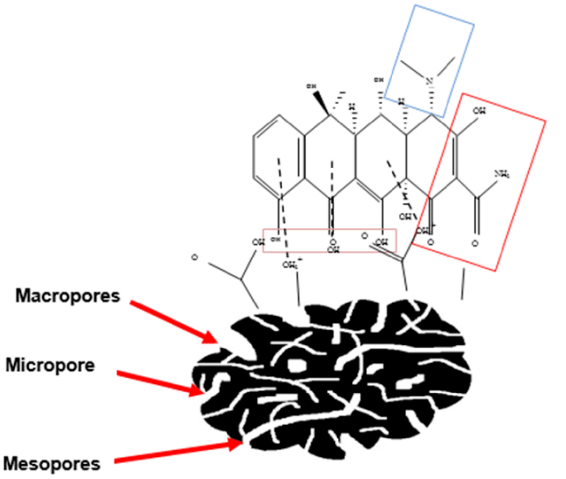

Figure 7. Schematic mechanism of OTC adsorption onto ACT.

leads to the acidic or basic character of the adsorbent surface. It causes the protonation states of OTC molecule and the structure that can involve different mechanisms of complex action responding to divers pH values of the solution with adsorbent [32].

Batch adsorption experiments were performed using a fixed dose of adsorbent (1 g·L^{-1}) at 25 °C, initial OTC concentration (50 mg·L^{-1}). The pH was adjusted over the range of 2 to 11 by adding either NaOH or HCl (0.1 M) solutions.

The obtained results are illustrated in Figure 6. As can be seen, the OTC uptake decreased at low pH when pH is below 5.8, and the removal capacity of OTC is affected by increasing pH from 2 to 4; the higher OTC removal is noted at pH ~ 4.81. However, the adsorption capacity decreased sharply from 16.5 to 30 mg·g^{-1} when pH varied from 4.88 to 10.44. These results were consistent with those found by Zhao *et al.* [33,34]. These adsorption values were consistent with the results of Zhao *et al.* [35,36]. They examined the adsorption of diclofenac onto goethite under different pH and found that the adsorption capacity strongly depends on the solution pH [35]. Earlier, they investigate the adsorption behaviours of OTC onto Sediment in the Weihe River at different solution pH. They did not remark any effect on the adsorption capacity at pH ranging from 4.0 to 7.0. Still, they noticed a decrease in the 2.0 to 4 and 7.0 to 9.0 ranges.

The decrease in adsorption capacity could be explained by the decreasing of electrostatic attractions between the ACT surface and $OTCH^{3+}$ (cationic or positive) species. Furthermore, at low pH values, the competition between H_3O^+ and $OTCH_3^+$ for the adsorbent sites possibly will partially overcome the OTC removal. At solution pH 2–7.81, the OTC is in its zwitterionic (neutral or amphoteric ion) form $OTCH_2$ 0. It is controversial that the significant OTC removal in its zwitterionic form at solution pH 4.81–7.86 could be subjected to other interactions such as complexation [37]. While solution pH > 7.86, OTC is negatively charged (anion), which resulted in increasing repulsion with the ACT adsorbent surface [38]. Different interactions mechanism can be illustrated in Figure 7.

3.2.2. *Effect of the adsorbent dose*

The adsorbent amount is considered a significant parameter in the adsorption phenomenon. Since the surface is available and subsequently, the ACT dose can considerably affect the overall performance of the adsorption process. Its effect on the OTC adsorption was investigated by introducing different amounts ranging from 0.2 to 2 g·L^{-1} into 100 mg·L^{-1} OTC solution at free pH~5.8 and 25 °C (Figure 8).

The OTC removal increases to 98.54% with raising the ACT dose to 1 g·L^{-1} and remains almost unchanged after that. It can be discerned that the amount of OTC adsorbed q_t (mg·g^{-1}) declined significantly from 99.43 to 51.058 mg·g^{-1} when raising the

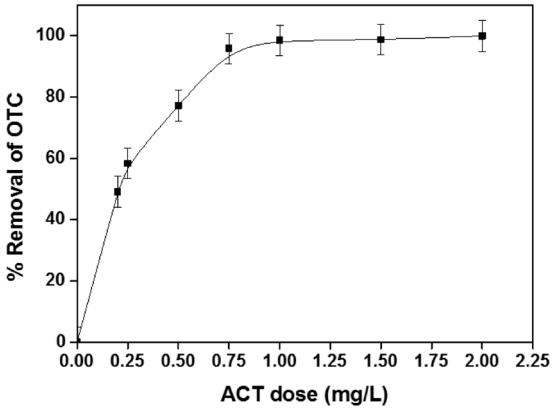

Figure 8. Removal versus adsorbent dose, pH = 5.5, [OTC] = 100 mg·L^{-1}.

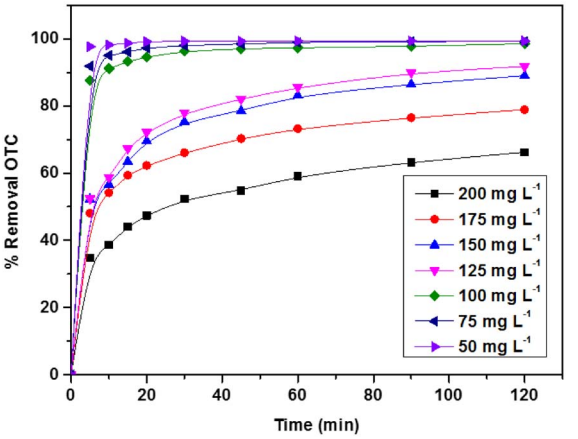

Figure 9. Effect of initial concentrations on the OTC removal (%) on ACT, pH = 5.5, ACT dose = 1 g·L^{-1}.

adsorbent dose. This trend can be accredited to the availability of many unsaturated binding sites on the adsorbent surface during the adsorption process [39] Figure 8. For an ACT concentration of 1 g·L^{-1}, the q_e and R (%) were 99.43 mg·g^{-1} and 98.54%, respectively, for 100 mg·L^{-1} of OTC.

This phenomenon may be due to the decrease in total adsorption surface area available to OTC resulting from overlapping or aggregating adsorption sites [40].

3.2.3. *Effect of OTC initial concentration and contact time*

The influence of OTC initial concentration on the mass transfer between the OTC bulk solution and the ACT solid phase is investigated in a batch reactor for various OTC concentrations varying between 50 and 200 mg·L^{-1}. Therefore, it is carried out with a fixed amount of adsorbent of 1 g·L^{-1} at pH ~ 5.5 and 25 °C. The obtained results are exposed in Figure 9. A sharp increase of the adsorption capacity with increasing initial pollutant concentrations can be seen. The same figure also reveals that the adsorption of OTC for different concentrations appeared to have similar kinetic behavior. However, at low concentrations, the rate of adsorption was higher and saturated rapidly related to more active sites for the adsorption. This behavior indicates that high concentration contributes to saturating the adsorption site and provides a significant driving force for the migration of OTC molecules to overcome the mass transfer resistance of OTC on the adsorbent solid surface [41].

In addition, the results shown in Figure 9 demonstrate that the adsorption kinetics are subdivided into two steps. The first step, the adsorption, is extremely rapid at the initial stage for the low initial concentration; this Behavior is related to the external diffusion and slows down as the diffusion of the adsorbate into the interior surface of the particles the adsorption proceeds. In the first 30 min, the percentages of total amounts adsorbed are about 99.26%, 96.28%, and 74.10% for initial OTC concentrations 50, 100, and 200 mg·L^{-1}, respectively. After that, the second step is slow until the constant concentration reaches an equilibrium time within 120 min due to the available OTC molecules in solution and their slow pore diffusion into the bulk of adsorbent [42].

The results can also be related to hydrophobic interactions between OTC molecules and ACT materials [43]. Furthermore, OTC aggregation may also occur on the adsorbate surface at high OTC concentrations. The OTC adsorption capacity (q_e) increases from 50 to 165 mg·g^{-1} with increasing initial OTC concentration from 50 to 200 mg·L^{-1}; this behavior indicates that ACT is not efficient at high OTC concentrations, and this step elucidates the intraparticle diffusion as the dominant mechanism in the kinetic adsorption process.

4. Equilibrium isotherms and kinetic models

The equilibrium adsorption isotherm study is fundamental to reveal that the adsorption performance could indicate the surface properties, the affinity of adsorbent, and the distribution between the solution and the adsorbent phase, instead of understanding the adsorption mechanism onto activated carbon, as well as the nature of molecular forces. Besides, this isotherm is valuable in estimating the adsorption capacity and the effectiveness of the adsorbent.

The adsorption data have been suggested to Langmuir and Freundlich [35]. All these models have been generally applied to express the experimental data of adsorption [36].

The Langmuir model form is given by:

$$\frac{C_e}{q_e} = \frac{1}{bq_m} + \frac{C_e}{q_o}. \tag{2}$$

The Freundlich model is given by:

$$\log q_e = \log K_f + \frac{1}{n}\log C_e \tag{3}$$

C_o and C_e are the initial and equilibrium OTC concentration (mg·L^{-1}) in these equations. q_e, q_m are the OTC adsorbed amount at equilibrium and maximal capacity (mg·g^{-1}). b: is the Langmuir constant (L·mg^{-1}).

k_f and n are the Freundlich constants related to the adsorption capacity and intensity, respectively. All the parameter models are summarized in the Table 3.

Furthermore, the essential characteristic of the Langmuir isotherm is described by a separation factor or dimensionless equilibrium parameter (R_L) shown in Table 3 [44]:

$$R_L = \frac{1}{1 + bC_o}. \tag{4}$$

It appears from the correlation coefficient (R^2) that the Langmuir model adequately fits the experimental results over the investigated concentrations range. At natural initial pH (5.6), the maximum adsorption capacity of dried *ACT* was q_m is 126.58 mg·g^{-1} indicating that this material is promising in treating OTC solutions (50–200 mg·L^{-1}).

According to the R_L values calculated for the initial OTC concentrations is $0.01 < R_L < 0.13$. Since the R_L values are within the range of 0–1, it can be concluded that the adsorption of OTC onto ACT appears to be a favorable process.

The adsorption is nonlinear when the n value is less than 1. This result indicates that the heterogeneous surfaces of ACT are weakly bonded to the adsorbate by weak free energies, so adsorption is essentially dominated by adsorption rather than partitioning [45].

The adsorption kinetic is undertaken to understand the dynamics of the adsorption reaction in terms of the rate constant and to determine the possible rate-controlling step of the adsorption mechanism.

The adsorption kinetic data were evaluated by using general linearized forms kinetic models, and the goodness of fit was estimated by the regression coefficient (R^2).

The pseudo-first-order and pseudo-second-order models are given, respectively by [46,47]:

$$\log(q_e - q_t) = \log(q_e) - \frac{k_1}{2.303}t \tag{5}$$

$$\frac{t}{q_t} = \frac{1}{k_2 q_e^2} + \frac{t}{q_e}. \tag{6}$$

In these equations, q_t and q_e (mg·g^{-1}), are the adsorption capacities at time t and equilibrium k_1, k_2 are the rate constant for pseudo-first-order and pseudo-second-order.

The intraparticle diffusion equation is expressed as Weber and Morris, 1963, [48]:

$$q_t = k_{\text{dif}} t^{0.5} + C, \tag{7}$$

where K_{dif} is the intraparticle diffusion rate (mg·g^{-1}·min) and C is the intercept.

The Elovich kinetic model is described by [49,50]:

$$q_t = \frac{1}{\beta \ln(\alpha\beta)} + \frac{1}{\beta}\ln(t), \tag{8}$$

where α and β are the Elovich constants.

The initial rates of adsorption reaction are calculated according to the pseudo-first-order and pseudo-second-order model by the following equations:

$$h_1 = k_1 q_e^2 \tag{9}$$

$$h_2 = k_2 q_e^2. \tag{10}$$

The constants and parameters calculated from all kinetic models tested are presented in the table.

The obtained results show the model's applicability on the dynamic adsorption of OTC onto ACT based on the regression coefficient and q_m values. In the actual study, the kinetic data were well fitted by the pseudo-second-order kinetic model. The

Table 3. Isotherms parameters models and separation factor R_L of OTC adsorption onto ACT

pH	Langmuir				Freundlich		
	R^2	b (L·mg^{-1})	q_m (mg·g^{-1})	R_L	R^2	n	K_f (L·g^{-1})
2.0	0.9937	0.0625	181.82	0.1379	0.7850	0.0670	129.02
4.0	0.9980	0.2960	136.98	0.0326	0.9310	0.0546	98.73
5.6	0.9989	0.5600	126.58	0.0175	0.9544	0.0753	87.54
8.0	0.9984	0.9050	105.26	0.0109	0.8653	0.0562	84.22
10.0	0.9950	0.9380	78.13	0.0105	0.3312	0.0416	66.49

Table 4. Parameters of different adsorption kinetics

Concentration (mg·L^{-1})	50	75	100	125	150	175	200
q_{exp} (mg·g^{-1})	48.59	73.49	99.94	122.12	143.22	156.68	164.98
				Pseudo-first-order			
q_e (mg·g^{-1})	0.1962	2.03	14.63	32.17	41.82	44.22	50.09
K_1 (g·mg^{-1}·min^{-1})	0.0109	0.0089	0.0201	0.0275	0.0297	0.0344	0.0337
h_1 (mg·g^{-1}·min^{-1})	0.0004	0.03	4.30	28.42	51.96	67.26	84.52
R^2	0.0125	0.2641	0.4462	0.7943	0.8448	0.8698	0.8839
				Pseudo-second-order			
q_e (mg·g^{-1})	50	75.02	99.80	121.95	142.85	77.94	71.42
K_2 (g·mg^{-1}·min^{-1})	0	0.0505	0.0109	0.0047	0.0035	0.0274	0.0575
h_2 (mg·g^{-1}·min^{-1})	0	284.02	108.76	69.89	72.04	166.33	291.60
R^2	0.9999	0.9997	0.9995	0.9993	0.9990	0.9967	0.9994
				Intraparticle diffusion			
K_i (mg·g^{-1}·min$^{-0.5}$)	2.64	4.26	5.85	7.62	9.07	9.72	10.46
C	30.66	43.21	53.81	58.5247	67.19	76.77	78.37
R^2	0.2333	0.3041	0.3525	0.4524	0.4725	0.4376	0.4637
				Elovich			
α	110.24	120.44	132.29	114.94	127.51	156.91	152.35
b	0.1255	0.0796	0.0594	0.0472	0.0399	0.0369	0.0348
R^2	0.4766	0.5579	0.6068	0.7013	0.7175	0.6849	0.7082

R^2 values obtained from the pseudo-second-order kinetic model were higher; this indicates the excellent agreement of this model to describe all the experimental adsorption data of OTC onto ACT material. Kinetics of OTC adsorption onto ACT process, suggests that the adsorption rate-limiting step may be the chemisorption's adsorption. The adsorption of OTC occurs probably via surface complexation reactions at specific sorption sites, highlighting the importance of the surface functional groups activated by our experimental condition. Also, it was perceived that the calculated (q_e) values increased with an increase in the initial concentration of OTC.

In addition, the calculated q_e (32.3 mg·g^{-1}) value close to the experimental data (30.85 mg·g^{-1}) indicated that the pseudo-second-order model than the pseudo-first-order one could approximate OTC adsorption onto activated carbon more favorably.

Pseudo-second-order kinetic model suggests that the predominant process here is chemisorption. Similar data were also reported by other investigates [51,52].

Based on the results presented in the table, the Elovich model did not fit perfect linear forms ($0.47 < R^2 < 0.70$) for the adsorption of OTC onto activated carbon.

5. Temperature effect and thermodynamic parameters of OTC adsorption

Temperature is a crucial parameter in the adsorption process [53]. It has two significant effects, i.e., it enhances the diffusion rate of the adsorbate molecules through the outer boundary layer and into the adsorbent particles' pores by decreasing the solution's viscosity. Moreover, it improves the solubility of the adsorbate.

To adequately understand the temperature influence on the adsorption of OTC by ACT, experiments were carried out in a temperature range from 15 to 55 °C.

This choice of temperature is justified by the climatic conditions prevailing during winter and summer, in which the elimination is carried out on an industrial scale. This study can be investigated under the operating conditions: ACT dose: 1 g·L^{-1}; contact time: 120 min; OTC initial concentration: 200 mg·L^{-1} and the free pH of the solution.

Figure 10 manifests the influence of temperature on the adsorption evolution of the OTC on the ACT. It can be noticed that the increase in temperature in the studied range promotes the OTC removal rate on ACT up to reaching equilibrium. This finding could be explained by higher energy input, which can break the associations between the OTC molecules and water. This phenomenon causes a decrease in the viscosity of the solution, resulting in a rise in the motion and diffusion rate of the OTC molecules in the film surrounding the ACT grain. At the same time as the pores amount expand and improve the diffusion in the pores.

In other words, the increase in energy in the process can reduce the restrictions in film diffusion and pore diffusion. In addition, the OTC molecules acquire more energy to establish stronger interactions with the active sites of the ACT. Several authors in the literature have reported this positive effect of temperature on adsorption [8].

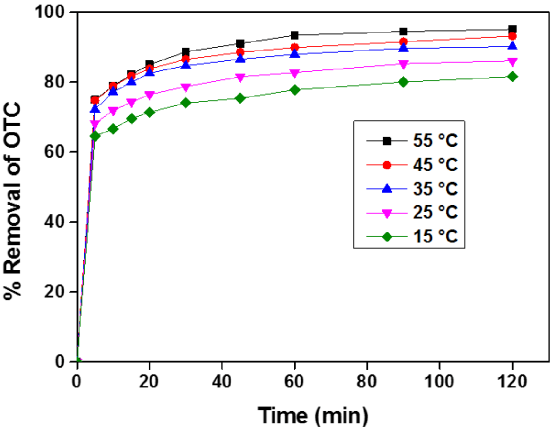

Figure 10. Temperature effect on Adsorption of OTC onto ACT, pH = 5.5, dose ACT = 1 g·L^{-1}, [OTC] = 200 g·L^{-1}.

The enthalpy (ΔH°_{ads}), entropy (ΔS°_{ads}), and free energy (ΔG°_{ads}) thermodynamic standard parameters changes are due to the transfer of OTC from the solution onto the solid–liquid interface. The thermodynamic parameters are an approach used to highlight the OTC adsorption mechanism (Table 5); they are computed according to the following equations:

$$\Delta G^\circ_{ads} = -RT \ln K_d \tag{11}$$

$$\Delta G^\circ_{ads} = \Delta H^\circ_{ads} - T\Delta S^\circ_{ads}, \tag{12}$$

where K_d is the equilibrium constant is calculated by the following relation [31,54]:

$$K_d = \frac{(C_o - C_e)}{C_o}. \tag{13}$$

The experiments were carried out from 288 to 328 K for an initial OTC concentration of 150 mg·L^{-1}, and the values of ΔH°_{ads} and ΔS°_{ads} were determined from the slopes and intercepts of the linear regression of $\ln(K_d)$ against $(1/T)$ linear plot (14) (see Supplementary Figure S2):

$$\ln K_d = \left(\frac{\Delta S^\circ}{R}\right) - \left(\frac{\Delta H^\circ}{RT}\right). \tag{14}$$

Based on the results of Table 4, the negative value of ΔG°_{ads} is given for all temperatures indicating that OTC adsorbed onto ACT is spontaneous.

Table 5. Thermodynamic parameters of OTC removal onto ACT

ΔH (J·mol^{-1})	ΔS (J·mol^{-1}·K^{-1})	ΔG (kJ·mol^{-1})				
		288 K	298 K	308 K	318 K	328 K
15.5469	72.31	−20.81	−21.53	−22.25	−22.97	−23.70

It was observed that with increasing temperature, ΔG°_{ads} decreases, implying that adsorption becomes thermodynamically more favorable. The positive ΔH°_{ads} further confirms the endothermic nature of the OTC adsorption process, while the value of ΔH°_{ads} is very tiny. This result may be due to a bit of desorption of pre-adsorbed water. Supports this assumption the positive entropy ΔS°_{ads} that means the increased disorder during the OTC adsorption process at the solid-solution interface. This behavior is probably due to the displacement of water molecules sorbed on the solid surface or some structural changes in the adsorbent and adsorbate during the adsorption process [31,55].

6. Computational studies

In this work, the configurations of OTC in water and vacuum media were optimized using DFT calculation and the corresponding FMO (Frontier Molecular Orbitals), resulting in HOMO (Highest Occupied Molecular Orbital) and LUMO (Lowest Unoccupied Molecular Orbital) are shown in Figure 11. The MEP (Molecular Electrostatic Potential) was computed to discuss the electrophile and nucleophile character position of OTC [56], illustrated by blue and red area, respectively (Figure 11).

The HOMO is located mainly on C=O N–C and C–OH groups. At the same time, the LUMO is situated on the C=C of the aromatic ring C–OH and a weak part on C=O, indicating that these molecular moieties are from active sites for adsorption [57]. Additionally, the MEP predicts a dominant electrophilic character of OTC except around the oxygen, in which strong negative potential was observed. This high polarity of OTC-molecule favors the intermolecular electrostatic and/or weak dipolar interactions [58].

Furthermore, an attempt has been realized to acquire in-depth erudition on the adsorption mechanism of OTC onto ACT. Two models of substrate surface were proposed, cellulose and cellulose-H_2PO_3, having the area of 16.40 × 20.76 Å^2 (Figure 11). The choice of the two surface models illustrates the adsorption on the raw biomass (Artichoke) before and after acid treatment (ACT). Figure 11 shows that the OCT molecule adsorbed longitudinally on both surfaces. The aromatic cycle is almost in a parallel configuration, indicating that π-electrons are strongly involved in the adsorption mechanism. Besides, the oxygen atoms of OTC are tilted toward the substrates, with distances close to covalent bonds, suggesting that these last may occur. Additionally, the adsorption energy values are given in Table 6. The adsorption energy was found to be −562.92 kJ·mol^{-1} and −116.84 kJ·mol^{-1} for cellulose and cellulose-H_2PO_3, respectively. These high energy values confirm again that OTC molecules are strongly adsorbed, maybe through the chemisorptive process, and their negative values indicate the spontaneity of the process. Therefore, the relative stability and adsorption energy for the two surfaces follow the order:

$$\text{OTC/cellulose} > \text{OTC/cellulose-}H_2PO_3.$$

Furthermore, the charges distribution of molecules was illustrated by the electrostatic potential maps, and the MEP maps of OTC-cellulose, and OTC-cellulose H_2PO_3 were calculated using the DFT method. From Figure 11, the MEP negative regions mentioned by red and yellow colors were located on the oxygen and nitrogen, indicating that these sites are the most appropriate for electrophilic attacks. Otherwise, electron transfer increases the adsorption and favors the intermolecular electrostatic interactions [58].

7. Comparison of the adsorption of OTC on various adsorbents

To evaluate the removal efficiency, a comparison of maximum adsorption capacity obtained from the

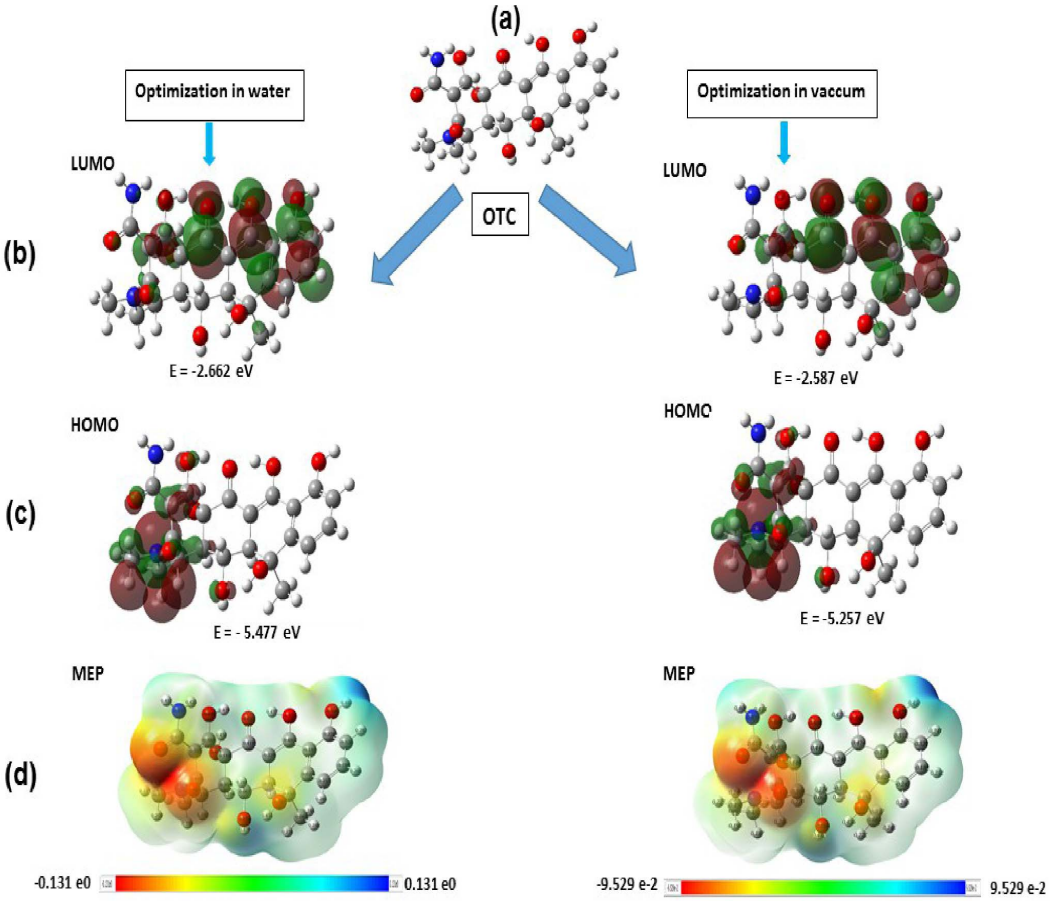

Figure 11. DFT-optimized configurations, FMOs (HOMO and LUMO) and MEP plots of OTC adsorption onto Cellulose and Cellulose-H_2PO_3 system.

Table 6. Adsorption values using different substrates (cellulose, cellulose-H_2PO_3)

Structure	Total energy (kJ/mol)	Adsorption energy (kJ/mol)	Rigid adsorption energy (kJ/mol)	Deformation energy (kJ/mol)	Oxytetracycline: dEad/dNi
Cellulose (2 × 2) (100)	74.45	−562.96	−31.59	−531.36	−562.96
Cellulose H_2PO_3 (2 × 2) (100)	72.60	−116.84	−34.65	−82.18	−116.84

Langmuir model of the prepared ACT with investigations findings towards the OTC drug removal at the optimum operating conditions is given in Table 7.

The obtained results revealed that ACT exhibits a great extent of adsorption performance compared to other adsorbents materials reported in the literature for the same contaminant. Moreover, this comparative study indicated that ACT could be a promising and satisfactory adsorbent for pharmaceuticals and dyes removal.

8. Conclusion

An undeniable and low-cost activated carbon produced from agriculture by-products, using the chemical activation, has been identified as an effective adsorbent for OTC removal from wastewater. Phosphoric acid was used to promote bond cleavage reactions and the formation of crosslinks through different mechanisms such as cyclization and condensation and its combination with organic species to form

Table 7. Comparison of the OTC maximum adsorption capacity obtained from Langmuir isotherm at optimal operating conditions on various adsorbents

No	Materials	q_m (mg/g)	References
1	The residue of Flueggea suffruticosa	129.9	[59]
2	Corn stalk	88.5	[60]
3	Aerobic granular sludge	91.74	[15]
4	Surfactants modified sepiolite	39.18	[61]
5	Sediment	81.8869	[62]
6	Forest	263.8	[63]
7	Wood	254.1	[63]
8	ACT	126.58	This work

phosphate and polyphosphate bridges that bond and crosslink fragments. These fragments were employed to remove OTC molecules as a pharmaceutical pollutant from an aqueous solution and achieve the status of green environmental policy. The techniques characterization of activated carbon the SEM image clearly showed a heterogeneous surface morphology of ACT signifying the presence of pores and appreciate surface area obtained after carbonization processes with H_3PO_4 acid treatment. The FTIR spectroscopy revealed the presence of different peaks corresponding to the functional groups formed after activation by reducing the hydroxyl group and creating a carboxylic function. XFR analysis indicates that the C, O, and P are the most elements composition. The XRD analysis confirmed that the ACT displayed a crystallinity structure characterized by an amorphous nature. The large surface area and the developed porous material structure after the activation process proved by BET analysis reveal that the adsorbent is a typical mesoporous material.

As the results of the experimental studies revealed, a minimum contact time for the adsorption equilibrium was less than 2 h, and for a fixed amount of adsorbent 1 g·L^{1-}, an increase in the initial concentration of the solution reduces the contact time required to reach equilibrium. In addition, the OTC adsorption increases with an increase in the temperature, thereby suggesting the process to be endothermic.

The description of adsorption behavior by DFT calculations showed superior ability and a good agreement between experimental and theoretical investigation due to the different interaction energies of adsorbent functional groups (C=O, –OH, C-POx) OTC molecules.

Finally, this study demonstrates the outstanding adsorption efficiency of ACT materials to OTC drugs from an aqueous solution, and it has provided feasible, economical, and valuable practical water treatment applications.

Conflicts of interest

Authors have no conflict of interest to declare.

Acknowledgments

This work was supported by the King Khalid University, Abha, Saudi Arabia (by grant G.R.P./206/42). We express our gratitude to the Deanship of Scientific Research, King Khalid University, for its support of this study. The authors are thankful to DGRSDT for helping through the analysis of the emerging pollutants project, research center CRAPC, for providing instrumental facilities for characterization materials in carrying out this work.

Supplementary data

Supporting information for this article is available on the journal's website under https://doi.org/10.5802/crchim.161 or from the author.

References

[1] Y. Sun, H. Li, G. Li, B. Gao, Q. Yue, X. Li, *Bioresour. Technol.*, 2016, **217**, 239-244.

[2] J. Fick, H. Soderstrom, R. H. Lindberg, C. Phan, M. Tysklind, D. G. Larsson, *Environ. Toxicol. Chem.*, 2009, **28**, 2522-2527.
[3] M. Gholami, R. Mirzaei, R. R. Kalantary, A. Sabzali, F. Gatei, *Iran. J. Environ. Health Sci. Eng.*, 2012, **9**, article no. 19.
[4] Q. Wang, S. R. Yates, *J. Agric. Food Chem.*, 2008, **56**, 1683-1688.
[5] Y. Sun, Q. Yue, B. Gao, Y. Wang, Y. Gao, Q. Li, *Powder Technol.*, 2013, **249**, 54-62.
[6] M. C. Ncibi, M. Sillanpää, *J. Hazard. Mater.*, 2015, **298**, 102-110.
[7] B. D. Blair, J. P. Crago, C. J. Hedman, R. D. Klaper, *Chemosphere*, 2013, **93**, 2116-2123.
[8] A. Mlayah, S. Jellali, A. A. Azzaz, M. Jeguirim, H. Sellalmi, N. Hamdi, *C. R. Chim.*, 2021, **24**, 7-22.
[9] J. Mittal, V. Thakur, A. Mittal, *Ecol. Eng.*, 2013, **60**, 249-253.
[10] M. Khnifira, A. Mahsoune, M. E. Belghiti, L. Khamar, M. Sadiq, M. Abdennouri, N. Barka, *Curr. Res. Green Sustain. Chem.*, 2021, **4**, article no. 100085.
[11] S. J. Ahmed Amine Azzaz, R. Souissi, K. Ergaieg, L. Bousselmi, *Environ. Sci. Pollut. Res.*, 2017, **24**, 18240-18256.
[12] D. G. Larsson, C. de Pedro, N. Paxeus, *J. Hazard. Mater.*, 2007, **148**, 751-755.
[13] J. Jjagwe, P. W. Olupot, E. Menya, H. M. Kalibbala, *J. Bioresour. Bioprod.*, 2021, **6**, 292-322.
[14] K. R. M. Shanmugasundaram Kamalakannan, K. Palanisamy, A. Thomas, R. Ben Said, M. Prakash, M. Hochlaf, *Chemosphere*, 2022, **286**, article no. 131612.
[15] H. Mihciokur, M. Oguz, *Environ. Toxicol. Pharmacol.*, 2016, **46**, 174-182.
[16] A. Guediri, A. Bouguettoucha, D. Chebli, N. Chafai, A. Amrane, *J. Mol. Struct.*, 2020, **1202**, article no. 127290.
[17] T. L. Jinlong Zhang, X. Li, Y. Liu, N. Li, Y. Wang, L. Xiaoping, *J. Hazard. Mater.*, 2021, **412**, article no. 125185.
[18] M. K. W. Boumya, A. Machrouhi, M. Abdennouri, M. Sadiq, M. Achak, G. Serdaroğlu, S. Kaya, S. Şimşek, N. Barka, *J. Mol. Liq.*, 2021, **331**, article no. 115706.
[19] L. C. Jianzhong Xu, H. Qu, Y. Jiao, J. Xie, G. Xing, *Appl. Surf. Sci.*, 2014, **320**, 674-680.
[20] A. H. Jawad, R. A. Rashid, M. A. M. Ishak, L. D. Wilson, *Desalination Water Treat.*, 2016, **57**, 25194-25206.
[21] A. H. Jawad, A. S. Abdulhameed, M. S. Mastuli, *J. Taibah Univ. Sci.*, 2020, **14**, 305-313.
[22] M. S. Shamsuddin, N. R. N. Yusoff, M. A. Sulaiman, *Proc. Chem.*, 2016, **19**, 558-565.
[23] Y. Kan, Q. Yue, D. Li, Y. Wu, B. Gao, *J. Taiwan Inst. Chem. Eng.*, 2017, **71**, 494-500.
[24] M. B. Ali, H. Jawad, M. Atikul Islam, M. Azharul Islam, S. Shatir, A. Syed-Hassan, S. N. Suripa, Z. A. Al Othman, M. Rizwan Khan, *Surf. Interfaces*, 2020, **21**, article no. 100688.
[25] O. B. Erni Misran, E. M. Situmeang, A. S. Purba, *Alex. Eng. J.*, 2021, **61**, 1946-1955.
[26] Q. Y. Yujiao Kan, D. Li, Y. Wu, B. Gao, *J. Taiwan Inst. Chem. Eng.*, 2017, **239**, 28-36.
[27] M. B. Ali, H. Jawada, M. Atikul Islam, M. Azharul Islam, S. Shatir, A. Syed-Hassan, S. N. Surip, Z. A. Al Othmane, M. Rizwan Khan, *Surf. Interfaces*, 2020, **21**, article no. 100688.
[28] K. S. Oluwatosin Oginnia, G. Oporto, B. Dawson-Andoh, L. McDonald, E. Sabolsky, *Bioresour. Technol. Rep.*, 2019, **8**, article no. 100307.
[29] A. Baghel, B. Singh, P. Pandey, R. K. Dhaked, A. K. Gupta, K. Ganeshan, K. Sekhar, *J. Hazard. Mater.*, 2006, **137**, 396-400.
[30] B. Hong, G. Xue, L. Weng, X. Guo, *Bio Resour.*, 2012, **7**, 4902-4913.
[31] L. Khezami, R. Capart, *J. Hazard. Mater.*, 2005, **123**, 223-231.
[32] K. Y. Foo, B. H. Hameed, *Chem. Eng. J.*, 2011, **173**, 385-390.
[33] Y. Zhao, F. Liu, X. Qin, *Chemosphere*, 2017, **180**, 373-378.
[34] D.-H. Cheng, S.-K. Yang, Y. Zhao, J. Chen, *J. Chem.*, 2013, **2013**, 1-10.
[35] H. Demiral, C. Güngör, *J. Cleaner Prod.*, 2016, **124**, 103-113.
[36] X. Lu, Y. Shao, N. Gao, J. Chen, Y. Zhang, Q. Wang, Y. Lu, *Chemosphere*, 2016, **161**, 400-411.
[37] P.-H. Chang, Z. Li, W.-T. Jiang, J.-S. Jean, *Appl. Clay Sci.*, 2009, **46**, 27-36.
[38] W. Yang, F. Zheng, Y. Lu, X. Xue, N. Li, *Ind. Eng. Chem. Res.*, 2011, **50**, 13892-13898.
[39] Y. N. Prajapati, B. Bhaduri, H. C. Joshi, A. Srivastava, N. Verma, *Chemosphere*, 2016, **155**, 62-69.
[40] V. K. Garg, R. Kumar, R. Gupta, *Dyes Pigm.*, 2004, **62**, 1-10.
[41] B. N. Bhadra, P. W. Seo, S. H. Jhung, *Chem. Eng. J.*, 2016, **301**, 27-34.
[42] V. C. Srivastava, M. M. Swamy, I. D. Mall, B. Prasad, I. M. Mishra, *Colloids Surf. A: Physicochem. Eng. Asp.*, 2006, **272**, 89-104.
[43] A. Vinu, K. Z. Hossain, G. Satish Kumar, K. Ariga, *Carbon*, 2006, **44**, 530-536.
[44] M. Rao, A. V. Parwate, A. G. Bhole, *Waste Manage.*, 2002, **22**, 821-830.
[45] J. Paul Chen, S. Wu, K.-H. Chong, *Carbon*, 2003, **41**, 1979-1986.
[46] F. Yu, J. Ma, S. Han, *Sci. Rep.*, 2014, **4**, article no. 5326.
[47] K. Mahmoudi, N. Hamdi, M. Ben Ali, S. Jellali, E. Srasra, *C. R. Chim.*, 2021, **23**, 689-704.
[48] N. M. Mahmoodi, Z. Mokhtari-Shourijeh, *J. Taiwan Inst. Chem. Eng.*, 2016, **65**, 378-389.
[49] R. Rostamian, H. Behnejad, *Process Saf. Environ. Prot.*, 2016, **102**, 20-29.
[50] M. Wakkel, B. Khiari, F. Zagrouba, *C. R. Chim.*, 2021, **23**, 671-687.
[51] E. Demirbas, N. Dizge, M. T. Sulak, M. Kobya, *Chem. Eng. J.*, 2009, **148**, 480-487.
[52] A. M. Aljeboree, A. N. Alshirifi, A. F. Alkaim, *Arabian J. Chem.*, 2014, **10**, S3381-S3393.
[53] S. E. I. Lebouachera, R. Chemini, M. Khodja, B. Grassl, M. A. Ghriga, D. Tassalit, N. Drouiche, *Eur. Phys. J. Plus*, 2019, **134**, article no. 436.
[54] L. Khezami, K. K. Taha, E. Amami, M. Ghiloufi, L. El Mir, *Desalination Water Treat.*, 2017, **62**, 346-354.
[55] M. C. Silva, L. Spessato, T. L. Silva, G. K. P. Lopes, H. G. Zanella, J. T. C. Yokoyama, A. L. Cazetta, V. C. Almeid, *J. Mol. Liq.*, 2021, **324**, article no. 114771.
[56] A. S. Girgis, M. N. Aziz, E. M. Shalaby, D. O. Saleh, N. Mishriky, W. I. El-Eraky, I. S. A. Farag, *Z. Kristallogr. Cryst. Mater.*, 2016, **231**, 179-187.
[57] R. Bourzami, L. Ouksel, N. Chafai, *J. Mol. Struct.*, 2019, **1195**, 839-849.
[58] I. A. Aguayo-Villarreal, D. Cortes-Arriagada, C. K. Rojas-Mayorga, K. Pineda-Urbina, R. Muniz-Valencia, J. Gonzalez, *J. Mol. Struct.*, 2020, **1203**, article no. 127398.

[59] H. Wang, X. Lou, Q. Hu, T. Sun, *J. Mol. Liq.*, 2021, **325**, article no. 114967.
[60] Y. X. Song, S. Chen, N. You, H. T. Fan, L. N. Sun, *Chemosphere*, 2020, **255**, article no. 126917.
[61] J. Wu, Y. Wang, Z. Wu, Y. Gao, X. Li, *Sci. Total Environ.*, 2020, **708**, article no. 134409.
[62] D.-H. Cheng, S.-K. Yang, Y. Zhao, J. Chen, *J. Chem.*, 2013, **2013**, article no. 652930.
[63] A. Aghababaei, M. C. Ncibi, M. Sillanpaa, *Bioresour. Technol.*, 2017, **239**, 28-36.

Comptes Rendus
Chimie
2022, Vol. 25, Special Issue S2, p. 27-41
https://doi.org/10.5802/crchim.155

Sustainable Biomass Resources for Environmental, Agronomic, Biomaterials and Energy Applications 3 / *Ressources de biomasse durables pour des applications environnementales, agronomiques, de biomatériaux et énergétiques 3*

Competitive bio-sorption of basic dyes onto petiole palm tree wastes in single and binary systems

Biosorption compétitive des colorants basiques sur des déchets de pétiole de palmier dans les systèmes simples et binaires

Sana Jmai [a], **Sami Guiza** [*, a], **Salah Jellali** [b], **Mohamed Bagane** [a] **and Mejdi Jeguirim** [c]

[a] Department of Chemical Engineering Process, National Engineering School of Gabes, University of Gabes, Tunisia

[b] Center for Environmental Studies and Research, Sultan Qaboos University, Al-Khoud 123, Oman

[c] Université de Haute-Alsace Institut de Sciences des Matériaux de Mulhouse 3 rue Alfred Werner 68093 Mulhouse, France

E-mails: sanajmai1@gmail.com (S. Jmai), sami_guiza@yahoo.fr (S. Guiza), s.jelali@squ.edu.om (S. Jellali), drmbag1420@yahoo.fr (M. Bagane), mejdi.jeguirim@uha.fr (M. Jeguirim)

Abstract. This work aimed to study petiole palm tree wastes (PTW) efficiency in removing two basic dyes: Rhodamine B (RB) and Victoria blue B (VBB) from aqueous solutions in single and binary systems under various experimental conditions including the effect of contact time, pH, initial concentration, and temperature. The PTW characterization shows that the PTW is a lingo-cellulosic material. The experimental results indicate that the removal of both dyes was relatively fast, spontaneous, exothermic and occurred on monolayers. Moreover, the adsorption competition between these two dyes on the adsorbent particles surface was important since the Langmuir's adsorption capacities were evaluated to 260.1; 440.1; 168.0; and 417.4 mg/g for RB and VBB in single and binary systems, respectively. These adsorption capacities, even in binary systems, are interesting compared to other raw materials and prove that this abundant agricultural waste can be considered as a promising material for an efficient dyes removal from aqueous effluents.

Résumé. Ce travail vise à étudier l'efficacité des déchets de pétiole de palmier (PTW) pour l'élimination de deux colorants basiques : la Rhodamine B (RB) et le Victoria bleu B (VBB) en solution aqueuse pour des systèmes simples et binaires dans diverses conditions expérimentales, y compris l'effet du temps de contact, le pH, la concentration initiale et la température. La caractérisation du PTW montre

* Corresponding author.

que ce dernier est un matériau ligno-cellulosique. Les résultats expérimentaux indiquent que l'élimination des deux colorants était relativement rapide, spontanée, exothermique et se produisait sur des monocouches. De plus, l'adsorption compétitive entre ces deux colorants basiques à la surface des particules PTW était importante puisque les capacités d'adsorption d'après le model de Langmuir ont été évaluées à 260.1 ; 440.1 ; 168.0 et 417.4 mg/g pour le RB et le VBB dans les systèmes simples et binaires, respectivement. Ces capacités d'adsorption, même en systèmes binaires, sont intéressantes par rapport à d'autres matières premières et prouvent que ces déchets agricoles abondants peuvent être considérés comme matériau prometteur pour une décoloration efficace des effluents aqueux.

Keywords. Petiole palm tree wastes, Dyes, Competition, Adsorption, Characteristics, Modeling.

Mots-clés. Déchets de pétiole de palmier, Colorants, Compétitive, Adsorption, Caractérisation, Modélisation.

Published online: 25 February 2022

1. Introduction

Contaminated effluents discharged by textile, paper, plastics, and dye industries are the main sources of aquatic pollution [1]. These industries generally generate huge amounts of wastewaters that contain mixture of organic and inorganic chemicals that potentially threat the environment quality [2,3] as well as public health [4,5]. For this reason, the treatment of these effluents has been identified as a global environmental concern. Color, which is mainly due to the presence of dyes, is one of the first aspects to be inspected when dealing with wastewater [6]. Even in small quantities (less than 1 ppm for some of them), dyes can be easily detected [7], and potentially toxic to humans and animals [8]. The RB and VBB, as cationic dyes, are widely used as coloring agents in several industries [9]. Their efficient removal from aqueous solutions is therefore a critical issue that has to be seriously taken into consideration.

Many techniques have been suggested for the removal and separation of dyes from contaminated waters, including photo-degradation [10] coagulation [11], electro-oxidation [12–14], and membrane filtration [15]. The real implementation of these technologies is generally hindered by several drawbacks including high capital and exploitation costs, sensitive operational conditions, use of large amounts of chemicals, and the presence of a secondary sludge or byproducts that have to be additionally treated [16].

Adsorption [17,18] has been identified, these last decades, as an attractive method, liable to be used separately or in combination with other technologies for efficient dyes removal from aqueous solutions [19]. The main advantages of adsorption compared to other technologies are simplicity, low cost, and efficiency [20].

Several organic and inorganic adsorbents such as clays [21,22], activated carbon [23,24], cellulose [25–27], carbon nano-tubes [28], magnetic composites [29], bio-composite [30,31], bio-wastes [32–34], industrial by-products, and natural materials such biopolymers, have been utilized in dye removal [35,36]. The use of raw agricultural materials, without any modification, is however highly recommended in order to limit the treatment cost.

In Tunisia, date palm oases generated huge amounts of biomass that can be valorized as a low cost material for wastewater treatment in general and dyes removal in particular. Indeed, more than 4.3 million date palm trees exist in the southern part of Tunisia occupying an area of almost 42,000 ha [37]. Nowadays, there is no specific management option of the produced wastes in these oases. Indeed, the majority of these biomasses are generally thrown away or openly burned raw which induces serious environmental risks.

Date palm wastes have been applied as raw materials for the removal of both organic and inorganic pollutants form wastewaters [38]. Other studies have focused on the synthesis of activated carbons from these wastes and their application for the removal of a wide range of pollutants such as chromium, phenol, methylene blue etc… [39–42]. However, the majority of these studies investigated the behavior of a single contaminant without an important accent on the involved mechanisms. Moreover, RB and VB removal studies are relatively rare compared to other common dyes such as methylene blue and methyl orange. Specific studies dealing with the impact of the presence of mixed dissolved dyes on their removal efficiency from effluents are of great interest.

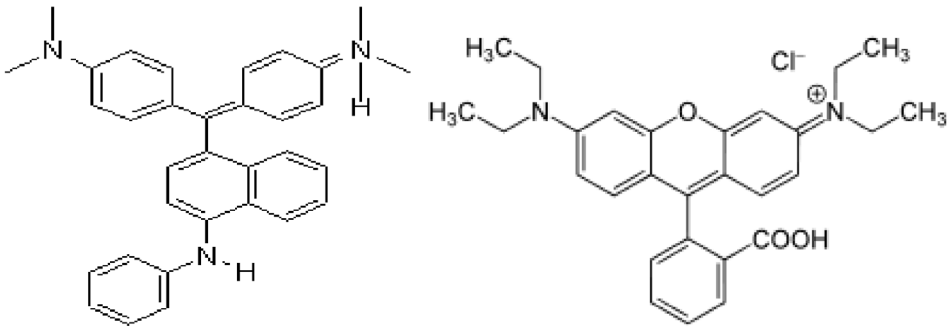

Figure 1. VBB and RB chemical structures.

The present work mainly aims to highlight the effect of the competition process between RB and VB on their removal from aqueous solutions by an abundant biomass (petiole palm tree wastes). For this aim, these two basic dyes removal efficiency from aqueous solutions was precisely assessed in single and binary systems under various experimental conditions such as contact time, pH, initial concentration, adsorbent dose, and temperature. The involved mechanisms were explored through kinetic and isotherm modeling as well as Fourier Transform Infrared (FTIR) analyses.

2. Materials and methods

2.1. *Adsorbent preparation and characterization*

The petiole palm tree waste used in this study was collected from the region of Gabes, southern region of Tunisia. It was ground and sieved in order to obtain a homogenous particles distribution. The mean size of the material is 250 μm. The obtained raw material was not subjected to any form of pretreatment before its use as an adsorbent for dyes removal from aqueous solutions.

The preliminary raw material characterization has targeted the determination of its zero-point charge pH (pH_{PZC}), at this point the surface charge of the adsorbent was neutral. This parameter was determined according to the approach given by Hammani *et al.* [43] for initial pH varying from 2 to 12. Besides the main functional groups of this adsorbent was performed through Fourier transform infra-red (FTIR) spectroscopy using a Brunker-tensor 27 spectrometer.

2.2. *Dye solution preparation and analysis*

Rhodamine B (chemical formula (CF): $C_{28}H_{31}ClN_2O_3$; molar weight (MW) = 479.01 g·mol^{-1}) and Victoria blue B (CF: $C_{33}H_{32}ClN_3$; MW = 506.09 g·mol^{-1}), used in this study for the preparation of the synthetic solutions, were purchased from Acros-Organics from (USA). Their molecular structures are represented in Figure 1. These dyes were used as supplied, without any prior purification.

During the adsorption tests, two stock solutions of RB and VBB of 1000 mg·L^{-1} were prepared and used for solutions preparation at desired concentrations. The efficiency of the adsorbent in removing RB and VBB under the different experimental conditions was determined through the assessment of their absorbance at wavelength values of 553.2 and 614.5 nm, respectively, using an UV spectrophotometer (Genesys 10S UV–Vis).

2.3. *Adsorption experiments*

RB and VBB adsorption experiments were conducted in a 2 L batch reactor provided with a water circulation arrangement to maintain the temperature at the desired value [44]. These experiments consisted in mixing given masses of the adsorbent in 1 L of synthetic solution containing these dyes at a desired concentration in single or binary modes for a fixed contact time. These mixtures were stirred with an

electromagnetic stirrer (Kika-Werke-RT 10 Power) at a constant speed of 200 rpm. The remaining dissolved RB or VBB concentrations were determined using the above cited UV–visible spectroscopy apparatus after centrifugation at 2000 rpm for 5 min with a CENTROMIX mod S-549 apparatus.

All these assays were performed in triplicate and the mean values were reported in this study. The standard deviation for all assays was lower than 5%.

2.3.1. *Effect of initial pH*

The influence of the pH on the adsorption of a series of colored solutions at 20 mg·L^{-1} in RB and VBB was monitored. The pH of the solutions was adjusted to values ranging from 3 to 8 since the behavior of the VBB used is considerably dependent on the pH of the water: at pH < 8, it is blue in color, but at pH > 8 it acquires a red color. The pH of the solutions has been adjusted by adding a few drops of HCl (0.1 N) or NaOH (0.1 N) solutions and the adsorbent dose used was fixed at 0.1 g/L. The mixtures were then stirred at 200 rpm for 3 h at room temperature 25 °C. The residual dye concentrations were determined by the spectrophotometer analysis.

2.3.2. *Effect of contact time- kinetic study*

The kinetic adsorption of RB and VBB by the raw PTW biomass in single and binary modes was assessed at times ranging between 5 and 120 min. These assays were carried out for initial dye concentrations ranging between 10 and 50 mg·L^{-1} in single mode and from 6 to 14 mg·L^{-1} in binary mode, a constant adsorbent dosage of 0.1 g·L^{-1}, and a fixed pH of 4 for both RB and VBB. The RB or VBB adsorbed amounts at a given time "t", (q_t) (1) and the corresponding removal yield (Y_t) (2) were assessed as follows:

$$q_t = \frac{(C_0 - C_t)}{D} \quad (1)$$

$$Y_t(\%) = \frac{(C_0 - Ct)}{C_0} \times 100 \quad (2)$$

where C_0 and C_t (mg·L^{-1}) are the dye concentrations at the beginning of the experiment and at a given time "t", respectively, and D is the used PTW dose (g·L^{-1}).

The RB and VBB adsorption kinetics measured data were fitted to three well-known models (Table 1), namely pseudo-first order (PFO), pseudo-second order (PSO), and Elovich. The original and the linearized equations of these four models are extensively cited in literature [45,46].

Table 1. Used kinetics models for the study of RB and VBB removal by PTW

Model	Equation
Pseudo first order	$\frac{dq_t}{dt} = k_1 \cdot (q_e - q_t)$
Pseudo second order	$\frac{dq_t}{dt} = k_2 (q_e - q_t)^2$
Elovich	$qt = \frac{1}{\beta} \cdot \ln(\alpha \cdot \beta) + \frac{1}{\beta} \cdot \ln(t)$

With: q_t adsorbed amount at given time t (mg/g), k_1 pseudo first order model constant (min^{-1}), k_2 second-order model constant (g/mg·min^{-1}), q_e equilibrium dye concentration on adsorbent (mg/g), t time (min), α Initial adsorption rate (mg/g), β Desorption constant (g/mg) during every one experiment.

The agreement between the measured and the calculated adsorbed amounts was determined according to the estimated values of the determination coefficients as well as the calculated average percentage errors (APE_{kin} (3)):

$$APE_{kin}(\%) = \frac{\sum_1^N |(q_{t,exp} - q_{t,theo})/q_{t,exp}|}{N} \times 100 \quad (3)$$

where $q_{t,exp}$ and $q_{t,theo}$ (mg·g^{-1}) are the measured and the theoretical adsorbed amounts at the time "t", N is the number of experiments.

2.3.3. *Effect of initial dye concentrations—isotherm study*

The effect of the initial dyes concentrations on their removal by the PTW was assessed at equilibrium for a contact time of 3 h, a pH of 4 and an adsorbent dose of 0.1 g·L^{-1}. The tested dye concentrations were adjusted to 10, 20, 30, 40 and 50 mg·L^{-1} in single mode and 6, 8, 10, 12 and 14 mg·L^{-1} in binary mode. The measured data were fitted to well-known models (Table 2), namely Freundlich, Langmuir and Temkin models. The original and linearized equations of these models as well as the assumptions and implications have been intensively developed in the literature [47,48].

As for the kinetic study, the concordance between the experimental and predicted adsorbed amounts

Table 2. Used isotherms models for the study of RB and VBB removal by PTW

Models	Equations
Langmuir	$q_e = \frac{q_m \cdot K_l \cdot C_e^{\frac{1}{n}}}{1 + K_l \cdot C_e}$
Freundlich	$q_e = K_f \cdot C_e^{\frac{1}{n}}$
Temkin	$q_e = B_l \cdot \ln(K_t) + B_l \cdot \ln(C_e)$

by the three used models was determined as follows (4):

$$\mathrm{APE}_{\mathrm{isotherm}}(\%) = \frac{\sum_1^N |(q_{t,\mathrm{exp}} - q_{t,\mathrm{theo}})/q_{t,\mathrm{exp}}|}{N} \times 100 \quad (4)$$

where $q_{e,\mathrm{exp}}$ and $q_{e,\mathrm{theo}}$ (mg·g^{-1}) are the measured and the theoretical adsorbed dyes quantities at equilibrium.

2.3.4. *Effect of adsorbent dose*

The effect of the adsorbent dosage on the RB and VBB removal efficiency was determined for contact times raging between 0 and 40 min, at initial dye concentrations of 10 mg·L^{-1} in single and binary modes. The PTW tested doses were equal to 0.05; 0.1; 0.15, and 0.2 g·L^{-1}. The dye percentage removal for a given dose and time is calculated using (2).

2.3.5. *Effect of temperature—thermodynamic study*

The effect of the temperature on RB and VBB removal efficiency was determined for a fixed contact time of 3 h, and an initial dye concentration of 10 mg·L^{-1} in single and binary modes. The tested temperatures were fixed to 20, 30, 40, 50, and 60 °C, at a constant adsorbent dosage of 0.1 g·L^{-1} and a fixed pH of 4 for both RB and VBB. The dye percentage removal for a given dose and time are calculated using (2).

The thermodynamic parameters of dyes adsorption onto the tested material have concerned the standard free energy changes $\Delta G°$ (kJ·mol^{-1}), the enthalpy $\Delta H°$ (kJ·mol^{-1}) and entropy changes $\Delta S°$ (kJ·mol^{-1}·K^{-1}). These parameters were calculated according to the following equations:

$$\Delta G° = -RT \log K_C \quad (5)$$

$$\Delta G° = \Delta H° - T\Delta S° \quad (6)$$

$$K_C = \frac{q_e}{C_e} \quad (7)$$

where R is the gas universal gas constant (8.31 J·K^{-1}·mol^{-1}), T is the temperature (K) and K_C is the distribution coefficient.

The Van't Hoff equation can be deduced from the combination of (5) and (6) as follows:

$$\log K_c = \frac{\Delta S°}{R} - \frac{\Delta H°}{RT}. \quad (8)$$

The Van't Hoff plot ($\log(K_C)$ as a function of $1/T$) permits the estimation of $\Delta H°$ and $\Delta S°$ through the calculus of its slope and intercept, respectively.

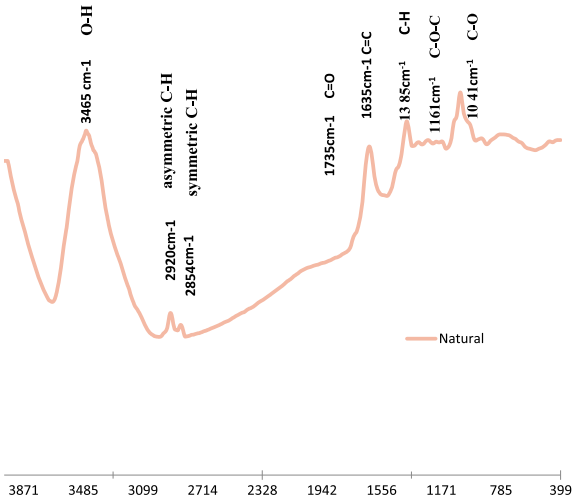

Figure 2. FTIR spectrum of the petiole palm tree waste.

3. Results and discussion

3.1. *Adsorbent characterization*

The $\mathrm{pH_{PZC}}$ value of the used adsorbent was found to be 3.8. According to the literature, values of 5.1, 6.13 and 6.5 were found in the case of the $\mathrm{pH_{PZC}}$ studies for mixture palm waste (seeds, leaves and bark) [49], date stone [43] and palm bark powder [50] respectively.

Therefore, the adsorbent's surface should be negatively charged for pH values higher than 3.8 which will favor the removal of the used cationic dyes. At

contrarily, for pH lower than 3.8, the solid surface should be positively charged.

On the other hand, the FTIR analysis of the used adsorbent (Figure 2) showed that this material contains various absorption peaks, which are characteristic of a lingo-cellulosic material [51].

The main existing bands were distributed as follows: (i) a broad and intense band around 3465 cm^{-1} corresponding to O–H bands [52], (ii) bands at 2920 cm^{-1} and 2854 cm^{-1}, that can be attributed to asymmetric C–H and symmetric C–H bands respectively [53], (iii) a band around 1735 cm^{-1} representing C=O and stretching vibration of ester group in hemicellulose [54], (iv) a band around 1635 cm^{-1}, showing the existence of C=C [55], (v) a band around 1635 cm^{-1} representing O–H bending of adsorbed water [55], and (vi) two bands around 1161 cm^{-1} and 1041 cm^{-1} attributed to the C–O–C asymmetric stretching vibration and C–O stretching ring in cellulose and hemicellulose, respectively [53].

The PTW's FTIR spectrum confirm the results of Belela *et al.* [56] who studied MB bio-sorption from aqueous solutions by date stones and palm-tree wastes. This spectrum confirmed that the PTW had various functional groups that would contribute to the VBB and RB removal from aqueous solutions.

3.2. *Adsorption studies*

3.2.1. *Effect of initial pH*

The value of pH_{PZC} indicated the type of active sites and biomass adsorption capacity. At a pH > pH_{PZC}, cationic dye adsorption was promoted, owing to the presence of functional groups such as OH– and COO– groups, whereas at a pH < pH_{PZC}, anionic dye adsorption was promoted, here the surface became positively charged [57].

The effect of the pH values on VBB and RB adsorption was studied under the experimental conditions in Section 2.3.1. It can be seen that the adsorption of the two dyes is influenced by the solutions pH values (Figure 3). Indeed, the lowest adsorption yields for VBB (20.2%) and RB (70.2%) were obtained for the lowest pH value (3). This may be due mainly to the fact at this pH, the adsorbent was mainly positively charged which induces a net reduction of the adsorption of the positively charged studied dyes. When used pH values are higher than the pH_{PZC}, the adsorption yields of both dyes increase. The corresponding average yields values for this range were assessed to 26%, and 79.6%, for VBB and RB, respectively. The highest adsorption yields were determined at a pH of 4. They were assessed to 85.4% and 35.2% for RB and VBB, respectively. Kataria *et al.* [58] observed that the maximum removal of Victoria blue b dye was achieved at pH 6, after that, it decreased with increase in pH when Al-Gheethi *et al.* [59] observed that the maximum removal of Rhodamine B dye was achieved at pH 4.69.

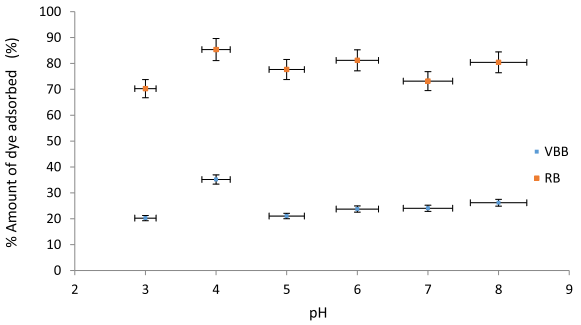

Figure 3. Effect of pH on the adsorption of VBB and RB by PTW (Concentration = 20 $mg{\cdot}L^{-1}$, contact time = 3 h and adsorbent dose = 0.1 g).

3.2.2. *Adsorption kinetics*

The adsorption kinetic of VBB and RB by PTW was carried out under the experimental conditions given in Figure 4. It can be clearly seen that this process is time and initial concentration dependent. Indeed, for a given constant initial concentration, the adsorbed dye amount in both modes highly increases at the beginning of the experiment until a contact time of 15 min. At this time duration, for a single mode and at a concentration of 50 $mg{\cdot}L^{-1}$, the VBB and RB adsorbed amounts represented about 47%, and 31% of the totally adsorbed amount at the end of the experiment. This short duration will be particularly appreciated when this process will be scaled up for real applications since it will permit high energy savings. After this duration, the VBB and RB adsorption continue to increase but with a much slower rate (Figure 4). After a longer contact period, the adsorbed amounts continue to increase but at a slower rate. This behavior can be

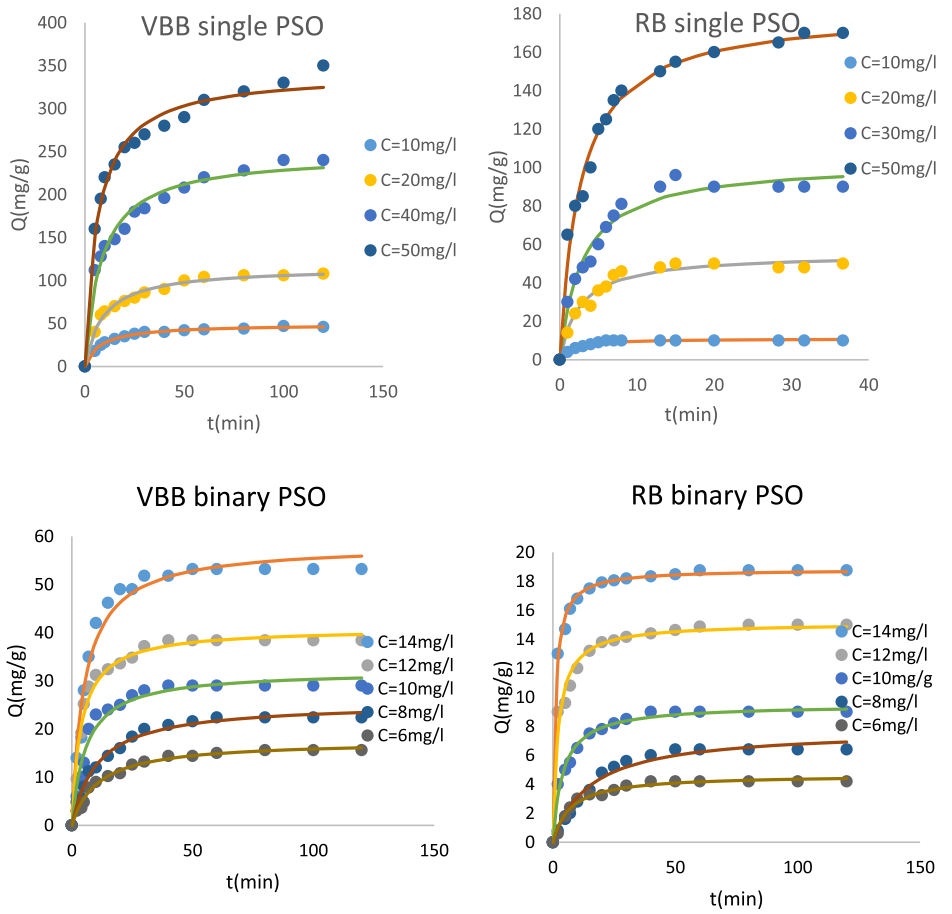

Figure 4. RB and VBB kinetic removal by the petiole palm waste at different initial concentrations in single and binary systems.

linked to intra-particle diffusion within the adsorbent pores and dye adsorption [60,61]. The equilibrium state which corresponds to almost constant adsorbed amounts was reached after a longer contact time. However, in all cases, duration of about 120 min was sufficient to reach this equilibrium state.

It is important to underline that the equilibrium time increases with the increase of the initial dye concentration. For example, in a single mode, for an initial concentration of 10 mg·L^{-1}, this time was assessed to 6 and 15 min for RB and VBB, respectively. These times increased to 20 and 60 min when the used initial dyes concentration was increased to 50 mg·L^{-1}. This behavior is mainly due to the fact that higher is the initial dye concentration, higher are the dyes molecules that will react with fixed adsorption sites on the surface of PTW [62]. Similar trend was observed for the binary mode (Figure 4). The increase of the adsorbed dyes amount in single and binary systems with the increase of the initial concentration will be deeply discussed in the isotherm section (Section 3.2.3). Moreover, the dyes removal efficiency decrease in binary mode in comparison with the single system will be examined in the same Section 3.2.3.

The fitting of the experimental data with the PFO, PSO, and Elovich kinetic models shows that the PSO was the best one. Indeed, the corresponding theoretical adsorption data for the two dyes and the two studied modes are more concordant with the experimental data in comparison with the other models. The PSO model exhibited the highest average calculated R^2 (0.979) and the lowest APE (5.33%) (Table 3). This result suggests that the dyes removal by PTW might mainly a chemical process including complexation with the adsorbent functional groups and cation exchange [63,64].

Table 3. Parameters of the kinetics models of the adsorption of RB, and VBB by PTW in single and binary modes at different initials concentrations (contact time = 3 h, pH = 4 and adsorbent dose = 0.1 g·L^{-1})

Dyes		Pseudo first order model				Pseudo second order model				Elovich model			
	C0 (mg/l)	q_e (mg/g)	k_1 (min^{-1})	R^2	APE	k_2 (10^{-3} min^{-1})	q_e (mg/g)	R^2	APE	α	$1/\beta$	R^2	APE
Rhodamine B, single mode	10	10.09	0.447	0.991	2.686	65.47	10.96	0.965	5.749	66.92	1.505	0.725	10.737
	20	49.31	0.280	0.980	5.643	6.996	55.23	0.969	5.605	65.7	9.945	0.870	10.035
	30	91.46	0.249	0.975	6.443	3.269	103	0.967	6.355	103.5	18.87	0.889	8.446
	50	161.9	0.272	0.926	7.023	2.068	181.7	0.984	4.227	231.6	31.92	0.958	5.183
		Average		0.968	5.448			0.971	5.484			0.860	8.600
Victoria Blue B, single mode	10	43.58	0.094	0.980	4.653	2.549	49.23	0.996	1.877	21.54	8.572	0.952	4.507
	20	101.6	0.083	0.956	7.628	0.948	115.5	0.988	3.611	39.43	20.96	0.970	3.769
	40	218.9	0.088	0.923	9.829	0.480	247.6	0.977	5.316	105.4	43	0.991	1.874
	50	305.4	0.114	0.935	7.864	0.456	342.1	0.982	3.679	250.5	54.366	0.987	2.122
		Average	0.948	7.493			0.983	3.620			0.975	3.068	
Rhodamine B, binary mode	14	18.03	0.505	0.963	4.599	49.85	18.83	0.995	1.317	6248	1.516	0.867	3.118
	12	14.28	0.264	0.923	7.134	31.35	15.13	0.977	3.510	221.2	1.641	0.916	3.858
	10	8.76	0.156	0.955	6.763	26.05	9.496	0.984	3.924	15.74	1.361	0.916	5.840
	8	6.545	0.059	0.995	4.124	8.524	7.785	0.977	9.303	1.15	1.633	0.935	13.425
	6	4.142	0.107	0.982	6.330	30.62	4.653	0.981	8.647	1.778	0.863	0.900	14.318
		Average		0.963	5.79			0.982	5.34			0.906	8.111
Victoria Blue B, binary mode	14	52.71	0.142	0.991	3.945	3.282	58.34	0.974	6.756	38.27	9.85	0.849	13.300
	12	37.42	0.184	0.979	5.226	6.303	40.92	0.979	6.275	52.29	6.209	0.839	12.519
	10	28.78	0.132	0.985	5.120	5.383	32.08	0.969	9.097	16.37	5.681	0.854	15.587
	8	22.12	0.078	0.986	6.234	3.751	25.47	0.989	5.966	5.94	5.025	0.955	8.334
	6	15.16	0.077	0.984	6.758	5.13	17.55	0.989	6.342	3.851	3.516	0.959	11.631
		Average		0.985	5.456			0.98	6.887			0.891	12.274

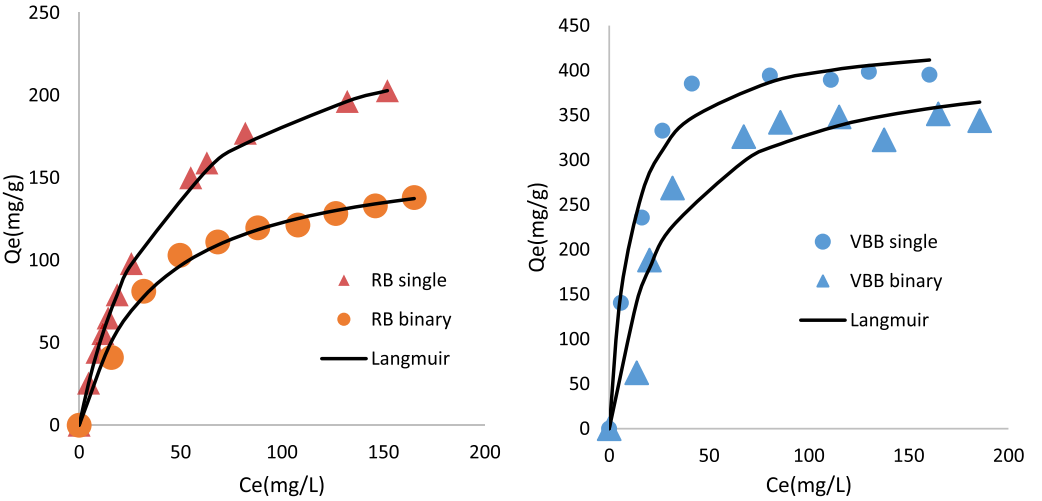

Figure 5. Isothermal experimental and fitted data with, Langmuir model for RB and VBB removal by PTW in single and binary mode (initial pH = 4; adsorbent dosage = 0.1 g·L^{-1}; contact time = 3 h; $T = 20 \pm 2$ °C).

Table 4. Calculated parameters of Langmuir, Freundlich and Temkin models regarding RB and VBB removal by TPW in single and binary mode

Dye	Langmuir				Freundlich				Temkin			
	K_L (L/mg)	Q_m (mg/g)	R^2	APE (%)	K_f (L/mg)	n	R^2	APE (%)	B (J/mol)	K_t	R^2	APE (%)
Rhodamine B, single mode	0.023	260.1	0.992	7.3	18.17	2.0	0.9587	20.4	56	0.243	0.982	6.9
Victoria Blue B, single mode	0.089	440.1	0.948	5.9	136.6	4.4	0.9183	13.3	77.32	1.63	0.864	10.1
Rhodamine B, binary mode	0.027	168	0.977	4.6	21.43	2.6	0.9137	9.1	38.86	0.227	0.968	5.6
Victoria Blue B, binary mode	0.037	417.4	0.860	20.1	71.73	3.1	0.7346	26.9	93.54	0.313	0.817	21.9

Similar results were reported in various research studies, namely the adsorption of methylene blue and crystal violet by palm kernel fiber [65] and the adsorption of Dye Basic Blue 41 and Basic Yellow 28 by activated carbon [66].

3.2.3. *Effect of dyes initial concentration—isotherm study*

The impact of the initial dyes concentrations in single and binary modes on their removal by PTW was evaluated under the experimental conditions given in Section 2.3.3. The used pH was fixed to 4 which correspond to the optimal value found in Section 3.2.1. The measured data as well as the theoretical ones calculated by Langmuir, Freundlich and Temkin models are given in Figure 5. The calculated constants of these three models are given in Table 4.

On the basis of Figure 5 and Table 4, it can be clearly deduced that the adsorbed amounts of RB and VBB in single mode were higher than the ones observed in binary system. Indeed, in single mode, the palm tree waste exhibited an uptake capacity of 440.1, and 260.1 mg·g^{-1} for VBB and

Table 5. Comparison of RB and VBB adsorption onto PTW with other materials

Adsorbent	Dye	Langmuir's adsorption capacity, q_m, (mg·g^{-1})	Reference
Seed husk of Bengal gram	RB, single mode	133.34	[67]
Ordered mesoporous carbon material ST-A	RB, single mode	83	[68]
Commercial adsorbent (activated carbon CWZ-22)	RB, single mode	58	[68]
Synthesized hybrid ion exchanger	RB, single mode	76.4	[69]
Montmorillonite/graphene oxide nanocomposite	RB, binary mode	178.6	[70]
Organo-vermiculites	RB, binary mode	261.97	[71]
Surfactant-modified three-dimensional Mg Al layered double hydroxide	RB, binary mode	49.6	[72]
Flower shaped Zinc 5 oxide nanoparticles	VBB, single mode	163.93	[58]
Incense stick ash	VBB, single mode	77.67	[73]
PTW	RB, single mode	260.1	Present work
	VBB, single mode	440.1	
PTW	RB, binary mode	168	Present work
	VBB, binary mode	417.4	

RB, respectively. These adsorption capacities diminished by 35.4%, and 5.2%, respectively in binary mode. This finding is mainly due to a competitive adsorption between the two dyes on the available adsorption sites [66,74,75]. On the other hand, the confrontation of the experimental data to the three used isotherm models showed that the Langmuir model was the most suitable one with relatively high correlation coefficients and lower APE (Table 4). In addition, the highest Langmuir's parameter values "$R_L = 1/(1 + K_{L*C_0})$" were estimated to 0.483 and 0.218 for RB and VBB in single mode 0.448 and 0.38 in binary mode. All these values are less than 1 which indicates that the two dyes adsorption by PTW is a favorable process. This result suggests that dyes adsorption onto PTW occurs on uniform monolayer coverage at the outer surface of the adsorbents [76]. On the other hand, under the studied conditions, the Freundlich parameter "n" varied between 2.2 and 4.4. They are in the range of 1–10, which suggests that the adsorption of these two dyes by the PTW is a favorable process. Values in the same range were determined by [77], and [78] when studying RB, and VBB removal by graphene–based nickel nano-composite, and activated carbon, Ba/alginate and modified carbon/Ba/alginate polymer beads, respectively.

Temkin model was also tested, under the studied conditions, The Temkin parameter "B" varied between 38.86 and 93.54 J/mol, these values are less than 8 kJ/mol which implies that the biosorption of the two dyes is physical in the simple binary system [79,80].

In order to situate our adsorbent efficiency in removing the studied dyes, we made a comparison of its removal efficiency (based on the Langmuir's adsorption capacity) with several other raw and modified adsorbents (Table 5). Results indicate that the PTW could be considered as an attractive low cost material for dyes removal from aqueous solutions. In fact, the adsorption capacity of the RB studied during this work in single mode was about 260.1 mg/g, this value is higher than results found by other researchers we quote for example 133.34 mg/g, 83 mg/g, 76.4 mg/g, and 58 mg/g.

Table 6. Effect of temperature on RB and VBB adsorption onto PTW

	T (°C)	Q_m (mg/g)	$\Delta G°$ (kJ·mol^{-1})	$\Delta H°$ (kJ·mol^{-1})	$\Delta S°$ (J·mol^{-1}·K^{-1})
Rhodamine B, single mode	20	260.1	−25.744	−11.312	49.107
	30	249.1	−26.251		
	40	258.8	−26.608		
	50	224.1	−27.0615		
	60	211	−27.814		
Victoria Blue B, single mode	20	440.1	−27.681	−9.740	62.515
	30	439.8	−29.110		
	40	414	−29.606		
	50	327.9	−29.823		
	60	313.5	−30.385		
Rhodamine B, binary mode	20	168	−24.591	−17.277	25.858
	30	168.3	−25.177		
	40	163.8	−25.714		
	50	149.5	−26.087		
	60	101.3	−25.341		
Victoria Blue B binary mode	20	417.4	−26.801	−16.518	35.832
	30	368.9	−27.666		
	40	322.1	−27.716		
	50	290	−28.334		
	60	227.6	−28.215		

3.2.4. *Effect of adsorbent dose*

The PTW mass effect on the dye was studied in single and binary systems under the experimental conditions given in Section 2.3.4. Results (Figure 6) indicated that the two dyes uptake yields increased with increasing the PTW doses. For instance, at a fixed time (25 min), increasing the dose of the adsorbent from 0.05 g/L to 0.2 g/L, increased the removal yields from about 6% to 24%, 40% to 81%, 24% to 40% and 6% to 13% for RB and VBB in single mode and for VBB and RB in binary system, respectively. This finding is mainly due to the increase of the available adsorption active sites that could react with the dyes molecules. Similar results were reported by [81,82], and [83] when studying the adsorption of lead (Pb(II)) from aqueous solutions by Lignite, five toxic dyes by industrial graphite, and cationic crystal violet dye by graham flour.

3.2.5. *Effect of temperature*

The experimental results of the dye adsorption in single and binary systems on PTW are shown in Figure 7 and Table 6.

On the basis of Figure 7 and Table 6, it appears that for all studied cases, the increase of the temperature has resulted in a decrease of the adsorbed amounts. Indeed, when rising temperature from 20 to 60 °C, the RB and VBB adsorbed amounts decreased by about 39.06%, and 34.84% in single mode and by 53.68%, and 55.77% in binary system.

The thermodynamic parameters of the studied cases are given in Table 6, the thermodynamic energy calculation showed that the studied biosorption is physical (ΔH less than 40 kJ/mol), spontaneous, and exothermic ($\Delta H < 0$) with an increase in disorder ($\Delta S > 0$) [84]. Similar results was observed by [85] and [86] when studying adsorption of Rhodamine-

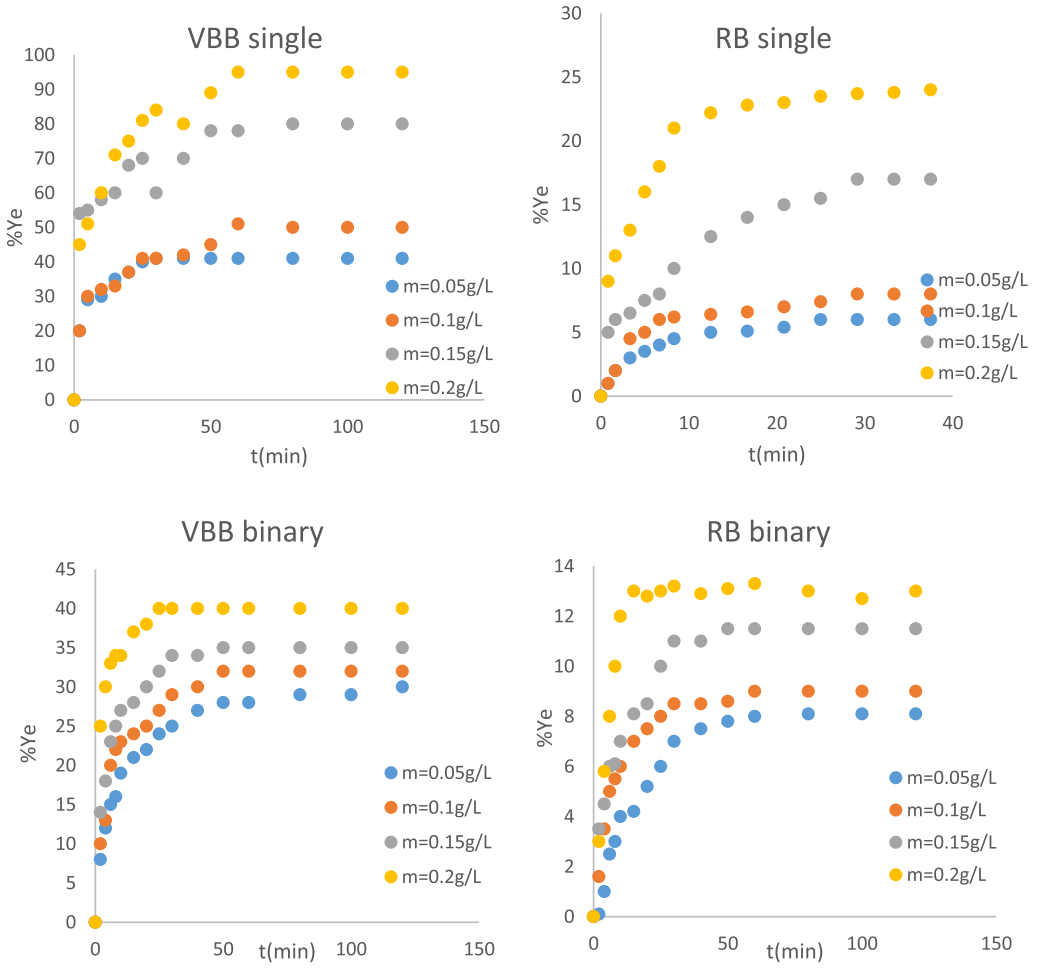

Figure 6. Effect of PTW doses on the removal yield of RB and VBB in single and binary systems.

B from aqueous solution by the use of natural adsorbent perlite and magnetic silica nanocomposite immobilized pseudomonas fluorescents respectively, while [87] observed that the removal of RB from aqueous solutions using MgO supported Fe–Co–Mn nano-particles was spontaneity and endothermic similar results was observed by [58] when studying the adsorption of VBB onto zinc oxide nanoparticles.

4. Mechanisms exploration

To remove contaminants from an aqueous solution, it is necessary to understand the mechanism of the solute adsorption onto the solid surface. During an adsorption mechanism there is intervention of ionic interactions of opposite charge namely dipole–dipole, dipole–induced dipole, hydrogen bonding, chemical bonding and ion exchange.

In order to interpret the adsorption of the solute, the adsorbent surface chemistry as well as its effect on the adsorption process is usually studied. Fourier transform infrared spectroscopy (FTIR) analysis is used to study the interaction between an adsorbate and the active sites on the adsorbent surface. The explanation of FTIR is based on the chemical structure of petiole palm tree wastes. PTW consists mainly of three compounds which are cellulose, hemicellulose and lignin. Cellulose and hemicellulose contain most of the oxygenated functional

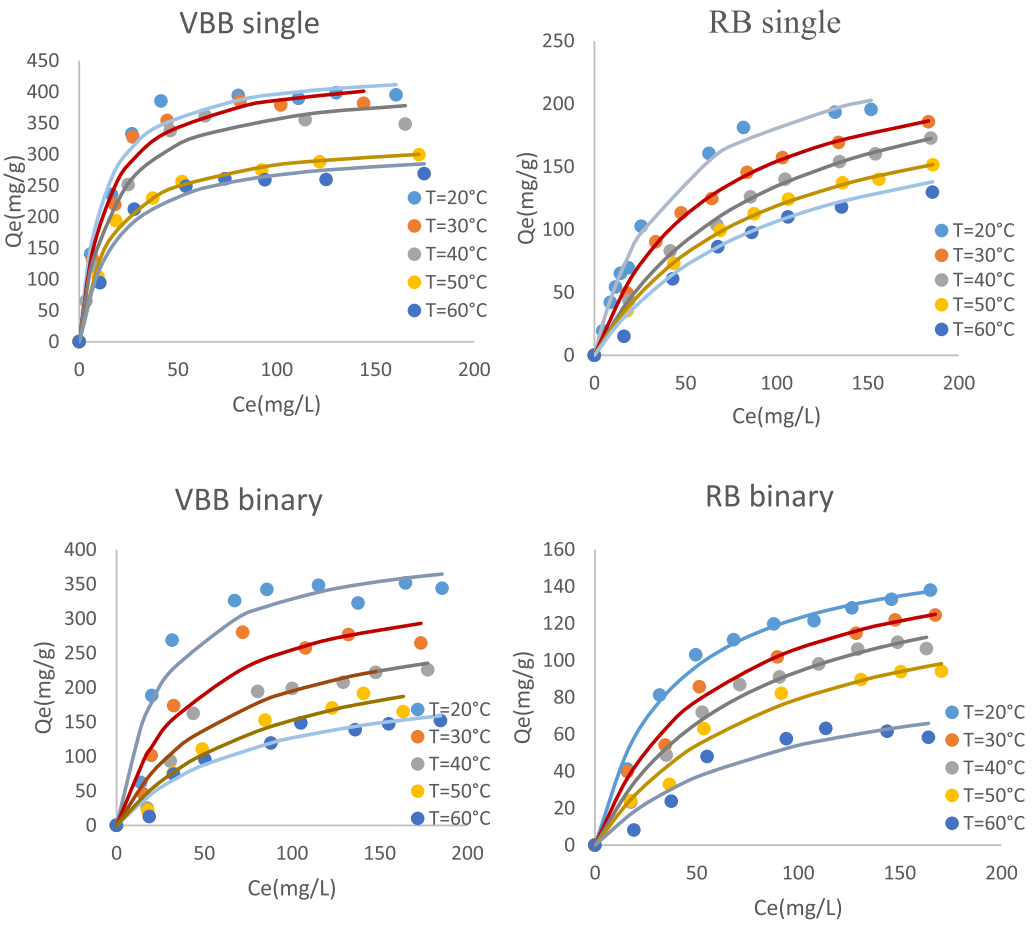

Figure 7. Effect of temperature on the adsorption of RB and VBB in single and binary system.

groups present in the lignocellulose product, while lignin is a complex, systematically polymerized and highly aromatic substance [38].

5. Conclusions

Rhodamine B (RB) and Victoria blue B (VBB) dye removal from aqueous solutions in single and heterogeneous solutions using petiole palm tree waste (PPTW) was experimentally determined.

Our findings were:

• In the single system:

The removal percentage increased with increasing initial dye concentration and adsorbent mass and decreased with increasing temperature. Langmuir and Freundlich's models described the adsorption isotherms well but Langmuir's model fitted better the experimental data with adsorption capacities of 260.1 and 440.1 mg/g for RB and VBB, respectively. The thermodynamic energy calculation showed that the studied biosorption is physical, spontaneous, and exothermic with an increase in disorder. Concerning the kinetic study, the optimum contact time for the initial dye concentration to reach equilibrium is 60 min and 20 min for (VBB) and (RBB), respectively. This result is due to the saturation of active sites. The experimental results showed that the chemical adsorption best followed the pseudo-second-order equation.

• In the binary system:

The removal percentage increased with the initial dye concentration and adsorbent mass but decreased with increasing temperature. In contrast to the other tested models, the Langmuir model fitted

the experimental data better with adsorption capacities, calculated from the linear Langmuir equation, equal to 168 and 417.4 mg/g for RB and VBB, respectively. The optimum contact time for the initial dye concentration to reach equilibrium was 40 and 20 min for VBB and RBB, respectively. This result is attributable to the negatively charged surface area. The adsorption curve followed the Pseudo-second order model.

Conflicts of interest

Authors have no conflict of interest to declare.

Acknowledgments

The authors would like to thank the National Engineering School of Gabes, Gabes University, Tunisia. Special thanks to Mrs. Rim Najjar for many helpful style corrections.

References

[1] G. Thompson, J. Swain, M. Kay, C. Forster, *Bioresour. Technol.*, 2020, **77**, 275-286.
[2] S. Gopi, A. Pius, S. Thomas, *J. Water Process. Eng.*, 2016, **14**, 1-8.
[3] V. Hernández-Montoya, M. A. Pérez-Cruz, D. I. Mendoza-Castillo, M. R. Moreno-Virgen, A. Bonilla-Petriciolet, *J. Environ. Manage.*, 2013, **116**, 213-221.
[4] S. T. Akar, A. S. Özcan, T. Akar, A. Özcan, Z. Kaynak, *Desalination*, 2009, **249**, 757-761.
[5] M. Singh, H. S. Dosanjh, H. Singh, *J. Water Process. Eng.*, 2016, **11**, 152-154.
[6] S. Guiza, L. Franck, M. Bagané, *Desalination Water Treat.*, 2018, **113**, article no. 22258.
[7] P. N. Tim Robinson, G. McMullan, R. Marchant, *Bioresour. Technol.*, 2001, **77**, 247-255.
[8] R. Ahmad, *J. Hazard. Mater.*, 2009, **171**, 767-773.
[9] A. M. Salah, D. K. Mahmoud, W. A. W. A. Karim, A. Idris, *A Compr. Rev.*, 2011, **280**, 1-13.
[10] B. H. U. G. Akpan, *J. Hazard. Mater.*, 2009, **170**, 520-529.
[11] A. K. Verma, R. R. Dash, P. Bhunia, *J. Environ. Manage.*, 2012, **93**, 154-168.
[12] A. A. Azzaz, S. Jellali, H. Akrout, A. A. Assadi, L. Bousselmi, *J. Clean. Prod.*, 2018, **201**, 28-38.
[13] L. B. Ahmed Amine Azzaz, A. Amine Assadi, S. Jellali, A. Bouzaza, D. Wolbert, S. Rtimi, *J. Photochem. Photobiol. A*, 2018, 111-120, [Online].
[14] V. Vijayakumar, R. Saravanathamizhan, N. Balasubramanian, *J. Water Process. Eng.*, 2016, **9**, 155-157.
[15] S. Cheng, D. L. Oatley, P. M. Williams, C. J. Wright, *Water Res.*, 2011, **46**, 33-42.
[16] Y. Cui, Q. Ge, X. Liu, T. Chung, *J. Membr. Sci.*, 2014, **467**, 188-194.
[17] M. Khan, I. M. C. Lo, *Water Res.*, 2016, **106**, 259-271.
[18] S. Jellali, B. Khiari, M. Usman, H. Hamdi, Y. Charabi, M. Jeguirim, *Renew. Sust. Energy Rev.*, 2021, **144**, article no. 111068.
[19] A. Hammami, C. Charcosset, R. Ben, *J. Membr. Sci. Technol.*, 2017, **7**, 1-8.
[20] P. Velmurugan, V. Rathina Kumar, G. Dhinakaran, *Int. J. Environ. Sci.*, 2011, **1**, 1492-1503.
[21] S. Guiza, M. Bagane, *J. Water Sci.*, 2013, **26**, 39-51.
[22] S. Guiza, M. Bagane, *J. Univ. Chem. Technol. Metall.*, 2012, **47**, 283-288.
[23] G. Mezohegyi, F. P. van der Zee, J. Font, A. Fortuny, A. Fabregat, *J. Environ. Manage.*, 2012, **102**, 148-164.
[24] X. L. W. Wang, G. Huang, C. An, X. Xin, Y. Zhang, *Appl. Surf. Sci.*, 2017, **405**, 119-128.
[25] M. Boutaieb, M. Guiza, S. Román, B. Ledesma Cano, S. Nogales, A. Ouederni, *C. R. Chim.*, 2020, **15**, 607-621, [Online].
[26] Suhas, V. K. Gupta, P. J. M. Carrott, R. Singh, M. Chaudhary, S. Kushwaha, *Bioresour. Technol.*, 2016, **216**, 1066-1076.
[27] H. Naeem, H. N. Batti, S. Sadaf, M. Iqbal, *Appl. Radiat. Isot.*, 2017, **123**, 94-101.
[28] J. Luan, P. X. Hou, C. Liu, C. Shi, G. X. Li, H. M. Cheng, *J. Mater. Chem.*, 2016, **4**, 1191-1194.
[29] L. R. Bonetto, F. Ferrarini, C. de Marco, J. S. Crespo, R. Guégan, M. Giovanela, *J. Water Process. Eng.*, 2015, **6**, 11-20.
[30] M. Akram, H. N. Batti, M. Iqbal, S. Noreen, S. Sadaf, *J. Environ. Chem. Eng.*, 2017, **5**, 400-411.
[31] Y. Safa, H. N. Bhatti, M. Sultan, S. Sadaf, *Desalination Water Treat.*, 2016, **57**, 25532-25541.
[32] S. Sadaf, H. Bhatti, *Desalination Water Treat.*, 2016, **57**, 11773-11781.
[33] S. Sadaf, H. N. Bhatti, S. Nausheen, M. Amin, *J. Taiwan Inst. Chem. Eng.*, 2015, **47**, 160-170.
[34] A. A. Azzaz, S. Jellali, R. Souissi, K. Ergaieg, L. Bousselmi, *Environ. Sci. Pollut. Res.*, 2017, **24**, 18240-18256.
[35] S. Kuppusammy, K. Venkateswarlu, Y. B. L. P. Thvamani, R. Naidu, M. Megharaj, *Ecol. Eng.*, 2017, **101**, 3-8.
[36] N. Boudouaia, Z. Bengharez, S. Jellali, *Appl. Water Sci.*, 2019, **9**, 1-12.
[37] N. El Kadri, M. Ben Mimoun, J. I. Hormaza, *Sci. Hortic. (Amsterdam)*, 2019, **253**, 24-34.
[38] T. Ahmad *et al.*, *Environ. Sci. Pollut. Res.*, 2012, **19**, 1464-1484.
[39] I. A. W. Tan, B. H. Hameed, A. L. Ahmad, *Chem. Eng. J.*, 2007, **127**, 111-119.
[40] S. Montoya-Suarez, F. Colpas-Castillo, E. Meza-Fuentes, J. Rodríguez-Ruiz, R. Fernandez-Maestre, *Water Sci. Technol.*, 2015, **37**, 21-27.
[41] M. Wakkel, B. Khiari, F. Zagrouba, *C. R. Chim.*, 2020, **23**, 671-687.
[42] A. A. Azzaz, S. Jellali, M. Jeguirim, L. Bousselmi, Z. Bengharez, H. Akrout, *C. R. Chim.*, 2021, **21**, 71-84.
[43] H. Hammani, M. El Achaby, K. El Harfi, M. A. El Mhammedi, *C. R. Chim.*, 2020, 589-606.
[44] S. Guiza, *Ecol. Eng.*, 2017, **99**, 134-140.
[45] C. Chakrapani, C. S. Babu, K. N. K. Vani, K. S. Rao, *E-J. Chem.*, 2010, **7**, 419-427.

[46] M. Firdaus, M. Yusop, M. A. Ahmad, N. A. Rosli, M. Edeerozey, A. Manaf, *Arab. J. Chem.*, 2021, **14**, 103-122.
[47] D. Suteu, T. Malutan, D. Bilba, *Desalination*, 2010, **255**, 84-90.
[48] A. Ergene, K. Ada, S. Tan, H. Kat, *Desalination*, 2009, **249**, 1308-1314.
[49] K. Azoulay, I. Bencheikh, A. Moufti, A. Dahchour, J. Mabrouki, S. El Hajjaji, *Chem. Data Collect.*, 2020, **27**, 1-29.
[50] Z. Chaouki, M. Hadri, M. Nawdali, M. Benzina, H. Zaitan, *Sci. Afr.*, 2021, **12**, 1-16.
[51] C. Xu *et al.*, *Sci. Total Environ.*, 2021, **790**, article no. 148089.
[52] K. Kanjana, P. Harding, T. Kwamman, W. Kingkam, *Biomass Bioenergy*, 2021, **153**, article no. 106206.
[53] H. Boumediri, A. Bezazi, G. G. Del Pino, A. Haddad, F. Scarpa, A. Dufresne, *Carbohydr. Polym.*, 2019, **222**, article no. 114997.
[54] C. B. T. L. Lee, T. Y. Wu, C. K. Cheng, L. F. Siow, I. M. L. Chew, *Ind. Crops Prod.*, 2021, **166**, article no. 113397.
[55] Y. Zhao *et al.*, *Ind. Crops Prod.*, 2015, **65**, 96-101.
[56] Z. Belala, M. Jeguirim, M. Belhachemi, F. Addoun, G. Trouvé, *Desalination*, 2011, **271**, 80-87.
[57] R. Chikri, N. Elhadiri, M. Benchanaa, Y. El, *J. Chem.*, 2020, **11**, 1-17.
[58] N. Kataria, V. K. Garg, M. Jain, K. Kadirvelu, *Adv. Powder Technol.*, 2016, **27**, 1180-1188.
[59] A. A. Al-gheethi *et al.*, *Chemosphere*, 2022, **287**, article no. 132080.
[60] J. Huang, K. Huang, S. Liu, A. Wang, C. Yan, *Colloids Surf. A Physicochem. Eng. Asp. J.*, 2008, **330**, 55-61.
[61] M. Haneda, H. Hamada, *C. R. Chim.*, 2021, **15**, 1-12, [Online].
[62] N. KhaledMahmoudi, M. Hamdia, S. Ben Alia, Jellalic, E. Srasraa, *C. R. Chim.*, 2020, **23**, 689-704.
[63] C. Duan, T. Ma, J. Wang, Y. Zhou, *J. Water Process. Eng.*, 2020, **37**, 101-339.
[64] S. Jellali, A. A. Azzaz, M. Jeguirim, H. Hamdi, A. Mlayah, *Water (Switzerland)*, 2021, **13**, 1-19.
[65] G. O. El-Sayed, *Desalination*, 2011, **272**, 225-232.
[66] A. Regti, A. El Kassimi, M. R. Laamari, *J. Assoc. Arab Univ. Basic Appl. Sci.*, 2016, **24**, 1-9.
[67] M. C. Somasekhara Reddy, V. Nirmala, *Arab. J. Chem.*, 2017, **10**, S2406-S2416.
[68] K. Jedynak, D. Wideł, R. Nina, *Colloids Interfaces*, 2019, **17**, 1-16.
[69] Saruchi, V. Kumar, *Arab. J. Chem.*, 2019, **12**, 316-329.
[70] M. Neelaveni, P. Santhana Krishnan, R. Ramya, G. Sonia Theres, K. Shanthi, *Adv. Powder Technol.*, 2019, **30**, 596-609.
[71] M. Yu, M. Gao, T. Shen, H. Zeng, *J. Mol. Liq.*, 2019, **292**, article no. 111408.
[72] Z. Zhu, M. Xiang, P. Li, L. Shan, P. Zhang, *J. Solid State Chem.*, 2020, **288**, article no. 121448.
[73] S. N. Jain, S. R. Tamboli, D. S. Sutar, V. N. Mawal, A. A. Shaikh, A. A. Prajapati, *Sustain. Chem. Pharm.*, 2020, **15**, article no. 100199.
[74] Y. Al-Degs, M. A. M. Khraisheh, S. J. Allen, M. N. Ahmad, G. M. Walker, *Chem. Eng. J.*, 2007, **128**, 163-167.
[75] M. A. Wahab, R. Ben Hassine, S. Jellali, *J. Hazard. Mater.*, 2011, **191**, 333-341.
[76] S. Liu, *J. Colloid Interface Sci.*, 2015, **450,**, 224-238.
[77] U. Jinendra, D. Bilehal, B. M. Nagabhushana, A. Praveen, *Heliyon*, 2021, **7**, article no. e06851.
[78] M. Kumar, R. Tamilarasan, V. Sivakumar, *Carbohydr. Polym.*, 2013, **98**, 505-513.
[79] R. Maryanti, A. B. D. Nandiyanto, T. I. B. Manullang, A. Hufad, Sunardi, *Sains Malays.*, 2020, **49**, 2977-2988.
[80] N. Ayawei, A. N. Ebelegi, D. Wankasi, *J. Chem.*, 2017, **2017**, 1-11.
[81] M. Haneda, H. Hamada, *C. R. Chim.*, 2016, **15**, 1-12, [Online].
[82] S. Ambika, V. Srilekha, *Environ. Adv.*, 2021, **4**, article no. 100072.
[83] K. T. Kubra, M. S. Salman, H. Znad, M. N. Hasan, *J. Mol. Liq.*, 2021, **329**, article no. 115541.
[84] A. Ausavasukhi, C. Kampoosaen, O. Kengnok, *J. Clean. Prod.*, 2016, **134**, 506-514.
[85] R. T. M. Dharmendirakumar, G. Vijayakumar, G. Vijayakumar, R. Tamilarasan, M. Dharmendirakumar, *J. Mater. Environ. Sci.*, 2015, **3**, 157-170.
[86] G. J. Joshiba, P. S. Kumar, M. Govarthanan, P. T. Ngueagni, A. Abilarasu, F. Carolin, *Environ. Pollut.*, 2021, **269**, article no. 116173.
[87] S. Rahdar, A. Rahdar, M. Nadeem, *J. Mater. Technol.*, 2019, **8**, 3800-3810.

Comptes Rendus
Chimie
2022, Vol. 25, Special Issue S2, p. 43-60
https://doi.org/10.5802/crchim.148

Sustainable Biomass Resources for Environmental, Agronomic, Biomaterials and Energy Applications 3 / *Ressources de biomasse durables pour des applications environnementales, agronomiques, de biomatériaux et énergétiques 3*

Industrial dye removal from tannery wastewater by using biochar produced from tannery fleshing waste: a road to circular economy

Khouloud Haddad [*, a], **Azza Hantous** [a, b], **Raouia Chagtmi** [a, b], **Hechmi Khedhira** [c], **Cherif Chaden** [c] and **Aïda Ben Hassen Trabelsi** [a]

[a] Research and Technology Centre of Energy, Technopole Borj-C'edria, B.P N 95, 2050 Hammam-Lif, Tunisia

[b] Faculty of Sciences of Tunis, Tunis El Manar University, Campus Universitaire El-Manar, 2092 El Manar, Tunisia

[c] TMM, Tanneries Mégisseries du Maghreb, Cité Antar, 8030 Grombalia, Tunisia

E-mails: Khouloud.had75@gmail.com (K. Haddad), hantousazza19@gmail.com (A. Hantous), chagtmiraouia@gmail.com (R. Chagtmi), hechmi.khdhira@tmm.com.tn (H. Khdira), chaden.cherif@tmm.com.tn (C. Cheden), aidabenhassen@yahoo.fr (A. Ben Hassen Trabelsi)

Abstract. In this study, the capacity of biochars, derived from the pyrolysis of tannery fleshing waste (TFW) at 400 °C; 500 °C and 600 °C, in removal of red dye Sella Fast Red (SFR) from aqueous solutions and tannery wastewater was investigated under various experimental conditions in batch mode. Results show that for all applied biochars, the removed kinetics data were well fitted by the pseudo-second-order model, and the equilibrium state was obtained after 240 min of contact time. For an aqueous pH of 6 and a red dye concentration of 75 $mg{\cdot}L^{-1}$, the removed amounts increased from 26 $mg{\cdot}g^{-1}$ to 39.86 $mg{\cdot}g^{-1}$ when the used pyrolysis temperature was increased from 400 °C to 600 °C. Moreover, SFR adsorption data at equilibrium were well fitted by Langmuir model suggesting a probable monolayer adsorption process with a maximal removal capacity of 62.7 $mg{\cdot}g^{-1}$ for BTFW-600 °C. The thermodynamic study demonstrated that SFR adsorption was endothermic for the three tested biochars. Desorption experiments with distilled water proved that SFR was significantly desorbed from the tested biochars, which offers possible reusability. On the other hand, BTFW-600 °C has demonstrated an important ability in removing SFR from real wastewater since only one dosage of 15 $g{\cdot}L^{-1}$ was enough to ensure more than 97% of dye removal. According to pH_{ZC} and FTIR analysis, the possible mechanism toward SFR dye removal was attributed to electrostatic interactions that occurred between biochar and functional groups of SFR. This work could provide guidance for the value-added utilization of tannery solid waste and a practical way to remove dyes from tannery wastewater.

* Corresponding author.

Keywords. Fleshing waste, Pyrolysis, Biochar, Dye removal, Tannery wastewater.
Published online: 16 February 2022

1. Introduction

Leather industry plays a prominent role in the world's economy, with an estimated global trade value of approximately US$100 billion per year [1]. Leather making consists of the transformation of animal skins and hides into valuable materials used in the manufacture of products such as shoes, leather goods, etc... requiring a series of chemical and mechanical processes [2]. During the leather process a large amount of solid wastes are generated such as hides and skins, fats, shavings and trimmings, buffing dust, process effluents, and sludge [3]. The most common way to manage solid wastes is by disposing of them on landfill sites [4]. Fleshing wastes are considered as major solid wastes (around 60%) generated from tannery and finite leather production [5]. The utilization of the same fleshings for glue manufacture is not economically viable. Similarly, fleshings obtained from hides treated with a high percentage of sodium sulfide are found to be unfit for the production of glue. They are at best disposed through landfill. Disposal of such fleshings is currently a serious problem and new ways for the disposal of tannery fleshing waste (TFW) need to be found.

Besides, in tannery manufacturing, a large amount of wastewater is generated through all tannery stages [6]. A great deal of dye wastewater is discharged during the tanning process, constituting about 30% of the total tannery wastewater [7]. Dyes have a critical impact on human health due to their toxicity and carcinogenicity [8] and therefore must be removed before their discharge into the water body. Various technologies such as coagulation, solvent extraction, and advanced oxidation process have been developed for removing these dye wastewaters in the past decades. However, these methods have some drawbacks such as high energy consumption, incomplete dye removal and toxic sludge generation. Among them, the adsorption process has been reported to be economical and easy to apply as well as effective in removing color from wastewater. Activated carbon is the most widely used adsorbent in various industrial sectors due to their highly porous structure, extremely large surface area to volume ratio and high degree of surface reactivity. However, especially due to its production and regeneration cost, the use of adsorption in industrial processes, as tanneries, is limited [5]. According to several researchers the concept of "circular economy" was proposed to be an idea of reducing environmental impact caused by discharged waste products and to increase the effective recycling system in order to minimize the wasted resources. Therefore, the use of industrial waste as alternative adsorbents has been considered, and solid waste generated in the leather processing operation has been used as alternative adsorbents for the removal of dyes, metals, oils, and surfactants [9–11]. Adsorbents are generally the key points of the adsorption method, which directly affect the adsorption capacity of pollutants and cost. Therefore, adsorbents with a high surface area and a simple preparation process attract considerable attention. Biochar [12] is the byproduct of biomass pyrolysis and is widely used in catalysis [13], storage material, [14] soil remediation, [15] and environmental pollution control [16]. Therefore, biochar especially is attracting attention as a low-cost adsorbent because it can be used as a substitute for activated carbon, which is used as a conventional adsorbent due to its ability to adsorb high levels of pollutants. The use of biochar as being eco-friendly for the removal of dye from wastewater has been examined in the past by several researchers [17–21]. However, in literature, there are few studies related to the production of biochars from tannery solid wastes and their application to wastewater treatment. Tang *et al.* [3] produced a modified biochar from non-tanned hide wastes which showed a remarkable potential to eliminate dye from effluent. Huang *et al.* [22] examined the capacity of biochar derived from leather shavings for Congo red removal. Payel *et al.* [23] produced biochar from the tannery liming sludge for in-house chromium adsorption from tannery wastewater. To date, there is still no study on dye removal by the biochar from TFW. Hence, this work aims to validate a new circular economy model based on the conversion of tannery solid wastes into biochar which will be applied for industrial dye removal from tannery wastewater. The novelty of the present study is to investigate the removal of industrial dyes used for leather tanning using biochar produced by the waste generated by the same tannery. In this context, the production of biochar using tannery fleshing solid

waste represents a new alternative sorbent to remove leather dyes from wastewaters. The new proposed adsorbent was characterized by elemental composition, SEM, optical microscopy, FTIR, and zeta potential. The adsorbent was used for the treatment of dye aqueous solutions and real tannery wastewater.

2. Materials and methods

2.1. *Biochar preparation*

TFW were collected from a Tunisian Leather Tannery factory (TMM Tannerie Megisserie du Maghreb), located in Grombalia region, Northern Tunisia. TFW were sampled directly at the end of the beamhouse production line and before the chrome tanning leather manufacturing process, in order to prevent TFW saponification. TFW samples were first finely crushed to small pieces (2 to 4 mm) and then air-dried for five days. Pre-dried TFW samples were stocked in glass bottles for further characterization and pyrolysis experiments. Afterwards, the pre-dried TFW was pyrolyzed in a fixed bed stainless reactor with a length of 30 cm and a diameter of 15 cm. During the pyrolysis tests, 300 g of TFW were placed in the reactor and heated by an electric furnace from room temperature until the desired temperature (400 °C; 500 °C and 600 °C) at a rate of 5 °C/min under 0.5 L·min^{-1} nitrogen flow. The generated biochars at pyrolysis temperatures of 400 °C; 500 °C and 600 °C were labeled BTFW-400, BTFW-500, and BTFW-600, respectively and used for the study of dye wastewater adsorption from aqueous solutions.

2.2. *Biochar characterization*

The biochar production yield (Y_{char}) was determined as the ratio between the weight of collected biochar (M_{char} (g)) and the weight of pre-dried TFW waste (M_{TFW} (g)) as follows:

$$Y_{\text{char}}\,(\text{wt\%}) = \frac{M_{\text{char}}}{M_{\text{TFW}}} * 100. \qquad (1)$$

Proximate analyzes were realized in triplicate using thermogravimetric analyzer (Mettler TGA/DSC 1) according to ASTM method. The pH of zero point charge (pH_{ZPC}) values of the studied biochars were determined according to the solid addition method using 0.01 M NaCl solutions, 1 g of solid matrix for initial pH values varying between 2 and 12. The particle size distribution of the two used solid matrixes was achieved using a Malvern Mastersizer STD06 laser granulometer. The mineral element contents of the different chars were measured by Atomic Absorption Spectrometry (AAS). The surface chemistry of biochars was provided through Fourier Transform Infrared spectroscopic (FTIR) analyzes using the KBr method with an IFTR-BX, Perkin Elmer apparatus. All biochar samples were carefully dried before mixing with KBr to avoid any additional effect due to the presence of water. The related spectral resolution is 1 cm^{-1} measured between 400 and 4000 cm^{-1}. The possible existence of any crystallographic structure in the tested biochars was assessed thanks to X-ray diffraction analysis (PW 1710). The morphologic and surface elemental composition of the biochars were characterized with a scanning electron microscopy (SEM) and energy dispersive EDX (X-ray spectrometry) (Philips XL30 FEG). Finally, biochar's textural properties were measured by carbon dioxide (CO_2) adsorption isotherms at 273 K.

2.3. *Dye adsorbate preparation*

SELLA Fast Red (SFR) RTN provided by TFL company is a mixture of direct and acid dyes. This was used as the dye adsorbate for the batch adsorption study. The formula and the complete structure diagram are not available. This dye solution showed a maximum absorbance at a wavelength of 465 nm. Distilled water was used for the preparation of dye solution throughout the study. The stock solution of 1000 ppm of SFR dye was prepared by dissolving 1 g of the dye powder in 1 L of distilled water in the volumetric flask. The desired concentrations of dye adsorbate were prepared by dilution with distilled water.

2.4. *Batch sorption experiment*

The assessment of SFR dye adsorption capacities of the elaborated biochars was performed through batch experiments. During this work, the impacts of contact time, initial SFR dye concentrations, solution pH, biochar dosages and temperature on SFR removal by the three tested biochars (BTFW-400, BTFW-500 and BTFW-600) were quantified. All these experiments were performed at 20 ± 02 °C in 120 mL capped flasks. For each run, a given biochar mass was

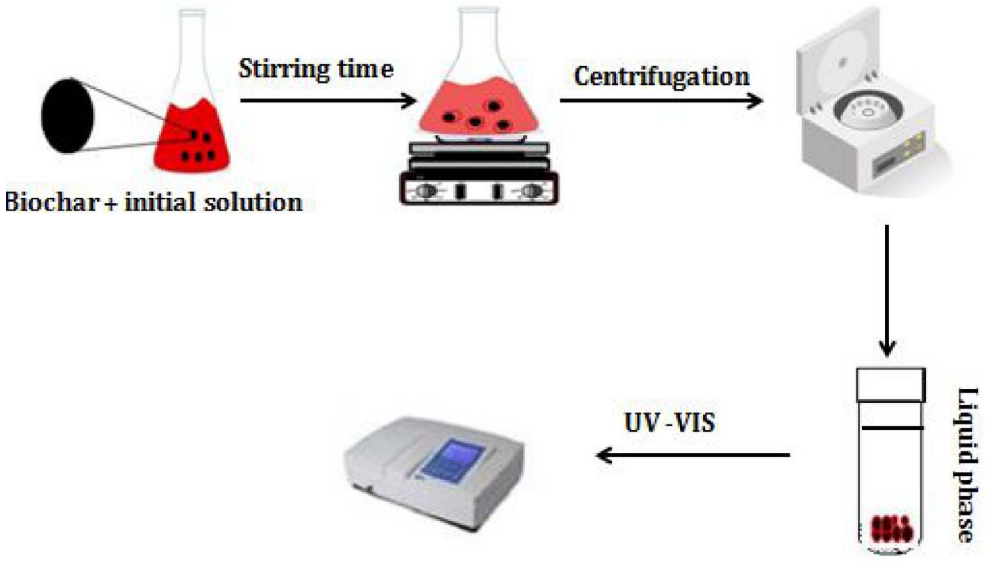

Figure 1. Setup of the flow sheet of the batch adsorption experiment.

added into 50 mL solutions of a desired dye concentration and shaken at 400 rpm using a magnetic stirrer (Figure 1). After the stirring time, the liquid phase was separated from the adsorbent particles by a laboratory centrifuge type NEOFUGE 1600R at a speed of 4000 rpm for 20 min. SFR color removal was evaluated by measuring absorbance decrease at 465 nm using an UV–Vis spectrophotometer ($T80^{+}$).

The adsorbed SFR dye amount at a given time, t, ($q_{t,P}$: mg·g^{-1}) by the three tested biochars was calculated as below:

$$q_t = \frac{C_0 - C_t}{M} * V, \tag{2}$$

where C_0 and C_t (mg·L^{-1}) are the initial and at time t aqueous SFR concentrations, respectively, V is the volume of the aqueous solution and M is the weight of the used biochar (g). It is important to underline that each analysis point given in this study was an average of three independent parallel sample solutions with a standard deviation of ±3%.

2.5. *Kinetic and isotherm studies*

Kinetic studies were carried out in order to establish the effect of contact time on the dye adsorption process by the three tested biochars. Kinetics were monitored at various times between 1 and 360 min. The initial SFR dye concentration, the biochar dosages, the aqueous pH and temperature were fixed to 75 mg·L^{-1}, 2 g·L^{-1}, 6 (natural: without adjustment) and 20 °C, respectively. The equilibrium adsorption data were assessed for the three studied biochars for initial SFR concentrations varying between 50 and 100 mg·L^{-1} and a constant contact time of 240 min. This time was determined on the basis of preliminary assays and judged to be sufficient to ensure an equilibrium state between dye molecules and the adsorbent particles. These experiments were performed for fixed adsorbent dosages, aqueous pH and temperature of 2 g·L^{-1}, 6 and 20 °C, respectively. Several models have been used in scientific literature to fit the kinetic and equilibrium adsorption experiments [24,25]. In the present study, we used the most common kinetic and equilibrium models namely, the pseudo-first-order, pseudo-second-order, intraparticle and film diffusion; and Freundlich and Langmuir models, respectively. The SFR kinetics of BTFW was fitted with the pseudo-first- and pseudo-second-order models. The related kinetic constant values of each model (K_1 and K_2), the correlation coefficients, R^2, the predicted removal dye amounts at equilibrium in comparison with the experimental ones are given in Table 3. Furthermore, in order to compare the applicability of these two kinetic models and their goodness of fit to the experimental data, the average percentage errors (APE) between the predicted removal of dye amounts "$q_{t,\mathrm{calc}}$ (mg·g^{-1})" and the experimental ones "$q_{t,\mathrm{exp}}$ (mg·g^{-1})" for each used

biochar were assessed as follows:

$$\mathrm{APE}\,(\%) = \frac{\sum_{i=1}^{i=N} \left| \frac{(q_{t,\mathrm{exp},i} - q_{t,\mathrm{cal},ic})}{q_{t,\mathrm{exp},i}} \right|}{N}, \qquad (3)$$

where N is the number of the experimental runs.

2.6. *Effect of pH, biochar dosages and temperature*

During these experiments, the default values of the tested parameters were fixed to 75 mg/L, 6.0, 2 g/L, 240 min, and 20 °C for initial aqueous SFR concentration, pH, contact time and temperature, respectively. The influence of the initial aqueous pH solutions on SFR removal from the synthetic solutions by the three tested biochars were investigated in a series of experiments for initial pH values of 3, 6, 9, and 12. The impact of the adsorbent dosages on SFR removal was assessed for the three biochar doses of 0.5, 1, 2, 4, 6, 12 g/L respectively. Finally, the effect of temperature on SFR removal was studied at four different temperatures, 20, 30, 40, and 50 °C. For all the assays cited previously, pH adjustment was carried out using small volumes (lower than 1 mL) of 0.1 M HNO3, and NaOH solutions. Moreover, each analysis point reported in this study is an average of at least three independent parallel sample solutions. The standard deviation of the results was 3%.

2.7. *Desorption test*

The SFR desorption from preloaded BTFW-600 °C at concentrations of 39.8 mg/g was performed using distilled water. During these experiments, 0.1 g of the dye-loaded adsorbents was shaken in 100 mL of distilled water at different initial pH values of 5, 7, 9, and 11, adjusted with NaOH (analytical grade) at 20 °C for 2 h. As for adsorption studies, the aqueous phase of the triplicate samples were separated from the solid ones by centrifugation before analysis with UV–Vis spectroscopy. The mass of desorbed SFR by unit of adsorbent weight at equilibrium, q_d (mg/g), and percent dye desorption (Y (%)) were determined based on the common equations given by Jain *et al.* [26].

2.8. *Batch experiments for SFR dye removal from real wastewaters*

BTFW-600 °C has been used to carry out additional assays regarding SFR dye removal from real wastewater. The main aim of this kind of experiment is to check the BTFW-600 °C efficiency for relatively complex solution compositions. The used wastewater has been collected from a Tunisian Leather Tannery factory (TMM Tanneries Megisserie du Maghreb), located in Grombalia region, Northern Tunisia. During these experiments, in order to compare the dye efficiencies observed for synthetic solutions, the initial aqueous pH was fixed to 6 for the used wastewater. The tested BTFW-600 °C doses were fixed to 1, 4, and 10 $g{\cdot}L^{-1}$. As for the synthetic solutions, triplicate experiments were performed for a contact time of 240 min.

3. Results and discussion

3.1. *Effect of pyrolysis temperature on biochars properties*

3.1.1. *Biochars yields*

The pyrolysis of the TFW demonstrated that the biochar yields were dependent on the used temperature (Table 1). Indeed, they decreased from about 52.5% to 33.3% when the temperature increased from 400 °C to 600 °C. This behavior is attributed to the fact that at low pyrolysis temperatures, lower condensation yields of aliphatic compounds and smaller transformations of fleshing waste components to CH_4, H_2 and CO were achieved [27]. Several researchers [28, 29] reported that the decrease in yield of biochar is due to moisture evaporation, devolatilization and char combustion. Similar observations were reported by Younis *et al.* [30] and Gil *et al.* [31] when studying the pyrolysis of tannery solid waste and wastes of vegetable tanning under different temperatures, respectively.

3.1.2. *Biochars characterization*

Physicochemical characterization of the three tested biochars, is shown in Table 1. As expected, the pyrolysis step produces an increase in fixed carbon content, a decrease in volatile matter and an increase in the ash concentration. The volatile matter contents of the biochars significantly decreased

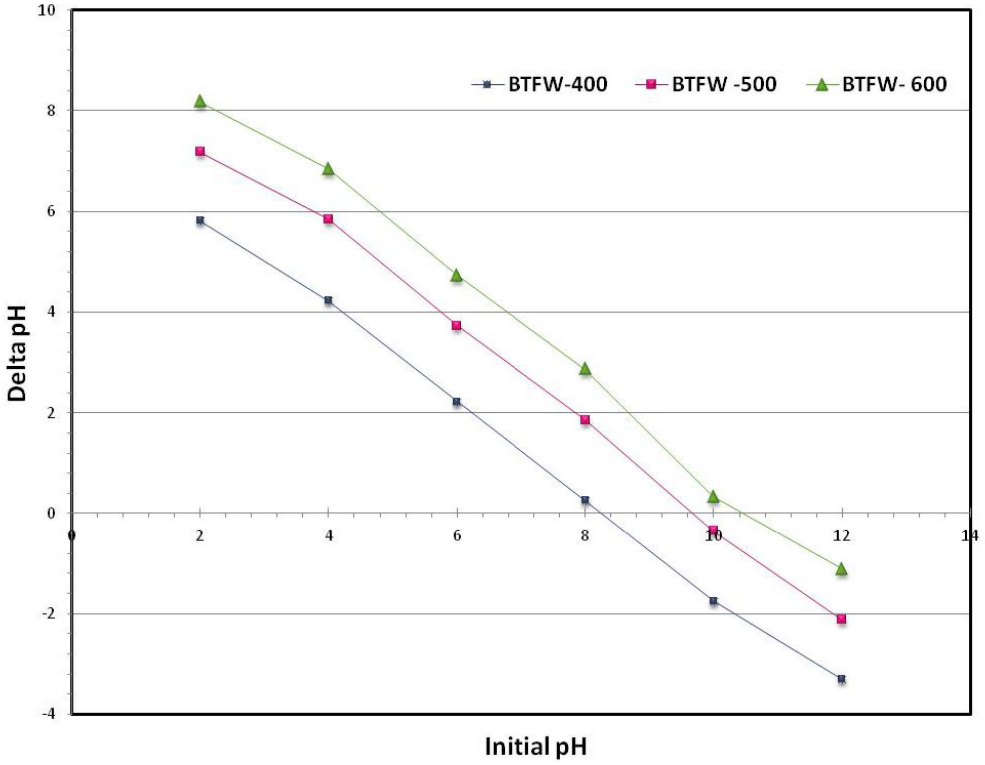

Figure 2. pH of zero point charge of the three tested biochars.

from about 46.29% to 12.3% when the applied pyrolysis temperature was increased from 400 to 600 °C. The relatively low concentration of volatile matter present in the char indicates that the material has been totally pyrolyzed and the volatile solid loss is primarily dependent on the quantitative share of protein, lipid and carbohydrates in the wastes and its thermal stability differences. The fixed carbon contents increased from 16.08% to 37.24% when the temperature was raised from 400 °C to 600 °C. On the other hand, ash content increased from 30.21% to 43.84% as the pyrolysis temperature increased from 400 °C to 600 °C. Ash contents was high due to the presence of salts and inorganic substances used in the pre-tanning process. A similar result was obtained by Velusamy *et al.* [32] when quantifying the impact of pyrolysis process on the characteristics of biochars produced from leather finished trimmings and chrome shavings from tanneries at a temperature of 500 °C. Results show a significant reduction in the volatile solids of the two tested materials from 75.7 and 74.7% in raw wastes to 27.4 and 32.1% in the char, respectively. Researchers also reported that pyrolysis process increased the ash content of this waste from 7.9–10.5% to 15.8–25.2%.

It is important to underline that the pyrolysis temperature has increased the pH_{ZPC} from 8.5 to 10.3. (Figure 2). This behavior could be probably due to the separation of alkali salts from the TFW at high temperatures. This means that the surface of biochars behaves as positively charged for solutions lower than these values. This finding is very promising since these biochars could contribute to the elimination of anionic dyes. These results agree with the overall literature about biochars that typically indicate basic properties [33,34] for this type of materials.

The particle size distribution of the three tested biochars shows that they are heterogeneous porous media since uniformity coefficient was higher than two. Indeed, their mean diameters are evaluated at about 16.5, 18.6 and 33.7 μm for BTFW-400, BTFW-500 and BTFW-600 respectively. The presence of relatively small sized particles in the used biochars should play an important role in physicochemical re-

Table 1. Main properties of the biochars pyrolyzed under temperature of 400–600 °C

	BTFW-400	BTFW-500	BTFW-600
Yields (%)	70.59	52.7	39.47
Ash content percentage (%)	30.21	40.61	43.84
Volatile matter (%)	46.29	20.98	12.30
Fixed carbon (%)	16.08	31.39	37.24
pH_{ZC}	8.5	9.25	10.3
Mean diameter d50 (mm)	16.5	18.6	33.7
Uniformity coefficient (UC)	6.42	5.95	6.22
Specific area ($m^2 \cdot g^{-1}$)	70.54	101.3	140.98
Volume micropore ($cm^3 \cdot g^{-1}$)	0.067	0.072	0.098

Table 2. Element content in the biochar in three tested biochars (mg/kg)

	Cu	Cr	Cd	Zn	Fe	K	Mg
BTFW-400	37	200	50	700	4120	23.37	3458
BTFW-500	101	300	190	1630	4710	26.56	5610
BTFW-600	324	500	70	1500	5205	77.21	6521

actions with the tested dye. On the other hand, it can be noticed that the specific surface area of the biochars was increased from 70.54 to 140.98 when the used temperature was increased from 400 °C to 600 °C (Table 1). Hence these biochars can be used as an adsorbent for treating dye contaminated wastewater. This result most likely is due to more decomposition of polymeric network and organic moieties [35]. A similar result was obtained by Younis *et al.* [30] when studying the impact of pyrolysis process on tannery solid waste. The surface area of biochar was 134.9 $m^2 \cdot g^{-1}$, which indicates the presence of fewer tiny pores. Suliman *et al.* [36] observed that the maximum surface area was in the range of 145–500 $m^2 \cdot g^{-1}$ from different biochars prepared at 400–600 °C. The extra volatile release, caused by higher temperatures, explains also the generation of higher microporosity, as the micropores get larger by 58% (from 0.062 to 0.098 $cm^3 \cdot g^{-1}$). The inorganic contents of the three studied biochars were determined thanks to AAS analyzes (Table 2). The tested biochars produced from TFW contained the heavy metals Cr, Cd, Zn, Cu, and Fe along with, K and Mg, with Fe being the highest as compared to all others. Among the essential metals, Mg was the highest followed by Fe and Zn (Table 2). The high metal content in the three biochars produced from TFW might be due to chemicals used in beamhouse treatment and tanning process This is in line with Younas *et al.* [37] who reported high concentration of Cr, Zn, Cu, and Pb due to the tanning process and bioaccumulation of fumes of burnt tannery solid waste. Furthermore we can see from Table 2 that the contents of K, Cr, Zn, Mg, Cd, Fe, and Cu increased by about 230%, 150%, 114%, 88% and 40%, 26% and 7.75% respectively, when the pyrolysis temperature was increased from 400 to 600 °C. The same trend was observed by Haddad *et al.* [38] when they explored the effect of pyrolysis temperature on biochar production yields from selected lignocellulosic biomasses. They suggested that temperature increase upgrades ash elemental concentrations relative to its yield.

3.1.3. *Surface functionalities*

The adsorption capacity of biochar produced from TFW depends on the chemical reactivity of functional groups at the surface. The FTIR spectra of three used biochars were compared and are given in Figure 3. The biochar peaks obtained were: The O–H symmetric stretching at 3230 cm^{-1} showed the presence of alcohol and carboxylic acid. An aliphatic asymmetric and symmetric stretching of C–H bond in CH_2 and CH_3 was observed at wavelength

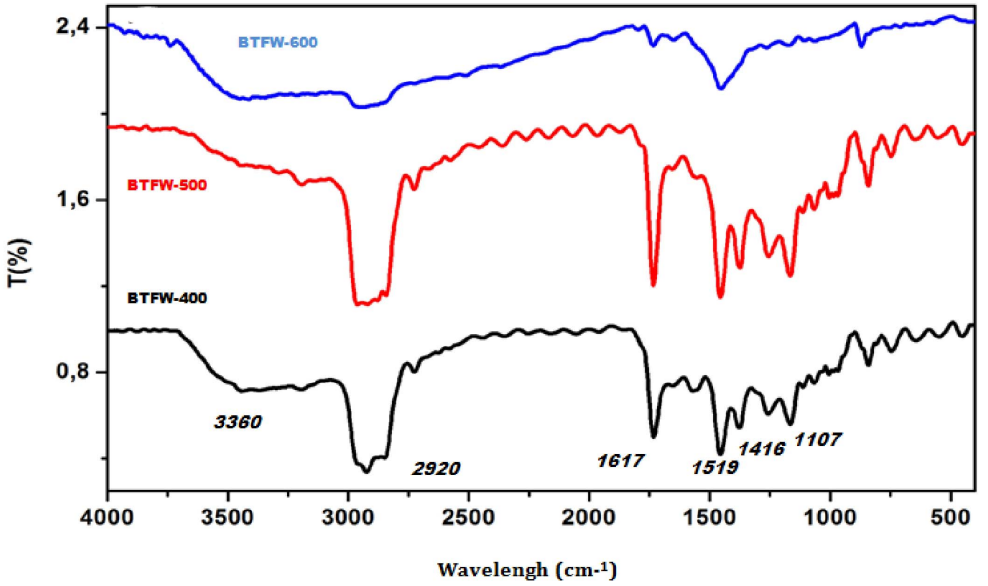

Figure 3. FTIR spectra of three tested biochar produced at different temperature.

2920.23 cm^{-1}. The peak formed at 1616.35 cm^{-1}, assigned to carboxyl C=N stretching, shows that amine groups stick to the surface of biochar [39]. The peak at 1519.91 cm^{-1} wavelength attributed to aromatic C=C bonds indicates the presence of unsaturated aryl substituent alkenes. The peak at 1404.18 cm^{-1} assigned to C–H bond confirms the aliphatic nature of biochar. The peaks at 1107 cm^{-1} formed due to C–O and C–C ring indicate the presence of alcohol and esters [40]. The spectra of all the studied biochars were relatively similar and no significant differences were noticed. The remaining peaks were 997.20 cm^{-1} C–H in plane bending, 871.82 cm^{-1} amines H–N, 746.45 cm^{-1} alkyl halide C–Cl, 673.45 cm^{-1} alkynes bend and 555.50 cm^{-1} alkyl halide C–Br. The resulting groups might enhance the adsorption process during the dye removal process and thus offer more fixation sites for dye molecule adsorption. Similar results were obtained by Palani *et al.* [41]. It was found that activated carbon derived from tannery fleshing compared to commercial activated carbon has more functional groups on the surface to trap the dye on the surface of adsorbent, which leads to higher adsorption capacity.

3.1.4. *SEM analyzes*

SEM analysis was employed to perceive the surface morphologies of the prepared biochars produced from TFW (Figure 4). The SEM image showed that BTFW has a homogenized surface mainly composed of spherical particles of 10 μm size that may be explained by the presence of high content of mineral deposited on the surface of biochars. Furthermore, Figure 4 reveals the presence of pores with different sizes. This high number of pores is expected to improve the rate of dye adsorption.

3.2. *Batch sorption experiments*

3.2.1. *Kinetic studies of SFR dye removal*

In order to determine the required adsorption equilibrium time of SFR onto three tested biochars as well as the probable involved mechanisms, a kinetic study was elaborated for contact times varying from 1 to 360 min at an initial dye concentration of 75 $mg{\cdot}L^{-1}$ for three tested biochars. As illustrated in Figure 5, experimental results showed that SFR adsorption process is clearly time dependent.

Indeed, the amounts of adsorbed SFR dye (q_t) rapidly rose for contact times lesser than 90 min. At this moment, they attained about 63%; 79% and

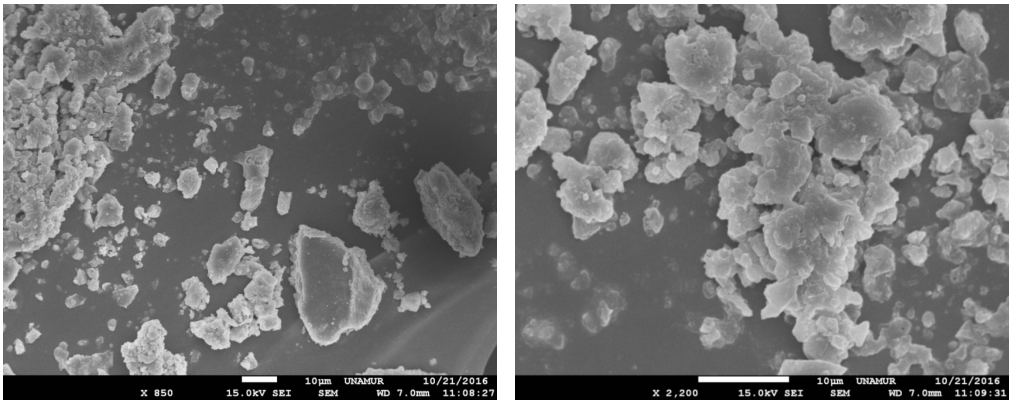

Figure 4. SEM observations of tested biochars produced at temperature of 500 °C.

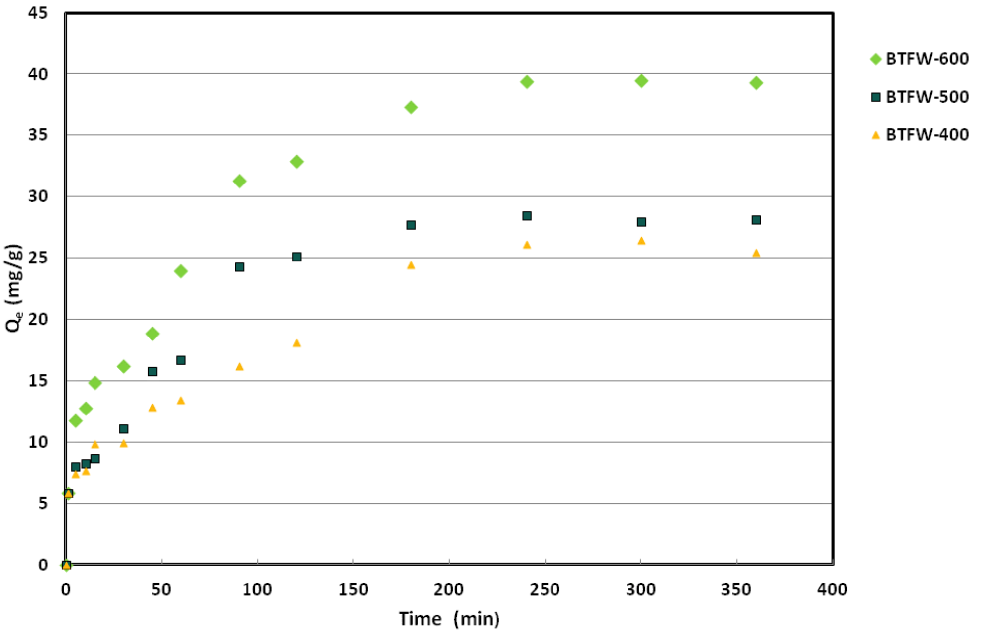

Figure 5. Effect of contact time on SFR dye adsorption by three tested biochars (C_0 = 75 mg·L^{-1} pH = 6; dosage = 2 g·L^{-1}; T = 20 °C).

86% of the whole adsorbed amounts for BTFW-400; BTFW-500 and BTFW-600, respectively. For duration greater than 90 min, the adsorbed SFR dye continued to increase but with a smaller slope. The equilibrium state, corresponding to quasi-constant amounts was observed at 240 min. The registered important red dye removal rate at the beginning of the assays could be attributed to the fact that SFR dye was mainly adsorbed at the exterior surfaces of the biochars. Afterwards, when the adsorption at the exterior surfaces of the studied biochars attained complete saturation, the SFR dye diffused inside the solid biochar particles and were adsorbed. This diffusion process is generally constituted of two steps: (i) the first one corresponds to dye diffusion through the boundary layer where the surface groups were saturated, then (ii) the second step is related to SFR dye diffusion through the intra-particle layer and the pores through the surface of the adsorbents for additional uptake [42]. It is important to underline that SFR

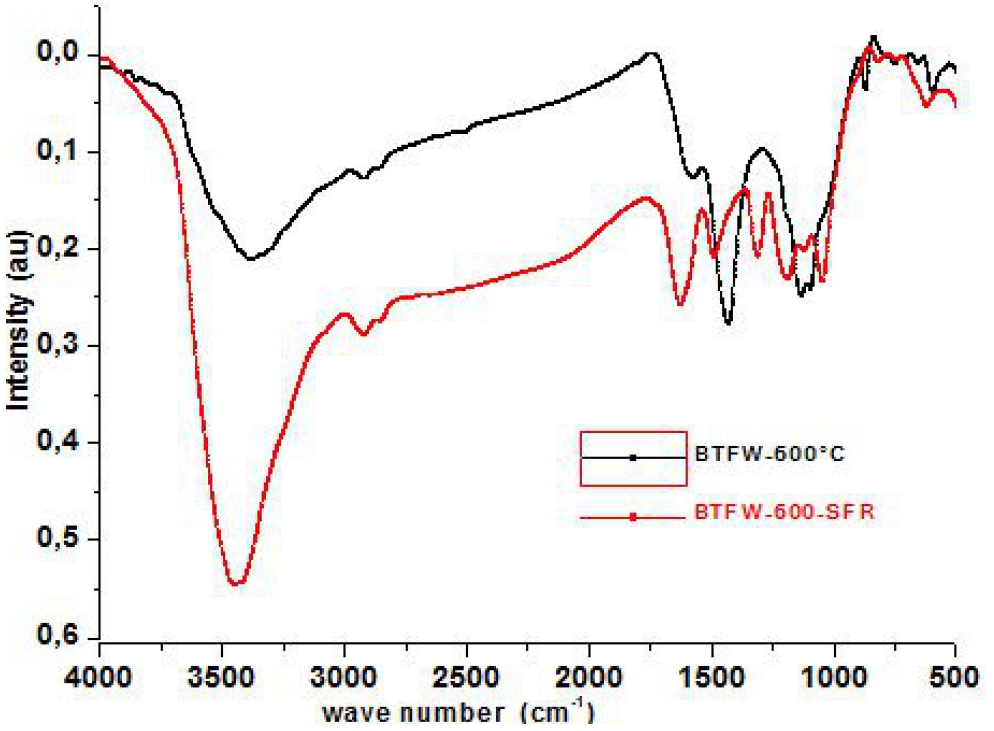

Figure 6. FTIR analyzes of BFTW-600 °C before and after SFR dye removal.

dye adsorption efficiency at equilibrium significantly increased when raising the pyrolysis temperature. Indeed, the SFR dye amounts were determined to about 26; 28,52 and 39,86 mg/g mg·g^{-1} for, BTFW-400; BTFW-500 and BTFW-600, respectively. This behavior should mainly be due to the modification of the physicochemical properties of the biochars induced by the pyrolysis treatment, especially the surface areas, and functional groups, which suggests that chemisorption would be the main driving force for the removal of SFR dye. Therefore, the adsorption of SFR dye onto the BTFW might be due to (1) active sites formed during the pyrolysis process, (2) high specific surface area from the porous structure of BTFW-600, and (3) chemical bonding between biochar compounds and SFR dye.

In order to better understand the chemical interaction between the dye molecules and the surface of the tested biochars, the FTIR spectra of BTFW-600 °C and biochar-dye were analyzed. As shown in Figure 6, the adsorption peaks of dye-bound biochar at 1515, 1451, 1421, 1385, 1034, and 800–500 cm^{-1} display a changed intensity of adsorption compared to those of the dye-free biochar. These indicate that the—NH_2, –OH, carboxyl, carbonyl, and alkyl functional groups are involved in the possible chemical adsorption process. According to some authors [18, 43] the possible actions in the intensities of the adsorption bands mentioned above can be attributed to: (1) hydrogen bond formation between nitrogen and oxygen containing functional groups of dyes and biochars; (2) π–π dispersion interaction between the aromatic rings in the dyes and biochars; (3) the interaction of sharing electron, in which the carbonyl oxygen present in biochar can act as electron acceptor and the aromatic ring of SFR dye can be as an electron acceptor; (4) the electrostatic interaction between dyes and biochars, which can be proved by the investigated results in the effects of pH.

The SFR dye adsorption by the three tested biochars was fitted with the pseudo-first- and pseudo-second-order models. The related kinetic constant values of each model (K_1 and K_2), the correlation coefficients, R^2, the predicted adsorbed dye amounts at equilibrium in comparison with the experimental ones are given in Table 3.

Table 3. SFR dye adsorption kinetic parameters of three tested biochars

Sample	First order				Second order			
	K_1	$q_{e,\mathrm{I}}$	R^2	APE (%)	K_2	$q_{e,\mathrm{II}}$	R^2	APE (%)
BFTW-400	0.008	20.98	0.9270	9.20	0.0008	20.41	0.9668	2.65
BFTW-500	0.0200	26.199	0.9449	8.12	0.0007	33.00	0.9652	3.36
BFTW-600	0.0020	37.96	0.922	11.3	0.0009	40.32	0.9895	4.21

Table 4. SFR dye isotherms parameter of three tested biochars

Sample	Freundlich				Langmuir			
	K_f	n	R^2	APE (%)	K_L	Q_m	R^2	APE (%)
BTFW-400	1.72	1.02	0.905	6.5	0.025	39.5	0.994	4.5
BTFW-500	2.56	1.13	0.919	12.6	0.03	**53.8**	0.996	3.7
BTFW600	4.50	1.37	0.858	15.6	0.18	62.7	0.999	2.6

From Table 3, it could be clearly noted that the correlation coefficients calculated for both pseudo-first-order and pseudo-second-order models were relatively high, indicating a good fit to the experimental data [44]. However, the calculated amounts of removed SFR dye at equilibrium ($q_{e,\mathrm{I}}$) for all the tested biochars by the pseudo-first-order model were very low compared to the experimental ones and the related APE was important, presuming that SFR dye removal kinetics is not a pseudo-first-order process. On the contrary, the "$q_{e,\mathrm{II}}$" values corresponding to pseudo-second-order kinetic model were very close to the experimental data. Besides, its APE values were significantly lower than the ones determined for the pseudo-first-order kinetic mode. As a consequence, for all the tested biochars, the pseudo-second-order model is most appropriate for the restitution of the experimental data (Table 3). This finding suggests that SFR dye adsorption by biochars derived from TFW might be mainly a chemisorption process including electronic bonding between the surface biochars' functional groups and the tested dye, since a similar finding has been reported [22] in which the adsorption and desorption of Congo red on biochars produced from leather shavings waste was investigated.

3.2.2. *Effect of initial dye concentrations, isotherm modeling*

The SFR dye uptake increased with increasing initial dye concentration. For instance, raising initial dye concentrations from 50 to 250 mg·L^{-1} allowed the BTFW-400, BTFW-500 and BTFW-600 to increase their recovery abilities from 14.52 to 33.9 mg·g^{-1} and from 16.2 to 36.62 mg·g^{-1} and from 19.11 to 59.54 mg·g^{-1}, respectively (Figure 7). This trend could be explained by the fact that the higher the initial aqueous dye concentration, the higher the concentration gradient between aqueous solution and biochar particles, which results in more important diffusion rates. Furthermore, for high initial aqueous concentrations, the contact probability between SFR dye contained in the aqueous phase and the adsorbent might be more privileged. The Langmuir and Freundlich constants, the corresponding correlation coefficients and APE are presented in Table 4. For all the tested biochars, the highest regression correlation coefficients (0.996) and the lowest APE values (13.8%) were observed for Langmuir model. Thus, this model successfully fits the experimental data (Figure 7). This finding suggests that SFR adsorption by the tested biochars occurs on a uniform surface with constant energy. The SFR dye Langmuir's adsorption capacity, $q_{\max}$, of BTFW-400, BTFW-500 and BTFW-600 were assessed to about 39, 53.8 and 62.7 mg·g^{-1}, respectively, confirming that the increase in pyrolysis temperature positively impacts the biochar's ability of red dye adsorption from aqueous solutions. The Langmuir's coefficient values ($R_L = 1/(1 + K_L C_{0,\mathrm{SFR}})$) for the studied aqueous concentrations range varied from 0.12 to 0.35 for BTFW-

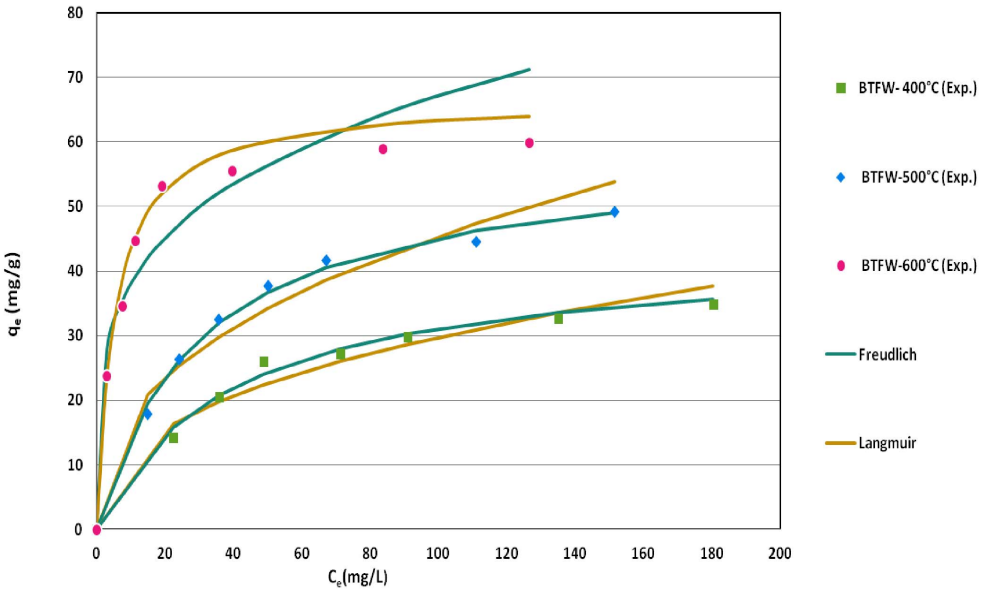

Figure 7. SFR at equilibrium by the biochars produced from TFW at different temperatures and their fitting by Langmuir and Freundlich isotherm models (contact time = 240 min; pH = 6; dosage = 2 g·L^{-1} , temperature = 20 °C).

400; from 0.13 to 0.33 for BFTW-500 and from 0.01 to 0.2 for BFTW-600, respectively. These values are low, showing that the SFR dye adsorption by these biochars is a favorable process. About Freundlich model which supposes the presence of a heterogeneous surface, its APE values were higher than the ones determined for Langmuir's model (Table 4 and Figure 7). On the other hand, the Freundlich exponent "n" values were estimated to 1.02, 1.13 and 1.37 for BFTW-400; BFTW-500 and BFTW-600, respectively (Table 4). These values were in the range of 1–10 which indicates a favorable adsorption of SFR dye by the used biochars. In order to situate the biochars generated from TFW efficiencies in recovering dye from aqueous solutions, a comparison with other biochars based on Langmuir's maximal recovery capacity "q_{max}" or otherwise its capacity at a given aqueous concentration was carried out (Table 5). According to this table, BTFW-600 has relatively higher recovery capacities compared to various biochars. As a consequence it could be considered as an attractive and promising material for red dye removal from aqueous solutions.

3.2.3. *Effect of pH*

The effect of initial aqueous pH on SFR dye removal by three tested biochars was performed according to the experimental conditions given in Section 2.5. Figure 8 showed that the initial aqueous pH plays an important role in removing SFR dye from aqueous solutions by the three tested biochars. Indeed, the biochars' removal capacities significantly decreased when increasing the initial pH. For example, for BTFW-600, for an initial concentration of 75 mg·L^{-1}, the removed dye amounts decreased from about 42.9 mg·g^{-1} at an initial pH of 3 to less than 35.9 and 25.6 mg·g^{-1} for initial pH values of 9 and 12. This trend is in concordance with those reported when investigating Congo red removal by vermicompost biochar [43] and biochar from crab shell [47]. The pH_{ZPC} is an important parameter to describe the adsorption behavior of the tested dye. The pH_{ZPC} of BTFW-400, BTFW-500 and BTFW-600 were 8.5, 9.25, and 10.3, respectively. It is well known that electrostatic attraction exists between the negative charge of the anionic dye and the protonated –OH and –COOH groups on the surface of the biochars as pH was lower than pH_{ZPC}. Therefore, the lower pH below the pH_{ZPC} will facilitate adsorp-

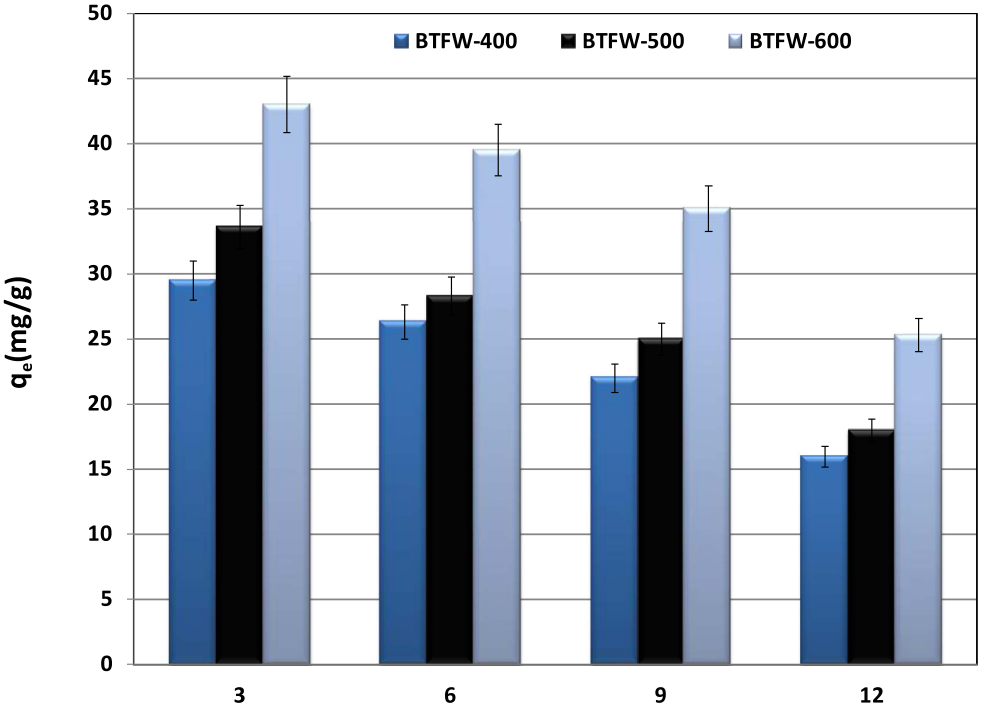

Figure 8. Effect of pH on SFR dye removal by three tested biochars (C_0 = 75 mg·L^{-1}; dosage = 2 g·L^{-1}; T = 20 °C).

Table 5. Comparison of red dye by biochars generated from the pyrolysis of TFW with other biochars

Biochar	Dyes	Adsorption capacity (mg·g^{-1})	Reference
Biochar from chrome-tanned leather shavings	Acid Black 210	44.4	[45]
Bamboo hydrochars	Congo red	33.7	[46]
Vermicompost-derived biochars	Congo red	20	[43]
Calcium-rich biochar from crab shell	Congo red	20.317	[47]
Biochar from liquefaction of rice husk with water	Malachite green dye	46.6	[48]
Coir pith carbon	Congo red	6.7	[49]
Biochar produced from TFW at 600 °C	SFR dye	62.7	This work

tion. When the pH was higher than pH_{ZPC}, the functional groups of the biochars were completely deprotonated and the electrostatic attraction was weakened with the pH increase, resulting in the decrease of SFR adsorption. In addition, the OH^- ions in the solution compete with the anionic SFR molecules for the adsorption sites, leading to a decrease in adsorption of the anionic dye at higher pH, especially in alkalinity.

3.2.4. *Influence of biochar dosages*

The effect of the used biochar dosages on SFR dye efficiencies was determined under the experimental conditions cited in Section 2.5. Results (Figure 9) indicated that for all the tested biochars, the SFR removal efficiencies increased with the increase in biochar dosages. Moreover, all the tested biochars could be considered as promising materials for SFR

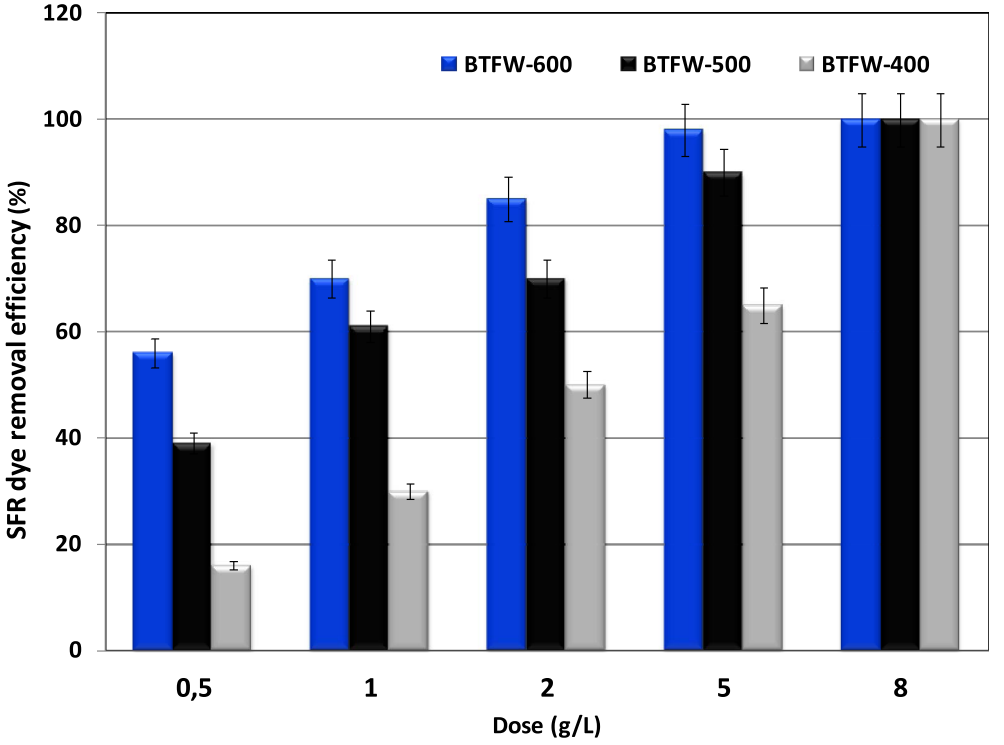

Figure 9. Effect of biochar dosage on SFR removal by the three tested biochars (C_0 = 75 mg·L^{-1}; pH = 6; T = 20 °C).

dye since even for a small dosage (5 g·L^{-1}), relatively high efficiencies of 97%, 88%, and 70% were registered for BTFW-600, BTFW-500, and BTFW-400, respectively. A complete SFR dye removal was obtained with low biochar dosage of 8 g·L^{-1} for the three tested biochars, which confirms the attractiveness of the used biochars. Therefore, the three tested biochars could be considered as interesting products for red dye removal from solutions compared to coffee-waste-activated biochar [50] and commercial activated carbon [51], where solid dosages of 20 and 10 g·L^{-1} were needed to ensure significant efficiencies. This finding is linked also to the existence of important available active sorption sites.

3.2.5. *Thermodynamic parameters*

The effect of temperature is another significant physicochemical parameter because any change in the temperature of reaction will directly contribute to the change in the adsorption efficiency and capacity of the adsorbent. The selected temperature values were set at 20, 30, 40, and 50 °C, and the results of this study is shown in Table 6. For the three biochars, adsorbed amounts increased with increase in temperature (Table 6). It rises from 39.8 mg/g at 20 °C to 50.98 mg/g at 50 °C for BTFW-600 °C. Increase in temperature may increase the rate of diffusion of the adsorbate molecules across the external boundary layer and in the internal pores of adsorbent particles and may decrease the viscosity of the solution [52]. The thermodynamic parameters associated with adsorption processes, namely standard free energy changes $\Delta G°$ (kJ/mol), enthalpy $\Delta H°$ (kJ/mol) and entropy changes $\Delta S°$ (kJ/mol/K), were investigated for a better understanding of the probable mechanisms leading to SFR sorption onto the three tested biochars. These parameters were calculated according to the following equations:

$$\Delta G° = -RT\ln(K_C) \quad (4)$$

$$\Delta G° = \Delta H° - T\Delta S° \quad (5)$$

$$K_C = q_e/c_e, \quad (6)$$

where R is the universal gas constant (8.314 J/mol/K), T is the temperature (K), and K_C is the distribution

Table 6. Thermodynamic parameters for SFR adsorption onto the three tested biochars

			$\Delta G°$ (kJ/mol)				q_e (mg/g)			
	$\Delta S°$ (kJ/mol/K)	$\Delta H°$ (kJ/mol)	293 K	303 K	313 K	323 K	293 K	303 K	313 K	323 K
BTFW-400	27.3	21.98	1.65	2.32	3.25	4.33	26.1	28.6	32.6	37.6
BTFW-500	46.8	23.35	2.65	2.77	3.87	5.36	28.9	31.5	35.6	40.5
BTFW-600	49.32	25.65	2.99	3.25	4.36	5.87	39.8	43.5	46.6	50.98

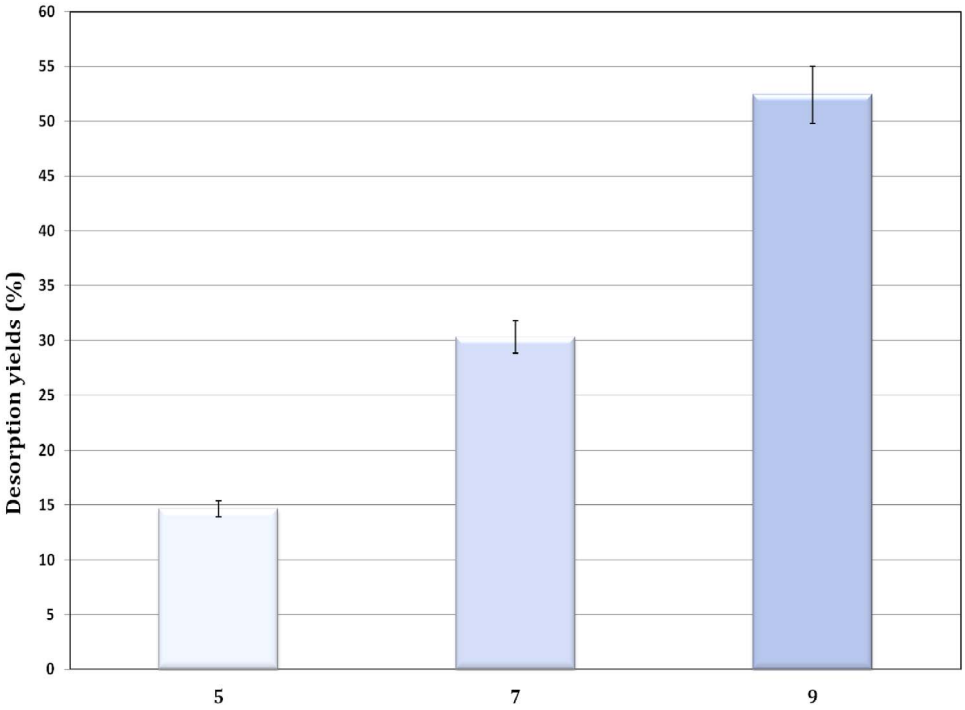

Figure 10. Effect of initial pH on SFR dye removal, BTFW-600 °C desorption from BTFW-600 °C (dose = 1 g/L; contact time = 2 h; temperature = 20 ± 2 °C).

coefficient. The thermodynamic parameters were calculated from the Van't Hoff plot of $\ln(K_C)$ as a function of $1/T$. The calculated slope and intercept from this plot were used to determine $\Delta H°$ and $\Delta S°$, respectively (Table 4). For all tested biochars the $\Delta H°$ value was positive confirming that the SFR adsorption process was endothermic. Besides, $\Delta S°$ was also positive which revealed the increase in randomness at the solid/solution interface during the SFR adsorption process [53]. In general, it is stated that sorption is considered as physical sorption if the enthalpy lies in the range between 2.1 and 20.9 kJ·mol^{-1}, while if the enthalpy lies in between 20.9 and 418 kJ·mol^{-1}, then it is termed as chemical sorption [52]. Since in our case the value of ΔH was higher than 20.9 kJ·mol^{-1}, for the three tested biochars, it is suggested that SFR anionic dye sorption onto biochar surface takes place due to chemisorption [53,54]. The findings from the adsorption thermodynamics study were in agreement with the results of adsorption kinetics and isotherm studies demonstrated earlier, which confirm chemisorption mechanism for CR anionic dye. Similar observations have been reported by Huang *et al.* [24] when investigating Congo red removal by biochar produced from leather waste.

3.3. *Desorption test*

The SFR desorption experiments were performed according to the experimental procedure presented in Section 2.6. The results, reported in Figure 10, showed that SFR dye desorption percent yields for BTFW-600 increase with increasing alkalinity of the used solutions. The desorption slowly increased from 14.66 to 52.4% with pH changing from 5 to 9. This regeneration yield could be significantly improved if successive cycles were applied. This finding could be attributed to the fact that the adsorption is dominated by electrostatic interaction and hydrogen bonding in the adsorption process [55,56]. The fact that these adsorbents have the ability to be easily regenerated, confirms that they could be considered as attractive and promising materials for anionic dye removal from aqueous solution. Similar results were obtained by Faheem *et al.* [57], who studied desorption of Congo red from biochar derived from Corncobs agricultural waste. The results confirmed that alkaline medium (NaOH) constitutes the best desorbing agent as it has the highest desorption efficiency of over 70%.

3.4. *Batch experiments for SFR dye removal from real wastewaters*

For further valorization of the studied biochar produced from the TFW, the adsorption of real textile industry effluent, containing SFR dye as the main dye, was investigated to assess the effectiveness of the treatment.

The effluent was characterized by determining its pH, conductivity, color, COD, BOD5, total solids, chloride and total chromium. The values of these parameters along with the Tunisia regulation are given in Table 7. The solution of the studied wastewater has a red color, a sign of the presence of a significant load of dye and suspended solids (MES). Table 7 shows that the effluent has a pH of about 7.2 and therefore does not require any neutralization. A conductivity of around 7.14 $ms{\cdot}cm^{-1}$ at 22 °C is explained by the high content of chloride. Likewise, the effluent has a very low value of biological oxygen demand (BOD_5) which is equal to 11 $mg{\cdot}L^{-1}$ and a chemical oxygen demand (COD) of 45 $mg{\cdot}L^{-1}$. The values of these two parameters indicate that the effluent is not too loaded with organic and mineral matter due to the physicochemical precipitation and biological treatment of real effluent conducted in the wastewater treatment plant of TMM industry. Red dye from real wastewater collected from a TMM industry has been performed using different doses of BTFW-600, since it has exhibited more efficiency compared to BTFW-500 and BTFW-400. The adsorption studies were conducted using 100 mL of textile wastewater with 2, 10, 15, 20, and 25 $g{\cdot}L^{-1}$ of BTFW-600 for 4 h of reaction time at 25 °C. The measurement of absorbance after treatment shows that 15 $g{\cdot}L^{-1}$ of BTFW-600 is the optimal dose. Figure 11 shows the absorbance spectra of the initial solution, after being diluted 50 times, and after 4 h of effluent treatment (without dilution), which clearly indicates its total discoloration. The main characteristics of textile wastewater after treatment are presented in Table 6. Besides the elimination of color, adsorption using BTFW-600 °C drastically decreases the significant characteristic parameters of the effluent. This treatment decreases the COD value and Cl concentration by about 98% and 90% respectively. Hence, except for the conductivity, the treated effluent has all the characteristic properties well within the specific limit values of rejection by textile industries. Only additional treatment is required in terms of conductivity to comply with the Tunisian regulations for the discharge.

4. Conclusion

The present work proved that biochars produced from TFW could be considered as highly effective, attractive and promising materials for dye removal from solutions compared to various previously studied biochars in term of both rapid kinetic and equilibrium recovery capabilities. The relatively high SFR dye desorption yields allow us to consider this low-cost material as an attractive solid matrix for the removal of basic dyes from aqueous solutions with the possibility of multiple reuse. For further application, 15 $g{\cdot}L^{-1}$ was found to be the optimum amount of biochar to treat the real wastewater. Besides the elimination of color, adsorption on biochar decreases drastically the main characteristic parameters of the effluent. Parameters are within the specified limit values of rejection by the textile industries except for the conductivity of the effluent. Hence, the biochar produced from the pyrolysis of TFW can be

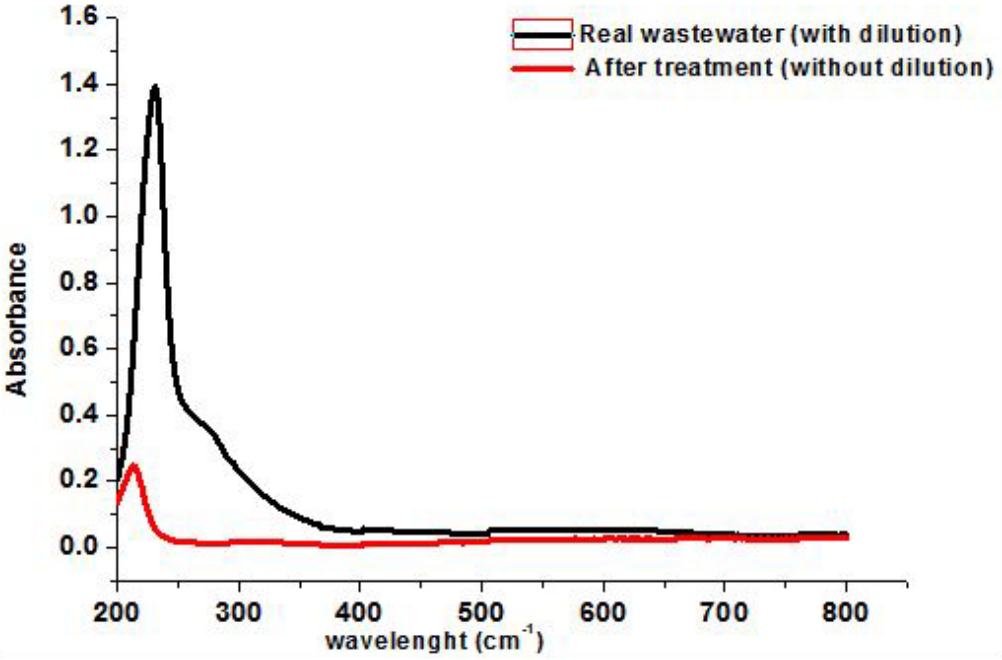

Figure 11. UV–Visible spectra of tannery wastewater before and after 4 h of treatment.

Table 7. Main physicochemical characteristics of the used real wastewater before and after treatment

Parameter	Before treatment	After treatment	Tunisian standard
Temperature (°C)	18	19	–
pH (–)	7.3	7.87	5.5–8.5
Electrical conductivity (mS/cm)	7.14	6.2	5
Color	Red	Colorless	Clear
COD ($mg{\cdot}L^{-1}$)	43	2	250
BOD_5 ($mg{\cdot}L^{-1}$)	11	10	50
Total solid ($mg{\cdot}L^{-1}$)	10	5	80
Cl (mg/L)	1.74×10^3	10	1200
Total chromium (mg/L)	0.293	–	<0.2

used efficiently for the treatment of textile effluents containing mainly SFR dye. It would be interesting to continue testing on real wastewater using not only batch processes but also column processes, on the pilot scale.

Conflicts of interest

Authors have no conflict of interest to declare.

References

[1] K. Chojnacka, D. Skrzypczak, K. Mikula, A. Witek-krowiak, G. Izydorczyk, K. Kuligowski, B. Paulina, M. Kułażyński, *J. Clean. Prod.*, 2021, **313**, article no. 127902.
[2] J. Hu, Z. Xiao, R. Zhou, W. Deng, M. Wang, S. Ma, *J. Clean. Prod.*, 2011, **19**, 221-228.
[3] Y. Tang, J. Zhao, Y. Zhang, J. Zhou, B. Shi, *Chemosphere*, 2021, **263**, article no. 127987.
[4] M. A. Moktadir, H. B. Ahmadi, R. Sultana, F.-T. Zohra, J. J. H. Liou, J. Rezaei, *J. Clean. Prod.*, 2020, **251**, article no. 119737.
[5] K. Fela, K. Wieczorek-Ciurowa, M. Konopka, Z. Woźny, *J. Cheml. Technol.*, 2011, **13**, 53-55.

[6] Q. Hu, L. Bin, P. Li, F. Fu, *J. Mol. Liq.*, 2021, **331**, article no. 115719.
[7] Y. Tang, T. Lin, S. Ai, Y. Li, R. Zhou, Y. Peng, *Int. J. Biol. Macromol.*, 2020, **159**, 98-107.
[8] Y. Xia, Y. Jin, J. Qi, H. Chen, G. Chen, S. Tang, *Environ. Technol. Innov.*, 2021, **23**, article no. 101659.
[9] S. Payel, M. A. Hashem, M. A. Hasan, *Environ. Technol. Innov.*, 2011, **24**, article no. 102010.
[10] S. Jellali, B. Khiari, M. Usman, H. Hamdi, Y. Charabi, M. Jeguirim, *Renew. Sust. Energ. Rev.*, 2021, **144**, article no. 111068.
[11] M. Jeguirim, M. Goddard, A. Tamosiunas, E. Berrich-Betouche, A. Azzaz, M. Praspaliauska, S. Jellali, *Renew. Energ.*, 2020, **149**, 716-724.
[12] C.-C. Kung, B. A. McCarl, C.-C. Chen, L.-J. Chen, *Energy Procedia*, 2014, **61**, 679-682.
[13] J. Lehmann, M. C. Rillig, J. Thies, C. A. Masiello, W. C. Hockaday, D. Crowley, *Soil Biol. Biochem.*, 2011, **43**, 1812-1836.
[14] L. Wang, C. Xue, X. Nie, Y. Liu, F. Chen, *J. Plant. Nutr. Soil Sci.*, 2018, **181**, 635-643.
[15] J. Zheng, X. Zhu, Q. Guo, Q. Zhu, *Waste Manage.*, 2006, **26**, 1430-1435.
[16] M. Ahmad, A. U. Rajapaksha, J. E. Lim, M. Zhang, N. Bolan, D. Mohan, M. Vithanage, S. S. Lee, Y. S. Ok, *Chemosphere*, 2014, **99**, 19-33.
[17] S. Fan, J. Tang, Y. Wang, H. Li, H. Zhang, J. Tang, *J. Mol. Liq.*, 2016, **220**, 432-441.
[18] X. Yang, W. Zhu, Y. Song, H. Zhuang, H. Tang, *J. Mol. Liq.*, 2021, **340**, article no. 116617.
[19] J. Wu, J. Yang, P. Feng, G. Huang, C. Xu, B. Lin, *Chemosphere*, 2020, **246**, article no. 125734.
[20] K. Mahmoudi, N. Hamdi, M. B. Ali, S. Jellali, E. Srasra, *C. R. Chim.*, 2020, **23**, 689-704.
[21] M. Wakkel, B. Khiari, F. Zagrouba, *C. R. Chim.*, 2020, **23**, 671-687.
[22] X. Huang, F. Yu, Q. Peng, Y. Huang, *RSC Adv.*, 2018, **8**, 29781-29788.
[23] S. Payel, M. A. Hashem, M. A. Hasan, *Environ. Technol. Innov.*, 2021, **24**, article no. 102010.
[24] X. Tan, Y. Liu, G. Zeng, X. Wang, X. Hu, Y. Gu, Z. Yang, *Chemosphere*, 2015, **125**, 70-85.
[25] A. Mlayah, S. Jellali, A. A. Azzaz, M. Jeguirim, H. Sellalmi, N. Hamdi, *C. R. Chim.*, 2021, **24**, 7-22.
[26] R. Jain, V. Gupta, S. Sikarwar, *J. Hazard. Mater.*, 2021, **182**, 749-756.
[27] K. Haddad, M. Jeguirim, S. Jellali, C. Guizani, L. Delmott, B. Simonna, L. Limousy, *Energy*, 2021, **134**, 10-23.
[28] S. Amdouni, A. Ben Hassen Trabelsi, A. Mabrouk Elasmi, *Fuel*, 2021, **294**, article no. 120423.
[29] T. Chen, Y. Zhang, H. Wang, W. Lu, Z. Zhou, Y. Zhang, *Bioresour. Technol.*, 2014, **164**, 47-54.
[30] H. Younis, A. Nazir, F. Bareen, *Pol. J. Environ. Stud.*, 2020, **30**, 453-462.
[31] R. R. Gil, R. P. Girón, M. S. Lozano, B. Ruiz, E. Fuente, *J. Anal. Appl. Pyrolysis*, 2012, **98**, 129-136.
[32] M. Velusamy, B. Chakali, S. Ganesan, F. Tinwala, S. Shanmugham Venkatachalam, *Environ. Sci. Pollut. Res.*, 2020, **27**, 29778-29790.
[33] M. I. Inyang, B. Gao, Y. Yao, Y. Xue, *Crit. Rev. Environ. Sci. Technol.*, 2016, **46**, 406-433.
[34] F. Li, X. Cao, L. Zhao, J. Wang, Z. Ding, *Environ. Sci. Technol.*, 2014, **48**, 11211-11217.
[35] Y. Palani, R. R. Jonnalagadda, N. F. Nishter, *Environ. Prog. Sustain Energy*, 2017, **36**, article no. 12637.
[36] W. Suliman, J. B. Harsh, N. I. Abu-Lail, A.-M. Fortuna, I. Dallmeyer, M. Garcia-Perez, *Biomass Bioenergy*, 2016, **84**, 37-48.
[37] F. Younas, N. K. Niazi, I. Bibi, M. Afzal, K. Hussain, *J. Hazard. Mater.*, 2022, **422**, article no. 126926.
[38] K. Haddad, S. Jellali, M. Jeguirim, A. Ben Hassen Trabelsi, L. Limousy, *J. Environ. Manage.*, 2018, **216**, 305-314.
[39] M. Chen, J. Wang, M. Zhang, M. Chen, X. Zhu, *J. Anal. Appl. Pyrolysis*, 2008, **82**, 145-150.
[40] W. Buss, M. C. Graham, J. G. Shepherd, O. Mašek, *Sci. Total Environ.*, 2016, **547**, 314-322.
[41] Y. Palani, R. R. Jonnalagadda, N. F. Nishter, *Environ. Prog. Sustain Energy*, 2018, **66**, 197-2012.
[42] K. Haddad, S. Jellali, S. Jaouadi, M. Benltifa, A. Mlayah, A. H. Hamzaoui, *C. R. Chim.*, 2021, **18**, 75-87.
[43] G. Yang, L. Wu, Q. Xian, F. Shen, J. Wu, Y. Zhang, *PLoS One*, 2016, **11**, article no. 154562.
[44] S. Jellali, A. A. Azzaz, M. Jeguirim, H. Hamdi, A. Mlayah, *Water*, 2021, **13**, article no. 164.
[45] J. A. Arcibar-Orozco, B. S. Barajas-Elias, F. Caballero-Briones, L. Nielsen, J. R. Rangel-Mendez, *Water Air Soil Pollut.*, 2019, **230**, article no. 142.
[46] Y. Li, A. Meas, S. Shan, R. Yang, X. Gai, H. Wang, N. Tsend, *Data Brief*, 2018, **19**, 49-54.
[47] L. Dai, W. Zhu, L. He, F. Tan, N. Zhu, Q. Zhou, M. He, *Bioresour. Technol.*, 2018, **267**, 510-516.
[48] L. Leng, X. Yuan, G. Zeng, J. Shao, X. Chen, Z. Wu, *Fuel*, 2015, **155**, 77-85.
[49] C. Namasivayam, D. Kavitha, *Dyes Pigm.*, 2002, **54**, 47-58.
[50] R. Lafi, I. Montasser, A. Hafiane, *Adsorp. Sci. Technol.*, 2019, **37**, 160-181.
[51] N. Kannan, M. Meenakshisundaram, *Water Air Soil Pollut.*, 2002, **138**, 289-305.
[52] E. Deliyanni, A. Arampatzidou, N. Tzoupanos, K. Matis, *Adsorp. Sci. Technol.*, 2012, **30**, 627-646.
[53] K. Litefti, M. S. Freire, M. Stitou, J. González-Álvarez, *Sci. Rep.*, 2019, **9**, article no. 16530.
[54] R. Muralikrishnan, C. Jodhi, *ChemistrySelect*, 2020, **5**, 7734-7742.
[55] A. A. Azzaz, S. Jellali, M. Jeguirim, L. Bousselmi, Z. Bengharez, H. Akrout, *C. R. Chim.*, 2021, **24**, 71-84.
[56] G. Ravindiran, R. M. Jeyaraju, J. Josephraj, A. Alagumalai, *ChemistrySelect*, 2019, **4**, 7437-7445.
[57] Faheem, J. Du, J. Bao, M. A. Hassan, S. Irshad, M. A. Talib, *Arab. J. Sci. Eng.*, 2021, **44**, 10127-10139.

Comptes Rendus
Chimie
2022, Vol. 25, Special Issue S2, p. 61-79
https://doi.org/10.5802/crchim.181

Sustainable Biomass Resources for Environmental, Agronomic, Biomaterials and Energy Applications 3 / *Ressources de biomasse durables pour des applications environnementales, agronomiques, de biomatériaux et énergétiques 3*

Cationic dye removal using *Pergularia tomentosa* L. fruit: kinetics and isotherm characteristics using classical and advanced models

Hafedh Belmabrouk [*, a, b], **Marwa Selmi** [c, b], **Thamraa Alshahrani** [d], **Zeineb Raddaoui** [e], **Abdullah Bajahzar** [f], **Mahjoub Jabli** [g] **and Thamer Alharbi** [a]

[a] Department of Physics, College of Science Al-Zulfi, Majmaah University, Al-Majmaah 11952, Saudi Arabia

[b] Laboratory of Electronics and Microelectronics, Faculty of Science of Monastir, University of Monastir, Monastir 5019, Tunisia

[c] Department of Radiological Sciences and Medical Imaging, College of Applied Medical Sciences, Majmaah University, Al Majmaah 11952, Saudi Arabia

[d] Department of Physics, College of Science, Princess Nourah bint Abdulrahman University, Riyadh 11671, Saudi Arabia

[e] Institut de Recherche sur les Céramiques (IRCER), UMR 7315 CNRS, Université de Limoges, 12 Rue Atlantis, F-87068 Limoges, France

[f] Department of Computer Science and Information, College of Science Al-Zulfi, Majmaah University, Al-Majmaah 11952, Saudi Arabia

[g] Department of Chemistry, College of Science Al-Zulfi, Majmaah University, Al-Majmaah 11952, Saudi Arabia

E-mails: Ha.Belmabrouk@mu.edu.sa, Hafedh.Belmabrouk@fsm.rnu.tn (H. Belmabrouk), m.selmi@mu.edu.sa (M. Selmi), thmalshahrani@pnu.edu.sa (T. Alshahrani), zeineb.raddaoui@unilim.fr (Z. Raddaoui), a.bajahzar@mu.edu.sa (A. Bajahzar), m.jabli@mu.edu.sa (M. Jabli), t.alharbi@mu.edu.sa (T. Alharbi)

Abstract. The agricultural crops prove to be low-cost and abundant biosorbents that are able to adsorb dyes from contaminant water. In the present study, different techniques were used to characterize the powdered *Pergularia tomentosa* fruit. After that, the biomaterial was exploited to investigate the adsorption of methylene blue in batch mode. The effects of initial pH, contact time, dye concentration, biosorbent dose, and temperature on the biosorption capacity have been performed. The fit of the adsorption isotherms was performed by means of several classical models and advanced models derived from statistical physics. The two-energy monolayer model proves to be the more suitable. It appears that two functional groups of the biosorbent are involved in the dye biosorption. The adsorption energy ranges from 14 to 18 kJ·mol^{-1} which indicates a physiosorption mechanism.

* Corresponding author.

The maximum adsorption capacity is 152 mg·g^{-1}. *Pergularia tomentosa* fruit proves to be attractive for the efficient removal of cationic dyes from polluted water.

Keywords. Biosorption, *Pergularia tomentosa* fruit, Dye removal, Statistical physics models, Adsorption energy, Methylene blue.

Published online: 4 May 2022

1. Introduction

Recently, the control of water quality and the protection of the environment prove to be important fundamental and industrial issues because of the development of industrial activities. Additionally, industrialization and urbanization lead to the accumulation of many pollutants which should be treated efficiently. Many biological, chemical, and physical techniques are available [1]. By taking advantage of adequate adsorbents, the adsorption mechanism can be used to resolve this issue and eliminate the contaminants. Pesticides, herbicides, drugs, heavy metals, and dyes are among the essential contaminants which are discharged from numerous industries such as pharmaceutics, cosmetics, plastics industry, textiles, food industry, etc. [2–13].

The contaminants' removal from polluted water may be achieved using several low or no-cost adsorbents which are attractive because of their abundance and availability. Many agricultural crops were studied as biosorbents in the literature They were extracted from leaves, steam, and fruits, of a large number of plants [14–17]. These crops contain, with different amounts, cellulose and other non cellulose compounds such as hemicellulose, lignin, and pectin. Therefore, they are expected to be rich in hydroxyl groups. As a result, the interaction of these biomaterials with several organic contaminants is enhanced which infers them a significant advantage and increases their attractiveness. The previous studies on cationic dyes removal by lignocellulosic materials have revealed the potential of many biomaterials. The present study will continue in this line and investigate a new biomaterial.

Pergularia tomentosa L. ranks among the family of Asclepiadacea. It is widespread in the desert regions of several African and Asian countries such as Tunisia and Saudi Arabia. A limited number of papers investigated the medicinal applications of this plant [18]. They are exclusively restricted to this kind of application. Sakji *et al.* and Sebeia *et al.* investigated the physicochemical characteristics and the adsorption capacity of the seed fibers of *Pergularia tomentosa* L. [19,20]. The adsorption energy was not accurately evaluated since empirical models were used. To overcome these shortcomings, we can take advantage of exploiting advanced models based on statistical physics. It should be mentioned that the research of many others [21–24] used only classical adsorption models and were unable to compute accurately the adsorption. In the present work, adsorption models derived from statistical physics will be employed. The superiority of advanced models is revealed since these models are naturally able to assign physical meanings to the parameters inherent to the different models. Furthermore, they lead to a more accurate value of the adsorption energy. Some intrinsic parameters, in particular, the adsorption energy, will be assessed. The main novelty of this work is to investigate a new low-cost and abundant biomaterial and to compare its capacity for cationic dye removal with other available biosorbents. The second novelty is related to the use of classical and advanced models to fit the adsorption isotherms and to evaluate some parameters related to the adsorption mechanism involved in the cationic dye removal.

Methylene blue is a cationic dye. It is a toxic and mutagenic product. In fact, wastewater containing methylene blue can cause tachycardia, cyanosis, eye damage, skin irritation, dyspnea, and paroxysms [25]. It can cause also vomiting, diarrhea, and nausea. It stops the penetration of sunlight into water, reduces the photosynthetic function in plants, and harms both marine vegetation and aquatic ecosystems. Many studies demonstrated the exploration of efficient adsorbents of methylene blue [26,27].

The first objective of this work consists of characterizing the new biosorbent and evaluating its ability to adsorb methylene blue (MB). Three characterization methods, explicitly FT-IR, SEM, and TGA were used. In the matter of adsorption kinetics, many models have been checked. Concerning the adsorption isotherms, several classical models are investigated. Then, three advanced models derived

from statistical physics are used to fit the adsorption isotherms.

2. Experimental

2.1. *Reagents*

All the chemical reagents used in this work were of analytical grade. No additional purification is operated. The cationic dye methylene blue was provided from Sigma-Aldrich. The molecular weight of this dye 319.85 g·mol^{-1}. To prepare methylene blue solutions, distilled water was employed.

2.2. *Preparation of Pergularia tomentosa fruit*

The collection of the biomaterial, i.e. *Pergularia tomentosa* fruit was operated in the littoral region of Monastir city (Tunisia) and the desert region of Zulfi city (Saudi Arabia) (Figure 1). Primary, the fruits were meticulously washed by tap water to remove the attached impurities on its surface, like sand particles and debris. A complementary wash of the fruits was then achieved using distilled water. After that, the fruits were firstly sun dried, and secondly dried in an oven for 24 h at 70 °C. Afterwards, they were grinded to fine powders. To remove the impurities that result from grinding, the obtained powders were washed, once more, using distilled water. Lastly, the sieved grains were dried in oven for 24 h at 70 °C, stored in air tied bottles and used for further experimental essays.

2.3. *Characterization techniques*

To characterize the biomaterial, three techniques have been used, namely, Fourier Transform Infrared spectroscopy (FT-IR), Scanning Electron Microscopy (SEM), and Thermogravimetric Analysis (TGA). The identification of the chemical group characteristics of the biomaterial was performed by means of a FT-IR spectrum. A Perkin Elmer model was used for this pupose. The spectral span extends over the interval from 4000 cm^{-1} to 400 cm^{-1}. The spectral resolution of the instrument is 2 cm^{-1}. The measurements are performed using the attenuated total reflection mode. The surface morphology of the biomaterial is investigated using a SEM Hitachi S-2360N apparatus. The powdered fruit was coated with Au by a vacuum sputter-coater with 30 kV accelerating voltage. Several magnifications have been tested. TGA measurements were performed in airflow at a heating rate of 10 °C/min in a Pt crucible with NETZSCH STA 449F3 apparatus. To obtain the point of zero charge pH_{pzc} of the biomaterial, the salt addition technique was used. Indeed, 0.1 g of powdered fruit was immersed in 10^{-1} M KNO_3 solutions (50 mL) at different pH values ranging from 2 to 11. To adjust the initial pH, HCl or NaOH was added. The solutions were shaken under magnetic stirring during 48 h. The final pH value (pH_f) was plotted versus the initial pH value (pH_i). The point of zero charge pH_{pzc} is defined by ($pH_f = pH_i$). More details are available in [28].

2.4. *Batch biosorption experiments*

In order to investigate the biosorption isotherms, batch adsorption experiments were performed in a set of 500 mL beakers containing 25 mL of methylene blue with different initial dye concentrations and 0.025 g of powdered fruits. To reach the equilibrium, the above mixture was stirred at a speed of 100 rpm and a temperature of 19 °C. A UV–Vis spectrophotometer calibrated at a maximum wavelength of 665 nm was used to measure the concentrations of MB in the solution before and after biosorption. The following equation is used to compute the biosorption capacity at equilibrium q_e (mg·g^{-1}):

$$q_e = \frac{C_0 - C_e}{m} V, \tag{1}$$

where C_e (mg·L^{-1}) is the equilibrium concentration of MB, C_0 is its initial concentration, V is the volume of the solution (L), and m is the mass of the absorbent used (g). To obtain the adsorption isotherms, the temperature was varied from 19 °C to 55 °C. The batch kinetic measurements for the MB adsorption onto *Pergularia tomentosa* fruit are monitored in an identical way as that followed to perform the experiments at equilibrium. The measurements are repeated for different periods of time ranging from 0 to 120 min. The effect of salt concentration (NaCl) on the biosorption of methylene blue onto *Pergularia tomentosa* fruit was studied in the range of 0–10 g·L^{-1}. MB adsorption assays were carried out in triplicate. This allows estimating the errors in the measurements. For this reason, some results will be

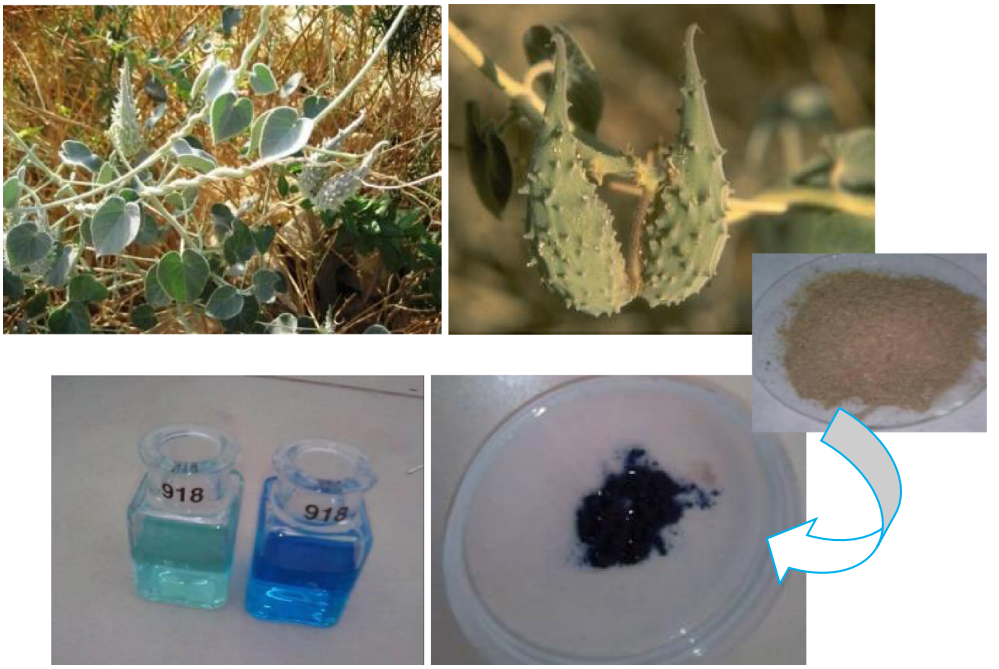

Figure 1. Picture indicating the plant, its fruits, and the fine powders.

plotted using bar errors. This concerns especially the parameters extracted from the isotherms.

In this paper, we will start by the characterization of the biomaterial as above mentioned. After that, the effect of contact time, pH, initial concentration, temperature will be investigated. The kinetic data will be fitted using several models. The adsorption isotherms will be fitted using classical models as well as models derived from theoretical considerations based on statistical physics. An important issue will be discussed is related to the comparison between classical and advanced models.

3. Theoretical models for the equilibrium isotherms

Two groups of models representing the adsorption isotherms are exploited in the present study. The first group integrates classical models which are fully empirical or semi-empirical. These models are very famous and have been extensively employed in the literature [8,21]. However, the physical meaning of the parameters involved are not always obvious. The second group contains more advanced models which are obtained from statistical physics theory. The assumptions considered to deduce the different expressions and the reasoning schemes are more explicit. Furthermore, a clear physical meaning is assigned to each parameter.

3.1. *Classical models*

In this first category, many models are elaborated to fit different types of experimental results and they involve many assumptions. In general, they contain two or three parameters to adjust the equilibrium isotherms [29–32]. The following isotherm models are used in present study: Langmuir, Freundlich, Hill, and Dubinin–Radushkevich models. It should be mentioned that there are many other models. However, they have some resemblance with one of the above models. For this reason, only the performance of the aforementioned five classical models will be evaluated.

3.1.1. *Langmuir isotherm model*

The Langmuir model is the most common one. It is deduced using many assumptions. Indeed, the adsorption process is assumed to be monolayer. A homogeneous surface and a constant energy are also

assumed. Furthermore, the interaction between adsorbate molecules on adjacent sites are neglected. The adsorbed pollutant amount at equilibrium q_e ($mg{\cdot}g^{-1}$) versus its concentration in water at equilibrium C_e ($mg{\cdot}L^{-1}$) is given by:

$$q_e = \frac{q_{\max} K_L C_e}{1 + K_L C_e}, \tag{2}$$

where $q_{\max}$ is the maximum adsorption capacity and K_L ($L{\cdot}mg^{-1}$) is the Langmuir constant.

3.1.2. *Freundlich isotherm model*

This model has been elaborated from empirical considerations in the aim to account for the multilayer adsorption. The adsorbed pollutant amount at equilibrium q_e is formulated by:

$$q_e = K_f (C_e^*)^{1/n} \quad \text{where } C_e^* = C_e / C_{\text{ref}}. \tag{3}$$

Two empirical parameters, viz. the constant K_f and the exponent $1/n$ are involved in this model. A reference constant $C_{\text{ref}} = 1$ mg/L is introduced to satisfy the requirements of dimension analysis and consequently express the unit of the parameter K_f in more eloquent manner. Obviously, the reduced concentration $C_e^* = C_e/C_{\text{ref}}$ is dimensionless. The unit of the constant K_f is the inverse of that of q_e, i.e. $mg^{-1}{\cdot}g$. The exponent n has no unit.

Depending on the surface heterogeneity, the value of n may be greater than one. Freundlich model assumes that the adsorption energy decays exponentially moving away from the surface. When the exponent n increases, the adsorption isotherm reaches rapidly the saturation and the adsorbed pollutant amount becomes smaller.

3.1.3. *Hill isotherm model*

In this model, the adsorption process is considered as a cooperative mechanism. The adsorbed pollutant amount at equilibrium q_e is expressed by:

$$q_e = \frac{q_{\max,H} (C_e^*)^{n_H}}{K_D + (C_e^*)^{n_H}}. \tag{4}$$

Three adjustable parameters are contained in this model. The fits one is $q_{\max,H}$ ($mg{\cdot}g^{-1}$). It represents the maximum adsorption capacity. The second parameter is n_H. It represents the Hill cooperativity coefficient of the binding reaction. The last parameter is the Hill constant K_D. The use of dimensionless equilibrium concentration C_e^* allows to obtain easily and accurately the units of the paramters K_D and $q_{\max,H}$.

3.1.4. *Dubinin–Radushkevich isotherm model*

The adsorbed pollutant amount at equilibrium q_e is given by [33]:

$$q_e = q_s \exp(-k_{\text{ad}} \varepsilon^2) \quad \text{and} \quad \varepsilon = RT \ln(1 + C_s/C_e). \tag{5}$$

This model involves two adjustable parameters, viz. the saturation capacity q_s ($mg{\cdot}g^{-1}$) and the constant k_{ad} ($mol^2{\cdot}kJ^{-2}$). The the solubility of the adsorbate C_s is also involved in the model. The mean free energy of adsorption E_{ad} ($kj{\cdot}mol^{-1}$) is related to the constant k_{ad} according to [34]: $E_{\text{ad}} = 1/\sqrt{2k_{\text{ad}}}$.

The temperature is explicitly involved in this model. Dubinin–Radushkevich model produces acceptable fitting in the intermediary range of concentrations. Nevertheless, at small and large concentrations, this does not match adequately the isotherm curve [35]. For that reason, unrealistic maximal adsorption capacities have been reported by several studies [8,21].

It is important to mention that erroneous expressions have been used by many authors to calculate the energy. Some well-known relations contain a problem of unit. They lead to a non-reliable estimation of the adsorption energy and other thermodynamic quantities. To avoid this problem, the units of all the quantities and mathematical expressions should be cautiously scrutinized.

3.2. *Advanced models derived from statistical physics*

As above mentioned, a large number of classical models have been elaborated to fit a wide variety of experimental data. The usefulness and potential of these models have been recognized. Nevertheless, they present some shortcomings. Actually, the elaboration of the classical model is, in general, empirical and is not bot based on theoretical considerations. Moreover, the physical significance of the parameters inherent to each model is not obvious. To overcome these shortcomings, an alternative method has emerged throughout recent decades. The number of models developed in this framework has continued to grow [36–41]. In parallel, the fields of application of these new models become widener and widener progressively. Among all the models recently developed, we will confront our data with only three models.

3.2.1. *Monolayer model characterized by one energy*

The monolayer model characterized by one energy presumes that only one layer participates to the adsorption mechanism over the adsorbent surface. Furthermore, all the receptor sites are linked to the adsorbate with the same energy. Nevertheless, each receptor site S is able can be linked to a fluctuating number n. The adsorption reaction reads: $nA + S \rightleftharpoons A_nS$ where A_nS denotes the produced complex. In fact, the steric or stoichiometric number n should be regarded as an average number. It is not necessarily an integer number and it may be greater or lesser than one. If $n > 1$, n corresponds to the average number of molecules attached to a particular receptor site. On the contrary, when $n < 1$, its inverse $n' = 1/n$ denotes the expected number of receptor sites occupied by one molecule [42,43].

When only the translation degrees of freedom are taken into account, the average number of occupied sites N_a or equivalently the adsorbed pollutant amount at equilibrium q_e as a function of the concentration C_e is given in Table 1 [44]. It is clear that three adjustable parameters are involved in this model. In particular, the half-saturation concentration is one of the parameters constituting the model. This quantity depends on the temperature T. More precisely, it is related to the temperature T and the adsorption energy E_a according to the relation [37]:

$$C_{1/2} = C_s e^{-E_a/RT}, \tag{6}$$

where C_s is the solubility of the adsorbate.

The physical significance attributed to each parameter is obvious. The mathematical relation of the one-energy monolayer model is identical to the classical Hill model. To grasp further the physical significance of the different parameters which are intrinsic to the model, a parametric study may be performed. This study may also help to evaluate the effect of the error on each parameter.

3.2.2. *Monolayer model characterized by two energies*

This model also accepts that only one layer is involved in the adsorption mechanism. However, this layer encloses two varieties of receptor sites. Each variety has its own energy. Therefore, two different energies E_{a1} and E_{a2} are engaged in the model. This model is in some ways a generalization of the one-energy monolayer model The expression of this model is given in Table 1 [45]. The energies E_{a1} and E_{a2} can be computed from the half-saturation concentrations C_1 and C_2 as previously specified. It should be mentioned that the subscripts 1 and 2 may be permuted without changing the model. Therefore, no constraint is imposed on the energies E_{a1} and E_{a2}.

3.2.3. *Double-layer model characterized by two energies*

The double-layer model characterized by two energies admits that two consecutive layers are involved in the adsorption process. Each layer is characterized by its own energy. We denote by E_{a1} and the E_{a2} the energy of the first and the second adsorbed layer respectively. It is straightforward to derive the model presented in Table 1 [38]. The energy E_{a1} related to the first layer should be greater than the energy E_{a2} that characterizes the second layer. Therefore, the half-saturation concentration C_1 should be smaller than the half-saturation concentration C_2. On the contrary of the above model, the subscripts 1 and 2 cannot be mutually permuted.

3.3. *Adsorption kinetic models*

To fit the kinetic data, a large number of kinetic models have been developed during the last decades. The majority of the models are empirical. They are described by an ordinary differential equation such as in the linear driving force model. They may also be formulated using a mathematical relationship such as the pseudo first order (PFO) model, pseudo second order (PSO), Elovich model, intra-particle diffusion model and Bangham model [46].

3.3.1. *PFO adsorption kinetic model*

At any the instant t, the pollutant adsorbed quantity is expressed by: $q_t = q_e(1 - e^{-k_1 t})$. This model involves the rate constant k_1 and the equilibrium adsorbed quantity q_e. The meaning of these two parameters is obvious. In particular, the rate constant is related to the slope of the curve at small contact times whereas the quantity q_e is reached at saturation.

3.3.2. *PSO adsorption kinetic model*

At any instant t, the pollutant adsorbed quantity is expressed by: $q_t = (k_2 q_e^2 t)/(1 + k_e q_e t)$. This model involves two adjustable parameters, namely the rate constant k_2 and the equilibrium adsorbed quantity q_e.

Table 1. Advanced models for the adsorption isotherms

Model	Equation	Parameters
Monolayer model with one energy	$q_e = \dfrac{nN_m}{1+(C_{1/2}/C_e)^n}$	N_m is the density of receptor sites of adsorbent. n is the number of adsorbed molecules per site. $C_{1/2}$ is the concentration at half saturation.
Monolayer model with two energies	$q_e = \dfrac{n_1 N_{m1}}{1+(C_1/C_e)^{n_1}} + \dfrac{n_2 N_{m2}}{1+(C_2/C_e)^{n_2}}$	N_{m1} and N_{m2} are the densities of the two kinds receptor sites. n_1 and n_2 are the numbers of adsorbed molecules per site. C_1 and C_2 are respectively related to the first and second kind of receptor sites.
Double-layer model with two energies	$q_e = nN_m \dfrac{\left(\frac{C_e}{C_1}\right)^n + 2\left(\frac{C_e}{C_2}\right)^{2n}}{1+\left(\frac{C_e}{C_1}\right)^n + \left(\frac{C_e}{C_2}\right)^{2n}}$	C_1 and C_2 are related to the first and second layer respectively.

3.3.3. *Elovich adsorption kinetic model*

At any instant t, the pollutant adsorbed quantity is expressed by: $q_t = (1/\beta)\ln(1+\alpha\beta t)$. It is clear that the constant α is called the adsorption rate ($\mathrm{mg{\cdot}g^{-1}{\cdot}min^{-1}}$). The unit of the constant β is $\mathrm{g{\cdot}mg^{-1}}$.

3.3.4. *Intra-particle diffusion kinetic model*

At any instant t, the pollutant adsorbed quantity is expressed by: $q_t = k_d\sqrt{t}/t_0^{3/2} + C$. This model also involves two adjustable constants, namely the intra particle diffusion rate constant k_d and the constant C which is associated to the boundary layer effect.

3.3.5. *Bangham adsorption kinetic model*

At any instant t, the pollutant adsorbed quantity is expressed by: $q_t = q_e[1-\exp(-k_b t^n/t_0^{n-1})]$. The Bangham model involves three adjustable parameters, namely the equilibrium adsorbed quantity q_e, the rate constant k_b but also the exponent n. The Bangham model is more universal than the PFO model since it contains the adjustable exponent n. It is expected that this model is susceptible to fit more accurately the experimental data.

The reference time is $t_0 = 1$ min. It is a judicious artefact that permits that all the rate constants k_1, k_d and k_b have the same unit. Moreover, the conversion from one system of units to another becomes straightforward using this reference time.

All the above models were expressed using the nonlinear formula. For each model, one or more linear form are available. However, the nonlinear form leads to more accurate results and proves to be more powerful.

3.4. *Error analysis*

To evaluate the parameters involved of a model, the root means square error (RMSE) function is minimized. This function is defined according to:

$$\mathrm{RMSE} = \left[\frac{1}{N}\sum_{i=1}^{N}(q_{e,\mathrm{fit},i} - q_{e,\mathrm{meas},i})^2\right]^{\frac{1}{2}}, \qquad (7)$$

where N is the total number of data for a particular curve, $q_{e,\mathrm{meas},i}$ is the ith measured value, and $q_{e,\mathrm{fit},i}$ is the ith theoretical value deduced using a particular model. It is clear that this theoretical value depends on the adjustable parameters to be identified. It is worth mentioning that the utilization of absolute errors is more convenient than relative errors since the concentration for the adsorption isotherms and the time for the kinetics data vary in a large interval.

Iterative algorithms are used to identify the parameters that minimize the above function. Matlab programs and built-in Microsoft Excel or Origin functions are used. The standard deviation related to each adjustable parameter is also calculated. This

quantity allows judging on the quality of the identification process and the model veracity to adjust the experimental data. Indeed, the standard deviation on all the identified parameters should vary in a small range to accept the model.

The first criterion used to coarsely qualify the performance of the fit process is the correlation coefficient R between the experimental and theoretical curves. This quantity is defined by:

$$R = \frac{\sum_{i=1}^{N}(q_{e,\mathrm{fit},i} - \overline{q_{\mathrm{fit}}})(q_{e,\mathrm{meas},i} - \overline{q_{\mathrm{meas}}})}{\left[\sum_{i=1}^{N}(q_{e,\mathrm{fit},i} - \overline{q_{\mathrm{fit}}})^2 \sum_{i=1}^{N}(q_{e,\mathrm{meas},i} - \overline{q_{\mathrm{meas}}})^2\right]^{\frac{1}{2}}}, \quad (8)$$

where $\overline{q_{\mathrm{fit}}}$ and $\overline{q_{\mathrm{meas}}}$ are the mean value of the theoretical results that obtained using the model and the mean value of the experimental data respectively. When the experimental and theoretical curves are very similar, the correlation coefficient R is close to one. However, this coefficient is not sufficient on its own. One or two further criteria prove to be necessary to accurately evaluate the conformity of the fitting process and the model. As above mentioned, the first additional criterion is the root mean square error. The model and the identification of the parameters are all the more adequate as this quantity is smaller. The second auxiliary criterion is standard deviation on the identified parameters.

4. Results and discussion

4.1. *Characterization of the biomaterial*

FT-IR spectroscopy was used to determine the main functional groups of the powdered biomaterial. Figure 2 exhibits the FT-IR spectrum. The most important absorption peaks are indexed. A broad absorption peak is recorded at 3292 cm^{-1}. It is attributed to the hydroxyl groups. Two absorption peaks are registered at 2918 cm^{-1} and 2848 cm^{-1}. They are respectively the sign of the existence of C–H and CH_2 groups [47]. The absorption peak observed at 1726 cm^{-1} is accredited to C=O group in hemicellulose composition [48]. The absorption peak shown at 1596 cm^{-1} is assigned to C=C aromatic groups present in the lignin composition [49]. The absorption peak observed at 1418 cm^{-1} is related to the angular deformation of CH groups in cellulose [50]. The absorption peak seen at 1235 cm^{-1} could be defined as the angular deformation of CH groups in hemicellulose [49]. The peak at 1012 cm^{-1} is related to C–O–C

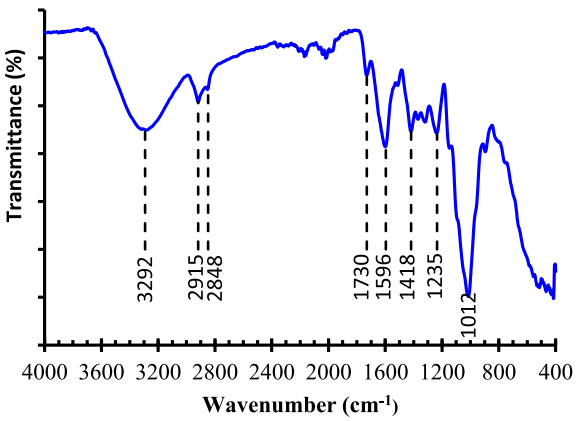

Figure 2. FT-IR spectrum of the biosorbent and identification of the main adsorption peaks.

ring stretching vibration of cellulose. These absorption peaks prove that *Pergularia tomentosa* fruit is rich of oxygeneous groups on its surface [51]. These massive oxygeneous groups are the origin of the interaction between MB dye and the cellulosic *Pergularia tomentosa* fruit through hydrogen bonding interaction.

Figure 3 exhibits the SEM features of *Pergularia tomentosa* fruit observed at different higher magnifications (×50 and ×500). The images of the powdered fruits show rough and heterogeneous surface. The particles have irregular shapes and present also some cavities. The surface structures are likely to enhance the number of receptor sites offered to the biosorption of methylene blue. The decomposition pattern and thermal stability of *Pergularia tomentosa* are shown in Figure 4. After decomposition, it was observed that the maximum weight loss of the biomaterial was around 73%. The first thermal decomposition was seen at 98 °C and it was accompanied by mass loss of 10%, which could be in general assigned to the moisture evaporation found in the hydrophilic biomaterial [52,53]. The second thermal decomposition registered at 233 °C indicated the decomposition of all organic compounds of the biomaterial including cellulose and non-cellulose compositions [54]. This behavior is in agreement with FT-IR results. The thermal decomposition at 393 °C could be assigned to the depolymerisation and decomposition of glycosyl units of the cellulosic biomaterial [55].

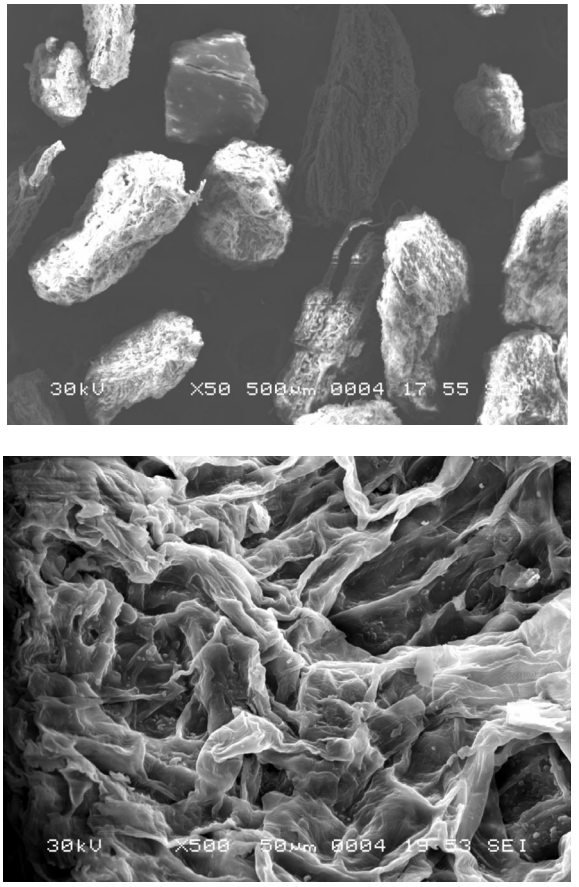

Figure 3. SEM images of *Pergularia tomentosa* fruit.

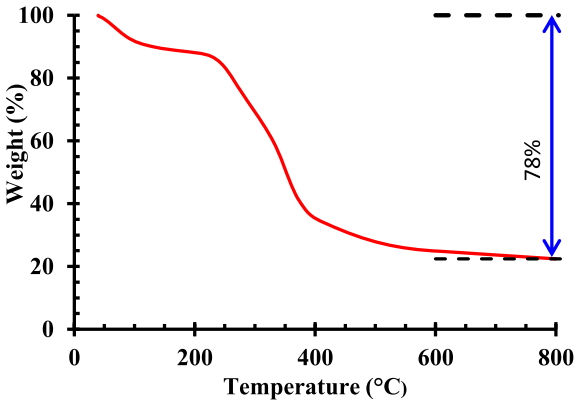

Figure 4. TGA curve of *Pergularia tomentosa* fruit.

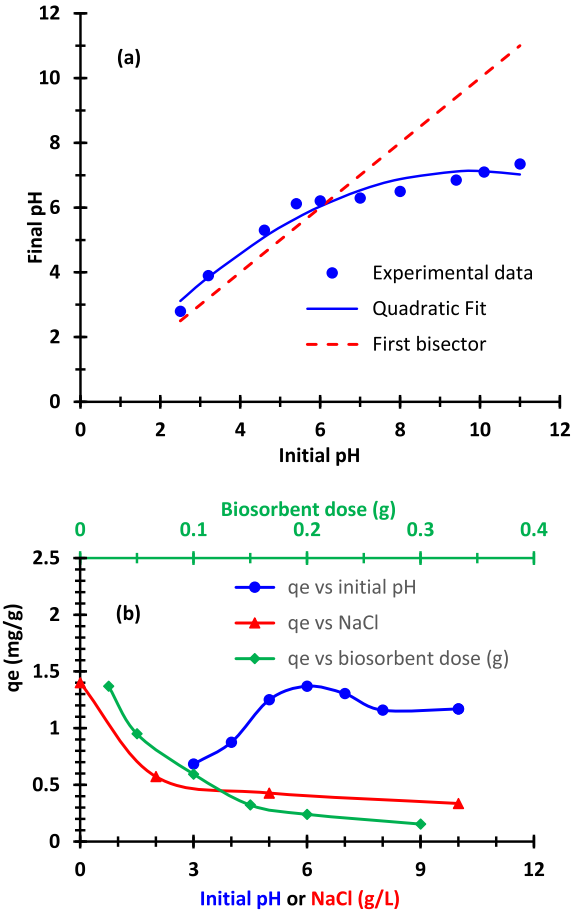

Figure 5. Parametric study on the biosorption of the cationic dye: (a) plot of final pH as a function of the initial pH, (b) (3 combined curves): effects of pH, biosorbent dosage and NaCl dosage. The initial dye concentration is $C_0 = 10$ mg·L^{-1}, the temperature $T = 19$ °C and contact time $t = 30$ min.

4.2. *Effect of the experimental parameters on the adsorption of methylene blue*

The main experimental parameters that affect the biosorption process are the final pH of the solution, the initial concentration of MB, the amount of fruit added, the temperature, and contact time. As explained above, to determine pH_{pzc} value of biosorbent, the final pH and the initial pH are measured. Figure 5a depicts the curve of the final pH (pH_f) versus the initial pH (pH_i). The experimental may be fitted a second order polynomial function.

The intersection of this curve with the first bisector correspond to the value $pH_f = pH_i = 6.1 \pm 0.2$. In other words, the point of zero charge corresponds to $pH_{pzc} = 6.1 \pm 0.2$. We deduce that the biomaterial was positively charged below the value of pH_{pzc} and it becomes negatively charged above this value. Figure 5b exhibits the evolution of the equilibrium adsorbed quantity q_e versus the initial pH value (blue curve and bottom horizontal axis). It appears clearly that when this pH increases from 3 to 6, the adsorbed quantity q_e increases significantly. Then it reaches a maximum value. When the pH continue to increase, the adsorbed quantity q_e decreases slowly. This trend corroborates the results related to the effect of initial pH (Figure 5a). The results obtained from FT-IR and TGA characterization indicated that *Pergularia* fruit has many oxygeneous groups allowing different behaviors at different pH values. Indeed, at acidic pH conditions, *Pergularia* surface was positively charged due to the protonation which opposed the positively charged methylene blue ions. At alkaline pH conditions, *Pergularia* surface was negatively charged due to deprotonation of oxygeneous groups favoring an electrostatic interaction with methylene blue. Comparable behaviors were obtained in some previous works [56,57].

The effect of *Pergularia* fruit dosage on the biosorption capacity of methylene blue is also plotted in Figure 5b (green curve and top secondary horizontal axis). It was observed that the biosorption amount decreased shapely with the increase of the biosorbent dosage. This adsorbed amount decreased from 1.37 to 0.15 mg·g^{-1} for an increase in the biosorbent dose from 1 g·L^{-1} to 12 g·L^{-1} (C_0 = 10 mg·L^{-1}, pH = 6, T = 19 °C). The high capacity observed within a dosage of 1 g·L^{-1} was attributed to the high biosorbent surface area and the large availability of sorption sites at this condition. However, the low biosorption capacities observed at high biosorbent dosage was due to the unsaturation of biosorbent sites, during the biosorption process. Quite similar results were reported in the literature [58,59]. The measurement of the adsorbed quantity q_t at the time t reveals that the time required to reach the biosorption equilibrium was observed at only a period of 30 min. Results indicated also that more than 95% of target biosorption occurred during the first 10 min (Figure 6). This indicated the efficiency of the use of *Pergularia tomentosa* fruit as biosorbent of

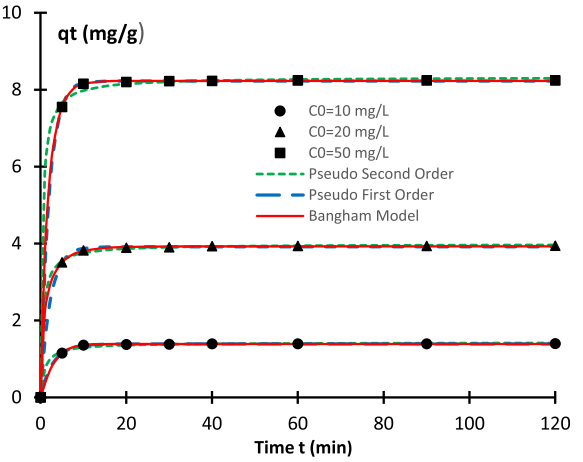

Figure 6. Time evolution of the adsorbed pollutant amount for three initial concentrations. Comparison between experimental results and the theoretical fits using three models.

cationic dyes from water with a very fast biosorption rate. Indeed, the vacant active sites accessible at the surface of *Pergularia* fruit during the initial period of time were the origin of the rapid biosorption of MB molecules. At approximately 30 min, the surface of the biosorbent became partly occupied and consequently no further increase in the biosorption capacity could be occur [60]. The results related to the kinetic data will be discussed in more detail in hereafter.

The measurement of the adsorbed quantity q_e at equilibrium shows that the process for reaching biosorption equilibrium was rapid for methylene blue concentration <500 mg·L^{-1} and it became almost stable at higher dye concentrations. The maximum capacity of the adsorbed dye was achieved at lower dye concentration due to the availability of adsorption sites in *Pergularia tomentosa* fruit surface [61,62]. At equilibrium, the maximum biosorption capacity was equal to 152 mg/g (pH = 6, t = 60 min, T = 19 °C). This capacity removal of the pollutant is compared to other published biosorbents Table 2. It suggested again the efficiency of *Pergularia tomentosa* to be used as inexpensive and effective biosorbent of cationic dyes from water. The decrease of the biosorption capacity with the increase in temperature was ascribed to the escaping of the adsorbed MB ions at higher energy or temperature. It decreased from 152 mg·g^{-1} to 132 mg·g^{-1} when the tempera-

ture moved from 19 °C to 55 °C. The results related to the isotherms will be analyzed with further detail in Section 3.4.

The effect of salt concentration on the biosorption of methylene blue onto *Pergularia tomentosa* fruit is also plotted Figure 5b (red curve and bottom horizontal axis). Data showed that the biosorption of methylene blue declined significantly with the increase in NaCl concentration from 0 to 10 g·L^{-1}. This was assigned to the decrease of interaction between methylene blue ions and the oxygeneous groups of *Pergularia* fruit surface. Indeed, Na^+ ions entered in competition with the nitrogen atom of methylene blue to interact with the hydroxyl groups of the biomaterial leading to lowest biosorption levels.

4.3. *Kinetic data modeling*

To understand the affinity between methylene blue and biomaterial during time, kinetic measurements were performed. The results may deliver evidences on the biosorption process. They also helps to decide on its kind (i.e. chemical or physical). They can also give evidence on the mass transport. Figure 6 exhibits the kinetics curves for the following initial concentrations C_0 = 10 mg·L^{-1}, C_0 = 20 mg·L^{-1}, and C_0 = 50 mg·L^{-1}. The five models above mentioned are used to fit the experimental data. The nonlinear expression is directly used to deduce the parameters inherent to each model. The convergence of the parameter identification and optimization is ensured by an iterative algorithm. Table 3 summarizes the kinetic parameters. It appears clearly that the obtained values of the correlation coefficient R are very close to one for four models, explicitly PFO model, PSO model, Bangham model, and Elovich model. However, the values of R are exceptionally small concerning the intra diffusion model. In the matter this model, even if the boundary layer constant C is taken into consideration, the correlation coefficient R does not come close to its nominal value one. We can conclude that, in the investigated samples, the kinetics is controlled by adsorption and pore diffusion and not by the intra-particle diffusion. It is also clear the behaviors of the different kinetic models are significantly dissimilar for short durations (approximately lesser than 15 min). The initial slope of the curves changes notably from one model to another. Gradually, when time increases, the various models lead

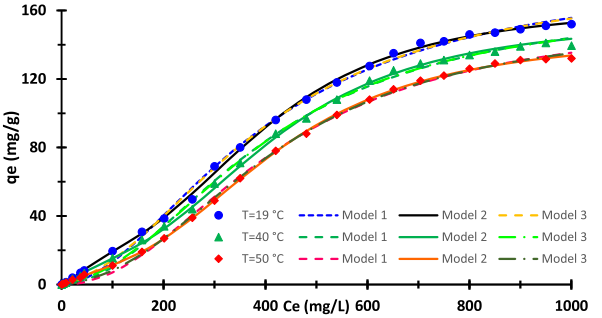

Figure 7. Equilibrium adsorption isotherms: experimental results and theoretical fits using advanced models.

to the same results and collapse. A more attentive inspection of the errors related to different models proves that Bangham and PFO models adjust more accurately the experimental data. We deduce that, in the present samples, the adsorption can be considered as a pore diffusion and physiosorption process. The values of the adsorption energy that will be obtained in the Section 4.6 will corroborate this result. The curves obtained from the theoretical PFO and PSO models are also represented in Figure 6 for the three studied initial concentrations. The equilibrium time may be evaluated by $\tau = 3/k_1$. In other words, depending on the initial concentration and using the values of the constant k_1, the equilibrium is approximately achieved in 6–8 min.

4.4. *Isotherms modeling using classical models*

As above mentioned, the adsorption isotherms will be fitted using classical models and advanced models based on statistical physics. In the matter of the first category, five models are exploited. Three of these models involve two adjustable parameters. These three models are Langmuir, Freundlich, and Dubinin–Radushkevich models. The Hill model includes three adjustable parameters. For this reason, it is expected that the last model is likely to fit more precisely the experimental data. Table 4 presents the parameters inherent to each model as well the correlation coefficient and the RMSE value. It appears clearly that all models fit accurately the experimental. Indeed, for all the models, the correlation coefficient R is approximately equal to one with an error smaller than 3%. Furthermore, the absolute error

Table 2. Comparison of the capacity of removal of methylene blue using many low-cost and abundant biosorbents

Biosorbent	Maximum removal capacity ($mg{\cdot}g^{-1}$)	Reference
***Pergularia tomentosa* fruit**	**122**	**Present work**
Mountain soursop seeds	89	[45]
Typha angustifolia (L.) dead leaves	107	[51]
Cocos nucifera	112	[27]
Rice (*Oryza sativa* L.)	158	[26]
Brazilian berries seeds	171	[63]
Nerium oleander fruit	259	[28]

Table 3. Values of the parameters involved in the kinetic models and error criteria

Kinetic models	Parameters involved in the model and error criteria	Dye initial concentration C_0 ($mg{\cdot}L^{-1}$)		
		10	20	50
Pseudo first order	q_e ($mg{\cdot}g^{-1}$)	1.390	3.915	8.224
	k_1 (min^{-1})	0.354	0.448	0.499
	R	0.9997	0.999	1.0000
	RMSE ($mg{\cdot}g^{-1}$)	0.007	0.024	0.013
Pseudo second order	q_e ($mg{\cdot}g^{-1}$)	1.426	3.983	8.326
	k_2 (min^{-1})	0.707	0.412	0.273
	R	0.9962	0.9994	0.9992
	RMSE ($mg{\cdot}g^{-1}$)	0.027	0.029	0.075
Elovich	α (mg/g·min)	1.32×10^7	3.33×10^{10}	7.30×10^{16}
	β ($mg{\cdot}g^{-1}$)	16.70	8.93	5.41
	R	0.9883	0.9966	0.9971
	RMSE ($mg{\cdot}g^{-1}$)	0.047	0.071	0.139
Intra-particle diffusion	k_d ($mg{\cdot}g^{-1}\cdot min^{-0.5}$)	0.183	0.519	1.090
	R	0.451	0.420	0.397
Bangham	q_e ($mg{\cdot}g^{-1}$)	1.389	3.927	8.228
	k_b (min^{-1})	0.286	0.809	0.592
	n	1.129	0.636	0.894
	R	0.9998	0.9999	1.0000
	RMSE ($mg{\cdot}g^{-1}$)	0.007	0.013	0.011

ranges from 2 to 9 $mg{\cdot}g^{-1}$ depending on the model. This error is relatively small compared to the maximum value of q_e. This confirms that all the investigated classical models prove to be satisfactory. In addition, it appears that Hill isotherm model is probably more suitable for smoothing experimental data curves. Figure 7 exhibits the adsorption isotherms. As above mentioned, Dubinin–Radushkevich model gives the opportunity the evaluate the mean free energy of adsorption E_{ad}. The values of this quantity are presented in Table 4 for several temperatures. It is clear that this energy does not vary significantly in the range of the investigated temperatures. It remains approximately in the range from 6 to 7 $J{\cdot}mol^{-1}$.

Table 4. Values of the parameters involved in the classical models of the adsorption isotherms and some error criteria

Classical models	Parameters involved in the model and error criteria	Temperature (°C)		
		19	40	50
Langmuir isotherm model	q_{max} (mg·g^{-1})	375	382	456
	K_L (L·mg^{-1})	7.71×10^{-4}	6.61×10^{-4}	4.61×10^{-4}
	R	0.988	0.987	0.985
	RMSE (mg·g^{-1})	6.9	6.8	6.8
Freunlich isotherm model	n	1.32	1.27	1.18
	K_f (mg·g^{-1})	0.905	0.686	0.426
	R	0.978	0.977	0.978
	RMSE (mg·g^{-1})	9.2	8.7	8.1
Hill isotherm model	$q_{max\cdot H}$ (mg·L^{-1})	184	168	157
	K_D	6.58×10^4	1.35×10^5	3.64×10^5
	n_H	1.85	1.97	2.12
	R	0.998	0.998	0.999
	RMSE (mg·g^{-1})	3.1	2.7	1.5
Dubinin–Radushkevich isotherm model	q_s (mg·g^{-1})	487	608	646
	k_{ad} (mol^2·kJ^{-2})	1.46×10^{-2}	1.11×10^{-2}	1.0×10^{-2}
	R	0.986	0.984	0.984
	RMSE (mg·g^{-1})	1.9	1.9	2.0
	E_{ad} (kJ·mol^{-1})	5.9 ± 0.2	6.7 ± 0.2	7.1 ± 0.2

We can deduce that the nature of the adsorption process taking place in the present biomaterial is physiosorption [45,64–66]. However, the above estimation of the adsorption energy is very rough. In the next section, we will obtain a more adequate value obtained from statistical models.

At first sight, the values of q_{max} obtained from the Langmuir model seem to be overestimated since the plateau region seems to appear. A more attentive screening of the curves reveals that the plateau is not reached. Different techniques are used to obtain the values of the two adjustable parameters involved in the Langmuir model, namely the saturation value q_{max} and the constant K_L. Among these techniques, we adopt the following linearized form of the Langmuir model:

$$\frac{C_e}{q_e} = \frac{1}{q_{max} K_L} + \frac{C_e}{q_{max}}. \tag{9}$$

As above mentioned, the Langmuir model involves only two adjustable parameters. The value of the constant K_L has an important effect on the slope of the curve at small concentrations whereas the value of q_{max} corresponds to the saturation value when the plateau is reached. One of the limitations of the model comes from that this model does not contain another parameter that allows the adjustment of the transition region for intermediate concentrations and the tuning of the curve inflection. For the concentrations in the range 600–1000 mg·L^{-1}, the saturation regime is not actually reached. For these reasons, the values of q_{max} are larger than the values of q_e in the region 600–1000 mg·L^{-1}. Langmuir's model is therefore not appropriate to adjust the present experimental data.

4.5. *Isotherms modeling using models based on statistical physics*

The second category for adjusting adsorption isotherms contains the advanced statistical models. As above mentioned, only three models will be

run. Table 5 encloses the values of the adjustable parameter intrinsic to each model as well as the correlation coefficient R and the RMSE. The values of the coefficient R is approximately equal to one with an error lesser than 0.2%. The values of the RMSE are also relatively small compared to the maximum value of q_e. The two-energy single-layer model is adopted since it is likely to lead to the best match of the data. Figure 7 displays also the curves related to the three statistical models. It is obvious that the monolayer model with one energy is identical to the Hill model. Indeed, the both models are represented by similar equations.

The saturation value is respectively equal to $q_{e,\text{sat}} = nN_m$, $q_1 + q_2 = n_1N_{m1} + n_2N_{m2}$, and $2nN_m$ for models 1, 2, and 3. These saturation values are reported on Table 5. Both models 1 and 3 are unsuccessful in assessing the actual saturation value. Only model 2 is capable of correctly evaluating this value. Models 1 and 3 fails to track the curves at large concentrations and therefore they diverge progressively from the real trend and yield a biased saturation value. This proves that the statistical models are more powerful than the empirical ones since the best classical model has been faulted using statistical models. Another argument that works against model 3 and consequently model 1 and Hill model is the fact of obtaining the constant C_2 less than C_1. This leads to assume that the adsorption energy of the second layer E_{a2} is greater than the ones characterizing the first layer E_{a1}. This result is meaningless. For all the above-indicated reasons, models 1 and 3 are rejected. The adoption of the model 2 is corroborated by SEM image (Figure 3) which reveal that the surface is rough, heterogeneous, and contains some cavities.

Figure 8 shows the variation of the evolution of the densities N_{m1} and N_{m2} as well as the saturation values $q_1 = n_1N_{m1}$, and $q_2 = n_2N_{m2}$ as a function of the temperature. All the aove quantitiesaturation values of the two kinds of receptors, namely $q_1 = n_1N_{m1}$, and $q_2 = n_2N_{m2}$ decrease when the temperature increases. It is obvious that these quantities are proportional to the number of adsorbed dye molecules per site and the concentration of receptor sites. When the temperature increases, the thermal collisions between dye molecules are intensified whereas the interaction between the adsorbate and adsorbent decays. This is a sign of the presence of a weak binding energy such as hydrogen bonding and/or Van der Waals interactions [45].

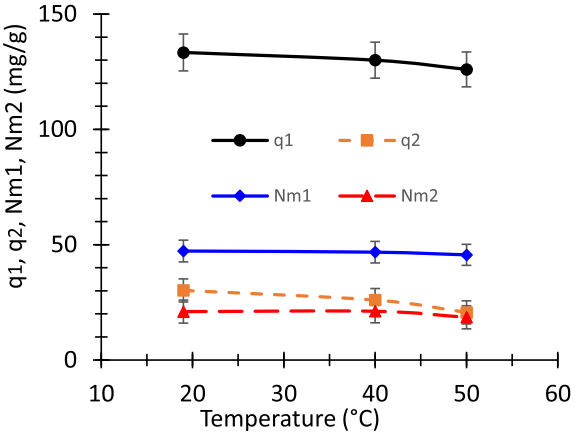

Figure 8. Evolution of the densities N_{m1} and N_{m2}, and the saturation values $q_1 = n_1N_{m1}$ and $q_2 = n_2N_{m2}$ as a function of the temperature.

The errors related to the different parameters are provoked by two sources. The first source of error is of course the unavoidable experimental uncertainty. The second source comes from the parameter identification process. Indeed, each parameter may vary in a more or less wide interval while the function to be minimized, i.e. the root means square error, does not change significantly. Therefore, an average value and a standard deviation are obtained for each parameter. Obviously, the model is only considered as acceptable if the standard deviation linked to each parameter is relatively small compared to the mean value of this same parameter. Otherwise, the model is considered unsatisfactory and does not unequivocally fit the experimental data. This criterion is crucial to evaluate the reliability of the parameters deduced from the fit. In the present work, it has been systematically checked. The dependence of the concentrations of receptor sites N_{m1} and N_{m2} on the temperature is depicted on Figure 8. The concentrations are almost independent of temperature.

It should be noted that since $q_2 = n_2N_{m2}$ and n_2 ranges in the interval from 1.11 to 1.44, the values of q_2 and N_{m2} are close to each other. However, since n_1 takes larger values ant it ranges in the interval from 2.76 to 2.82, the values of q_1 and N_{m1} are significantly different from each other. This behavior appears clearly in Figure 8.

Table 5. Values of the parameters involved in the advanced models of the adsorption isotherms and some error criteria

Models	Parameters involved in the model and error criteria	Temperature (°C)		
		19	40	50
Model 1: monolayer model with one energy	$q_{e\cdot\text{sat}} = nN_m$ (mg·g^{-1})	184	168	157
	$C_{1/2}$ (mg·L^{-1})	396	401	422
	n	1.86	1.97	2.12
	R	0.998	0.998	0.999
	RMSE (mg·g^{-1})	3.1	2.7	2.0
Model 2: monolayer model with two energies	$q_1 = n_1 N_{m1}$ (mg·g^{-1})	133	130	126
	C_1 (mg·L^{-1})	409	426	430
	n_1	2.82	2.78	2.76
	$q_2 = n_2 N_{m2}$ (mg/g)	30.2	26.0	20.7
	C_2 (mg·L^{-1})	85.4	100	122
	n_2	1.44	1.23	1.11
	R	0.9994	0.9993	0.9998
	RMSE (mg·g^{-1})	1.4	1.5	0.7
Model 3: double-layer model with two energies	nN_m (mg·g^{-1})	91.7	84.0	78.7
	C_1 (mg·L^{-1})	487	489	531
	C_2 (mg·L^{-1})	396	402	424
	n	1.31	1.39	1.47
	R	0.9982	0.9985	0.9993
	RMSE (mg·g^{-1})	6.3	4.6	3.6
Model 1	$q_{e,\text{sat}} = nN_m$ (mg·g^{-1})	184	168	157
Model 2	$q_1 + q_2$ (mg·g^{-1})	164	156	147
Model 3	$2nN_m$ (mg·g^{-1})	183	168	157

The steric numbers n_1 and n_2 are two other important parameters that describe the adopted model. The values of the stoichiometric numbers n_1 and n_2 versus the temperature are reported in Table 5. These quantities are none other than the numbers of dye molecules captured for each one of the two types of available receptor sites. It appears that both n_1 and n_2 are greater than one. Therefore, the biosorbent could be attached to 1 or 2 or perhaps 3 dye molecules per site. The stoichiometric number n_2 ranges in the interval from 1 to 2 (the limits of the interval should be integer numbers). Therefore, the receptor sites of the second kind are susceptible to be linked to 1 or 2 dye molecules. We designate x_{21} and x_{22} be the corresponding percentages of occupation: $x_{21}+x_{22} = 1$. The number n_2 is regarded as an average value of 1 and 2 which are weighted by the percentages x_{21} and x_{22}. We deduce $n_2 = x_{21} \times 1 + x_{22} \times 2$. The two above equations permit the computation of the above percentages. By solving the linear set with two variables and two equations, we obtain percentages x_{21} and x_{22} concerning the second kind of receptor sites. More precisely, we obtain that, at the temperature 19 °C, 56% of the occupied sites are linked to only one dye molecule while 44% of the occupied sites are linked to two dye molecules. These percentages vary the temperature. Their respective values are 77% and 23% at 40 °C and 89% and 11% at 50 °C.

According to Table 5, the stoichiometric number n_1 ranges in the interval from 2 to 3 (the limits of the interval should be integer numbers). We deduce that the receptor sites of the first kind can be linker

to 1 or 2 or 3 dye molecules. We designate by x_{11}, x_{12}, and x_{13} the corresponding percentages of occupation. These percentages satisfy the equation $x_{11} + x_{12} + x_{13} = 1$. Since the number n_2 is regarded as an average value of 1, 2, and 3 which are respectively weighted by the percentages x_{11}, x_{12}, and x_{13}, we deduce that $n_1 = x_{11} \times 1 + x_{12} \times 2 + x_{13} \times 3$. The two above equations are not sufficient to obtain the values of x_{11}, x_{12}, and x_{13}. The range of each quantity can be computed. For example, when the temperature is 40 °C, x_{11} varies from 0 to 11%. We deduce that x_{12} and x_{13} vary from 22% to 0% and from 78% to 89% respectively. These values depend on the temperature. It appears that the value of x_{13} is larger than x_{11} and x_{12}. We can conclude that the predominant part of first-type receptor sites adsorbs three MB molecules. Hanafy *et al.* used a multilayer model to investigate the removal of remazol black B dye using natural and carbonized pine-fruit shells. The obtained steric number n ranges from 0.83 to 1.83 for the natural product, and from 1.10 to 2.88 for the carbonized product [65]. The increase of the value of number of the adsorbed dye molecule by adsorbent binding site was imputed to the generation of adsorbent porosity. The number n depend on many factors and principally the temperature. When, the number n increases, the adsorption capacity increases also. Pang *et al.* investigated the adsorption of indigotine blue dye onto a $CoFe_2O_4$/chitosan magnetic composite. Depending on the temperature, the number of dye molecules per adsorbent site varies from 3.66 to 3.83. Pang *et al.* speculated that each receptor site was anchored to an average number of dye molecules varying in the range from 3 to 4. They consequently deduced the proportion related to each case [5]. Sellaoui *et al.* studied the adsorption of MB on Brazilian berries seeds. They showed that the monolayer model with two energies is the most adequate one to fit the experimental data. Two functional groups are therefore involved in the pollutant removal. The steric numbers obtained may be smaller or greater than one. They ranges from 0.35 to 2.44 [63]. It should be mentioned that the value of steric number n also informs us on the nature of the anchorage orientation. In fact, three cases may be generally encountered. The first situation correspond to the case $n > 1$. The inclination of dye molecules captured the biosorbent is called horizontal inclination. Indeed, each receptor site is linked may one or more dye molecules [3]. In the second case, the steric number ranges between 0.5 and 1: $0.5 < n < 1$. In this configuration, a mixed inclination occurs. Parallel and horizontal are simultaneously present. The steric number n may be decomposed as: $n = x \times 0.5 + (1-x) \times 1$ where x is the percentage of molecules having a parallel orientation while $(1-x)$ is the percentage of molecules having a non-parallel orientation [64]. In the third configuration, we have $0 < n \leq 1$. The biosorbent captures a fraction of a dye molecule. This case is called parallel orientation or multi-molecular mechanism. A dye molecule is shared by several receptor sites. To obtain the number of sites involved, one can use the decomposition of the anchorage number $1/n$ [45,64].

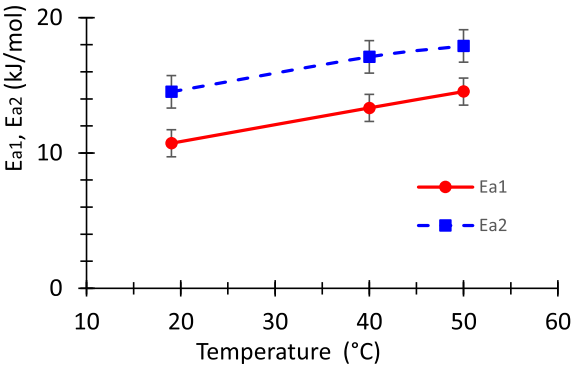

Figure 9. Evolution of the adsorption energies E_{a1} and E_{a2} as a function of the temperature.

The half-saturation concentrations C_1 and C_2 are the last two parameters involved in model 2. These values give the concentration for which half available sites, of each type, are occupied. The greater this quantity, the more the isotherm will be dilated and the saturation will be reached for greater values of the concentration. Table 5 indicates that the half-saturation concentration C_1 is almost independent of temperature however C_2 varies moderately versus the temperature above the investigated range. It appears that C_1 is almost four times greater than C_2. We deduce that the adsorption energy E_{a1} is about 1.4 times smaller than the activation energy E_{a2}.

The adsorption energies E_{a1} and E_{a2} associated to the two types of receptor sites are calculated from values of half-saturation concentrations C_1 and C_2. Figure 9 shows the curves of these energies versus the

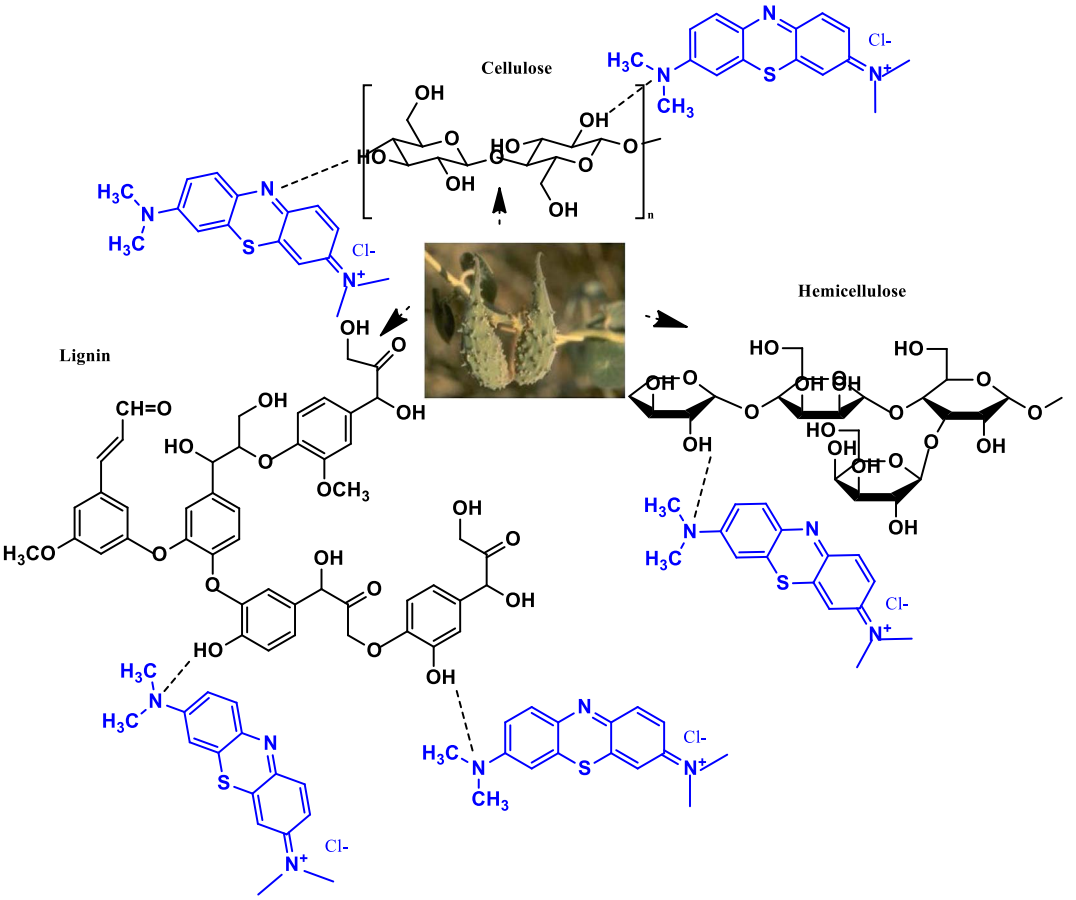

Scheme 1. Probable adsorption mechanisms for the binding between the dye and biosorbent surface.

temperature. A continuous increase of these energies is observed versus the temperature. The obtained results have the same order of magnitude as that reported in previous papers [42,43,63]. The obtained values of the adsorption energy corroborate the several above mentioned comments about the physio sorption nature of the adsorption mechanism occurring in the current samples. The value of the adsorption energy obtained by the advanced model is considered to be more truthful compared to that obtained by the classical models. Indeed, the monolayer model having two kinds of receptors proves to be the most suitable to represent the experimental results. This model takes into account the heterogeneities on the biosorbent surface. The above discussion reveals clearly that not only the experimental results are important, but also the data processing process.

4.6. *MB adsorption mechanisms exploration*

The probable adsorption mechanisms concerning the interaction between the cationic dye and the investigated biomaterial is depicted in Scheme 1.

5. Conclusion

The first part of this work focused on the characterization of a low-cost biomaterial, namely the *Pergularia tomentosa* fruit. The second part is dedicated to investigating the capacity of this biomaterial for the adsorption of methylene blue. The kinetic curves prove to be accurately adjusted by either pseudo first order and Bangham models. The biosorption isotherms have been adjusted by classical and statistical models. Concerning the classical models, Hill model proves to be the most suitable to

adjust the experimental data. In addition, the mean free energy E_{ad} for the adsorption of the cationic dye onto the biomaterial is about 7 kJ/mol according the Dubinin–Radushkevich model. Concerning the advanced statistical physics models, it appears that the most appropriate model is the monolayer model which involves two types of receptors sites. Each receptor has its own adsorption energy, namely E_{a1} and E_{a2}. In other words, two functional groups are involved in the dye removal process. Furthermore, each receptor site can be linked to a variable number of dye molecules. The superiority of this model over the classical models has been demonstrated. The adsorption energy E_{a1} ranges in the interval from 10 to 15 kJ/mol while the adsorption energy E_{a2} varies in the interval from 14 to 18 kJ/mol for the investigated temperature. This implies that the nature of the adsorption process taking place in the present biomaterial is physiosorption. These values are of course more accurate than that estimated from Dubinin–Radushkevich model. The half-concentrations have also been computed. Concerning the stoichiometric numbers inherent to the adopted model, it appears that the investigated biosorbent can be attached to a variable number of dye molecules per site. This number varies from one to three depending on the temperature and the involved functional group. The error on the above parameters due either to experimental uncertainty or the identification process has been evaluated. In summary, the investigated biomaterial proves to be attractive for the efficient elimination of cationic dyes from contaminated water.

Conflicts of interest

The authors declare no conflict of interest.

Authors contributions

All co-authors (HB, MS, TA, ZR, AB, MJ, and TA) contributed in all parts of the manuscript.

Funding

Deputyship for Research & Innovation, Ministry of Education, Saudi Arabia, Project Number (IFP-2020-11).

Acknowledgments

The authors extend their appreciation to the deputyship for Research & Innovation, Ministry of Education in Saudi Arabia funding this research work through the project number (IFP-2020-11).

References

[1] H. Xue, X. Wang, Q. Xu, F. Dhaouadi, L. Sellaoui, M. K. Seliem, A. B. Lamine, H. Belmabrouk, A. Bajahzar, A. Bonilla-Petriciolet, *Chem. Eng. J.*, 2022, **430**, article no. 132801.

[2] M. Bouzid, L. Sellaoui, M. Khalfaoui, H. Belmabrouk, A. B. Lamine, *Phys. A: Statist. Mech. Appl.*, 2016, **444**, 853-869.

[3] L. Zhang, L. Sellaoui, D. Franco, G. L. Dotto, A. Bajahzar, H. Belmabrouk, A. Bonilla-Petriciolet, M. L. Oliveira, Z. Li, *Chem. Eng. J.*, 2020, **382**, article no. 122952.

[4] Z. Li, L. Sellaoui, D. Franco, M. S. Netto, J. Georgin, G. L. Dotto, A. Bajahzar, H. Belmabrouk, A. Bonilla-Petriciolet, Q. Li, *Chem. Eng. J.*, 2020, **389**, article no. 124467.

[5] X. Pang, M. Bouzid, J. M. dos Santos, M. hichem Gazzah, G. L. Dotto, H. Belmabrouk, A. Bajahzar, A. Erto, Z. Li, *Colloids Surf. A: Physicochem. Eng. Aspects*, 2020, **589**, article no. 124467.

[6] A. Mlayah, S. Jellali, A. A. Azzaz, M. Jeguirim, H. Sellalmi, N. Hamdi, *C. R. Chim.*, 2021, **24**, 7-22.

[7] S. Jellali, B. Khiari, M. Usman, H. Hamdi, Y. Charabi, M. Jeguirim, *Renew. Sustain. Energy Rev.*, 2021, **144**, article no. 111068.

[8] S. Jellali, A. A. Azzaz, M. Jeguirim, H. Hamdi, A. Mlayah, *Water*, 2021, **13**, article no. 164.

[9] S. Jellali, L. El-Bassi, Y. Charabi, M. Uaman, B. Khiari, M. Al-Wardy, M. Jeguirim, *J. Environ. Manage.*, 2022, **305**, article no. 114368.

[10] A. Mokhtar, S. Abdelkrim, A. Djelad, A. Sardi, B. Boukoussa, M. Sassi, A. Bengueddach, *Carbohydrate Polym.*, 2020, **229**, article no. 115399.

[11] A. Djelad, A. Mokhtar, A. Khelifa, A. Bengueddach, M. Sassi, *Int. J. Biol. Macromol.*, 2019, **139**, 944-954.

[12] A. Mokhtar, S. Abdelkrim, A. Sardi, A. Benyoub, H. Besnaci, R. Cherrak, M. Hadjel, B. Boukoussa, *J. Polym. Environ.*, 2020, **28**, 1710-1723.

[13] A. Mokhtar, S. Abdelkrim, F. Zaoui, M. Sassi, B. Boukoussa, *J. Inorg. Organomet. Polym. Mater.*, 2020, **30**, 3826-3831.

[14] T. Ahmad, M. Danish, *J. Environ. Manage.*, 2018, **206**, 330-348.

[15] Y. Dai, Q. Sun, W. Wang, L. Lu, M. Liu, J. Li, S. Yang, Y. Sun, K. Zhang, J. Xu, *Chemosphere*, 2018, **211**, 235-253.

[16] C. Ammar, Y. El-Ghoul, M. Jabli, *Int. J. Phytoremediation*, 2021, **23**, 1-10.

[17] H. Akrout, S. Jellali, L. Bousselmi, *C. R. Chim.*, 2015, **18**, 110-120.

[18] M. Miladi, K. Abdellaoui, A. B. Hamouda, I. Boughattas, M. Mhafdhi, F. Acheuk, M. B. Halima-Kamel, *J. Integr. Agric.*, 2019, **18**, 2823-2834.

[19] N. Sakji, M. Jabli, F. Khoffi, N. Tka, R. Zouhaier, W. Ibala, H. Mohamed, B. Durand, *Fibers Polym.*, 2016, **17**, 2095-2104.

[20] N. Sebeia, M. Jabli, A. Ghith, Y. El Ghoul, F. M. Alminderej, *Int. J. Biol. Macromol.*, 2019, **121**, 655-665.

[21] K. Mahmoudi, N. Hamdi, M. B. Ali, S. Jellali, E. Srasra, *C. R. Chim.*, 2020, **23**, 689-704.
[22] A. A. Azzaz, S. Jellali, H. Akrout, A. A. Assadi, L. Bousselmi, *J. Cleaner Product.*, 2018, **201**, 28-38.
[23] A. A. Azzaz, S. Jellali, M. Jeguirim, L. Bousselmi, Z. Bengharez, H. Akrout, *C. R. Chim.*, 2021, **24**, 1-14.
[24] M. Wakkel, B. Khiari, F. Zagrouba, *C. R. Chim.*, 2020, **23**, 671-687.
[25] S. Arabi, M. R. Sohrabi, *Water Sci. Technol.*, 2014, **70**, 24-31.
[26] A. H. Jawad, N. Hum, A. M. Farhan, M. S. Mastuli, *Desalination Water Treat.*, 2020, **190**, 322-330.
[27] A. H. Jawad, R. A. Rashid, R. M. Mahmuod, M. A. M. Ishak, N. N. Kasim, K. Ismail, *Desalination Water Treat.*, 2016, **57**, 8839-8853.
[28] Y. O. Al-Ghamdi, M. Jabli, R. Soury, S. Ali Khan, *Polymers*, 2020, **12**, article no. 2539.
[29] N. Singh, G. Nagpal, S. Agrawal, *Environ. Technol. Innov.*, 2018, **11**, 187-240.
[30] J. Wang, X. Guo, *Chemosphere*, 2020, **258**, article no. 127279.
[31] M. A. Al-Ghouti, D. A. Da'ana, *J. Hazard. Mater.*, 2020, **393**, article no. 122383.
[32] B. Tural, E. Ertaş, B. Enez, S. A. Fincan, S. Tural, *J. Environ. Chem. Eng.*, 2017, **5**, 4795-4802.
[33] Q. Hu, Z. Zhang, *J. Mol. Liquids*, 2019, **277**, 646-648.
[34] S. Rangabhashiyam, N. Anu, M. G. Nandagopal, N. Selvaraju, *J. Environ. Chem. Eng.*, 2014, **2**, 398-414.
[35] K. Y. Foo, B. H. Hameed, *Chem. Eng. J.*, 2010, **156**, 2-10.
[36] A. B. Lamine, Y. Bouazra, *Chem. Senses*, 1997, **22**, 67-75.
[37] M. Khalfaoui, S. Knani, M. Hachicha, A. B. Lamine, *J. Colloid Interface Sci.*, 2003, **263**, 350-356.
[38] S. Knani, M. Mathlouthi, A. B. Lamine, *Food Biophys.*, 2007, **2**, 183-192.
[39] F. Aouaini, S. Knani, M. Ben Yahia, N. Bahloul, N. Kechaou, A. Ben Lamine, *Dry. Technol.*, 2014, **32**, 1905-1922.
[40] M. B. Manaa, N. Issaoui, Y. O. Al-Ghamdi, H. Belmabrouk, A. B. Lamine, *RSC Adv.*, 2020, **10**, 27615-27632.
[41] A. Bajahzar, M. Bouzid, C. Briki, F. Nasri, H. Belmabrouk, A. Jemni, *Int. J. Hydrog. Energy*, 2020, **45**, 15281-15293.
[42] X. Pang, L. Sellaoui, D. Franco, G. L. Dotto, J. Georgin, A. Bajahzar, H. Belmabrouk, A. B. Lamine, A. Bonilla-Petriciolet, Z. Li, *Chem. Eng. J.*, 2019, **378**, article no. 122101.
[43] P. Hua, L. Sellaoui, D. Franco, M. S. Netto, G. L. Dotto, A. Bajahzar, H. Belmabrouk, A. Bonilla-Petriciolet, Z. Li, *Chem. Eng. J.*, 2020, **383**, article no. 123113.
[44] Z. Li, G. L. Dotto, A. Bajahzar, L. Sellaoui, H. Belmabrouk, A. B. Lamine, A. Bonilla-Petriciolet, *Chem. Eng. J.*, 2019, **373**, 1247-1253.
[45] X. Pang, L. Sellaoui, D. Franco, M. S. Netto, J. Georgin, G. L. Dotto, M. K. A. Shayeb, H. Belmabrouk, A. Bonilla-Petriciolet, Z. Li, *Chem. Eng. J.*, 2020, **391**, article no. 123617.
[46] A. Hashem, A. Fletcher, H. Younis, H. Mauof, A. Abou-Okeil, *Int. J. Biol. Macromol.*, 2020, **164**, 3193-3203.
[47] Y. Feng, Y. Liu, L. Xue, H. Sun, Z. Guo, Y. Zhang, L. Yang, *Bioresour. Technol.*, 2017, **238**, 675-683.
[48] R. N. Oliveira, M. C. Mancini, F. C. S. d. Oliveira, T. M. Passos, B. Quilty, R. M. d. S. M. Thiré, G. B. McGuinness, *Matéria (Rio de Janeiro)*, 2016, **21**, 767-779.
[49] X. Chen, R. Xu, Y. Xu, H. Hu, S. Pan, H. Pan, *J. Hazard. Mater.*, 2018, **350**, 38-45.
[50] M. Poletto, A. J. Zattera, R. M. Santana, *J. Appl. Polym. Sci.*, 2012, **126**, E337-E344.
[51] S. Boumaza, A. Yenounne, W. Hachi, F. Kaouah, Y. Bouhamidi, M. Trari, *Int. J. Environ. Res.*, 2018, **12**, 561-573.
[52] H. Kargarzadeh, I. Ahmad, I. Abdullah, A. Dufresne, S. Y. Zainudin, R. M. Sheltami, *Cellulose*, 2012, **19**, 855-866.
[53] D. Trache, A. Donnot, K. Khimeche, R. Benelmir, N. Brosse, *Carbohydrate Polym.*, 2014, **104**, 223-230.
[54] S. Thambiraj, D. R. Shankaran, *Appl. Surf. Sci.*, 2017, **412**, 405-416.
[55] D. Trache, K. Khimeche, A. Donnot, R. Benelmir, "FTIR spectroscopy and X-ray powder diffraction characterization of microcrystalline cellulose obtained from alfa fibers", in *XXXIX Jeep—39th Edition of the Joint European Days on Equilibrium between Phases* (N. David, J. N. Jaubert, R. Privat, eds.), EDP Sciences, Les Ulis, France, 2013.
[56] Y. R. Wang, X. F. Zhang, X. He, W. Zhang, X. X. Zhang, C. H. Lu, *Carbohydrate Polym.*, 2014, **110**, 302-308.
[57] D. Mitrogiannis, G. Markou, A. Celekli, H. Bozkurt, *J. Environ. Chem. Eng.*, 2015, **3**, 670-680.
[58] W. Wei, L. Yang, W. Zhong, S. Li, J. Cui, Z. Wei, *Dig. J. Nanomater. Biostruct.*, 2015, **19**, 1343-1363.
[59] N. Sebeia, M. Jabli, A. Ghith, Y. Elghoul, F. M. Alminderej, *Int. J. Biol. Macromol.*, 2019, **135**, 152-162.
[60] L. Zeng, M. Xie, Q. Zhang, Y. Kang, X. Guo, H. Xiao, Y. Peng, J. Luo, *Carbohydrate Polym.*, 2015, **123**, 89-98.
[61] S. Khattri, M. Singh, *J. Hazard. Mater.*, 2009, **167**, 1089-1094.
[62] Y. Zeroual, B. Kim, C. Kim, M. Blaghen, K. Lee, *Water Air Soil Pollut.*, 2006, **177**, 135-146.
[63] L. Sellaoui, D. Franco, H. Ghalla, J. Georgin, M. S. Netto, G. L. Dotto, A. Bonilla-Petriciolet, H. Belmabrouk, A. Bajahzar, *Chem. Eng. J.*, 2020, **394**, article no. 125011.
[64] Z. Li, L. Sellaoui, G. L. Dotto, A. B. Lamine, A. Bonilla-Petriciolet, H. Hanafy, H. Belmabrouk, M. S. Netto, A. Erto, *J. Mol. Liquids*, 2019, **285**, 165-170.
[65] H. Hanafy, L. Sellaoui, P. S. Thue, E. C. Lima, G. L. Dotto, T. Alharbi, H. Belmabrouk, A. Bonilla-Petriciolet, A. B. Lamine, *J. Mol. Liquids*, 2020, **299**, article no. 112099.
[66] M. Benjelloun, Y. Miyah, R. Bouslamti, L. Nahali, F. Mejbar, S. Lairini, *Chem. Afr.*, 2022, **5**, 1-19.

Comptes Rendus
Chimie
2022, Vol. 25, Special Issue S2, p. 81-92
https://doi.org/10.5802/crchim.152

Sustainable Biomass Resources for Environmental, Agronomic, Biomaterials and Energy Applications 3 / *Ressources de biomasse durables pour des applications environnementales, agronomiques, de biomatériaux et énergétiques 3*

Investigations on potential Tunisian biomasses energetic valorization: thermogravimetric characterization and kinetic degradation analysis

Jemaa Mabrouki [a], Mohammed Ammar Abbassi [a], Besma Khiari [*, b], Salah Jellali [c] and Mejdi Jeguirim [d]

[a] Unité de Recherche Matériaux, Energie et Energies Renouvelables (MEER), Faculté des Sciences de Gafsa, B.P.19, Zarroug, Gafsa, 2112, Tunisia

[b] Wastewaters and Environment Laboratory, Water Research and Technologies Center (CERTE), Technopark Borj Cedria, University of Carthage, P.O. Box 273, Soliman 8020, Tunisia

[c] Center for Environmental Studies and Research, Sultan Qaboos University, Al-Khoud 123, Muscat, Oman

[d] The institute of Materials Science of Mulhouse (IS2M), University of Haute Alsace, University of Strasbourg, CNRS, UMR 7361, F-68100 Mulhouse, France

E-mails: jemaa_mabrouki@hotmail.com (J. Mabrouki), abbassima@gmail.com (M. A. Abbassi), besmakhiari@yahoo.com (B. Khiari), s.jelali@squ.edu.om (S. Jellali), mejdi.jeguirim@uha.fr (M. Jeguirim)

Abstract. In this work, six Tunisian local biomasses, namely ziziphus wood (ZW), almond shells (AS), olive stones (OS), vine stems (VS) and date palm leaflets (DPL) and trunks (DPT) were slowly pyrolyzed under inert atmosphere at a heating rate of 5 °C/min through thermogravimetric (TG) analyses. The thermal degradation of samples involves the interaction in a porous media of heat, mass and momentum transfer with chemical reactions. Heat is transported by conduction, convection and radiation and, mass transfer is driven by pressure and concentration gradients. Thermal degradation curves have been studied with minute details for each degradation step. The Coats–Redfern model was used to extract the kinetic parameters from the TG data, then the kinetic parameters such as the activation energy, the pre-exponential factor and the order of the reaction were calculated. Results showed that the total mass losses amounts and kinetics are dependent on the type of the used biomass. Moreover, the devolatilization could be described by the first order model, while the char formation stage was better described by the second and third order reactions model. The physico-chemical characteristics of these samples were also determined. The volatile matter (VM) content varies considerably, with values ranging from 67.19% for AS to 77.4% for ZW. The maximum values were obtained for ZW and VS with values of 77.4% and 71.9%, respectively. The lowest value (67.19%) was determined for AS. In addition, the ash contents vary between 0.8% for OS and 5.66% for DPT.

* Corresponding author.

The ashes vary significantly from one sample to another, with the values being even lower than 1% for OS, whereas the higher values in the DPT is 5.66%. Further, activation energies corresponding to main devolatilization regions were 59.5, 47.0, 55.8, 41.1, 89.1, 45.2 kJ/mol for ZW, AS, OS, VS, DPL, and DPT respectively. Among all the tested biomasses, the ZW and VS appear to have an important potential to be used for energy production.

Keywords. Biomass, Characterization, Thermal degradation, Kinetic parameters, Zizphus wood.
Published online: 25 February 2022

1. Introduction

The utilization of renewable resources derived from plant biomasses for energetic purposes will reduce the reliance on the limited fossil fuels and has various positive environmental impacts such as the reduction of greenhouse gas emissions and the preservation of water resources against pollution [1]. Biomasses have been considered as the oldest source of energy since several millennia. Nowadays, biomasses represent about 14% of the overall available world's primary energy reserves and its use accounts for 3% and 35% for developed and developing countries, respectively [2]. Energy recovery from biomasses is currently considered as an attractive and sustainable management option as long as there is no overexploitation of these resources [3]. In addition, the use of biomasses as an energy source participates in the natural carbon cycle. Indeed, the quantity of carbon dioxide released during the thermal treatment of biomasses corresponds substantially to that absorbed by photosynthesis during plants growth. Basically, thermogravimetric analysis (TGA) is an analytic method that allows the following of the mass loss of a given sample versus temperature or time. The application of this technique for biomasses has also various applications such as the determination of their thermal stability, the impurities, the hydration rate, and the volatile matter, the fixed carbon and the ash contents [4]. It is also the adapted tool for calculating the main kinetic parameters such as the activation energy, the involved reaction order and the frequency factor [5,6]. The thermogravimetric analysis was applied and discussed for various biomasses [7–9]. The use of kinetic models for the interpretation of the thermal degradation of biomasses experimental data could be very helpful for the optimization of the overall pyrolysis process [10]. For instance, Gasporovic *et al.* studied the thermal degradation of wood wastes. They found that this operation occurs in three stages corresponding to water evaporation, an active, and a passive degradation phase, respectively [11]. Moreover, Gronli *et al.* investigated the thermal decomposition of two types of wood (hardwoods and softwoods) [12]. Comparison between these samples thermal behavior shows that the degradation of softwood starts at lower times and the hemicellulose and cellulose decomposition zones are wider than the hardwood biomass. Besides, Slopiecka *et al.* examined the kinetic degradation of a poplar wood, using three different models, namely Kissinger, Kissingere–Akahirae–Sunose (KAS) and Flynne–Walle–Ozawa (FWO) methods [13]. The results showed that both FWO and KAS models fitted well the experimental date and were suitable for the assessment of the involved mechanisms during the degradation of the used lignocellulosic materials. Thermogravimetric analysis is the most common technique used to estimate the kinetic triplets and thermodynamic parameters of pyrolysis process [14,15]. In addition, Jeguirim *et al.* investigated the thermal degradation behavior of five tropical biomasses using thermogravimetric method [16]. Their research highlighted the importance of a better understanding of the involved mechanisms in the thermal degradation for the optimization of energy production. This is a very important step for the pyrolysis process design, expediency, assessment and scaling up for industrial processes. It is however very important to underline that the involved mechanisms during the pyrolysis of biomasses is still misunderstood due mainly to the little real progress made on the precise quantification of the chemical reactions on the solid matrix [17]. In Tunisia, various agricultural residues and agro-industrial byproducts are produced in relatively important amounts all over the year. Among these wastes, zizyphus wood, almond shell, olive residues, vine stems and date palm residues are abundant lignocellulosic biomass resources in Tunisia [18]. The sustainable management of these wastes has been stressed by the national concerned stakeholders

since several decades ago. The thermochemical conversion of these biomasses for energy and resources recovery has been pointed out as technically feasible, economically attractive and environmentally friendly option [19–22]. For instance, in 2017, the produced olive mill solid wastes in Tunisia were evaluated to 0.450 million tonnes. Different valorization options have been studied at small laboratory scale. They included their combined treatment through adsorption onto sawdust and electrocoagulation [23], their thermal conversion through pyrolysis into biofuels and biochars for energetic, environmental and agronomic purposes [7,24] as well as their thermochemical modification for the generation of activated carbons for efficient industrial effluent treatment [25–27]. The use of kinetic models for fitting the experimental data obtained during the pyrolysis of these wastes is a very important. The thermal kinetics of date palm residues samples can be examined under non-isothermal conditions at various different heating rates [18]. The calculation of these parameters are usually based on the Arrhenius equation and, the linear regression method is often used [4,9,28]. However, to the best of our knowledge, this task has not been carried out for the ziziphus wood. The main aim of the current work is to assess the devolatilization kinetic parameters characterizing six Tunisian biomasses: ziziphus wood, almond shell, olive stones, vine stems and date palm leaflets and trunks by using the experimental data from non-isothermal TG and the Coats and Redfern calculation method. In addition, a comparison of these thermal characteristics was carried out in order to determine their ability for bioenergy production.

2. Materials and methods

2.1. *Biomasses preparation, characterization and TG analysis procedure*

The six used biomasses (Figure 1) were collected form the region of Gafsa (south of Tunisia). They were firstly air-dried under sunlight for a period of 7 days. Then, they were manually crushed and grounded in order to obtain homogenous samples. The retained fraction during this work has particle dimensions lower than 1 mm. Elementary composition was investigated with a CHNS-O Analyzer model 2400. The proximate analysis was based on the thermogravimetric analysis (TGA) results carried out by using the ATG/ATD Setaram Setsys Evaluation instrument. Inherent moisture content is determined by heating an air-dried sample at 105 °C–110 °C under specified conditions until a constant weight is obtained. Volatile matter is defined as the gases removed when the sample is heated to 950 °C under inert atmosphere. The ash content is the amount left when oxygen is injected at 950 °C after volatiles removal. Fixed carbon is obtained by difference.

The thermal degradation behavior of the differents samples were performed using TG analysis. During these analyses, 10 mg of each sample was heated up to a final temperature of 800 °C for a fixed heating gradient of 5 °C/min. These assays were carried out by using nitrogen as an inert gas at a flow rate of 12 NL/h. The used parameters, final temperature reactions of 800 °C, 10 mg of each sample, and the heating rate of 5 °C/min are chosen when doing TGA-experiments for kinetic studies which are considered one important task to decide the heating rate with an appropriate sample size [6]. The optimal condition, which causes minimal heat and mass transfer problems, can be obtained by using very low heating rates and very small sample size. The determination of kinetic mechanisms is mainly carried out under regimes controlled by chemical kinetics, by using very small samples in powder form so that effects of transport phenomena such as heat and mass transfer can be neglected [29–31].

2.2. *Thermal degradation kinetics assessment*

The obtained experimental data (TG and DTG) curves for all the six followed biomasses were used to determine the corresponding kinetic parameters in a first step and then to deduce the most probable involved degradation mechanisms.

The biomass degradation kinetic model is typically given by the Arrhenius equation as follows:

$$\frac{\mathrm{d}\alpha}{\mathrm{d}t} = k(T)f(\alpha) \tag{1}$$

where α represents the degree of degradation of the biomass, $f(\alpha)$ is a function depending on the involved decomposition mechanism, $k(T)$ is the decomposition rate function, T is the temperature and t the time.

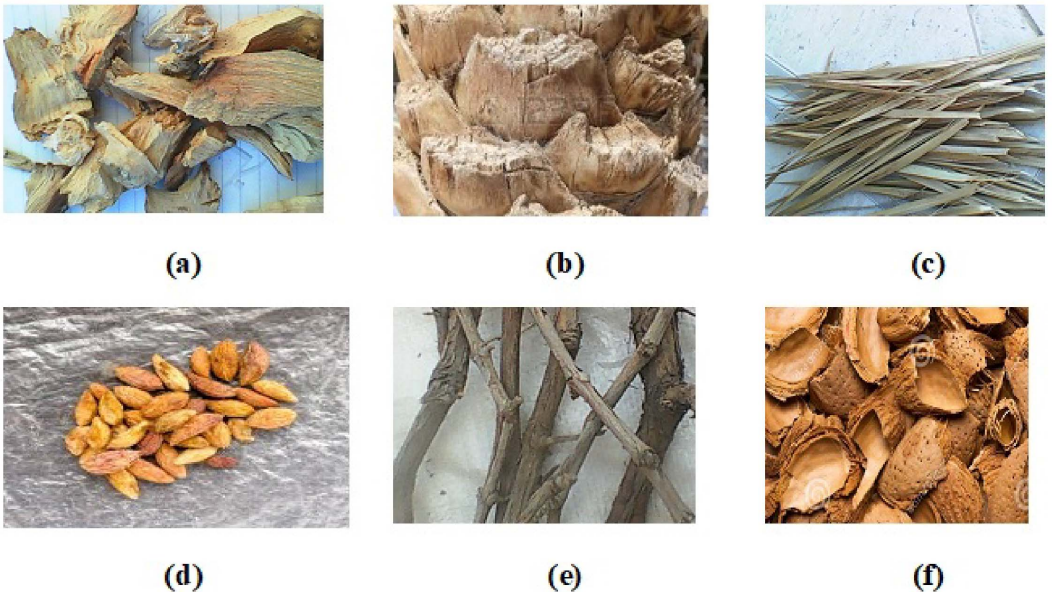

Figure 1. Lignocellulosic materials: (a) ziziphus wood, (b) date palm trunk (c) date palm leaflets, (d) olive stone, (e) vine stems, (f) almond shell.

The α parameter can be calculated for the TG curves as below:

$$\alpha = \frac{m_i - m_t}{m_i - m_f} \tag{2}$$

where m_i, m_t and m_f are the initial biomass mass, at a given time t and at the end of the analysis, respectively.

The function $f(\alpha)$ depends on the order of the reaction "n" as follows:

$$f(\alpha) = (1-\alpha)^n. \tag{3}$$

The constant rate $k(T)$ is given by the Arrhenius equation:

$$k_i = k_{0i}\left(\frac{-E_{ai}}{RT}\right) \tag{4}$$

where k_{0i} is the pre-exponential factor (time^{-1}), E_{ai} is the activation energy (kJ·mol^{-1}), T is the temperature (°C) and R is the universal gas constant (J·K^{-1}·mol^{-1}).

In the case of a constant heating rate (β): $\beta = \mathrm{d}T/\mathrm{d}t = cste$, the variation of degree of decomposition can be written as a function of temperature as follows:

$$\frac{\mathrm{d}\alpha}{\mathrm{d}T} = \frac{A}{\beta}\exp\left(-\frac{E}{RT}\right) f(\alpha) \tag{5}$$

where A is the Arrhenius—pre-exponential factor.

$$\frac{\mathrm{d}\alpha}{f(\alpha)} = \frac{A}{\beta}\exp\left(-\frac{E}{RT}\right)\mathrm{d}T. \tag{6}$$

The integration of (6) gives:

$$g(\alpha) = \int_0^\alpha \frac{\mathrm{d}\alpha}{f(\alpha)} = \frac{A}{\beta}\int_0^T \exp\left(-\frac{E}{RT}\right)\mathrm{d}T. \tag{7}$$

The right hand side of (7) has no exact analytical solution. However, its resolution can be carried out by the asymptotic approximation according to the Coats and Redfern method. When neglecting the high order terms of this solution, the (7) can be transformed as follows:

$$g(\alpha) = \frac{ART^2}{\beta E}\left(1 - \frac{2RT}{E}\right)\exp\left(-\frac{E}{RT}\right). \tag{8}$$

Then, after division by T^2 and taking logarithms, Equation (8) becomes:

$$\mathrm{Ln}\frac{g(\alpha)}{T^2} = \mathrm{Ln}\frac{AR}{\beta E}\left(1 - \frac{2RT}{E}\right) - \frac{E}{RT}. \tag{9}$$

Since ($2RT/E \ll 1$), the (9) can be transformed in:

$$\mathrm{Ln}\frac{g(\alpha)}{T^2} = \mathrm{Ln}\frac{AR}{\beta E} - \frac{E}{RT}. \tag{10}$$

The plots giving $\ln[g(\alpha)/T^2]$ versus $1/T$ give access to the E parameter through the calculus of the corresponding slope. The term $\mathrm{Ln}(AR/\beta E)$ is nearly

Table 1. Algebraic expressions of functions used for biomass thermal degradation

Kinetic model	$f(\alpha)$	$g(\alpha) = \int_0^\alpha \frac{d\alpha}{f(\alpha)}$	Symbol
First order	$1-\alpha$	$-\ln(1-\alpha)$	F1
Second order	$(1-\alpha)^2$	$[1/(1-\alpha)]-1$	F2
Third order	$(1-\alpha)^3$	$(1/2)([1/(1-\alpha)^2]-1)$	F3

constant and its calculus permits the assessment of the Arrhenius—pre-exponential factor A [18]. The expressions of the functions $f(\alpha)$ and $g(\alpha)$ depend on the conversion mechanism and its corresponding mathematical models. Table 1 gives the kinetic models used in the current study for deducing, from the TG curves, the most probable mechanisms during the pyrolysis of the six studied biomasses. Three chemical reaction models were used, namely the first-order (F_1), the second order (F_2) and the third order (F_3) models.

3. Results and discussion

3.1. *Biomasses characterization*

The ultimate and proximate analysis for the six studied biomasses were carried out according to the experimental protocols given in Section 2.1 and the corresponding results are given in Tables 2 and 3 and compared with some reults of literature [33]. Table 2 gives the elementary analysis as well as the "H/C" and "O/C" ratios of the ziziphus wood (ZW), almond shell (AS), olive stones (OS), vine stems (VS) and date palm leaflets (DPL) and trunks (DPT) which are 0.13, 0.14, 0.10, NC, 0.13, 0.13 and 0.79, 1.06, 0.86, 1.03, 0.79, 0.82 respectively. All samples have an elementary composition close to the classical value for lignocellulosic biomass [34]. From Table 2, it can be seen that all the studied biomasses have relatively high C and O contents. The maximum C contents were observed for olive stones followed by vine stems with respective values of about 52.9% and 48.2%, respectively. This might be attributed to the high lignin percentage in OS and VS. Actually, the lowest C contents were observed for DPL and DPT with values of about 46.2% and 43.7%, respectively. The O contents varied between about 36.2% and 49.9% for DPT and VS, respectively. Similar results were reported by Slopiecka *et al.* for Poplar wood [13]; the elements of carbon (C), hydrogen (H), nitrogen (N) and oxygen (O) were 45.5%, 6.26%, 1.04% and 47.2%, respectively. According to Pala *et al.*, apple pomace also have the greatest elemental amount of carbon (47.98%) and oxygen (37.44%) [35]. In addition Kim *et al.* also reported similar results for Pinyon pine wood. Carbon, hydrogen, nitrogen and oxygen O were 41.92%, 6.0%, 2.97% and 49.11%, respectively [36]. Present results revealed O/C ratios ranging from 0.79 to 1.06. The comparison of the different samples shows that ZW, DPL have the lowest O/C ratio while the highest O/C ratios are for AS and VS. Furthermore, the S contents were low for AS and ZW (Table 2) indicating that the SO_x gas emissions during the pyrolysis of these biomasses would be low for these two biomasses as previously reported by Grioui *et al.* for the Tunisian olive wood [37]. In general, N and S contents are low (around 1% or lower). Yet, small amounts of N and S might be advantageous because they could minimize the corrosion problems associated with the formation of acids in the process equipment [38]. Unfortunately, N and S contents were high for the two date palm biomasses and therefore the related emissions of NO_x and SO_x could result in corrosion problems. These results are consistent with previous reports in the scientific literature [39]. On the other hand, the proximate analysis results showed that, for all the studied biomasses, volatile matter (VM) contents are quite high (Table 3). Volatiles vary considerably, with values ranging from 67.19% for AS to 77.4% for ZW. The VM correspond mainly to the cellulose and hemicellulose that will be degraded during the pyrolysis process for the formation of biofuels (biogas and bio-oil). This composition makes, therefore, AS and ZW attractive materials for bioenergy production. Similar results concerning for example the grape pomace biomass were reported [40]. In addition, the ash contents vary between 0.8% for OS and 5.7% for DPT. These values are in the range of reported values in the literature [41–43]. The fixed

Table 2. Ultimate analyses of the used biomasses

Biomass	Carbon	Hydrogen	Oxygen	Nitrogen	Sulfur	H/C ratio	O/C ratio	
ZW	46.21 ± 0.85	5.78 ± 0.09	36.54 ± 1.44	0.51 ± 0.02	$0.021 \pm 9\times10^{-4}$	$0.13 \pm 4\times10^{-3}$	0.79 ± 0.02	
AS	46.86 ± 0.92	6.19 ± 0.10	49.75 ± 1.24	<0.5	<0.05	$0.14 \pm 4\times10^{-3}$	1.06 ± 0.037	
OS	52.89 ± 1.31	5.28 ± 0.11	45.85 ± 1.65	ND	ND	$0.10 \pm 3\times10^{-3}$	0.86 ± 0.01	This work
VS	48.16 ± 1.46	ND	49.85 ± 1.34	ND	ND	NC	1.03 ± 0.04	
DPL	46.16 ± 1.76	5.84 ± 0.14	36.54 ± 1.41	2.15 ± 0.08	0.39 ± 0.01	$0.13 \pm 5\times10^{-3}$	0.79 ± 0.01	
DPT	43.74 ± 1.11	5.66 ± 0.12	36.20 ± 1.66	0.69 ± 0.02	0.35 ± 0.01	$0.13 \pm 4\times10^{-3}$	0.82 ± 0.02	
Cassava pulp residue	35.89	5.47	58.27	0.36	ND	1.829	1.218	[32]
Palm kernel cake	47.19	6.38	43.28	3.15	ND	1.622	0.688	[32]
Longan fruit seed	43.75	6.30	48.81	1.14	ND	1.350	0.668	[32]
Coconut shell	49.76	5.60	44.30	0.35	ND	1.727	0.837	[32]

Table 3. Proximate analyses of the used biomasses

Biomass type	Moisture	FC	VM	Ash	HHV (MJ/kg)	
DPT	7.32 ± 0.34	17.26 ± 0.67	69.76 ± 2.11	5.66 ± 0.02	17.68 ± 0.72	
AS	7.07 ± 0.52	22.3 ± 0.92	67.19 ± 1.96	3.45 ± 0.01	19.76 ± 1.13	
VS	6.45 ± 0.29	19.94 ± 0.88	71.9 ± 2.32	1.71 ± 0.03	NC	This work
ZW	5.75 ± 0.12	15.44 ± 0.54	77.44 ± 3.12	1.37 ± 0.01	18.50 ± 0.54	
DPL	6.75 ± 0.29	17.67 ± 0.76	70.21 ± 3.11	5.37 ± 0.04	18.52 ± 0.79	
OS	9.19 ± 0.04	22.68 ± 1.08	67.33 ± 2.09	$0.80 \pm 2\times10^{-3}$	20.84 ± 0.32	
Cassava pulp residue	ND	11.83	81.98	6.19	22.41	
Palm kernel cake	ND	16.74	79.57	3.69	21.91	[33]
Longan fruit seed	ND	14.80	84.51	0.70	21.16	
Coconut shell	ND	16.33	82.38	1.29	21.28	

carbon values of the studied biomasses vary between 15.4% and 22.7% for ZW and OS, respectively. This is typical for biomass types derived from hard tissues such as trunks, while in case of soft tissues (such as leaves, young branches, bushes, grasses, etc.), the content is as low as 17.67% for DPL. Moreover, the low ashes (1.37%) and the high volatiles (77.44%) for ziziphus wood, are characteristic of lignocellulosic materials, which make this biomass very attractive for the thermal degradation processes. The vegetable biomass samples coming from different plant types or even from different parts of the same plant have significantly different fixed carbon and ash contents [44,45]. The higher ash content associated with AS, DPL and DPT would likely make lignin difficult to decompose during the pyrolysis; the generated solid residue would be very high. The mineral composition of the followed biomasses is given in Table 4. The presence of K, Na and Ca elements in biomasses with important contents could negatively impact their thermal degradation and therefore promote the formation of biochars. Moreover, the calculus of the sum of the main contents (P and Mg) is particularly important to highlight if the generated biochars could be valorized as biofertilizers in agriculture. To sum up, it is interesting to note that the low moisture and ash content and high volatile make ziziphus wood and vine stems two potential sources for energy generation and/or bio-chemicals production in Tunisia. Finally, for the feedstock producing higher amounts of ash during pyrolysis, ash removal systems should be envisaged when designing the conversion process. composition of biomasses is volatile contents and carbon and oxygen are the major elements. The gross heating values of all biomasses varied approximately from 17.68 to 20.84 MJ/kg. According to Damartzis *et al.* who studied the Tthermal degrada-

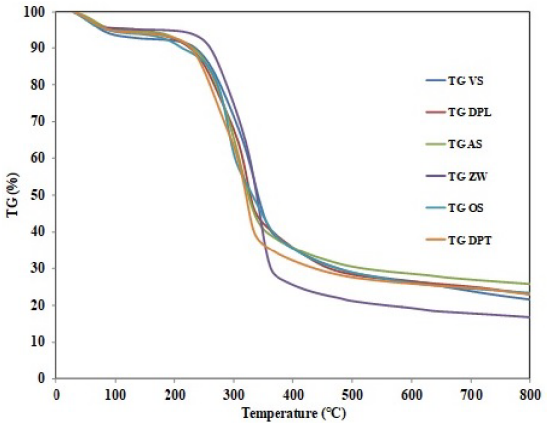

Figure 2. TGA curves of the different samples under nitrogen atmosphere.

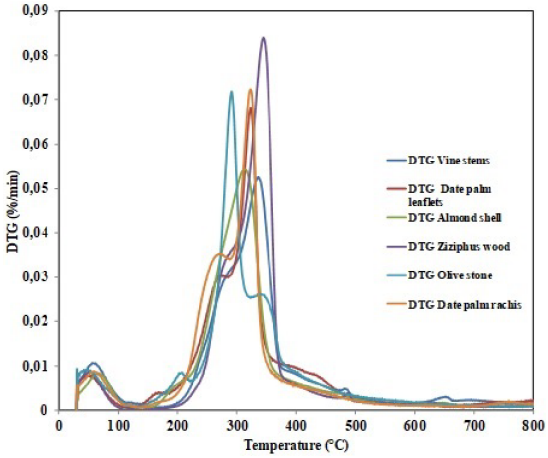

Figure 3. DGA curves of the different samples under nitrogen atmosphere.

tion and kinetic modeling of cardoon (Cynara cardunculus) pyrolysis using thermogravimetric analysis (TGA), the highest calorific value corresponded to stems (21.5 MJ/kg), due to their lower ash and higher volatiles content while the HHV value of Cardoon leaves was 17.9 MJ/kg. The stems are lower in inorganic constituents than the leaves (ash content 7.6%) [46]. In fact, even if the main goal of this study is to identify the biomass that is considered the most energetic for the production of three components: bio-oil, gas, and char, the yielded char characteristics are so interesting that it may be used in different applications, such as the production of chemicals, activated carbon, carbon nanotubes, carbon fibers, etc. The produced char is also a better fuel than the precursor biomass, which means that it can be used as a high-efficiency solid fuel (converted into briquettes alone or mixed with biomass) in boilers.

3.2. *Thermal analysis*

The thermal analysis of the six studied biomasses was carried out under the experimental conditions given in Section 2.2. The corresponding TGA and DTG profiles were given in Figures 2 and 3, respectively. For all the followed biomasses, the curves revealed the presence of three identical degradation zones corresponding to the moisture evaporation, the decomposition of the volatile matter and the production of the solid residue, in agreement with previous findings [47,48]. The deshydratation zone is observed at temperature values between room temperature and 105 °C, 108 °C, 90 °C, 145 °C, 90 °C and 110 °C respectively for ZW, AS, OS, VS, DPL and DPT. During this phase, the mass loss is negligible attributed to the removal of moisture and the start of polysaccharide hydrolysis [49,50]. The second stage of mass loss depicted in Figures 2 and 3 ranged from 145 °C to 400 °C and corresponds mainly to the degradation of hemicelluloses, cellulose and lignin. Hemicelluloses typically decomposes between 160 and 360 °C, while cellulose degrades at higher interval of 240–390 °C. The third stage of decomposition (from 400 to 900 °C) is attributed to lignin. The degradation of lignin typically happens at a slow rate over a much wide temperature range of 180–900 °C [51]. Such variations in the lignin starting degradation temperatures of the six biomasses could be linked to the differences in their elemental and chemical compositions. The maximum weight loss occurs in the range 200–400 °C. During this period, the hemicelluloses and cellulose were degraded and, volatiles, gases, and primary bio-char are produced [52]. According to Miranda *et al.*, this stage of biomass decomposition corresponds to the beginning of secondary decomposition of heavier volatiles and the formation of char [53]. Furthermore, a similar behavior was observed by Ceylan *et al.* during the pyrolysis of hazelnut shells at 5 °C/min [54]. The authors assumed that the decomposition of a part of the biomass (hemicellulose and cellulose) occurs in two ways. In the

Table 4. Mineral composition of the studied biomasses (%)

Element	ZW	AS	OS	VS	DPL	DPT
Na	0.216	0.089	–	0.319	0.100	0.102
Mg	0.080	0.084	0.115	0.198	0.281	0.575
Al	0.023	0.050	0.008	0.042	0.024	0.011
Si	0.081	0.146	0.058	0.096	0.223	0.187
P	0.058	0.089	0.110	0.019	0.261	0.148
Cl	0.070	0.038	0.132	0.273	1.858	2.847
K	0.063	0.956	0.435	0.176	2.544	2.485
Ca	0.779	0.732	0.085	0.645	0.494	0.492
Fe	0.063	0.061	0.103	0.050	0.035	0.026
Cu	0.029	0.018	0.019	0.015	0.041	0.040
Zn	0.322	0.047	0.091	0.070	0.021	0.035
Sr	0.011	0.013	–	0.017	0.04	0.005

first mode, which occurs at low temperature (up to 355 °C in their study), the boundaries of the polymers decompose and generate CO and CO_2 gases as well as the carbon residue. In the second way, which occurs at high temperatures, leads to the formation of a liquid. In the third stage, the mass loss of the ZW, VS, OS, AS, DPL and DPT was less than that obtained in the second stage. The authors also showed that lignin is the main compound responsible for the production of char. The percentage of this carbonaceous residue is in the range 45–50% of the initial mass. The same percentage of char (40%) was found by Yang *et al.* in a wider temperature range (160–900 °C) [55]. These authors stated that in terms of energy consumption during pyrolysis, the behavior of cellulose differs from hemicellulose and lignin. During the first decomposition zone, the DTG curves of all biomasses show two distinct peaks (Table 5).

On the DTG profiles, the temperatures at which the maximum rate of mass loss occurred are described by the position of the peaks in the curve. The DTG peaks are much closer to each other for ZW than for OS and the maximum of hemicelluloses and cellulose peaks occurring at lower temperatures. Orfão *et al.* reported that the DTG peak during the decomposition of pure cellulose occurred at (332 °C, 0.9 wt%·s^{-1}) [56]. The second DTG peak, has a much higher rate of weight loss than the first stage. The thermal decomposition depends on the chemical composition of the biomasses as individual components of lignocellulosic materials have different thermal behaviors. Numerous studies on the thermal degradation of lignocellulosic materials indicated that the decomposition of hemicelluloses starts first, followed by the cellulose cracking and ends with the lignin degradation [57–59].

The comparison between the samples thermal behavior shows that the degradation of softwood starts at lower temperature and the hemicellulose and cellulose decomposition zones are wider than the hardwood biomass. It has been debated in the literature that the two different regions of weight loss observed for wood pyrolysis may be represented as a combination of the individual decomposition of hemicellulose and cellulose. The decomposition of parts of the biomass, due to pyrolysis, takes place in two ways because the kinetic model supposes that degradation reactions are beginning separately. First, hemicellulose and cellulose decompose and then lignin. For each decomposition reaction kinetic parameters are determined but they are only valid for a temperature domain.

The different chemical composition of wood, i.e. the different percentage of cellulose, hemicellulose and lignin, the different amount and composition of inorganic matter which leads to different starting degradation temperature.

This is consistent with the relatively simple chemical structure of cellulose, hemicellulose and lignin. However, some differences may be observed with respect to: (1) the width of the DTG peaks; (2) the temperature where the maximum rate of decomposition

Table 5. Peaks of pyrolysis DTG

	First peak		Second peak	
Biomass	Temperature (°C)	Mass loss rate (%·s^{-1})	Temperature (°C)	Mass loss rate (%·s^{-1})
ZW	285	0.035	344	0.084
VS	287	0.031	330	0.053
AS	207	0.006	310	0.054
OS	205	0.031	290	0.071
DPL	270	0.031	326	0.067
DPT	269	0.035	320	0.071

occur (Tpeak); and (3) the final char yield among the different samples analyzed. The Ziziphunus wood has different behavior due to higher cellulose content comparing the other polymers. In fact, it is well known that in the pure cellulose decomposition peak temperature is around 360 °C in similar TGA conditions. Woody biomasses are known to have higher cellulose content. For the other biomasses, the content of hemicellulose and cellulose is quite similar. Therefore, the peak of decomposition occurs earlier at lower decomposition rate.

In contrast to cellulose, lignin shows a gradual loss of weight from about 200 °C to the final temperature of 500 °C consistent with the wide variety of functional groups and hence bond strengths exhibited in the structure of lignin. In order to prove this behavior, one can see the weight or percentage of char at the final temperature (approximately 50% of the original lignin substance), which means that the lignin part of wood is mainly responsible for the char portion of the products.

Other studies of xylan have indicated a much lower char yield for the hemicelluloses and that they are the least thermal stable major component of wood. This is probably due to their lack of crystallinity.

ZW and DPL have almost similar chemical composition, which is reflected by their almost similar thermal fingerprints. It has been shown in the literature that the two different regions of weight loss observed for wood pyrolysis may be represented as a combination of the individual decomposition of hemicellulose and cellulose.

3.3. *Kinetics parameters*

The kinetic parameters obtained during the pyrolysis of the six studied biomasses are presented in Table 6. Initial pyrolysis temperatures, the peaks position and height in TGA and DTG curves show the reactivity of these samples. Samples with the highest cellulose content have the highest activation energies. In deed, the energy activation value of cellulose is the highest one (between 100–200 kJ/mol). When cellulose is present in significant amount, the activation energies or the frequency factors are higher (case of Ziziphunus Wood). The calculated average activation energies are comparable to those met in literature [60,61]. For example, Parthasarathy *et al.* carried out a similar study on rice husk [62]. They reported an activation energy around 55 KJ/mol for the first reaction zone of dehydration, 84.1 KJ/mol for the second zone (hemicelluloses and cellulose cracking) and 21.2 KJ/mol for the third reaction zone (lignin degradation). The kinetic approach shows that the devolatilization step could be described by the first order chemical reaction model (F1) while the second and third reaction orders (F2, F3) could fit the char formation. Moreover, several investigations showed that F1 could be a reasonable mechanism for describing the devolatilization phase of the biomass species. A similar conclusion was reached by Gil *et al.* who noted also two devolatilization stages during their work on the thermal behavior of pine and pine/coal blends [63]. The chemical reaction F1 mechanism could not be selected as an effective mechanism for this type of tropical biomass. Finally, the activation energy values do agree reasonably well with those obtained for other agricultural and forestry residues while applying the Coat Redfern

Table 6. Kinetics parameters of the thermal degradation of the studied biomasses

Biomass	Temperature range	Activation energy ($kJ \cdot mol^{-1}$)	Frequency factor (s^{-1})	R^2	Function $f(\alpha)$
ZW	241–362	59.5	182.6	0.9908	F1
	362–612	17.9	0.092	0.9965	F2
	362–612	48.3	527.1	0.9979	F3
AS	228–362	47.0	17.64	0.9906	F1
	362–645	18.8	0.091	0.9968	F2
	362–645	50.3	505.3	0.9982	F3
OS	241–362	55.8	18.5	0.9908	F1
	362–612	17.7	0.088	0.9965	F2
	362–612	49.2	29.3	0.9979	F3
VS	228–378	41.1	3.233	0.9933	F1
	378–553	14.6	0.026	0.9924	F2
	378–553	38.4	26.90	0.9908	F3
DPL	241–362	89.1	4.78	0.9968	F1
	362–612	15.88	0.067	0.9908	F2
	362–612	58	505.9	0.9987	F3
DPT	241–362	45.2	3.88	0.9956	F1
	362–612	19.3	0.077	0.9906	F2
	362–612	45	405.3	0.9986	F3

method [5,32].

4. Conclusions

Thermal decomposition of six Tunisian biomasses was analyzed by the thermogravimetric technique, which helped (i) assessing the main thermal characteristics such as the degradation temperature corresponding to the loss of mass and (ii) calculating the kinetic constants (the activation energy and the pre-exponential factor). The kinetic approach showed that the devolatilization step could be fitted by the first reaction order model while the char formation is better described by the second and third reaction orders. The average activation energies ranged from 15 to 89.1 kJ/mol for the first decompistion, from 14.6 to 19.3 kJ/mol for the second one and, from 38.4 to 58 kJ/mol in the last one. Ziziphus wood (ZW), almond shell (AS), olive stones (OS), vine stems (VS), date palm leaflets (DPL) and date palm trunks (DPT) have low sulphur and ash contents. The high volatile matter contents, related to the oil contentment of the residues, make them interesting sources for thermal energy production, notably for ziziphus wood and vine stems, which appear to be more desirable feedstock for pyrolysis and upgrading applications compared to other samples. As for the feedstock that produce higher amounts of ash during pyrolysis, ash removal systems should be set up when designing the conversion process.

Conflicts of interest

Authors have no conflict of interest to declare.

Acknowledgement

This work was supported by the Tunisian Ministry of Higher Education and Scientific Research under grant 20/PRD-22.

References

[1] M. Jeguirim, B. Khiari, L. Limousy, "Biomass feedstocks", in *Char and Carbon Materials Derived from Biomass*, Elsevier, 2019, 1-38.

[2] J. Popp, S. Kovács, J. Oláh, Z. Divéki, E. Balázs, *N. Biotechnol.*, 2021, **60**, 76-84.

[3] S. S. Siwal, Q. Zhang, N. Devi, A. K. Saini, V. Saini, B. Pareek, S. Gaidukovs, V. K. Thakur, *Renew. Sustain. Energy Rev.*, 2021, **150**, article no. 111483.

[4] B. Khiari, I. Ghouma, A. I. Ferjani, A. A. Azzaz, S. Jellali, L. Limousy, M. Jeguirim, *Fuel*, 2020, **262**, 116654-116665.

[5] M. Raza, B. Abu-Jdayil, A. H. Al-Marzouqi, A. Inayat, *Renew. Energy*, 2022, **183**, 67-77.

[6] N. Zouaoui, J. F. Brilhac, F. Mechati, M. Jeguirim, B. Djellouli, P. Gilot, *J. Therm. Anal. Calorim.*, 2010, **102**, 837-849.

[7] A. A. Azzaz, M. Jeguirim, V. Kinigopoulou, C. Doulgeris, M.-L. Goddard, S. Jellali, C. Matei Ghimbeu, *Sci. Total Environ.*, 2020, **733**, article no. 139314.

[8] B. Khiari, M. Jeguirim, "Tunisian agro-food wastes recovery by pyrolysis: thermogravimetric analysis and kinetic study", in *2019 10th Int. Renew. Energy Congr. (IREC)*, IEEE, Hammamet, Tunisia, 2019.

[9] B. Khiari, M. Massoudi, M. Jeguirim, *Environ. Sci. Pollut. Res.*, 2019, **26**, 35435-35444.

[10] M. Belhachemi, B. Khiari, M. Jeguirim, A. Sepúlveda-Escribano, "Char and Carbon Materials Derived from Biomass" (M. Jeguirim, L. Limousy, eds.), Elsevier, Amsterdam, Netherlands, 2019, 69-108.

[11] L. Gašparovič, Z. Koreňová, Ľ. Jelemenský, *Chem. Pap.*, 2010, **64**, 174-181.

[12] M. G. Grønli, G. Várhegyi, C. Di Blasi, *Ind. Eng. Chem. Res.*, 2002, **41**, 4201-4208.

[13] K. Slopiecka, P. Bartocci, F. Fantozzi, *Appl. Energy*, 2012, **97**, 491-497.

[14] A. Aboulkas, *J. Therm. Anal. Calorim.*, 2016, **123**, 1657-1666.

[15] A. Tabal, A. Barakat, A. Aboulkas, K. El harfi, *Fuel*, 2021, **283**, article no. 119253.

[16] M. Jeguirim, J. Bikai, Y. Elmay, L. Limousy, E. Njeugna, *Energy Sustain. Dev.*, 2014, **23**, 188-193.

[17] I. Díaz, M. Rodríguez, C. Arnaiz, G. San Miguel, M. Domínguez, "Biomass pyrolysis kinetics through thermogravimetric analysis", in *23 European Symposium on Computer Aided Process Engineering* (A. Kraslawski, I. Turunen, eds.), Computer Aided Chemical Engineering, vol. 32, Elsevier, Amsterdam, Netherlands, 2013, 1-6.

[18] M. Jeguirim, Y. Elmay, L. Limousy, M. Lajili, R. Said, *Environ. Prog. Sustain. Energy*, 2014, **33**, 1452-1458.

[19] E. A. N. Marks, V. Kinigopoulou, H. Akrout, A. A. Azzaz, C. Doulgeris, S. Jellali, C. Rad, P. Sánchez Zulueta, E. Tziritis, L. El-Bassi, C. Matei Ghimbeu, M. Jeguirim, *Sustainability*, 2020, **12**, 6081-6096.

[20] A. Chouchene, M. Jeguirim, B. Khiari, G. Trouvé, F. Zagrouba, *J. Anal. Appl. Pyrolysis*, 2010, **87**, 168-174.

[21] A. Agrifoglio, A. Fichera, A. Gagliano, R. Volpe, *C. R. Chim.*, 2021, **24**, 1-17.

[22] A. Gagliano, F. Nocera, F. Patania, M. Bruno, D. G. Castaldo, *C. R. Chim.*, 2016, **19**, 441-449.

[23] M. Bargaoui, S. Jellali, A. A. Azzaz, M. Jeguirim, H. Akrout, *Environ. Sci. Pollut. Res.*, 2021, **28**, 24470-24485.

[24] K. Haddad, M. Jeguirim, S. Jellali, N. Thevenin, L. Ruidavets, L. Limousy, *Sci. Total Environ.*, 2021, **752**, article no. 141713.

[25] K. Mahmoudi, N. Hamdi, M. Ben Ali, S. Jellali, E. Srasra, *C. R. Chim.*, 2021, **23**, 689-704.

[26] L. Limousy, I. Ghouma, A. Ouederni, M. Jeguirim, *Environ. Sci. Pollut. Res.*, 2017, **24**, 9993-10004.

[27] S. Jellali, E. Diamantopoulos, K. Haddad, M. Anane, W. Durner, A. Mlayah, *J. Environ. Manage.*, 2016, **180**, 439-449.

[28] B. Khiari, A. Ibn Ferjani, A. A. Azzaz, S. Jellali, L. Limousy, M. Jeguirim, *Biomass Convers. Biorefinery*, 2021, **11**, 325-337.

[29] B. Khiari, M. Jeguirim, L. Limousy, S. Bennici, *Renew. Sustain. Energy Rev.*, 2019, **108**, 253-273.

[30] S. Kordoghli, B. Khiari, M. Paraschiv, F. Zagrouba, M. Tazerout, *Int. J. Hydrogen Energy*, 2019, **44**, 11289-11302.

[31] A. Chouchene, M. Jeguirim, B. Khiari, F. Zagrouba, G. Trouvé, *Resour. Conserv. Recycl.*, 2010, **54**, 271-277.

[32] S. Ali, S. A. Hussain, M. Z. Mohd. Tohir, A. A. Nuruddin, *Mater. Today Proc.*, 2021, **42**, 178-185.

[33] P. Weerachanchai, C. Tangsathitkulchai, M. Tangsathitkulchai, *Suranaree J. Sci. Technol.*, 2011, **17**, 387-400.

[34] M. Jeguirim, S. Dorge, A. Loth, G. Trouvé, *Int. J. Green Energy*, 2010, **7**, 164-173.

[35] M. Pala, I. C. Kantarli, H. B. Buyukisik, J. Yanik, *Bioresour. Technol.*, 2014, **161**, 255-262.

[36] D.-I. Kim, Y. Matsuyama, S. Nagasoe, M. Yamaguchi, Y. Ho, Y. Oshima, N. Imada, T. Honjo, *J. Plankton Res.*, 2004, **26**, 61-66.

[37] N. Grioui, K. Halouani, A. Zoulalian, F. Elhalouani, *Thermochim. Acta.*, 2005, 23-30.

[38] X. Hu, M. Gholizadeh, *J. Energy Chem.*, 2019, **39**, 109-143.

[39] A.-C. Johansson, L. Sandström, O. G. W. Öhrman, H. Jilvero, *J. Anal. Appl. Pyrolysis*, 2018, **134**, 102-113.

[40] S. Sri Shalini, K. Palanivelu, A. Ramachandran, V. Raghavan, *Biorefinery*, 2020, **280**.

[41] N. Boukaous, L. Abdelouahed, C. Mustapha, C. Mohabeer, A. Meniai, B. Taouk, *C. R. Chim.*, 2021, **23**, 623-634.

[42] H. Hammani, M. El Achaby, K. El Harfi, M. Mhammedi, A. Aboulkas, *C. R. Chim.*, 2020, 1-18.

[43] S. A. El-Sayed, M. E. Mostafa, *Energy Convers. Manag.*, 2014, **85**, 165-172.

[44] R. Charvet, F. Silva, L. Ruivo, L. Tarelho, A. Matos, J. Figueiredo da Silva, D. Neves, *Energies*, 2021, **14**, article no. 2537.

[45] Y.-E. Lee, D.-C. Shin, Y. Jeong, I. Kim, Y.-S. Yoo, *Energies*, 2019, **12**, article no. 4538.

[46] T. Damartzis, D. Vamvuka, S. Sfakiotakis, A. Zabaniotou, *Bioresour. Technol.*, 2011, **102**, 6230-6238.

[47] M. Boutaieb, M. Guiza, S. Román Suero, B. Ledesma, S. Nogales, A. Ouederni, *C. R. Chim.*, 2020, **23**, 607-621.

[48] A. Anca-Couce, C. Tsekos, S. Retschitzegger, F. Zimbardi, A. Funke, S. Banks, T. Kraia, P. Marques, R. Scharler, W. de Jong, N. Kienzl, *Fuel*, 2020, **276**, article no. 118002.

[49] A. A. Azzaz, B. Khiari, S. Jellali, C. M. Ghimbeu, M. Jeguirim, *Renew. Sustain. Energy Rev.*, 2020, **127**, article no. 109882.

[50] H. Bouaik, A. Tabal, A. Barakat, K. Harfi, A. Aboulkas, *C. R. Chim.*, 2021, **24**, 1-15.
[51] S. Niksa, *Fuel*, 2020, **263**, article no. 116649.
[52] L. Reyes, L. Abdelouahed, C. Mohabeer, J.-C. Buvat, B. Taouk, *Energy Convers. Manag.*, 2021, **244**, article no. 114459.
[53] N. Toscano Miranda, I. Lopes Motta, R. Maciel Filho, M. R. Wolf Maciel, *Renew. Sustain. Energy Rev.*, 2021, **149**, article no. 111394.
[54] S. Ceylan, Y. Topçu, *Bioresour. Technol.*, 2014, **156**, 182-188.
[55] H. Yang, R. Yan, H. Chen, C. Zheng, D. H. Lee, D. T. Liang, *Energy & Fuels*, 2006, **20**, 388-393.
[56] J. J. M. Orfão, F. J. A. Antunes, J. L. Figueiredo, *Fuel*, 1999, **78**, 349-358.
[57] A. Brillard, J. F. Brilhac, *Renew. Energy*, 2020, **146**, 1498-1509.
[58] K. N. Yogalakshmi, T. Poornima Devi, P. Sivashanmugam, S. Kavitha, R. Yukesh Kannah, S. Varjani, S. AdishKumar, G. Kumar, J. Rajesh Banu, *Chemosphere*, 2022, **286**, article no. 131824.
[59] C. Pedroza-Solis, J. De la Rosa, C. Lucio-Ortiz, D. De Haro-Del Rio, D. Casamachin, T. García, G. Escamilla, E. Carrillo-Pedraza, I. López, D. Bustos, D. Garcia-Gutierrez, L. Sandoval-Rangel, *C. R. Chim.*, 2021, **24**, 1-17.
[60] L. Luo, X. Guo, Z. Zhang, M. Chai, M. M. Rahman, X. Zhang, J. Cai, *Energy & Fuels*, 2020, **34**, 4874-4881.
[61] D. K. Ojha, D. Viju, R. Vinu, *Energy Convers. Manag. X.*, 2021, **10**, article no. 100071.
[62] P. Parthasarathy, K. S. Narayanan, L. Arockiam, *Biomass Bioenergy*, 2013, **58**, 58-66.
[63] M. V. Gil, D. Casal, C. Pevida, J. J. Pis, F. Rubiera, *Bioresour. Technol.*, 2010, **101**, 5601-5608.

Comptes Rendus
Chimie
2022, Vol. 25, Special Issue S2, p. 93-112
https://doi.org/10.5802/crchim.178

Sustainable Biomass Resources for Environmental, Agronomic, Biomaterials and Energy Applications 3 / *Ressources de biomasse durables pour des applications environnementales, agronomiques, de biomatériaux et énergétiques 3*

D-optimal design optimization of unsaturated palm fatty acid distillate and trimethylolpropane esterification for biolubricant production

Majd Ahmed Jumaah [a], **Nadia Salih** [*, b] **and Jumat Salimon** [*, b]

[a] Salah Al-Din Health Department, Ministry of Health, Tikrit, Iraq

[b] Department of Chemical Sciences, Faculty of Science and Technology, Universiti Kebangsaan Malaysia, 43600 Bangi, Selangor, Malaysia

E-mails: majd_ahmad73@yahoo.com (M. A. Jumaah), nadiaalnami@hotmail.com (N. Salih), jumatsal@gmail.com (J. Salimon)

Abstract. An edible palm oil processing industries produces an economical by-product or waste of palm fatty acid distillate (PFAD). Many researchers have put an effort to utilize uneconomical PFAD to produce valuable, versatile and high-end products. In this work, polyol ester of green biolubricant base oil was synthesized through the esterification of unsaturated palm fatty acid distillate (USFA PFAD) with polyhydric alcohol, trimethylolpropane (TMP) in the occurrence of sulphuric acid catalyst. The optimization process was conducted by using D-optimal design of the response surface methodology (RSM). The results showed that the highest yield percentage of resultant polyol ester, USFA-TMP ester was obtained at $96.0 \pm 0.5\%$ with $99.9 \pm 0.9\%$ of tri-ester selectivity. These were obtained at the esterification optimal condition at reaction temperature of 150 °C for 6 h with 5% H_2SO_4. The polyol ester chemical structure was characterized by using spectroscopy analysis techniques of infrared (FTIR), proton (^{1}H) and carbon (^{13}C) nuclear magnetic resonance (NMR). The resultant USFA-TMP ester recorded viscosity index of 163, pour points at −45 °C, flash points at 298 °C, and thermal oxidative stability temperatures at 215 °C. I was found that the ester product as a Newtonian fluid with viscosity grade lubricant ISO VG 46. In overall, the resultant polyol ester has shown good lubrication properties that make it conceivable to be used for many industrial green biolubricant applications.

Keywords. D-optimal design, Esterification, Green biolubricant, Trimethylolpropane, Unsaturated palm fatty acid distillate.

Published online: 26 April 2022

1. Introduction

Transportation and industrial sectors are now using lubricants based on plant oils as its renewable resource [1]. Since products based on plant oil are less toxic and friendly to the environment, their

* Corresponding authors.

waste disposal will less delinquent to the surrounding. Erhan *et al* [2], Salimon *et al* [3], Srivastava and Sahai [4] noted that plant oils could not be used on its own as a base stock for lubricants, as they were thermally and cold-flow naturally unstable. Therefore, plant oil-based oleochemical esters could be improved upon these characteristics or to be converted into plant oils-based polyolesters. Trimethylolpropane (TMP) and pentaerythritol (PE) are the examples of the polyhydric alcohols used to produce polyolesters for the industrial green biolubricants application [5–8]. The advantages of these polyolesters for biolubricants application are due to the good lubrication properties such as excellent fluidity at low temperatures, high in thermal oxidation stability, viscosity index and volatility. Although they are not meant for extremely high temperatures biolubrication application, they can still be used in more moderate conditions [9–11].

Monounsaturated fatty acid-based biolubricants have advantages over the saturated fatty acid-based lubricants in terms of low cloud point and pour point, better wear protection performance and moderate viscosity index [3,12]. Plant oils in the same sense, high degree of unsaturation poses a better pour point compare to the plant oils with less degree of unsaturation [13]. Therefore, fatty acid composition of specific interested plant oil being used as raw materials in the production of biolubricants should be "know-how" selected. Non-edible oils and waste oils are among researchers of interest to be known prior the production and formulating of good green biolubricants.

The refining process of crude palm oil (CPO) produces by-product or waste known as palm fatty acid distillate (PFAD). PFAD is a semi-solid at room temperature and turn to liquid on mild heating. It colours change from light brown to darker brown liquid upon melt. PFAD comprises mixtures of palm fatty acid (PFAs) (>80%), nonlipids and impurities. These large amounts of PFAs in PFAD were recovered from the deodorization process. Oleochemical industries have used PFAD as the raw materials for an intermediate product to make plastic, animal feed, and for medium-grade cleaners. Some researchers have reported the promising PFAs extracted from PFAD for biodiesel production [14–18].

PFAD comprises palmitic acid and oleic acid as the major saturated and unsaturated FAs composition, respectively. Its major fatty acids are the same as the major fatty acid composition in CPO. The remaining components are partial glycerol and nonlipids substances such as unsaponifiable matters, vitamin E, sterols, squalene, and volatile substances [19–21]. Numerous researchers have analysed the chemical composition of PFAD. Malaysian PFAD samples showed the major fatty acid composition were $45.7 \pm 1.3\%$ of palmitic ($C_{16:0}$) and $40.2 \pm 1.2\%$ of oleic ($C_{18:1}$) acids, respectively [22,23]. Surveys on the characteristics and properties of PFAD from Malaysia refineries have been conducted by Ping and Yusof (2009) [24] and the results show PFAD consist of more than 80% fatty acids comprises of myristic; $C_{14:0}$ (1.2%), palmitic; $C_{16:0}$ (46.9%), palmitoleic; $C_{16:1}$ (0.15%), stearic; $C_{18:0}$ (4.3%), oleic; $C_{18:1}$ (36.7%), linoleic; $C_{18:2}$ (9.1%), linolenic; $C_{18:3}$ (0.3%), arachidic; $C_{20:0}$ (0.2%) and others (0.1%). This study seems to be in line with the findings by Jumaah *et al* [25] and Baharudin *et al* [26], who noted that palmitic acid (47.1%) was the dominant fatty acid in the Malaysian PFAD, followed by oleic acid (36.6%) and linoleic acid (9.6%), respectively. Beside that PFAD consists of 14.4% glycerol, 0.5% vitamin E, 0.8% squalene, 0.4% sterols and 2.2% others [27,28].

The development of specific biolubricants industrial application has attracted many researchers to isolate and separate saturated palm fatty acids distillate (SFA-PFAD) and unsaturated palm fatty acids distillate (USFA-PFAD). For example, the separation of USFA-PFAD from PFAD through low temperature methanol solvent recrystallization (LTSC) has produced significant difference in unsaturated fatty acids composition in its liquid fraction. Under the optimum separation conditions, the percentage of USFA-PFAD in liquid fraction was determined to be 93% and 7% of SFA-PFAD with 48% yields. Oleic acid as the main unsaturated fatty acid constituent surged from 37.6% in PFAD to 76% in USFA-PFAD, while main constituent of saturated palmitic acid declined from 49% in PFAD to 6.2% in USFA-PFAD [25].

To date, there was no single work has been reported the use of USFA-PFAD to produce available or high-end oleochemical products such as polyol ester based biolubricant. Therefore, our aim of the research was to utilize the USFA-PFAD obtained from the separation process by using LTSC technique, in the synthesis of green biodegradable biolubricants base stock oil production through the esterification

process. The unsaturated oleic acid was chosen as the representative of USFA-PFAD due to its major composition (76%) with the ratio of 4.4:1 to linoleic acid (17%). In this paper, the esterification reactions between the USFA-PFAD with selected polyhydric alcohol of trimethylolpropane (TMP) to produce polyol ester, USFA-trimethylolpropane (USFA-TMP) as potential base stock for green biodegradable biolubricants. Polyol ester-based TMP biolubricants has been reported as highly potential versatile green product for the replacement of the petroleum-based lubricants [1,7,17]. The process was optimized by using Response Surface Methodology (RSM) of D-optimal design software to produce high yield and tri-ester selectivity of the final polyol ester product, USFA-TMP. The effects of different reaction parameter conditions toward the reaction responses of the percent yields and the tri-ester selectivity were optimized and resolute by using D-optimal design approach. The results of this study could portray that the high-end USFA-PFAD based polyol ester biolubricant can be produced through conventional esterification strategy to large-scale esters production, which is an encouraging approach to achieve cost-effective polyol ester production from palm oil processing by-product of palm oil processing.

2. Materials and method

2.1. *Materials*

Unsaturated palm fatty acid distillate (USFA-PFAD) represented by oleic acid (76%) was obtained from PFAD separation by low-temperature methanol crystallization [25]. Alcohol used was trimethylolpropane (TMP) purchased from Sigma Aldrich. All analytical grade chemicals, e.g., sulfuric acid, methanol and sodium hydrogen carbonate were used without further purification.

2.2. *Structural characterization analysis*

The structure of synthesized ester was determined and confirmed by using Nuclear Magnetic Resonance (FT-NMR) and Fourier Transform infrared spectroscopy (FTIR). FT-NMR JEOL-ECP 400 spectrometer (^{1}H and ^{13}C NMR) was used for molecular structural analysis. The spectra were recorded by using $CDCl_3$ solvent. Perkin Elmer Infrared Spectrophotometer was used to record the FTIR spectra between wavenumber of 700 and 4000 cm^{-1}. The ester composition was analyzed by Shimadzu GC-17A Gas Chromatography furnished with Flame Ionization Detector. High temperature column of DB-5HT (30 m × 0.25 mm × 0.25 μm) was used to separate the sample eluent. In a vial of 10 mL, 0.5 mL ester sample was diluted with 5 mL GC grade ethyl acetate solvent prior to the GC injection. The GC oven was first set at initial temperature of 100 °C for 1 min. The oven temperature was then increased by a step increment of 5 °C/min to 380 °C and allowed constant for 25 min. The GC column temperature was then attuned at 100 °C and amplified to 380 °C with a 5 °C/min temperature rate increments. The column temperature was kept constant at 380 °C for 20 min. The injector and detector temperatures were set at 380 and 400 °C, respectively. Helium was used as the GC carrier gas system at a flow rate of 1ml/min. The ester sample (1 μL) was used for the GC-FID analysis according to Nowicki *et al* [28]. The ester peaks were recognized by the retention times comparison to the authentic standards.

2.3. *Lubrication characterization analysis*

The lubrication characteristics of the esters were determined according the American Society for Testing Materials standards (ASTM). The ASTM D-97 was used for pour point [29] and ASTM D-93 for flash point determination [30]. The pressurized Differential Scanning Calorimeter was used for thermal oxidative stability determination [31]. A controlled DSC822e Metter Toledo Differential Scanning Calorimeter was used to determine the oxidative property. The instrument was set with a temperature sensitivity of 0.2 $mV{\cdot}cm^{-1}$ and maximum sensitivity of 5 $mV{\cdot}cm^{-1}$. A hermetically sealed type aluminum pan was used to place a 3.0 mg sample with a pinhole lid for sample interaction with the reactant gas (dry air). The hole greatly restricts the volatilization of the ester sample by controlled diffusion of the gas through while still allowing for saturation of the liquid phase with air. Less than 1 mm film thickness was required to warrant appropriate ester-air interaction and to eradicate any inconsistency in the result due to gas diffusion limitations. The unit was first temperature calibrated using indium metal (melting point of

156.6 °C) at 10 °C·min^{-1} heating rate. Dry air was harried in the unit at a persistent pressure of 3450 kPa with a scanning rate of 10 °C·min^{-1} throughout the experiment. The peak onset (T_o) temperature and height (T_p) were calculated from the exotherm plots whereas the induction time (I_t) was restrained from an isothermal scanning rate. Kinematic viscosity was measured by using Anton Paar Physical MCR 301 Rheometer Instruments (Germany). The kinematic viscosity and viscosity index (VI) were premeditated according to ASTM D 2270-93 method [32]. In a hot plate heater set at 40 and 100 °C, 1 ml of sample was used for the measurement. According to ASTM reference table, the L and H values were calculated by using the kinematic viscosity value at 100 °C. The viscosity index of USFA-TMP ester was then calculated from the L and H values, and the kinematic viscosity at 40 °C (U) by using (1):

$$\text{Viscosity index} = \frac{L-U}{L-H} \times 100. \quad (1)$$

Where; Viscosity index was calculated in cSt, U: kinematic viscosity at 40 °C of the ester, L: kinematic viscosity at 40 °C of an ester of zero viscosity index having the same kinematic viscosity at 100 °C as the ester, H: kinematic viscosity at 40 °C of an ester of 100 viscosity indexes having the same kinematic viscosity at 100 °C. The viscosity index was reported as a mean ± SD of triplicate determinations.

2.4. *Esterification reaction*

Biolubricant was synthesized from the esterification reaction between USFA with high degree polyhydric alcohols, TMP according to Jumaah *et al* [15]. In a flask with a reflux condenser and three necks, USFA-PFAD (0.037 mol, 104.7 g) was mixed with 1 mole trimethylolpropane (0.037 mol, 5 g) at molar ratio of 3.5:1 in Dean-Stark distillation unit. The esterification was carried out in oil bath equipped with stirrer magnetic heater at reaction temperature between 110–160 °C. At required temperature, 2% concentrated H_2SO_4 (as weight percentage of USFA-PFAD) was added at specific reaction time. About 20–30 mL of toluene as azeotrope distillation agent was then slowly added to the mixture during the esterification process. After the reaction end, the flask was allowed to cool at room temperature, followed with the removal of toluene by using rotary evaporator at 100 °C. The reaction product was dissolved into 100 ml of ethyl acetate and transferred into a 150 ml separation funnel. About 30 ml of saturated sodium bicarbonate ($NaHCO_3$) was added to the separation funnel and shaken for neutralization of the remaining USFA-PFAD and acid catalyst. The funnel separator was left until two layers formed. The aqueous layer at the bottom was removed, leaving the organic layer. The organic layer was further cleaned three times with $NaHCO_3$ solution. Subsequently, the organic layer was further washed with 20 ml of 26% saturated sodium chloride (NaCl) and 20 ml of distilled water twice to avoid formation of emulsion. Once the two layers were formed, the bottom aqueous layer was removed. The washing process was repeated until the organic layer with pH7 was obtained. Then, the sample was poured into a round flask and connected to a rotary evaporator apparatus (90–100 °C) to remove any excess toluene and unreacted alcohol. The remaining water in the sample was absorbed by sodium sulfate (Na_2SO_4) over night and filtered off. The ethyl acetate solvent was then removed by rotary-evaporator at 80 °C, producing a yellowish viscous liquid polyol ester product.

2.5. *Experimental design and statistical analysis*

Many studies used response surface methodology (RSM) to optimize of the intended procedure such as in the esterification process of the polyhydric alcohols with fatty acids. D-optimal design is one of the reliable common RSM mode of optimization. It is generated for both quantitative and qualitative factors with multi-factor experiments. It is constructed to diminish the total comprehensive variance of the predictable regression constants. As a result, the "optimality" of a specified D-optimal design is model reliant on. In this study, the optimization of esterification reactions of USFA-PFAD with TMP by using D-optimal design will be cost operative by reducing the amount of experimentation numbers. To assess the esterification reaction, the D-optimal design was applied with the Design-Expert version 11 (Stat-Ease, USA) software. Three independent variables, acid catalyst (X_1), esterification time (X_2), and esterification temperature (X_3), The self-determining variables denoted as X_1 for H_2SO_4 (%) concentration (as a percentage of the weight of USFA-PFAD), X_2 for esterification time (h) and X_3 for esterification temperature (°C) were used to conduct the RSM. This is be-

Table 1. Parameters and levels for D-optimal design for the esterification reaction of the synthesized USFA-TMP

Independent variables	Factor	Variable levels		
		−1	0	+1
H_2SO_4 catalyst amount (%)	X_1	1	3.20	5
Reaction time (h)	X_2	3	4.38	6
Reaction temperature (°C)	X_3	110	130	150

cause these variables affected the reaction response of yield % and tri-ester %. On the other hand, through the manual one factor optimization has shown that the molar ratio of reactants was insignificant affect toward the reaction responses (unpublished data). The low value (−1) and high value (+1) of X_1, X_2 and X_3 as can be realised from Table 1 were comparable with the series set of each parameter: 1–5% for X_1, 2–6 h for X_2 and 110–150 °C for X_3. The ester yield, Y_1 (%) and composition of triester Y_2 (%) as (2) and (3) were determined.

$$\text{Ester yield} = \left[\frac{\text{Weight final}}{\text{Weight reactants}}\right] \times 100 \quad (2)$$

$$\text{Selectivity of triester} = \left[\frac{\text{Area tri}}{(\text{Area di} + \text{Area tri})}\right] \times 100. \quad (3)$$

The D-optimal design was generating 18 experimental runs, as presented in Table 2.

Table 2. Design of experiment runs parameters and response of the USFA-TMP synthesis of Biolubricant base stocks

Experiment run	Variables levels, X			Responses, Y	
	X_1	X_2	X_3	Y_1	Y_2
1	5.00	4.00	150.00	92	89
2	5.00	2.00	150.00	56	82
3	1.00	6.00	110.00	70	67
4	5.00	2.00	110.00	49	59
5	1.00	6.00	150.00	91	94
6	3.00	4.00	110.00	67	72
7	5.00	6.00	110.00	90	90
8	1.00	2.00	150.00	56	61
9	3.00	6.00	130.00	82	75
10	1.00	2.00	110.00	43	28
11	4.00	3.00	130.00	64	55
12	5.00	6.00	150.00	96	99
13	1.00	4.00	130.00	69	40
14	3.00	2.00	150.00	51	66
15	1.00	6.00	110.00	75	47
16	5.00	6.00	110.00	91	90
17	1.00	6.00	150.00	93	93
18	1.00	2.00	110.00	44	30

Notes: X_1 = Acid catalyst (%); X_2 = Time (h); X_3 = Temprature (°C); Y_1 = Yield (%); Y_2 = Tri-ester (%).

3. Results and discussion

3.1. *Esterification reaction of USFA*

Varieties of acid catalysts have been used for the esterification of plant oils/fatty acids to biodiesel or fatty acid-based esters. Heterogenous acid catalysts such as hydrophilic sulfonated silica (SiO_2–SO_3H) [29], heterogeneous magnetic acid catalyst of MoO_3/$SrFe_2O_4$ [30], propyl sulfonic acid-functionalized silica, SiO_2–Pr–SO_3H [31–33], Lewis acids such as scandium(III) triflate [34] and quaternary ammonium salts, Aliquat 336 (ionic liquid) or $[(Bu_4^n N)(BF_4)]$ [29] are among versatile acid catalysts due to their performant, repeatability and clean process. On the other hands among good homogenous acid catalysts used for the esterification process are hydrochloric acid (HCl), sulphuric acid (H_2SO_4) and p-toluene sulfonic acid. In this study the esterification reaction was performed under the influence of strong acid catalyst, H_2SO_4 to form resultant polyol ester of USFA-TMP. The mechanism of the acid-catalysed esterification was well known [35]. In this esterification process required strong acid catalyst and therefore there is no a self-catalytic effect due to the weak carboxylic acid dissociation. The carbonyl carbocation group of fatty acids reacted with one of trimethylolpropane (TMP) OH group. The same process will occur with the second and the third trimethylolpropane OH groups. The esterification starts with a proton donation (H^+) from an acid catalyst. This proton (H^+) was attacked by a single pair of electrons of the carbonyl group of fatty acid, and a bond was formed with the carbonyl oxygen (intermediate resonance and reactive to attack). The electrophilic capacity of carbonyl carbon increased, which caused a nucleophilic attack by the

oxygen of the alcohol, followed by deprotonation to form an active intermediate compound. Protonation of one of the hydroxyl groups of this intermediate compound formed oxonium ion (oxygen cation with three bonds). Removal of water molecule from the oxonium ion, followed by deprotonation process to produce polyol ester. The schematic mechanism reaction and chemical structure of polyol ester USFA-TMP ester is shown in Figure 1.

3.2. *Response surface methodology optimization*

The esterification reaction of USFA-PFAD with TMP to synthesize biolubricant was optimized by using D-optimal design of Response Surface Methodology (RSM). The percent yields (Y_1) of resultant USFA-TMP ester and the percentage or selectivity (Y_2) of tri-ester in the product were investigated. The possessions of dissimilar progression conditions on the responses were also optimized and determined. The response factors and values were determined via initial screening steps. In this step, parameters of acid catalyst (X_1), reaction time (X_2), and reaction temperature (X_3) were used to represent the experimental variables, respectively. Each variable was evaluated by fluctuating their values within a lowest and highest value, as presented in Table 1. The reaction responses experimental data of the reaction yield (Y_1) and tri-ester selectivity percentage (Y_2) of the sample are shown in Table 2.

3.3. *D-optimal design model fitting*

A quadratic polynomial model signifies the relationship between the self-determining variables and the percentage of the yield of ester and percentage of tri-ester selectivity in USFA-TMP ester. The D-optimal model using the 18 experimental results data has calculated and produced basis correlation equation to estimate the variable coefficients toward the reaction responses of ester yield and ester selectivity as quote in (4) and (5).

$$\begin{aligned}&\text{USFA-TMP yield } (Y_1)\\&= +71.60 + 4.25X_1 + 18.53X_2 + 6.10X_3\\&\quad + 2.20X_1X_2 - 2.02X_1X_3 + 1.01X_2X_3 + 4.69X_1^2\\&\quad - 9.81X_2^2 + 3.42X_3^2 \qquad (4)\end{aligned}$$

$$\begin{aligned}&\text{USFA-TMP selectivity } (Y_2)\\&= +59.25 + 11.25X_1 + 14.70X_2 + 11.18X_3\\&\quad - 1.21X_1X_2 - 5.10X_1X_3 + 0.2056X_2X_3 - 5.69X_1^2\\&\quad - 2.14X_2^2 - 13.45X_3^2. \qquad (5)\end{aligned}$$

The coefficient estimate represents the expected change in response per unit change in factor value when all remaining factors are held constant. The intercept in an orthogonal design is the overall average response of all the runs. The coefficients are adjustments around that average based on the factor settings. When the factors are orthogonal the variance inflation factor (VIF) are one. VIFs greater than one indicates multi-collinearity, the higher the VIF the more severe the correlation of factors. All VIFs values in (4) and (5) are less than 10 which are tolerable.

The regression coefficients and the model's analysis of variance (ANOVA) for the yield percent (Y_1), and tri-ester selectivity percent (Y_2) are shown in Tables 3 and 4, respectively. The R-squared values, which assess the response variability reduction, were based on the independent variables; a model with good fit has a high R^2 correlation value. The fit of a regression model can also be assessed using the adjusted R-squared correlation [36]. The model was significant concerning Y_1 and Y_2, with R-squared values of 0.9522 and 0.9354, respectively. R-squared values for all responses show a respectable connection among the predicted values and the actual outcomes of the dependent variable's resultant from the model [37].

Furthermore, as regards the percentage of reaction yield (Y_1), the 0.9522 R-squared value indicates that about 95% of the dissimilarity on the response can be explicated by the model, and the model did not describe only 5% of the variations. The adjusted R-squared value (adj. R-squared = 0.8985) shows that the model is noteworthy, and its value is slightly adjacent to the R-squared value of 0.9522. Also, regarding the percentage of tri-ester selectivity (Y_2), the 0.9354 R-squared value indicates that 93.5% of the variation on the response can be explained by the model leaving only 6.5% of response variations not described.

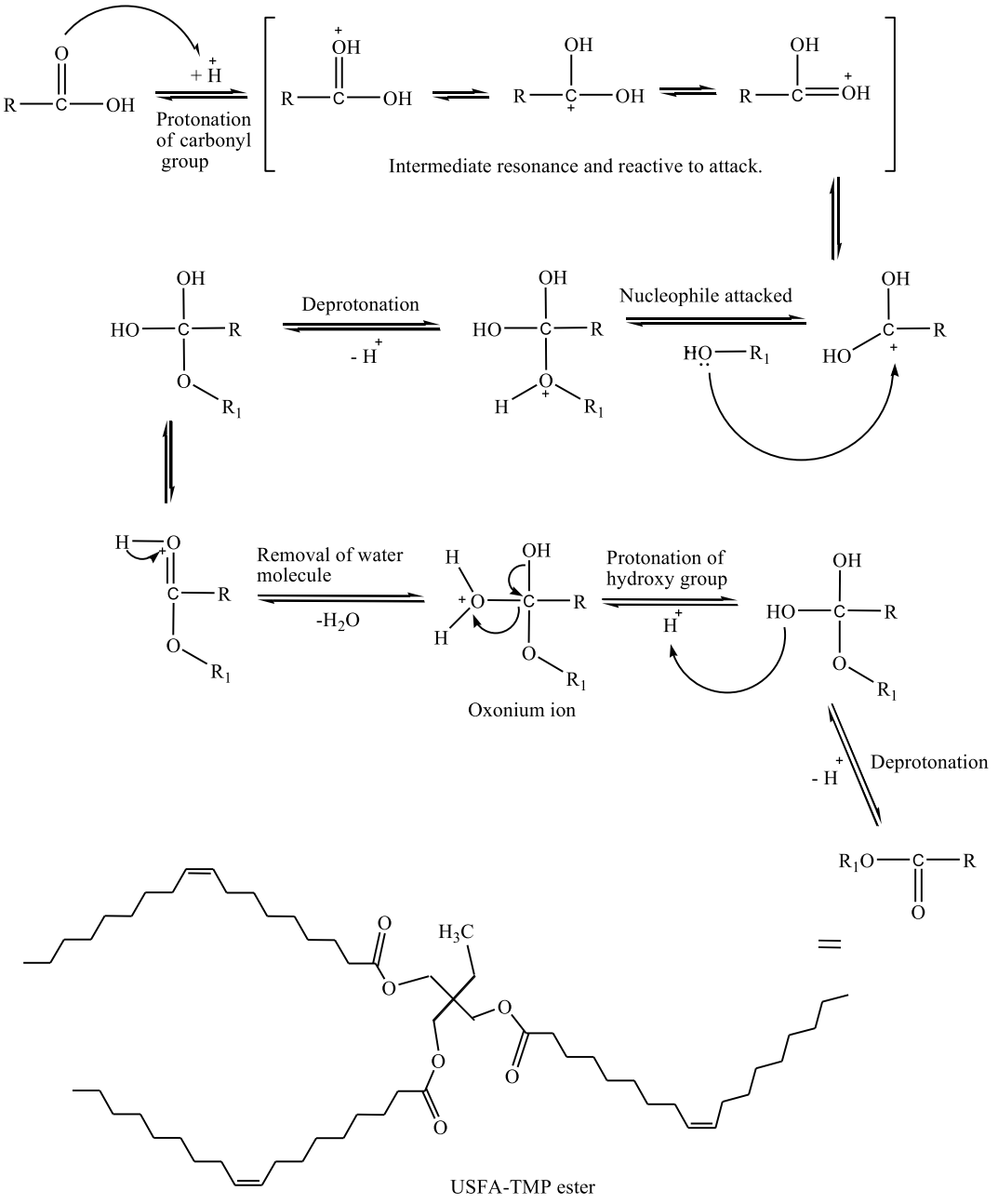

Figure 1. Schematic reaction of esterification to synthesis and molecular structure of USFA-TMP ester.

Meanwhile, 0.8628 was the adjusted *R*-squared value, showing that the model is important, and its value is somewhat close to the *R*-squared value of 0.9354.

The quadratic regression constant was accomplished by using a nominal squares method to envisage quadratic polynomial models for the USFA-TMP tri-ester yield (Y_1) and selectivity of USFA-TMP tri-ester (Y_2) as shown in Table 3. Table 3 presents the combined ANOVA data of yield of USFA-TMP tri-ester and Selectivity of USFA-TMP tri-ester. The model with sum of square value of 5691.37 for the yield (Y_1) and of 8110.83 for tri-ester (Y_2) showed reasonable variance to the mean value with adequate mean square of 632 and 901, respectively.

Table 3. ANOVA analysis data and a regression model for synthesis of USFA-TMP

Responses	ANOVA value	Factors and their interaction										
		Model	X_1	X_2	X_3	X_1X_2	X_1X_3	X_2X_3	X_1^2	X_2^2	X_3^2	Lack of fit
USFA-TMP yield	Sum of squares	5691.4	232.0	4399.7	529.2	54.1	49.8	12.4	46.4	202.7	19.9	58.1
	d*f*	9	1	1	1	1	1	1	1	1	1	4
	Mean square	632.4	232.0	4399.7	529.2	54.1	49.8	12.4	46.4	202.7	19.9	14.5
	F-value	68.76	25.23	478.40	57.55	5.88	5.4	1.35	5.04	22.04	2.17	3.75
	P-value	<0.0001	0.0010	<0.0001	<0.0001	0.0415	0.0484	0.2784	0.0549	0.0016	0.1786	0.1144
	Status	***	***	***	***	***	***			***	***	
	$R^2 = 0.9522$, adjusted $R^2 = 0.8985$, predicted $R^2 = 0.9904$, adequate precision = 14.768											
	Regression model	USFA-TMP yield (Y_1) = $71.60 + 4.25X_1 + 18.53X_2 + 6.10X_3 + 2.20X_1X_2 - 2.02X_1X_3 - 9.81X_2^2 + 3.42X_3^2$ (6)										
USFA-TMP selectivity	Sum of squares	8110.8	1622.1	2770.1	1775.6	68.2	9.6	650.9	16.4	315.9	0.514	182.3
	d*f*	9	1	1	1	1	1	1	1	1	1	4
	Mean square	901.2	1622.1	2770.1	1775.6	68.2	9.6	650.9	16.4	315.9	0.514	45.6
	F-value	18.74	33.72	57.59	36.92	1.42	0.1999	13.53	0.3400	6.57	0.0107	9.01
	P-value	0.0002	0.0004	<0.0001	0.0003	0.2679	0.6667	0.0062	0.5759	0.0335	0.9202	0.1539
	Status	***	***	***	***			***		***		
	$R^2 = 0.9354$, Adjusted $R^2 = 0.8628$, Predicted $R^2 = 0.9803$, adequate precision = 11.331											
	Regression model	USFA-TMP selectivity (Y_2) = $59.25 + 11.25X_1 + 14.70X_2 + 11.18X_3 + 0.2056X_2X_3 - 2.14X_2^2$ (7)										

Note X_1: Catalyst amount, X_2: Reaction time, X_3: Reaction temperature, ***: Significant at $P < 0.05$% level.

Table 4. Optimization criteria for dependent variables

Variables	Goal	Lower limits	Upper limits
Acid catalyst (%) (X_1)	In the range	1	5
Esterification time (h) (X_2)	In the range	2	6
Esterification temperature (°C) (X_3)	In the range	110	150
Yield (%), (Y_1)	Maximize	43	96.2
Tri-ester (%), (Y_2)	Maximize	28	99.9

The respective model *F*-values of 68 for yield (Y_1) and 18 tri-ester % (Y_2), implied that the model is highly significant. These indicated that the model can be used to elaborate on the synthesis of USFA-based trimethylolpropane tri-ester with an adequate precision of 14.768 and 11.331. The lack of fit for all models shown by *F*-values of 3.75 for ester yield (Y_1) and 9.01 for tri-ester (Y_2) that showed about 11.4% and 15.4% chance for the lack of fit due to the noise, respectively [36]. These indicate the models are insignificant relative to the pure error. Analysis of variance (ANOVA) was further achieved to determine the consequence and the fitness of the quadratic model. The final equations for yield of USFA-TMP tri-ester (Y_1) and selectivity of USFA-TMP tri-ester (Y_2) in a quadratic model as shown in (6) and (7), respectively. It is known that the numerical simulations have been proved to be useful to find safe and efficient operating conditions through a Pareto chart approach and tested with some laboratory experiments [38]. However, D-optimal model design used in this study use probability of seeing the observed *F*-value (Prob > *F* value) if the null hypothesis is true (there are no factor effects). Small probability values call for rejection of the null hypothesis. The probability equals the integral under the curve of the *F*-distribution that lies beyond the observed *F*-value. Prob > *F* value is very small (less than 0.05 by default) then the source has tested significant. Significant model terms probably have a real effect on the response. Significant lack of fit, on the other hand, indicates the model does not fit the data within the observed replicate

variation.

A Prob-test was focussed to evaluate the coefficients. Vastly significant values of P ($P < 0.01$) were attained for the percentage yield (Y_1) and (X_1), (X_2), and (X_3), which represent the linear and quadratic forms of an acid catalyst, reaction time and reaction temperature, respectively. Meanwhile, all the variables (X_1, X_2, and X_3) in linear and quadratic forms were also initiated to have a significant connection ($P < 0.01$) with the tri-ester (Y_2), as shown in Table 3. Comparative to the pure error, the lack of fit of all models showed F-values of 0.1144 and 0.5394, and so is predictable insignificant [36]. Therefore, the experimental values had a respectable fit with the regression model [39].

3.4. *Model adequacy check*

An adequacy check was employed to check the model accuracy. This is important because a valid mathematical model with high accuracy would enhance the real process while an inaccurate model may give poor or false results [40]. The plot of adequacy check of studentized residuals against the predicted percentage of the yields of ester and the percentage tri-ester can be seen in Figure 2a and b, respectively. The studentized plots of residuals against values of fitted response show catered random distribution of points around the boundary of 0 ± 4. This earning that for all response values, the discrepancy is constant. It can, therefore, be established that the models are appropriate for application without any alterations to decrease the scatter [38].

Instead, the distribution of plots of the actual data compared to the predicted values of the yields of ester, and percentages of tri-ester are shown in Figure 3a and b, respectively. The preliminary experimental results in Table 2 were used as actual data, while the model provided the predicated data. It is discernible that all data points gathering around the line, which designates the models fit with the empirical data. Therefore, the models should be able to predict ester yields and the percentages of tri-ester that concur curiously with the real experimental values. This was statistically confirmed by the values of R^2 and R^2adj, as shown in Table 3, indicating a reliable prediction of results. Later, it was required to progress to the next stage of investigation using the optimization tool.

3.5. *Optimization conditions and response surface analysis*

The esterification of USFA-PFAD with TMP to produce USFA-TMP ester involves many variables, the interaction of which is investigated using 3-D response surfaces and contour graphs. The response surfaces of the consequence of an acid catalyst, esterification time, and esterification temperature on the proliferation of yield percentages of ester shown in Figure 4a, b, and c and the same factor in the tri-ester as shown in Figure 5a, b, and c.

The interaction effect between the acid catalyst and reaction time is presented in Figure 4a. The plot demonstrated that the ester yield % was increased from 44 to 96% with an increase in acid catalyst amount from 1 to 5%. The 3D graph shows that thoroughgoing yields % was attained at an acid catalyst of 5% and a temperature of 150 °C (Figure 4b). The combined effect of the reaction time and temperature demonstrated that the ester yield % was improved with an increase in time (Figure 4c). The results demonstrated that the determining reaction variable of both acid catalyst amount and reaction were significantly affect the ester yield %. This is in agreement with finding for di-TMP tetraester CPKO [41]. It was observed that the maximum yield at 96% was obtained at an acid catalyst amount of 5% and reaction time of 6 h.

The interaction consequence among acid catalyst and time towards the tri-ester selectivity is revealed in Figure 5a. The 3D plot displays that increasing tri-ester selectivity from 28% to nearly optimum in relation of increasing acid catalyst from 1% to 5%. In essence, the tri-ester selectivity composition percentage of USFA-TMP ester continuously improved up to 78% at 5% acid catalyst. The outcome of acid catalyst and temperature relation directed to slight increase of tri-ester % with an increase in acid catalyst and temperature (Figure 5b). The impact of reaction time and temperature also occasioned in an increase of tri-ester % up to 99.9% with an increase in the reaction time and temperature (Figure 5c). The results demonstrated that the determining reaction variable of both reaction time and reaction temperature were significantly affect the tri-ester selectivity [15]. The highest tri-ester selectivity of 99.9% was observed for reaction time of 6 h at 150 °C and 5% acid catalyst.

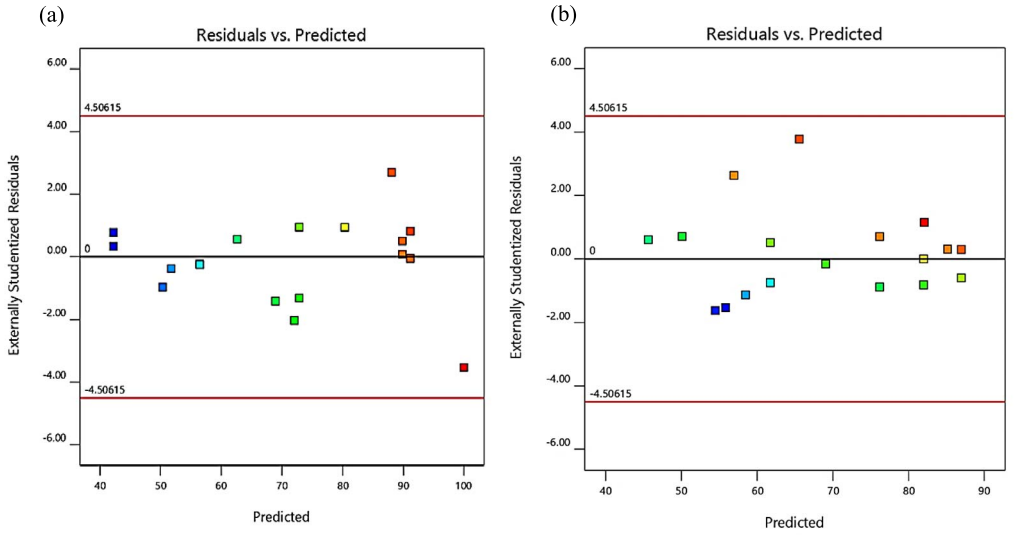

Figure 2. Studentized residuals against predicted value for the USFA-TMP ester percentages of the yield (a) and tri-ester (b).

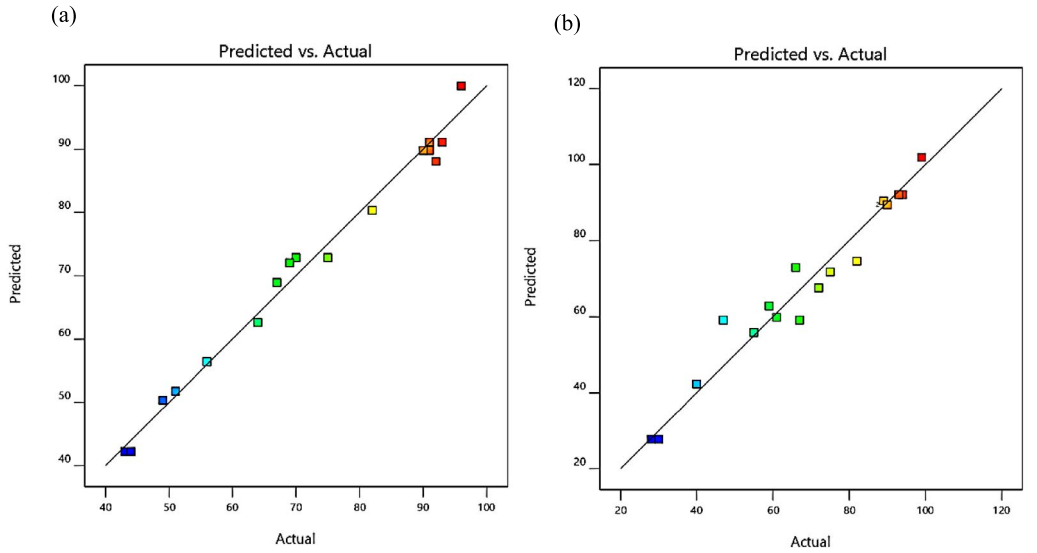

Figure 3. Regression plot of predicted values versus actual data of USFA-TMP ester percentages of the yield (a) and tri-ester (b).

3.6. *Validation model and confirmation of experiment*

The conditions for optimality for the response variables were found, which demands the predicted model be used, so the model was validated using a desirability function. The optimal conditions include yield of ester, and the percentage of tri-ester with maximum values, as shown in Table 4 and Figure 6. A justification test was carried out to approve the rationality of the predicted model. Optimum conditions were conducted in triplicate, comprising acid cata-

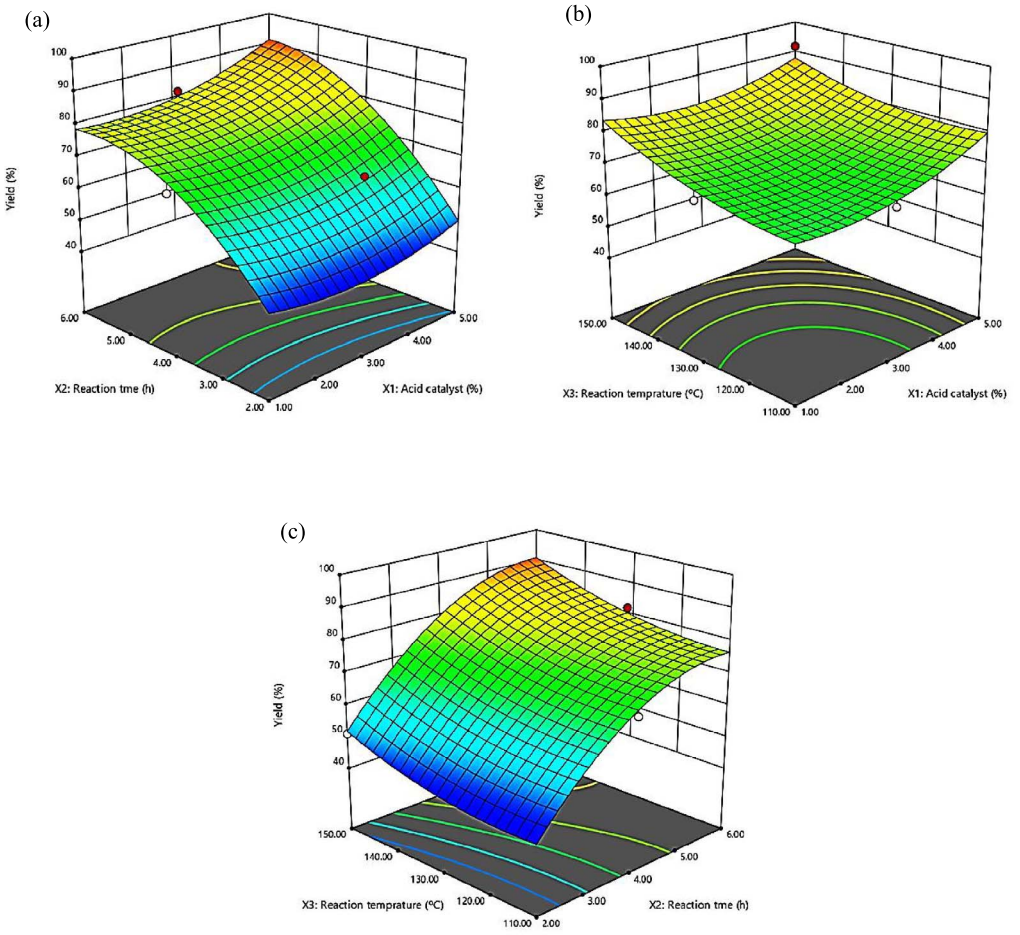

Figure 4. Three-dimensional response surface (3D) of yield (%) (Y_1) as a function of acid catalyst (X_1, %) and time (X_2, h) (a), acid catalyst (X_1, %) and temperature (X_3, °C) (b), time (X_2, h) and temperature (X_3, °C) (c).

lysts of 5%, esterification time 6 h, and esterification temperature of 150 °C. As shown in Table 5, the yield of approximately 96 ± 0.5% and tri-ester 99 ± 0.9% were obtained at the optimized condition for the esterification of USFA-PFAD with TMP.

Results from the study showed that the RSM optimization by using D-optimal design has high efficiency to predict and select an optimum condition for the esterification reaction between USFA-PFAD and TMP. The resultant ester yield was increased up to 96 ± 0.5% and tri-ester composition selectivity was increased up to 99 ± 0.9%. These results were par better as compare to manual optimization method where gave tri-ester yields of 91% with 87% tri-ester selectivity, respectively, as shown in Table 5.

3.7. *USFA-TMP ester structural characterization*

The chemical structure of optimized synthesized USFA-TMP ester was analysed and verified by using FTIR, NMR (^{1}H and ^{13}C) spectroscopy and GC-FID chromatography. FTIR functional group analysis was conducted to approve the accomplishment of the esterification reaction. Mainly FTIR was used to verify the existence of ester carbonyl functional group and the disappearance of acid carbonyl functional group (mainly from oleic and linoleic acids). Due to the resemblance of ester chemical structure, the FTIR

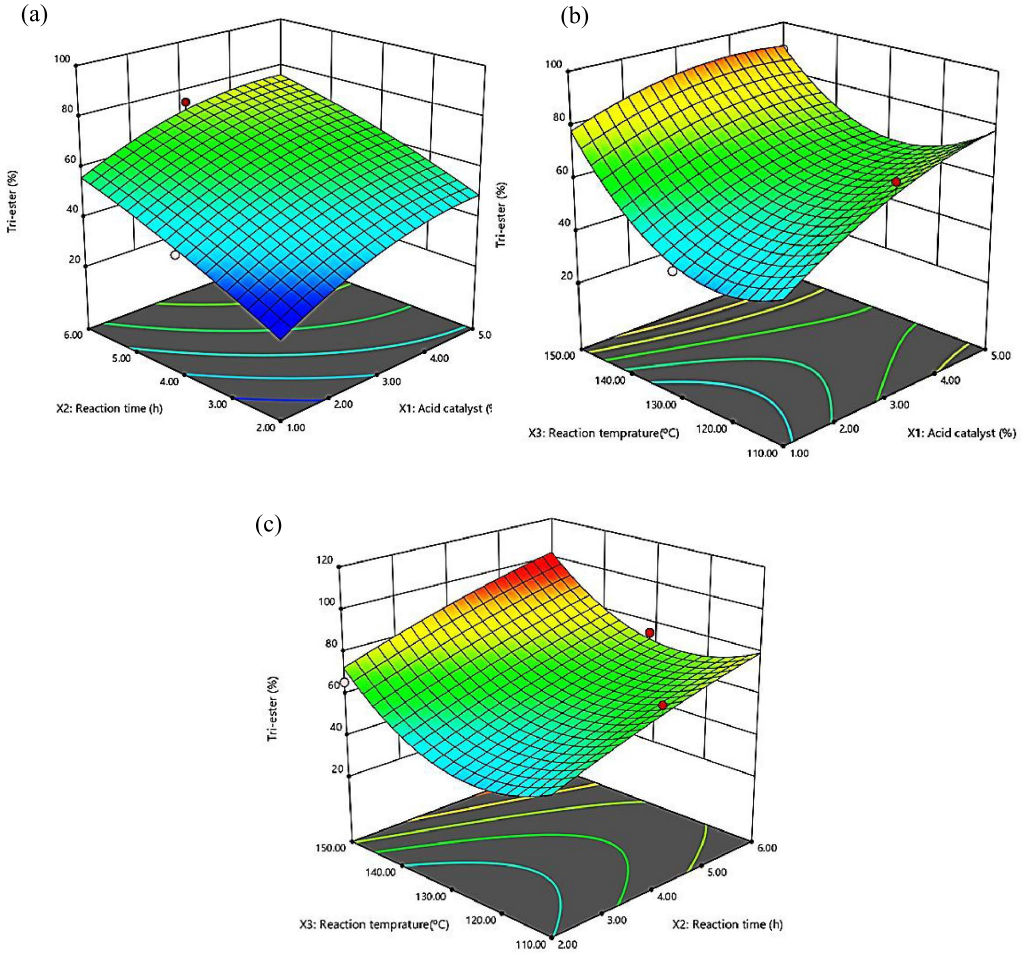

Figure 5. Three-dimensional response surface (3D) of tri-ester percentage (Y_2) as a function of acid catalyst (X_1, %) and time (X_2, h) (a), acid catalyst (X_1, %) and temperature (X_3, °C) (b), time (X_2, h) and temperature (X_3, °C) (c).

Table 5. Result of model validation at the experimental optimum condition (verification test)

Factors	Acid catalyst, (X_1) (%)	Esterification time, (X_2) (h)	Esterification temperature, (X_3) (°C)	Yield (Y_1) (%)	Tri-ester, (Y_2) (%)
Predicted	5	6	150	98.1	99.3
Actual	5	6	150	96 ± 0.3	99 ± 0.7
Manual/classical optimization	2	6	150	91 ± 0.5	87 ± 0.5

spectrum of each of the carbonyl ester exhibits a similar pattern at the same wave number.

Figure 7 displays the FTIR spectra of USFA-TMP ester and USFA-PFAD starting material. The unsaturated aliphatic carbon atoms of fatty acid or ester manifest peaks at 3003–3010 cm^{-1}. The unsaturated alkene carbon atoms of USFA-PFAD and USFA-TMP ester are manifested the peak at 3008 cm^{-1} correlating to the unsaturation −C=C–H bond. The acid carbonyl group ($C{=}O_{acid}$) of USFA-PFAD displayed a peak that appeared at 1704 cm^{-1}. As the USFA-PFAD underwent esterification, the resul-

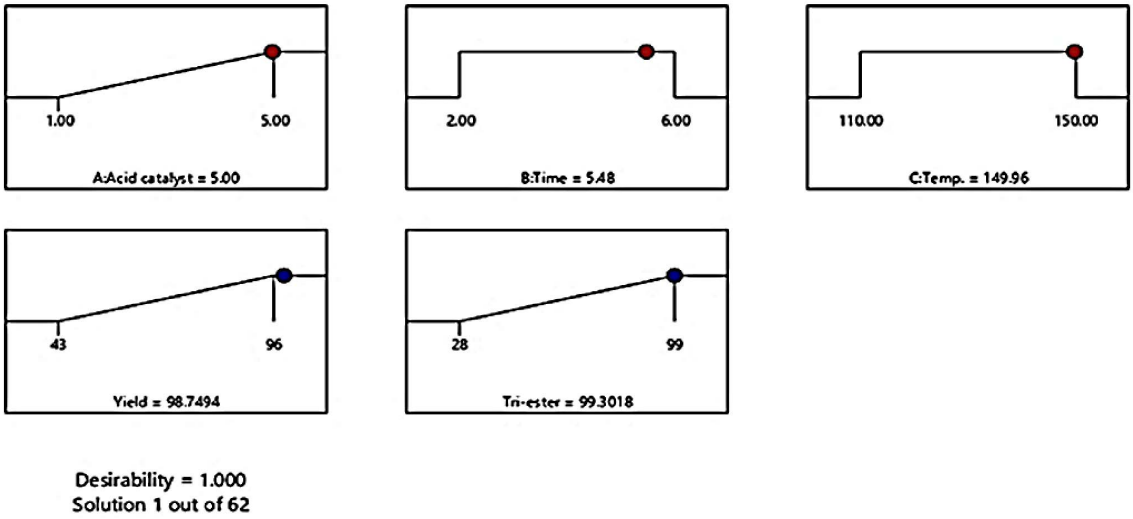

Figure 6. Predicted conditions to produce desirable results of dependent variables using D-optimal design.

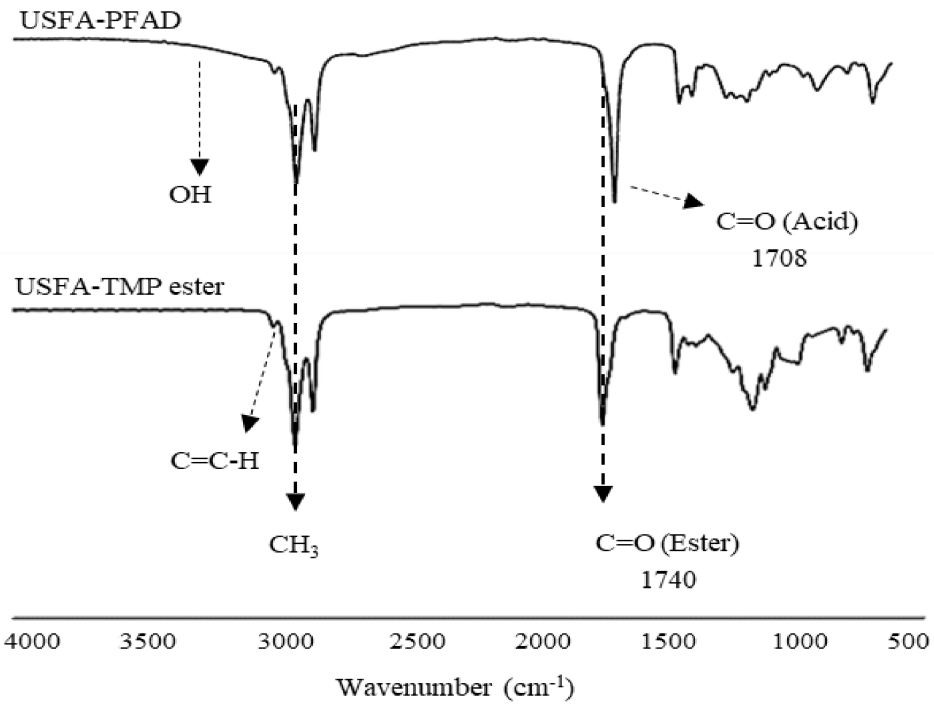

Figure 7. FTIR spectra of USFA-PFAD and synthesized USFA-TMP ester.

tant product USFA-TMP ester produced a peak at 1740 cm^{-1} of the ester carbonyl group stretching vibrations ($C{=}O_{ester}$). It can be observed that the unreacted alcohol and acids had disappeared from the final product (ester). The ester spectrum showing that there were no peaks for stretching vibrations

Table 6. The fatty acids composition of USFA and USFA-TMP ester

Fatty acids	USFA	USFA-TMP ester
Myristic acid $C_{14:0}$	0.5	0.2
Palmitic acid $C_{16:0}$	6.2	6.0
Stearic acid $C_{18:0}$	0.5	0.3
Oleic acid $C_{18:1}$	75.6	76.5
Linoleic acid $C_{18:2}$	17.2	17
∑ Saturated fatty acid	7.2	6.5
∑ Unsaturated fatty acid	92.8	93.5

of alcohol (OH) and stretching vibrations of acids (–COOH). This distinguishable difference (complete disappearance peak at 1704 cm^{-1} and the appearance peak at 1740 cm^{-1}) verifies that the given reaction conditions have resulted in a complete esterification process toward USFA-PFAD production. Meanwhile, the visible bands at 1237–1161 cm^{-1} and 2921–2852 cm^{-1} represent the stretching vibration of C–O and the $-CH_3$ groups, respectively.

Highly valuable techniques of ^1H and ^{13}C NMR spectra analysis have great advantage and benefit toward the chemical structure prediction. The combination of the outcomes from FTIR with ^1H and ^{13}C NMR spectra analysis further prove the success of the esterification reaction. The ^1H and ^{13}C NMR spectra of USFA-TMP ester are indicated by Figures 8 and 9, respectively. The disappearance of the ^1H chemical shift of the proton (H) of the carboxylic acid group (–COOH) at 11.0 ppm, and for the alcohol group (–OH) at 4.7 ppm [42], confirmed the success of the esterification reaction. ^1H chemical shift ranges for aliphatic protons ($-CH_2$) was detected, normally at about 1.25–1.56 ppm. However, the two protons of the $-CH_2$–O–C=O ester group shift appeared at about 3.80 to 4.0 ppm [43].

The fatty acids of USFA-PFAD mixture are dominated by oleic acid (76%) and linoleic acid (17%) [25]. It is plausible to predict that the same fatty acid acyls groups recompose in USFA-TMP ester as shown in Table 6. Alkene functional groups can be identified to determine the present of unsaturated fatty acids. The methylene proton signal (–CH–CH–) was lifted to lower frequency at 5.32–5.38 ppm, representing the unsaturated fatty acids in USFA-TMP ester [44].

The ^{13}C NMR spectrum of USFA-TMP ester is shown in Figure 9. The signal at 171.09–174.07 ppm designates the ester carbonyl ($C=O_{ester}$) in USFA-TMP ester. A comparable result assigning a chemical shift of 170–185 ppm to ester carbonyl (C=O) at palm-based polyurethane Awang *et al* [42]. A peak at 60.32–64.14 ppm, signalling $-CH_2$–O–CO–R for carbon atom devoted to the TMP alcohol. Another characteristic signal was observed at 127.87–130.12 ppm, which denotes to the unsaturated carbon atoms (C=C) of unsaturated fatty acids in USFA-TMP ester. Furthermore, a signal at 40.57–42.44 ppm was found to resemble to the quaternary carbon atom of TMP [45]. The aliphatic carbon chain atoms of $-CH_2$ peaks were identified from 22.16–36.46 ppm. It is denoting common saturated alkyl chain presence in organic compounds [46]. The terminal methyl ($-CH_3$) peak appeared at 14.04–14.08 ppm.

In this study, USFA-TMP ester was synthesized and ester chemical composition was identified. Three advanced reactions have happened throughout the esterification of USFA-PFAD with TMP that elaborate the intermediate establishment of mono-ester, di-ester and tri-ester, which was associated to the three –OH groups in TMP. The final tri-ester composition was determined by using high-temperature column GC-FID analysis. Figure 10 shows the GC chromatogram of resultant USFA-TMP ester. The tri-ester peaks starting to appear at 51.20 min retention time (Rt) up to Rt 72 min. The results show a 99.9% major tri-ester composition indicating the successful conversion of the three OH functional groups in TMP to USFA-TMP ester group [48].

3.8. *USFA-TMP ester lubrication properties*

3.8.1. *Viscosity and viscosity index*

The viscosity index was attained according to ASTM D 2270 where the kinematic viscosity at 100 °C was used to find the *L* and *H* values right from the ASTM reference table [49]. The viscosity index was then calculated on the source of *L* and *H*. As shown in Table 7, USFA-TMP ester has a kinematic viscosity of 43.7 cSt at 40 and 100 °C, USFA-TMP ester has 9.83 cSt kinematic viscosity. These values would remark USFA-TMP in the range of ISO viscosity grade (VG) 46 mineral oil, those obligatory for high-temperature applications such as hydraulic oil

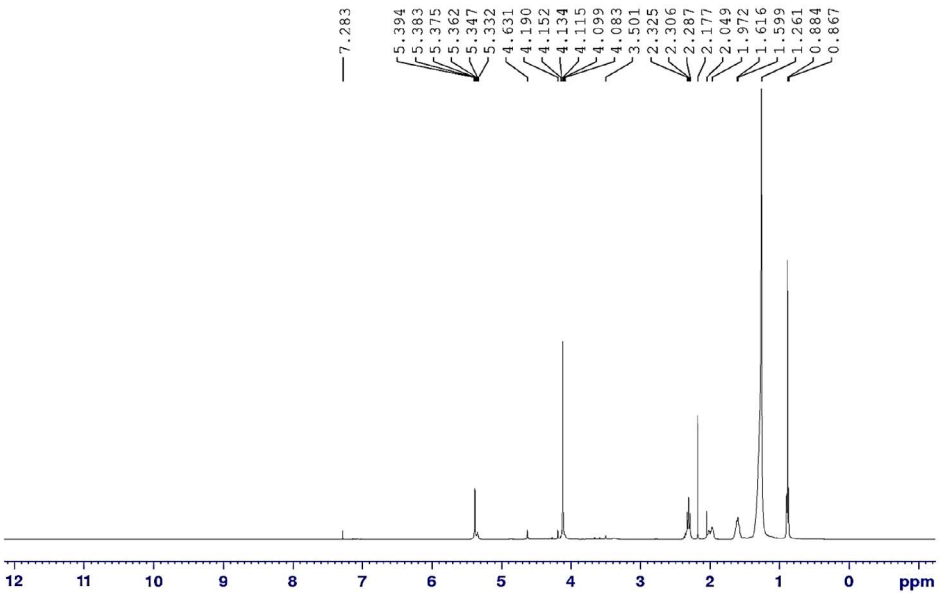

Figure 8. ^{1}H NMR spectrum of USFA-TMP ester.

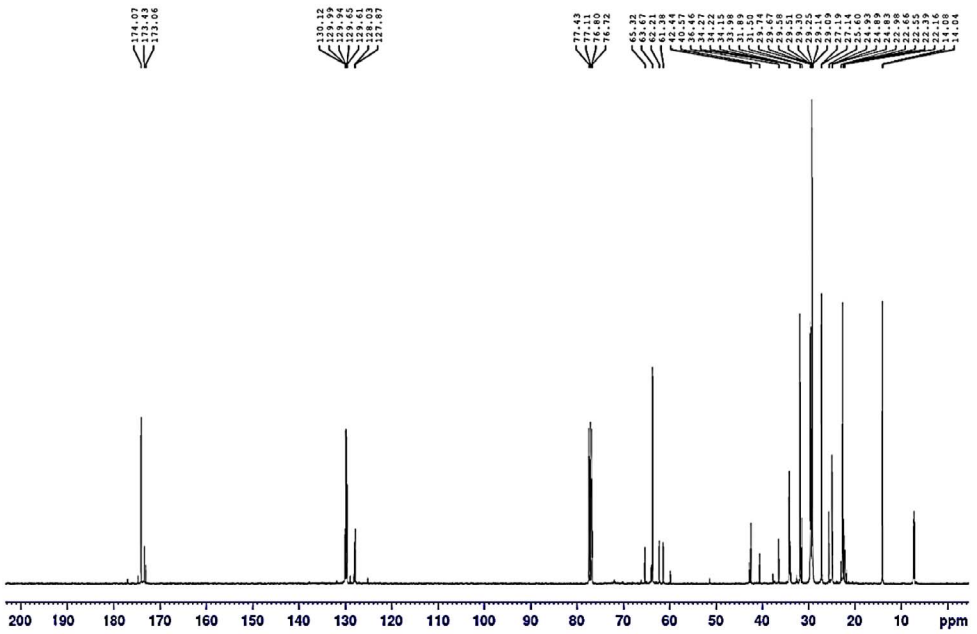

Figure 9. ^{13}C NMR spectrum of USFA-TMP ester.

and compressor oil [50]. It is intriguing to find that USFA-TMP ester possess viscosity index (VI) of 163 that similar to a commercial Mobil hydraulic ISO 46, but higher than other commercial lubricants such as Polyalphaolefin 8 (PAO8) of 136, Paraffin ISO VG 46 of 102, and ISO VG 32 of >90 [51]. The higher the viscosity index, the better the lubricant. So far, USFA-TMP can be perceived as high-quality biolubricant with regards to the viscosity index.

The lubricants kinematic viscosity in the range of

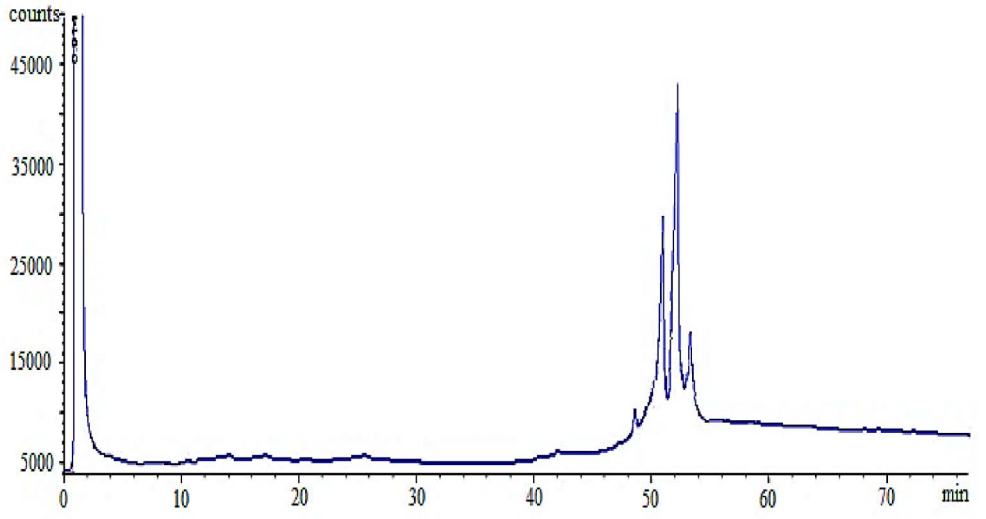

Figure 10. High temperature column GC-FID Chromatography of USFA-TMP ester.

Table 7. Lubrication properties of USFA-TMP ester and commercial lubricants

Esters/Lubricants	KV @ 40 °C (cSt)	KV @ 100 °C (cSt)	VI	OS_T, °C	PP, °C	FP, °C	ISO VG	FC @ 40 °C	FC @ 100 °C
USFA-TMP	43.7 ± 0.5	9.13 ± 0.6	163	215 ± 3	−42 ± 2	298 ± 2	46	0.22	0.20
TMP triolate*	68.0 ± 0.6	12.5 ± 0.3	189	213 ± 2	−41 ± 3	300 ± 2	68	0.25	0.21
PE tetraolate*	65.0 ± 0.3	14 ± 0.6	185	252 ± 4	−30 ± 2	>300	68	N/A	N/A
Mobil hydraulic ISO VG 68	68.4 ± 0.6	11.7 ± 0.5	135	N/A	−38 ± 5	241 ± 6	68	N/A	N/A
Mobil hydraulic ISO VG 46	45.6 ± 0.5	8.45 ± 0.5	165	N/A	−43 ± 4	232 ± 5	46	N/A	N/A
SubsTech hydraulic oil ISO VG 46	46.3 ± 0.7	6.94 ± 0.6	106	N/A	−38 ± 2	241 ± 2	46	0.31	0.28
Denicol compressor oil ISO VG 46	45.7 ± 0.6	6.8 ± 0.7	103	198 ± 3	−23 ± 3	237 ± 4	46	0.40	0.31
Maxoline turbine oil R&O, ISO 46	46 ± 0.4	6.7 ± 0.5	98	210 ± 4	−30 ± 2	213 ± 2	46	0.25	0.23

*Source [47].

Notes: KV = Kinematic viscosity; VI = Viscosity index; PP = Pour point; FP = Flash point; OS_T = Oxidative stability temperature; ISO VG no. = International standards organization viscosity grade number; FC = Friction coefficient.

5–15 cSt at 100 °C is obligatory for industrial applications usage. Generally, most polyol esters hold kinematic viscosities in the range between 5 and 225 cSt at 40 °C and 2–20 cSt at 100 °C to give a good viscosity index [52]. The viscosity index also be contingent on the length of the fatty acids in their molecular structure. It upsurges with longer linear C-chain length and higher degree of unsaturation, but less branched in the structure [53].

3.8.2. *Pour point*

The pour point is the utmost vital low-temperature property of any polyol ester used as a lubricant. It is demarcated as the lowest temperature at which a liquid polyol ester remains pourable (i.e., the ester liquid performs as a fluid) [54]. The pour point of USFA-TMP ester was restrained in accordance with ASTM D97 and are brief in Table 7. The obtained pour point of USFA-TMP was −42 °C. The low pour point was probably due the molecular structure of the polyol esters, which composes about 94% unsaturated fatty acids. However, the pour point of USFA-TMP with high degree of unsaturation was lower compared to many commercial lubricants as shown in Table 7. This could be due to more effective interruption of the close-fitting molecular padding at low temperature. Polyol esters with short-chained saturated fatty acids (C_4–C_{12}), high unsaturated fatty acids, and high number branching are exceedingly good and appropriate for application in low functioning temperatures, predominantly as winter automotive engine oils [50,55]. Polyol esters with low pour points are best suited for hydraulic systems and machine device applications [56].

3.8.3. *Flash point*

The flash point should be high enough to warrant safe operation with high fire resistance and lowest volatilization at the extreme operational temperature [57]. The flash point of USFA-TMP is relatively high, 298 °C compare to other commercial lubricants such as SubsTech hydraulic oil ISO VG 46 and Mobil hydraulic ISO VG 68 (Table 7). This is owing to its high molecular weight of carbon chain C_{18} fatty acids and number of ester functional groups [47]. The high flash point (298 °C) would make USFA-TMP ester practical to be used as engine oil at high temperature. Esters with a flash point of ≥165 °C are suitable as hydraulic oils [58].

3.8.4. *Oxidative stability*

Another important property of biolubricants is the ability of a constituent to resist oxidative degradation. The oxidative stability of USFA-TMP ester was screened to measure it's an onset (T_o) exothermic peak corresponding to oxidation stability temperature (OS_T) by using PDSC. T_o was premeditated from a plot of heat flow (W/g) versus temperature generated by the sample upon degradation [5]. Higher OS_T temperature reflects a greater degree to sustain against oxidation and evaporation [58]. The effects of evaporation designated by tailing, split peaks, and change in baseline were due to loss of sample mass in the DSC thermogram. These effects were apparent at temperatures higher than the initial oxidation peak. The OS_T temperature indicating the thermal oxidation degradation of USFA-TMP was observed starting at temperature of 215 °C. This remark is in agreement with finding by Wu *et al* for triolate-TMP (213 °C) [59]. This moderately low thermal oxidation stability compared to many commercial lubricants is due to USFA-TMP contains high unsaturated fatty acids about 94%. The esters with excellent oxidative stability have a tendency to work better under high temperatures and extreme environments [47]. However, the overall lubrication properties of USFA-TMP are excellent as shown in Table 7. These results indicated that USFA-TMP ester is suitable for biolubricant at moderate temperature operating condition and at high temperature operating with anti-oxidants addition.

In general, the results are indicative that the USFA-TMP ester has good lubrication properties. The comparison of USFA-TMP ester to its starting material USFA-PFAD creating them as a good contender for the green biolubricant. The results showed that the separation of USFA-PFAD and followed by the esterification reaction with TMP are the modification process that might appreciably adopted to produce high-end product such as biolubricant base stocks. USFA-TMP ester is thus of plausible to be used in formulating a suitable green biolubricants for both cold and warm climates and tropical such as Malaysia, South East countries etc.

4. Tribological analysis

The interactions of the biolubricant with any moving metal surfaces are depend on the its tribological performances. The biolubricants performance of under boundary or hydrodynamic lubrication environments highly count on their chemical composition and molecular structures. The existence of polar head and nonpolar straight-chain carbon tail groups in their molecular structure of the synthesized esters ended them amphiphilic characteristic in nature.

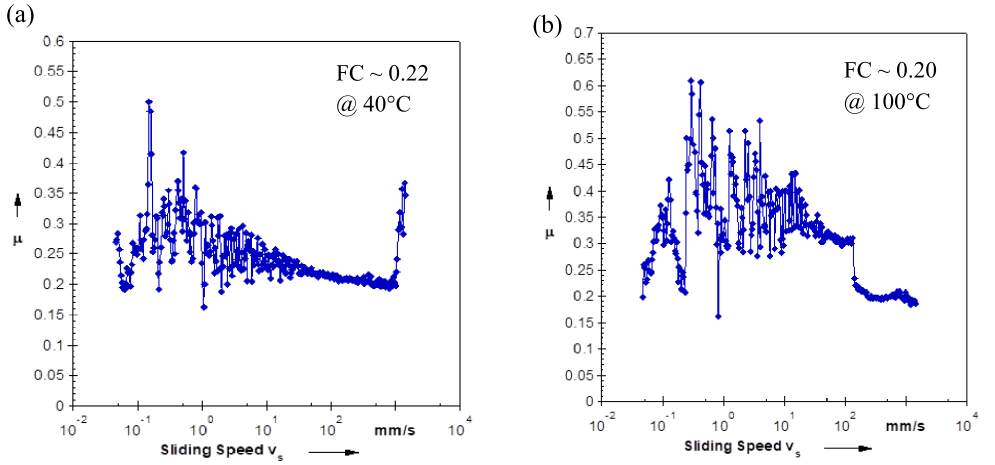

Figure 11. Effect of the sliding speed on the FC at 40 and 100 °C of USFA-TMP ester.

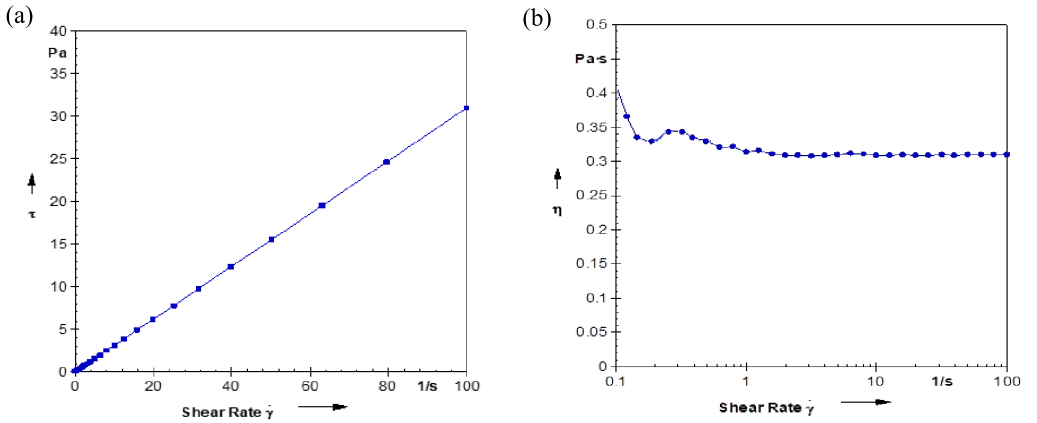

Figure 12. Shear rate plot versus (a) shear stress (b) viscosity of USFA-TMP ester at 25 °C.

Therefore, most esters can be worked as boundary lubrication condition. Adsorption of the polar head groups on a metal surface will minimize the surface energy and causes a decrease of the friction coefficient (FC) [60]. In turn, polarity of the biolubricant upsurges its effectiveness in reducing wear. The results of this study showed that USFA-TMP ester designated a minimum FC for the hydrodynamic conditions at 40 °C of 0.22 whereas at 100 °C was 0.20 as shown in Figure 11. It exhibited lower coefficient of friction values compared to of SubsTech Hydraulic Oil ISO 46, Denicol Compressor Oil ISO 46 and Maxoline Turbine Oil R&O, ISO 46 lubricants (Table 7). The biolubricant USFA-TMP ester logged a low friction coefficient below 0.5 at 40 and 100 °C as recommended for commercial lubricants [61]. The chemical composition and molecular structure of USFA-TMP ester with high polarity has high propensity to form an adsorbed shielding layer on the metal surfaces. This is good characteristic quality of tribological properties and is able to participate with many commercial lubricants in the market.

5. Rheological properties

The rheological property of the USFA-TMP ester was identified through its connection between shear stress and shear rate. The classification either as Newtonian or non-Newtonian fluids depends on their viscosity behaviour when shear rate increase. The ester is classified as Newtonian fluid when the relationship is linear as shear rate increase. On the

other hand, non-linear or inconstant viscosity when shear rate increase is known as non-Newtonian [61–63]. Figure 12 shows a linear relationship between shear stress and shear rate (a) and a constant viscosity against shear rate (b) at regions of 10–100 s^{-1}. This indicates that USFA-TMP ester shows a Newtonian fluid characteristic. The viscosity of USFA-TMP ester will not change as the shear stress increases and would be working well in the hydrodynamic lubrication environment.

6. Conclusions

The D-optimal approach was successfully used for optimization of the esterification of USFA PFAD with TMP to produce resultant polyol ester of USFA-TMP. The possessions of the interactions between self-determining variables on the USFA PFAD with TMP esterification were successfully investigated. The ANOVA results confirming a constancy among the predictions results from the model and the experimental data. The study results established that the determining reaction variable of both acid catalyst amount and reaction were significantly affected the ester yield % whereas both reaction time and reaction temperature were significantly affected the tri-ester selectivity. The optimal condition for the esterification was obtained at reaction temperature of 150 °C for 6 h and with 5% H_2SO_4. The USFA-TMP was successfully produced in high yields ($96 \pm 0.5\%$) with high selectivity of tri-esters ($99 \pm 0.9\%$). The resultant USFA-TMP ester shows good lubrication properties such as high VI, low PP, high FP as well as good thermal oxidative stability. It is classified as a Newtonian fluid with viscosity grade lubricant ISO VG 46. The resultant USFA-TMP ester is credible to be used as green biolubricant in many industrial applications.

Conflicts of interest

Authors have no conflict of interest to declare.

Acknowledgments

The authors would like to thank the Universiti Kebangsaan Malaysia for providing laboratory facilities and the financial support through the research grant no. GUP-2016-058 and Sime Darby ST-2014-019.

References

[1] J. Salimon, N. Salih, E. Yousif, *Arabian J. Chem.*, 2012, **5**, 135-145.
[2] S. Z. Erhan, B. K. Sharma, J. M. Perez, *Ind. Crops Prod.*, 2006, **24**, 292-299.
[3] J. Salimon, N. Salih, E. Yousif, *Ind. Crops Prod.*, 2012, **38**, 107-114.
[4] N. H. Arbain, J. Salimon, N. Salih, W. A. Ahmed, *Appl. Sci. Eng. Progress*, 2022, **15**, article no. 5552, in press.
[5] J. Salimon, N. Salih, E. Yousif, *Eur. J. Lipid Sci. Technol.*, 2010, **112**, 519-530.
[6] W. A. Ahmed, N. Salih, J. Salimon, *Asian J. Chem.*, 2021, **33**, 1363-1369.
[7] S. Samidin, N. Salih, J. Salimon, *Biointerface Res. Appl. Chem.*, 2021, **11**, 13638-13651.
[8] N. Salih, J. Salimon, *Biointerface Res. Appl. Chem.*, 2021, **11**, 13303-13327.
[9] A. Campanella, E. Rustoy, A. Baldessari, M. A. Baltanás, *Bioresour. Technol.*, 2010, **101**, 245-254.
[10] L. A. Quinchia, M. A. Delgado, J. M. Franco, H. A. Spikes, C. Gallegos, *Ind. Crops Prod.*, 2012, **37**, 383-388.
[11] N. A. M. Aziz, R. Yunus, U. Rashid, A. M. Syam, *Ind. Crops Prod.*, 2014, **62**, 305-312.
[12] N. Salih, J. Salimon, *Biointerface Res. Appl. Chem.*, 2021, **12**, 1185-1207.
[13] G. Karmakar, P. Ghosh, B. Sharma, *Lubricants*, 2017, **5**, article no. 44.
[14] A. A. Japir, N. Salih, J. Salimon, *Turkish J. Chem.*, 2021, **45**, 585-599.
[15] M. A. Jumaah, N. Salih, J. Salimon, *Turkish J. Chem.*, 2021, **45**, 1391-1407.
[16] A. A. Kiss, C. S. Bildea, *J. Chem. Technol. Biotechnol.*, 2012, **87**, 861-879.
[17] J. Calero, D. Luna, E. D. Sancho, C. Luna, F. M. Bautista, A. A. Romero, A. Posadillo, J. Berbel, C. Verdugo-Escamilla, *Renew. Sustain. Energy Rev.*, 2015, **42**, 1437-1452.
[18] F. M. J. Vernon, "Firelighter with palm fatty acid distillate", 2018, Standard Brands (UK) Ltd U.S. Patent Application 15/749,703.
[19] N. Z. A. Kapor, G. P. Maniam, M. H. A. Rahim, M. M. Yusoff, *J. Cleaner Prod.*, 2017, **143**, 1-9.
[20] N. M. Nor, N. Salih, J. Salimon, *Asian J. Chem.*, 2021, **33**, 67-75.
[21] J. R. Carlton, S. Arpith, L. M. Pradeep, *J. Bio- Tribo-Corrosion*, 2017, **3**, article no. 18.
[22] I. M. Lokman, M. Goto, U. Rashid, Y. H. Taufiq-Yap, *Chem. Eng. J.*, 2016, **284**, 872-878.
[23] S. F. Ibrahim, N. Asikin-Mijan, M. L. Ibrahim, G. Abdulkareem-Alsultan, S. M. Izham, Y. H. Taufiq-Yap, *Energy Convers. Manage.*, 2020, **210**, article no. 112698.
[24] B. T. Y. Ping, M. Yusof, *Oil Palm Bull.*, 2009, **59**, 5-11.
[25] M. A. Jumaah, F. M. Y. Mohamad, J. Salimon, M. Bahadi, *Malaysian J. Chem.*, 2019, **21**, 8-16.
[26] K. B. Baharudin, Y. H. Taufiq-Yap, J. Hunns, M. Isaacs, K. Wilson, D. Derawi, *Microporous Mesoporous Mater.*, 2019, **276**, 13-22.
[27] M. A. Jumaah, N. Salih, J. Saliomn, *Bioenergy Res.*, 2022.
[28] S. Widodo, K. Khoiruddin, D. Ariono, S. Subagjo, I. G. Wenten, *J. Environ. Chem. Eng.*, 2020, **8**, article no. 103789.

[29] S. L. Barbosa, A. C. Pereira Rocha, D. L. Nelson, M. S. de Freitas, A. A. P. Fulgêncio Mestre, S. I. Klein, G. C. Clososki, F. J. Caires, D. L. Flumignan, L. K. dos Santos, A. P. Wentz, V. M. Duarte Pasa, R. D. Fernandes Rios, *Molecules*, 2022, **27**, article no. 953.

[30] M. A. Gonçalves, E. K. L. Mares, J. R. Zamian, G. N. D. R. Filho, L. R. V. da Conceição, *Fuel*, 2021, **304**, article no. 121463.

[31] K. A. Shah, J. K. Parikh, B. Z. Dholakiya, K. C. Maheria, *Chem. Paper*, 2014, **68**, 472-483.

[32] G. M. Ziarani, A. Badiei, M. Hassanzadeh, S. Mousavi, *Arabian J. Chem.*, 2014, **7**, 335-339.

[33] P. Gholamzadeh, G. M. Ziarani, N. Lashgari, A. Badiei, P. Asadiatouei, *J. Mol. Catal. A: Chem.*, 2014, **391**, 208-222.

[34] M. Canakci, J. Van Gerpen, *Trans. Am. Soc. Agric. Eng.*, 1999, **42**, 1203-1210.

[35] T. Lieu, S. Yusup, M. Moniruzzaman, *Bioresour. Technol.*, 2016, **211**, 248-256.

[36] Z. Zhang, H. Zheng, *J. Hazard. Mater.*, 2009, **172**, 1388-1393.

[37] S. Weisberg, *Applied Linear Regression*, 3rd ed., John Wiley & Sons Inc., New York, USA, 2005.

[38] N. Zora, T. Rigaux, J. C. Buvat, D. Lefebvre, S. Leveneur, *J. Loss Prev. Process Ind.*, 2021, **72**, article no. 104551.

[39] S. K. Behera, H. Meena, S. Chakraborty, B. C. Meikap, *Int. J. Mining Sci. Technol.*, 2018, **28**, 621-629.

[40] D. Granato, G. Ares, *Mathematical and Statistical Methods in Food Science and Technology*, Wiley-Blackwell, Chichester, England, 2014.

[41] M. Bahadi, J. Salimon, D. Derawi, *Renew. Energy*, 2021, **171**, 981-993.

[42] R. Awang, M. R. Ghazuli, M. Basri, *Am. J. Biochem. Biotechnol.*, 2007, **3**, 163-166.

[43] B. K. Sharma, A. Adhvaryu, Z. Liu, S. Z. Erhan, *J. Am. Oil Chem. Soc.*, 2006, **83**, 129-136.

[44] M. Bahadi, N. Salih, J. Salimon, *Appl. Sci. Eng. Progress*, 2021, **14**, 175-186.

[45] D. L. Pavia, G. M. Lampman, G. S. Kriz, J. R. Vyvyan, *Introduction to Spectroscopy*, 5th ed., Cengage Learning, Inc., Boston, USA, 2015.

[46] E. Alexandri, R. Ahmed, H. Siddiqui, M. I. Choudhary, C. G. Tsiafoulis, I. P. Gerothanassis, *Molecules*, 2017, **22**, article no. 1663.

[47] R. M. Mortier, M. F. Fox, S. Orszulik, *Chemistry and Technology of Lubricants*, 3rd ed., Springer, New York, USA, 2010.

[48] M. A. Jumaah, F. L. Khaleel, N. Salih, J. Salimon, *Biomass Convers. Biorefin.*, 2022.

[49] W. Gwidon, A. W. B. Stachowiak, *Engineering Tribology*, 4th ed., Elsevier Inc., Amsterdam, Netherlands, 2014.

[50] L. R. Rudnick, in *Synthetics, Mineral Oils, and Bio-based Lubricants Chemistry and Technology* (L. R. Rudnick, ed.), Taylor & Francis Group, Boca Raton, London, New York, LLC, 3rd ed., 2020, 1-36.

[51] J. A. Cecilia, D. B. Plata, R. M. A. Saboya, F. M. de Luna, C. L. Cavalcante, E. Rodríguez-Castellón, *Processes*, 2020, **8**, article no. 257.

[52] M. Gul, H. H. Masjuki, M. A. Kalam, N. W. M. Zulkifli, M. A. Mujtaba, *Bioenergy Res.*, 2020, **13**, 1-22.

[53] D. Kania, R. Yunus, R. Omar, S. A. Rashid, B. M. Jan, *J. Petroleum Sci. Eng.*, 2015, **135**, 177-184.

[54] N. A. Zainal, N. W. M. Zulkifli, M. Gulzar, H. H. Masjuki, *Renew. Sustain. Energy Rev.*, 2018, **82**, 80-102.

[55] N. M. Nor, N. Salih, J. Salimon, *Hem. Ind.*, 2021, **75**, 117-128.

[56] H. Ji, B. Wang, X. Zhang, T. Tan, *RSC Adv.*, 2015, **5**, 100443-100451.

[57] K. Kamalakar, G. N. V. T. S. Manoj, R. B. N. Prasad, M. S. L. Karuna, *J. Agric. Food Chem.*, 2014, **62**, 11980-11987.

[58] N. Salih, J. Salimon, E. Yousif, B. M. Abdullah, *Chem. Central J.*, 2013, **7**, article no. 128.

[59] Y. Wu, W. Li, X. Wang, *Lubrication Sci.*, 2015, **27**, 369-379.

[60] J. Salimon, W. A. Ahmed, N. Salih, M. A. Yarmo, D. Derawi, *Sains Malaysiana*, 2015, **44**, 405-412.

[61] P. Coussot, L. Tocquer, C. Lanos, G. Ovarlez, *J. Non-Newtonian Fluid Mech.*, 2009, **158**, 85-90.

[62] M. A. Jumaah, N. Salih, J. Salimon, *Iranian J. Chem. Chem. Eng.*, 2021, in press.

[63] G. E. Totten, S. R. Westbrook, R. J. Shah, *Fuels and Lubricants Handbook: Technology, Properties, Performance, and Testing*, ASTM International, New York, USA, 2003.

Comptes Rendus
Chimie
2022, Vol. 25, Special Issue S2, p. 113-127
https://doi.org/10.5802/crchim.170

Sustainable Biomass Resources for Environmental, Agronomic, Biomaterials and Energy Applications 3 / *Ressources de biomasse durables pour des applications environnementales, agronomiques, de biomatériaux et énergétiques 3*

CFD multiphase combustion modelling of oleic by-products pellets in a counter-current fixed bed combustor

Modélisation CFD de la combustion multiphases des pastilles de sous-produits oléiques dans une chambre de combustion à lit fixe à contre-courant

Mohamed Ali Mami [a], **Marzouk Lajili** [*, a] **and Tarek Echekki** [*, b]

[a] University of Monastir, Preparatory Institute of Engineering Studies of Monastir (IPEIM), Ionized and Reactive Media Studies Research Laboratory (EMIR), 15 Avenue Ibn El Jazzar Monastir 5019, Tunisia

[b] North Carolina State University, Department of Mechanical & Aerospace Engineering, 1840 Entrepreneur Drive Campus Box 7910 Raleigh, NC 27695-7910, USA

E-mails: hama.mami@yahoo.com (M. A. Mami), Marzouk.lajili@ipeim.rnu.tn, abouhechem@gmail.com (M. Lajili), techekk@ncsu.edu (T. Echekki)

Abstract. A transient two-dimensional multiphase model was built to study the combustion of pellets of oleic by-products (Olive Pits (OPi)) in a cylindrical counter-current 40 kW fixed bed combustor. The fixed bed is modelled as a porous medium, which is randomly packed with spherical particles of equal size. A $\kappa - \varepsilon$ model for low Reynolds number flows was used for turbulence Modelling. Primary and secondary air injections were supplied at the bed (solid phase combustion) and at the freeboard zone (gas phase combustion), respectively. The mass loss history, the temperature distribution at different heights inside the reactor and the gas emissions of CO, CO_2, O_2, H_2, CH_4 and C_{org} were computed. Key parameters related to the reaction front velocity, the mass conversion rate and the progress of ignition were also computed. We show that computational results are in good agreement with experimental measurements obtained using a similar reactor fed with the same pellet types. These results also motivate the implementation of the present formulation and its extension to industrial scale furnaces, having established the results for the comparison with pilot-scale experiments.

Keywords. CFD, Porous medium, Fixed bed reactor, Olive pits pellets, Multiphase combustion.
Published online: 29 March 2022

* Corresponding authors.

1. Introduction

Biomass when burned properly could be considered as a renewable and an environmentally friendly source of energy. Indeed, it can be used for the generation or the cogeneration of heat and/or electricity [1]. Biomass combustion is relatively complex to model due to the presence of reaction at different phases involving charcoal, tars and volatile mixtures of organic compounds. Moreover, the presence of large amounts of ash and minerals are a source of corrosion and slagging inside the combustion chamber. However, fixed bed reactors powered by solid fuels offer high automation and low costs. The Modelling and experimentation on the complex phenomena inside these reactors and the solid biomass conversion process must address the coupling of different processes, including heat and mass transfer, gas flow, moisture evaporation, pyrolysis and the combustion and the gasification processes. Yet, Computational Fluid Dynamics (CFD) of biomass combustion can provide important insight, and often complementary information to experiments, to these complex processes [2–4].

Details on the Modelling of biomass combustion as well as on the solid phase and on the gas phase reactions are reported in the literature [5–14]. Typically, a configuration consisting of two coupled zones (the bed and the free-board) is considered [15–17] in which the two zones are separated by an interface allowing mass and energy exchanges [2,6,17–20]. Two general types of models are incorporated that are associated with the homogeneous and heterogeneous phases of the process [5,18,21]. Based on the solid phase combustion in the heterogeneous models, one may use continuous models (macro-scale models), which treat the solid phase as a porous medium [6,10, 18,22] and discrete element models (DEM) (micro-scale models), which describe particles in a moving grate [18,23,24]. Currently, most studies have focused primarily on the solid phase combustion in fixed beds, but, the simultaneous Modelling of both the solid and the gas phases is still needing more attention [5,6,11,13,22,25–27].

Gollaza *et al.* studied a transient 3D CFD model for the combustion of densified wood [6]. The computational domain was divided into two zones: a fixed bed described as a porous medium and the free-board. They simulated both the gas and the solid temperature profiles at different positions inside the reactor. Their results reproduced many of the key features of the experiments. Mehrabian *et al.* [5] developed a transient 3D CFD model for biomass combustion in similarly coupled zones (fixed bed and free-board). The authors also measured the gas concentrations of CO, CO_2, CH_4, H_2O, H_2 and O_2 and the temperature at various heights in the reactor for both the bed and the freeboard. Moreover, they evaluated the reaction front velocity. Their predicted results were also in a good agreement with experiments. Sun *et al.* [28] carried out a 2D unsteady CFD using municipal solid waste in a fixed bed reactor. They showed that their predictions of the gaseous species emissions CO, CO_2, O_2 and CH_4 and the temperature profiles at different heights as a function of time for different moisture content were also in agreement with experimental data. These above studies underscore the importance of coupled 2-zone models for fixed bed reactors.

The objective of this study is to investigate numerically the combustion of pellets prepared from oleic by-products, and more precisely, Olive Pits (OPi) in a 40 kW counter-current fixed bed reactor. Indeed, Olive solid wastes (Olive Pomace and Olive Pits) when dried and free of residual oil, could be blended with woody biomass and densified as pellets, briquettes or logs in order to be used as fuels for feeding boilers, stoves and furnaces in many countries such as Spain and Italy. This energy policy is justified by the renewable character of the biomass and by its high heating value reaching 19 MJ/kg. Hence, it is highly important by the present study to simulate the combustion of OPi in a fixed bed reactor in order to give guidance later on the reactor design and geometry, the manner of feeding it by the primary and the secondary air, and on the level of gaseous emissions that should be reduced.

The simulations based on a cylindrical reactor are implemented using a transient 2D configuration using the COMSOL Multiphysics software. Consistently with earlier studies, the computational domain was divided into two zones: the bed and the freeboard zones. Due to the strong coupling of the mass and heat transfer between the two zones, equations describing the various sub-models were solved simultaneously to represent moisture evaporation, VOC devolatilization, pyrolysis, gasification, gas phase combustion and residual char combustion.

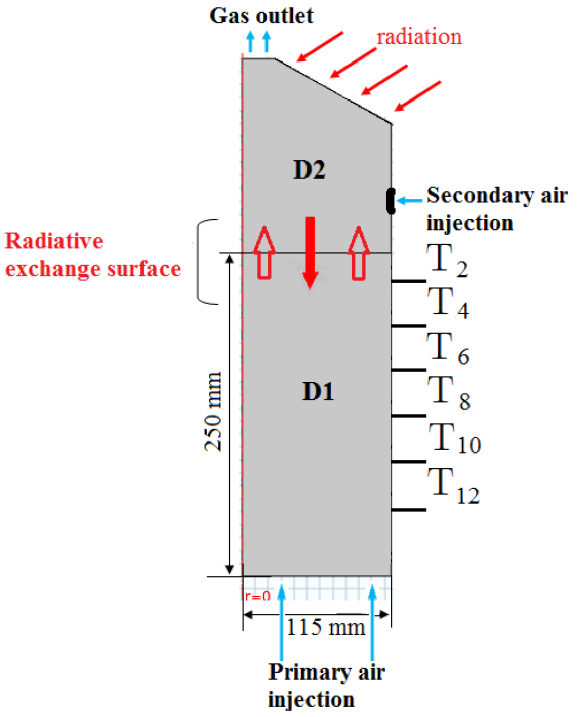

Figure 1. The 2D geometry model.

The homogenous gas phase reactions are modelled for a fuel mixture of CO, CO_2, O_2, CH_4, H_2 and H_2O in the freeboard zone. A weak turbulence $\kappa - \varepsilon$ model is used for turbulence closure. From the simulations, we report the temperature profiles at different heights inside the reactor in the two regions and the gaseous emissions and the mass loss as a function of elapsed time. The CFD were validated using experimental data from a prior experiment [29] as well as additional data reported in the literature [5,11,22,28,30–32].

2. Model description and hypothesis

2.1. *Computational configuration and modelling assumptions*

The 2D axisymmetric model used is a cylindrical geometry with 400 mm height (H) and 115 mm diameter (d) is shown in Figure 1. The cylinder is divided into two zones: the fixed bed denoted (D1) and the freeboard (D2).

The model used to simulate the entire combustion process is based on the following assumptions and conditions:

- The computational domain is divided into two fully coupled zones: the fixed bed and the freeboard.
- The fixed bed is bounded by adiabatic walls and treated as a porous medium.
- In the counter-current configuration, the ignition starts from the top towards the bottom of the bed during which the combustion evolves layer by layer.
- The solid phase and the gas phase are modelled with their own energy equation while allowing for mass and energy exchange between the two zones via a permeable interface.
- The biomass particles are modelled as perfectly spherical and randomly packed.
- The evaporation process occurred at a specific temperature and is assumed thermally controlled.
- The pyrolysis phase of the Olive Pits pellets (OPi) is modelled by a three-step reaction mechanism yielding biogas, tars and Volatile Organic Compounds (VOC).
- The solid fraction and the particles' sizes vary during the residual char combustion and gasification.
- VOC produced during pyrolysis and gasification is mainly CO, CO_2, H_2, CH_4 and H_2O_{vap}. The combustion of the residual char (in the bed zone), CO, H_2 and CH_4 in the freeboard zone governs the entire process.
- The residual char obtained by pyrolysis is gasified by CO_2 and H_2O and oxidized by air. A flame front starts at the top bed and propagates to the bottom with a characteristic speed.
- No assumptions are used concerning the heat transfer and the three modes; conduction, convection and radiation are considered. The radiative transfer is modelled using an effective thermal conductivity.
- The gas emissions and the heat leaving the packed bed (D1) are considered as the inlet conditions for the freeboard zone (D2).
- The bed, which is electrically heated in the experiment, is assumed to be heated by

incident radiative transfer from the walls with a prescribed constant wall temperature, T_{wall}, equals to 1173.15 K.
- The incoming radiation flux from the freeboard region is modelled as an incident radiative heat to the fixed bed.

The reactor is fed by two air inlets: the primary air with a flow rate of 10 Nm^3/h is injected under the bed bottom and passes through the fixed particles. Whereas the secondary air used to enhance the gas phase combustion is introduced at the side of the freeboard zone with a flow rate of 25 Nm^3/h as illustrated in Figure 1. Both air injections occur at an ambient temperature of 298.15 K. In the actual experimental study [29], the fixed bed was equipped with thirteen type K-thermocouples, which are spaced at 20 mm increment along the reactor, but, only six type K-thermocouples (Figure 1) are considered during the present numerical study in order to reduce the simulation time.

2.2. *Modelling of rate processes*

The overall combustion process can be divided into four different sub-processes: drying, pyrolysis and combustion of VOC, and combustion and gasification of the residual char. In this study, the drying process is modelled as a heterogeneous reaction at the solid temperature [32–34]. This process is represented by a first-order kinetic reaction based on the Arrhenius law:

$$\text{Humidity} \xrightarrow{k_v} \text{Water vapor} \tag{1}$$

with

$$k_v = A\exp\left(-\frac{E_v}{RT_s}\right) \tag{2}$$

and

$$\dot{w} = k_v \rho_s Y_{\text{H}_2\text{O},s}. \tag{3}$$

Here, A is the frequency factor, E_v is the activation energy and $\dot{w}_{\text{moist}}$ is the reaction rate (kg/(m^3·s). The values of these rate constant parameters are given in Table 1.

Pyrolysis is a complex process, which involves a number of coupled chemical reactions [10,35–38]. Here, the lignocellulosic samples containing mainly hemicelluloses, cellulose and lignin produce, via pyrolysis, three products; biogas, tars and biochar. The rate contents of these products depend on the type of samples and especially on the type of pyrolysis (slow, fast or flash). The total devolatilization rate [34] is modelled as follows:

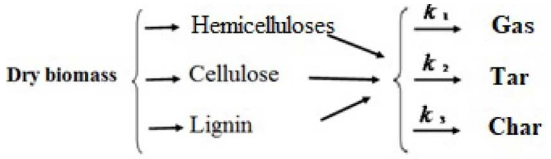

$$\dot{w}_{\text{py}} = (K_1 + K_2 + K_3)\rho_{\text{moist}} = \rho_{\text{moist}} \sum_{i=1}^{3} A_i \exp\left(\frac{E_i}{RT_s}\right) \tag{4}$$

where the rate constant parameters for K_1, K_2 and K_3 are given in Table 1.

The reaction of the combustion and gasification of the residual char is considered as a heterogeneous and exothermic reaction [39,40]. The oxidation of the residual char with the O_2 of injected primary air is described by the following 2-step reactions:

$$\text{C} + \text{O}_2 \rightarrow \text{CO}_2 \tag{5}$$

$$\text{C} + \tfrac{1}{2}\text{O}_2 \rightarrow \text{CO} \tag{6}$$

while the gasification processes with CO_2 and H_2O as gasifier can be represented by:

$$\text{C} + \text{H}_2\text{O} \rightarrow \text{H}_2 + \text{CO} \tag{7}$$

$$\text{C} + \text{CO}_2 \rightarrow 2\text{CO} \tag{8}$$

The reaction rates of (5)–(8) are estimated using the following expressions:

$$\dot{w}_{\text{C}}^{\text{O}_2} = K_1 [\text{O}_2]; \quad K_1 = A_1 \exp\left(-\frac{E_1}{RT_s}\right) \tag{9}$$

$$\dot{w}_{\text{C}}^{\text{O}_2} = K_2 [\text{O}_2]^{0.5}; \quad K_2 = A_2 \exp\left(-\frac{E_2}{RT_s}\right) \tag{10}$$

$$\dot{w}_{\text{C}}^{\text{H}_2\text{O}} = K_3 [\text{H}_2\text{O}]; \quad K_3 = A_3 \exp\left(-\frac{E_3}{RT_s}\right) \tag{11}$$

$$\dot{w}_{\text{C}}^{\text{CO}_2} = K_4 [\text{CO}_2]; \quad K_4 = A_4 \exp\left(-\frac{E_4}{RT_s}\right). \tag{12}$$

The combustion of gaseous emissions is modelled using the following reactions:

$$\text{CH}_4 + \tfrac{1}{2}\text{O}_2 \rightarrow 2\text{H}_2 + \text{CO},$$

$$\text{with } \dot{w}_{\text{CH}_4} = A_5 [\text{CH}_4] [\text{O}_2]^{0.5} \exp\left(\frac{E_5}{RT_g}\right) \tag{13}$$

$$\text{CO} + \text{O}_2 \rightarrow \text{CO}_2,$$

$$\text{with } \dot{w}_{\text{CO}} = A_6 [\text{O}_2] [\text{CO}] \exp\left(\frac{E_6}{RT_g}\right) \tag{14}$$

$$\text{H}_2 + \text{O}_2 \rightarrow \text{H}_2\text{O},$$

$$\text{with } \dot{w}_{\text{H}_2} = A_7 [\text{O}_2] [\text{H}_2] \exp\left(\frac{E_7}{RT_g}\right). \tag{15}$$

The values of the different constants A_i and E_i are given in Table 1. The parameters presented in Table 1 are not taken from literature because there isn't any

Table 1. Rate constant's parameters

Olive pits pellets	Pre-exponential factor A (1/s)	Activation energy E (kJ/mol)
Drying	1.06×10^3	88.5
Pyrolysis		
Cellulose	2×10^{12}	185
Hemicellulose	3.5×10^{11}	105
Lignin	10^8	192
Tar	1.5×10^5	192
Residual char combustion	9×10^8	2.25×10^5 (k_1)
	7×10^9	1.3×10^3 (k_2)
Residual char gasification	1.6×10^6	2.2×10^4 (k_3)
	3.5×10^7	225×10^4 (k_4)
Combustion of pyrolysis gases	10^7	1.89×10^5 (k_5)
	1.674×10^5	1.25×10^3 (k_6)
	1.95×10^7	1.67×10^5 (k_7)

reported work using the same fuel type as us. Hence, we are inspired by a similar reported work in the literature [11] to calibrate our model so that it matches our previous experimental results [29].

2.3. *Governing equations in the fixed bed and the freeboard*

Solid and gas phase equations are solved as a transient two-dimensional formulation in cylindrical coordinates. Various conservation equations describing the fuel conversion of mass, momentum and energy were solved in two coupled zones as reported in literature for similar studies [2–4,10–13]. The gases emitted from the bed, CO, CO_2, H_2 and CH_4, and their composition are prescribed as inlet conditions for the freeboard zone. These gases are likely to react with oxygen in the secondary air. In order to lighten the text to the readers, all equations with meanings of all variables and parameters are provided in Appendices A and B.

2.4. *Fuel properties*

The size of the olive solid by-products pellets as olive pits used in our numerical simulation ranged from approximately 2.5 to 3.5 cm and with an equivalent diameter up to 6 mm. Ultimate analysis as %C, %H, and %O and proximate analysis as Volatile Matter (%VM), %Ash and Fixed Carbone (%C) and energy contents as the bulk density of the olive solid by-products pellets are assumed to be the same as the values published in [29]. On the other hand, the ash content evolution is not taken into account.

2.5. *Mesh and numerical resolution*

The finite element method was used to discretize the unsteady governing equations. To establish grid convergence, we considered 5 mesh resolutions, which are summarized in Table 3.

Calculations show that the meshes named coarse or normal did not yield grid convergence. However, finer or extra-fine meshes required extensive computational times four to five weeks on a mini-workstation. The "fine" mesh resolution provides a reasonable compromise where grid convergence is established while a reasonable computational time of approximately 24 h is achieved. The corresponding mesh size is approximately 1.5 mm, whereas the calculation time was automatically defined by the solver.

Finally, a moving mesh was adopted in order to refine our calculations at the interface between the two computational zones as shown on Figure 2.

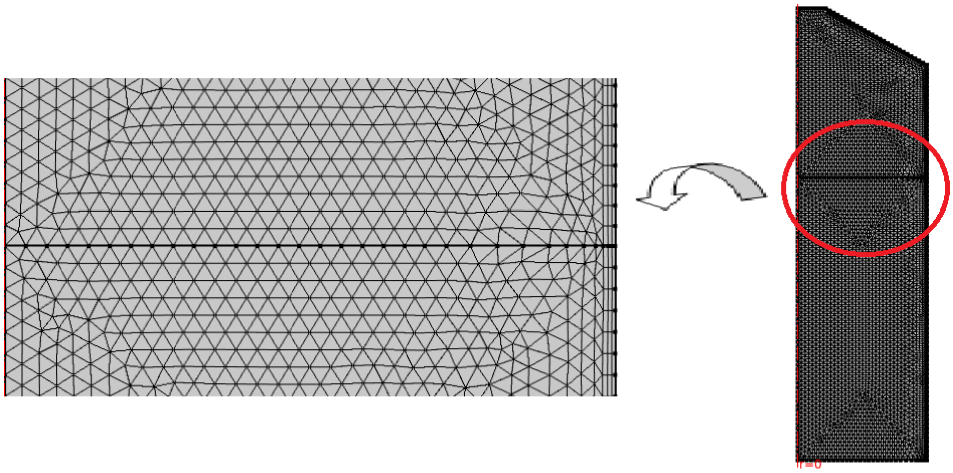

Figure 2. Mesh grid structure.

Table 2. Summary parameter's values and correlations

Property	Correlation/value	Reference
Permeability	$K_R = \dfrac{d_p^2 \varepsilon_s^2}{180(1-\varepsilon_s^2)}$	[41]
Solid thermal conductivity	$\lambda_s = \varepsilon_s \lambda_g + \sum_i Y_i \lambda_i$ $\lambda_{\text{rad}} = 4\varepsilon_s \sigma \omega d_p T_s^3$	[10,42,43]
Emissivity	0.9	
Bed porosity	0.5	
Specific surface	$S_p = \dfrac{6(1-\varepsilon_s)}{d_p}$	
Heat transfer coefficient	$h_{sg} = \dfrac{N_u \lambda_{\text{eff},g}}{d_p} = -h_{gs}$	
Nusselt number	$N_u = 2 + 1.1 R_e^{0.6} P_r^{1/3}$	
Gas density	$\rho_g = \dfrac{pM_g}{RT_g}$	

3. Results and discussion

3.1. *Mass loss*

The accurate prediction of the temporal evolution of the mass loss of the olive pit pellets is an important test of the overall performance of the computational study. This mass loss is prescribed by the following equation:

$$\frac{\partial m}{\partial t} = -\sum_{i=1}^{4} \dot{w}_i. \tag{16}$$

Accounts for the contributions of all relevant reaction processes that include: drying, pyrolysis, combustion and gasification of the residual char [5,44]. In (16), the $\dot{w}_i$ represents the reaction rates associated with each process (kg/m^3·s).

Figure 3 compares the temporal evolutions of the modelled (dashed) and measured (solid) mass loss [29]. The comparison shows a good agreement between measurements and computations. The mass loss could be divided into three phases (I), (II) and (III) on Figure 3: the first phase (I) corresponds to moisture evaporation, the second phase (II) corresponds to the devolatilization and combustion of gases, and. the final phase (III) corresponds to the residual char combustion. Similar

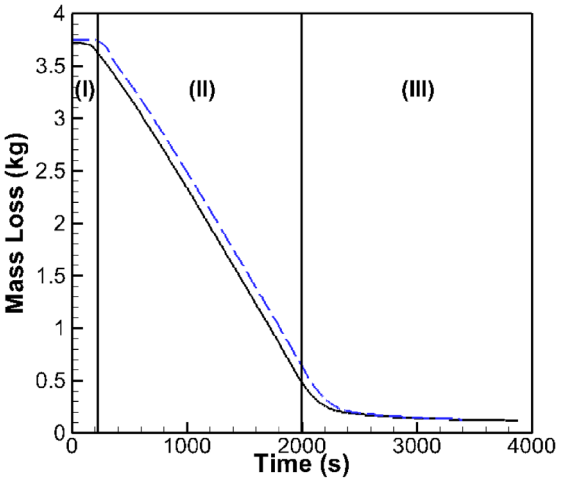

Figure 3. Mass loss history. Experiment (solid), Simulation (dashed).

Table 3. Different mesh resolutions considered with their boundary and domain elements

Meshes	Domain elements	Boundary elements
Coarse	2,129	154
Normal	4,525	224
Fine	7,305	285
Finer	11,176	354
Extra-fine	49,944	748

results were reported in literature for both numerical simulations [14,45] and experimental measurements [46–48].

3.2. *Temperature and gas velocity evolutions inside the reactor*

The temporal evolution of the temperature distribution inside the reactor is shown in Figure 4. The figure also serves to highlight the propagation of the combustion processes both in the freeboard zone and in the fixed bed. As shown, ignition started from the top at $t = 0$ s, and then the flame propagates rapidly in the gas phase. This process continues into the solid phase, yet at a slower rate, until the bottom of the bed is reached [31].

However, the gas velocity profile as a function of the radial distance of the reactor, as illustrated in Figure 5, reveals that the gas flows in the opposite direction to the ignition front propagation, hence, the counter-current nature of the bed [49]. The decrease of the temperature near the interface between the gas and solid phases can be attributed to convective cooling associated with secondary air [26,50]. For a height up to approximately 0.3 m, the gas velocity profile remains flat ($\approx$0.075 m·s^{-1}). However, as the mixture of gases and secondary air reach the activation temperature, the combustion in the gas phase is started and the gas velocity increases rapidly reaching about 5 m/s. This is a typical value for gas phase combustion [26].

To better understand the combustion process in the fixed bed, we attempt to look closely at the solid phase combustion. Figure 6 compares the computed and measured temperature profiles of the olive pit pellets at different heights along the reactor centreline corresponding to 5, 45, 85 and 165 mm, which also correspond to 4 different placements of the thermocouples in the experiment [29,51]. The simulation was undertaken under the same experimental conditions with a primary air flowrate of 10 Nm^3/h injected at ambient conditions (10^5 Pa, 298.15 K). The secondary air flowrate was 25 Nm^3/h under the same standard conditions of temperature and pressure. The figure shows a reasonable agreement between computation and experiment, exhibiting both similar temporal trends and magnitudes.

The discrepancy between experimental and simulated temperature (overestimation of its maximum) can be attributed to two possible sources. First, radiative absorption is not taken into account in our computations. Species like CO_2, CO and water vapour are characterized by reasonably high absorption coefficients. Second, the presence of ash subject to melting and agglomeration at high temperatures may inhibit the air circulation through the porous medium. Nevertheless, these results show again that the self-sustained progression of the combustion front evolves from the upper to the lower layers of the bed. In addition, the appearance of an odd little peak at a given time for every fixed bed depth corresponds to the condition of maximum efficiency of reactivity because of maximum yields of CO, H_2 and C_{org} as it is shown on Figure 8. Consequently, there is a maximum heat release by reactions manifesting with a maximum temperature.

Figure 7 compares computed temporal evolutions of temperature of the solid and gas phases inside the fixed bed (zone D1) at the 5 different thermo-

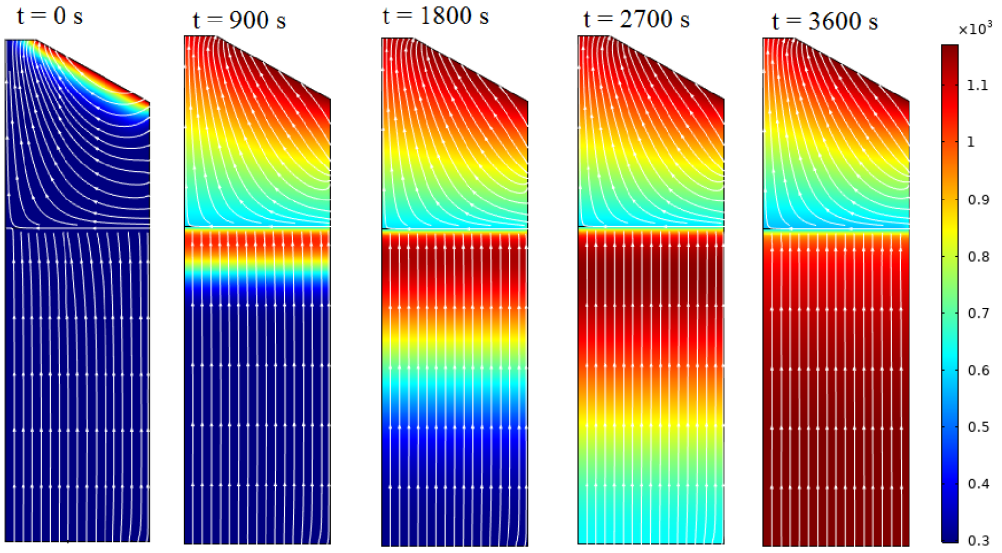

Figure 4. The temperature distribution inside the reactor at different instants.

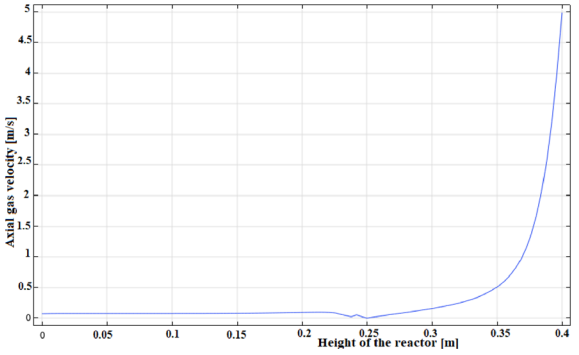

Figure 5. Gas velocity profile.

couple positions corresponding to 2, 45, 85, 165 and 205 mm. The result shows that both solid and gases phases are in thermal equilibrium inside the porous medium. Hence, it is possible to consider a single energy conservation equation and to exclude the convective term between the gas phase and the solid phase. Such an assumption can greatly simplify the model formulation and improve the efficiency of the computations.

3.3. *Gaseous emissions in the freeboard zone*

Figure 8 compares the temporal evolutions of the computed and measured gaseous emissions for O_2, CO, CO_2, H_2, CH_4, H_2O_g, and C_{org} whenever such comparisons are available. We observe the presence of discrepancies between simulated and experimental profiles: There is temporal delay between curves and simulated profiles do not exhibit the fluctuations observed in the experimental results. We believe that the discrepancy may be attributed to ash accumulation, which prevents the inlet air circulation. Moreover, the physical presence of thermocouples could affect measurements, but above all, the kinetics of reactivity should be improved.

The increase of water vapour concentration can be attributed to the fuel evaporation and to the combustion of H_2 and CH_4 as shown in (15) and (18). Moreover, the sudden decrease of O_2 concentration marks the onset of the combustion process. This process is accompanied by an increase in CO_2 and CO concentrations. One observes that the concentration of CO_2 increases rapidly and remains at a roughly constant level of about 15% (against around 14% for the experiment measurements). In contrast, the increase of concentration of CO and H_2 could be explained by the gasification of the residual char in the presence of gasifiers CO_2 and water vapour, not to mention the contributions of CH_4 reactions described by (9), (10) and (15). Moreover, the behaviour of methane gas is similar to what was reported in some numerical simulation studies in literature [4,44,52]. A decrease in H_2O, H_2, CO and CO_2 was noted at the end of the combustion process

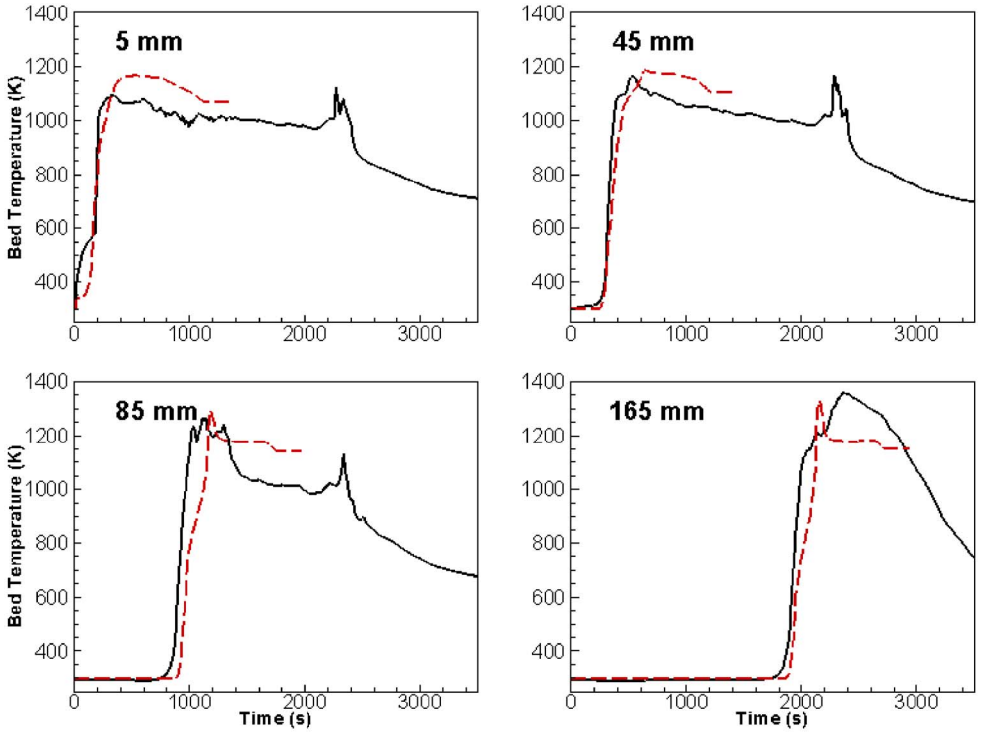

Figure 6. Comparison of temperature profiles obtained numerically and experimentally. Experiment (solid), Simulation (dashed).

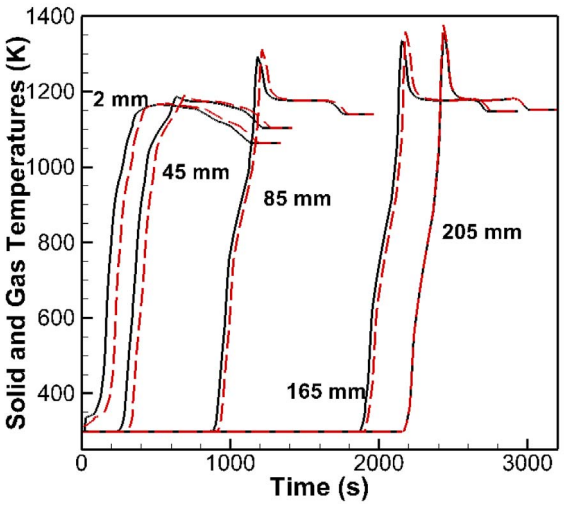

Figure 7. Simulated temperatures of the solid and gas inside the fixed bed (D1 zone). Solid temperature (solid), gas temperature (dashed).

(the fuel is completely consumed), while the O_2 mole fraction is again 21%.

Regardless, the slight difference between the simulation and the experiment in Figure 8 can be due to the sub models associated with the flow, turbulence and chemistry as well as the choice of the axisymmetric geometry. Also, during the experiment measurements certain systematic and non-systematic errors may be at the source of some fluctuations.

4. Characteristic parameters

Some characteristic parameters, which describe the combustion behaviour including the reaction front velocity, the mass conversion rate and the ignition rate are obtained from the measurements can be modelled. The comparisons of the temporal evolution of these parameters are shown in Figures 9a and b as a function of time. The comparison between these measurements and calculated parameters shows a relatively good agreement. However, these dependencies characteristics can provide a basis to transfer the fixed bed reactor to the situation of a grate incinerator.

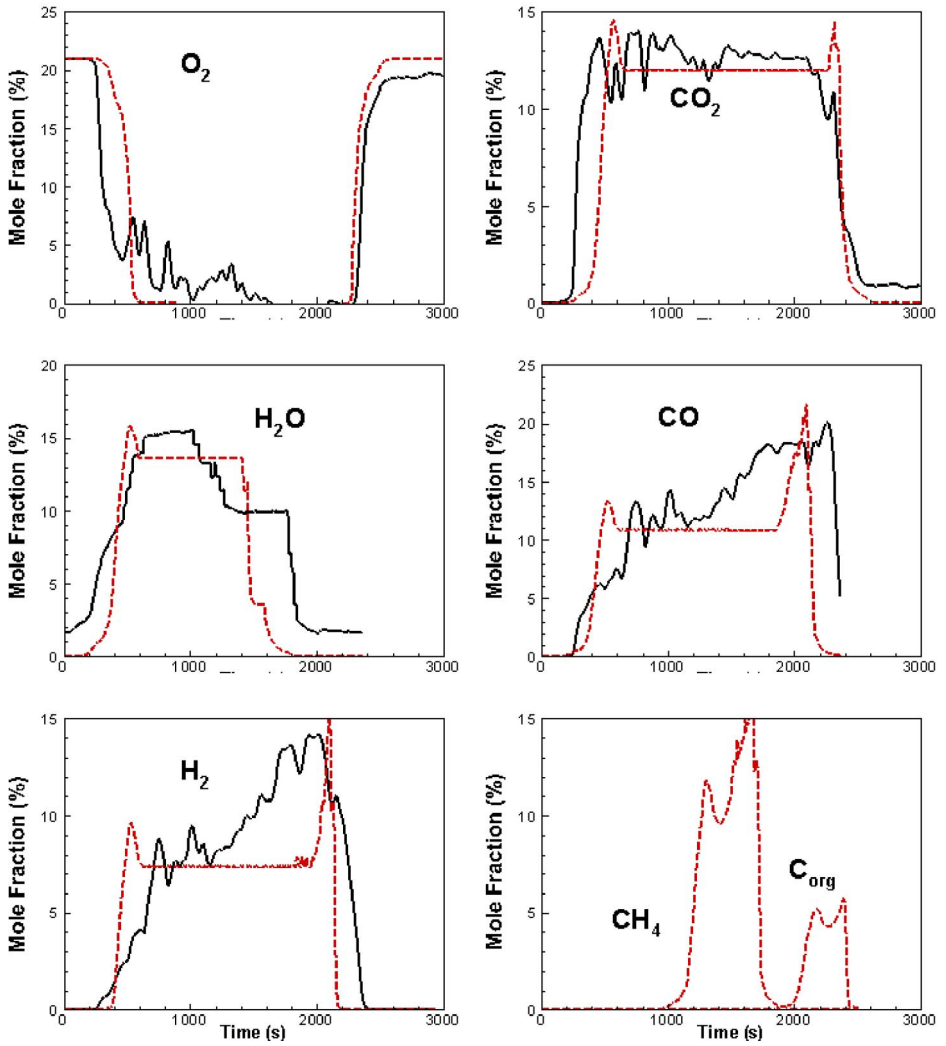

Figure 8. Gaseous emissions in the freeboard zone: comparison between simulated and experimental results. Experiment: Solid, Simulation: Dashed.

5. Main variables evolution in the model

Finally, we present profiles of the mass densities of the solid fraction (top left), the char density (top right), the moisture density (bottom left) and the dry olive pits pellets density (bottom right). These computed profiles are compared to those of the experiment in Figure 10. These modelled results correspond to the CFD simulations for the fixed bed reactor (zone D1) at time $t = 3900$ s and a primary airflow equal to 310 kg·h^{-1}·m^{-2}. The figure shows that a large zone of char density remains constant at the vicinity of 170 kg·m^{-3}. In this large zone, the primary airflow injection may not have been sufficient for a rapid consumption of the generated char. Consequently, this may have delayed the homogenous reaction of the char. This observation was also reported in the literature for the same conditions of airflow (0.05 kg·s^{-1}·m^{-2}) [49].

6. Conclusion

A transient 2D axisymmetric CFD simulation was carried out to simulate the multiphase combustion

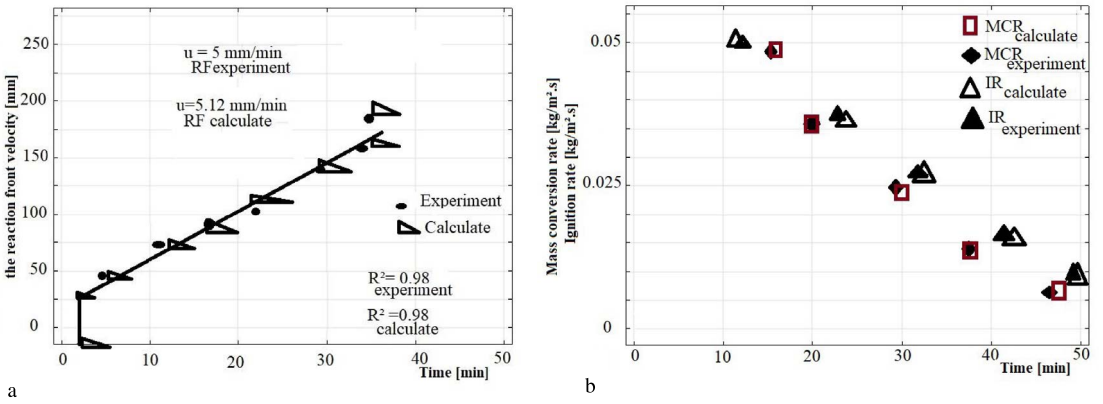

Figure 9. (a) A comparison between the measurement and the calculated of the reaction front velocity. (b) A comparison between the measurement and the calculated of the mass conversion rate and the ignition rate.

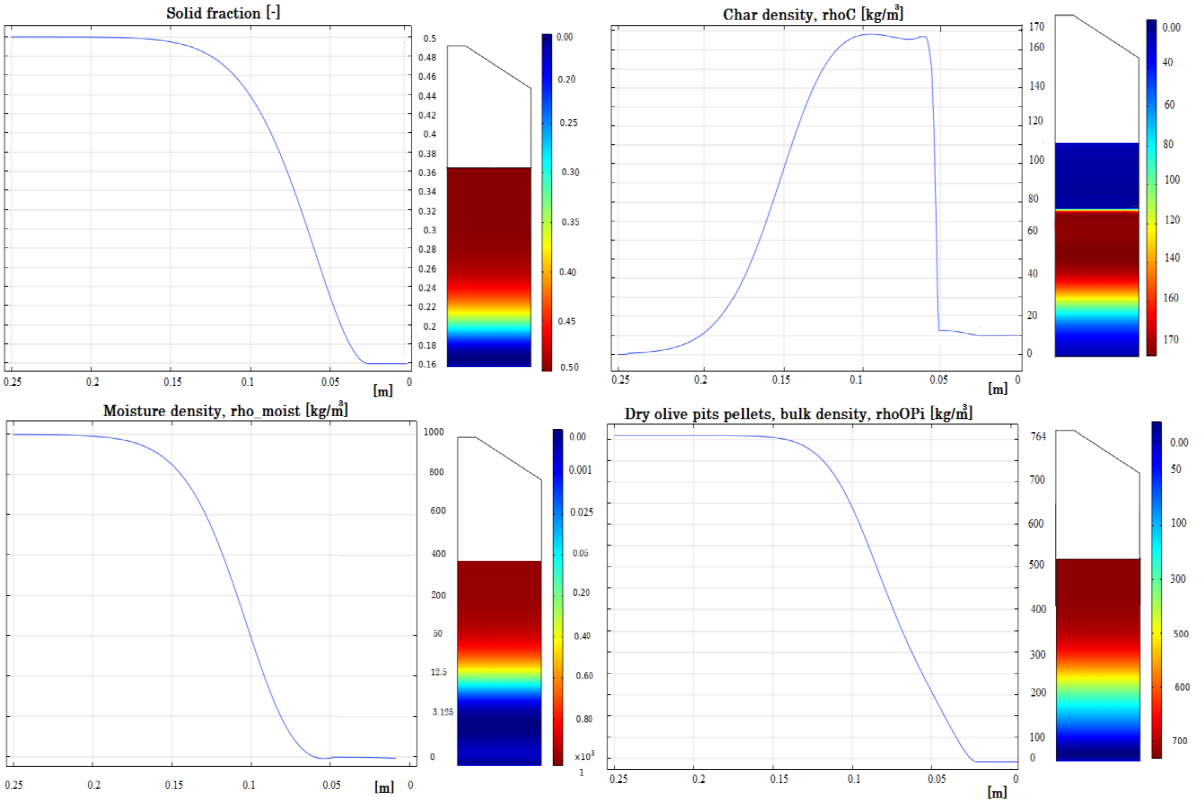

Figure 10. Evaluation of solid fraction and densities of char, moisture, and dry olive pits pellets at 3900 s.

of lignocellulosic solid biofuels (olive pits pellets) in a counter-current fixed bed reactor. The simulations were implemented using COMSOL Multiphysics 5.5. The reactor is divided into two zones: D1 and D2 representing the fixed bed and the freeboard. Reduced kinetic schemes were used in the solid and the gas

phases. Moreover, an Euler/Euler approach was used to model the porous fixed bed. The turbulent flow was described by the $k-\varepsilon$ model. Results show that the present formulation adequately reproduces experimental observations related to over-the-bed gas concentrations, temperatures and mass loss. Calculated characteristic parameters like reaction front velocity, mass conversion rate and ignition rate are reproduced in close agreement with the experiment. However, the models developed for the pilot scale fixed bed reactor can be extended to an industrial-scale plant for example using an incinerator grate.

Nomenclature

u	Velocity	$\mathrm{m{\cdot}s^{-1}}$
A	Pre-exponential factor	$\mathrm{s^{-1}}$
D	Diffusion coefficient	$\mathrm{m^2{\cdot}s^{-1}}$
Y	Mass fraction	–
S_i	Source term	$\mathrm{kg{\cdot}m^{-3}{\cdot}s^{-1}}$
p	Pressure	Pa
g	Gravitational acceleration constant	$\mathrm{m{\cdot}s^{-2}}$
C_p	Specific heat	$\mathrm{J{\cdot}kg^{-1}{\cdot}K^{-1}}$
S	Surface	$\mathrm{m^{-2}}$
h	Convective heat transfer coefficient	$\mathrm{W{\cdot}m^{-2}{\cdot}K^{-1}}$
ΔH_R	Enthalpy of reaction	$\mathrm{J{\cdot}kg^{-1}}$
Q_{rad}	Radiative source	$\mathrm{W{\cdot}m^{-3}}$
d	Diameter	m
E	Activation energy	$\mathrm{J{\cdot}kmol^{-1}}$
S_k	Source term of the turbulent energy production	$\mathrm{kg{\cdot}m^{-1}{\cdot}s^{-3}}$
S_ϵ	Source term of turbulent dissipated energy	$\mathrm{kg{\cdot}m^{-1}{\cdot}s^{-4}}$
T	Temperature	K
X, x	Mole fraction	–
R	Ideal gas constant	$\mathrm{J{\cdot}mol^{-1}{\cdot}K^{-1}}$
$\dot{w}$	Reaction rate	$\mathrm{kg{\cdot}m^{-3}{\cdot}s^{-1}}$
t	Time	s
H	Reactor height	m
z	Axial position	m
r	Net production rate of the gas species	$\mathrm{kg{\cdot}m^{-3}{\cdot}s^{-1}}$
M	Atomic molar mass	$\mathrm{kg{\cdot}mol^{-1}}$
N_u	Nusselt number	–
R_e	Reynolds Number	–
P_r	Prandtl Number	–
k	Turbulent kinetic energy	$\mathrm{m^2{\cdot}s^{-2}}$
K_R	Permeability	$\mathrm{m^2}$
r	Radial position	m
$\dot{m}$	Air flow	$\mathrm{kg{\cdot}s^{-1}}$
a	Bed cross-section	$\mathrm{m^2}$
k_i	Kinetic rate constant	$\mathrm{s^{-1}}$
f	Pressure loss	$\mathrm{N{\cdot}m^{-3}}$

Greek symbols

ε	Porosity	–
λ	Thermal conductivity	$\mathrm{W{\cdot}m^{-1}{\cdot}K^{-1}}$
μ	Dynamic viscosity	Pa·s
ρ	Density	$\mathrm{kg{\cdot}m^{-3}}$
σ	Stefan–Boltzmann constant	$\mathrm{W{\cdot}m^{-2}{\cdot}K^{-4}}$
ϵ	Turbulent kinetic energy dissipation	$\mathrm{m^2{\cdot}s^{-3}}$
λ	Stoichiometric air coefficient	–
β	Absorption coefficient	–
ω	Emissivity	–
α	Mass of the compound i produced per kg of pyrolyzed	–
$\sigma_{i,j}$	collision cross-section	Å
$\Omega_{i,j}$	collision integral	–
$\tau_{i,j}$	Stress tensor	–

Subscripts

app	Apparent
eff	Effective
t	Total
rad	Radiation
pyr	Pyrolysis
g	Gas
s	Solid
i, j	Relating to components I and j
p	Particle
v	Vaporisation
a	Ash
c or C	Carbon
CFD	Computational Fluid Dynamics

Conflicts of interest

Authors have no conflict of interest to declare.

Appendix A. Solid phase modelling

The mass conservation for the moisture, the dry OPi pellets and the residual char, respectively, are written as:

$$\frac{\partial(\varepsilon_s\rho_m)}{\partial t} = \dot{w}_{\text{moist}}\varepsilon_s \tag{17}$$

and

$$\frac{\partial(\varepsilon_s\rho_{\text{dry,olive}})}{\partial t} = -\dot{w}_{\text{pyr}}\varepsilon_s \tag{18}$$

$$\frac{\partial\left(\varepsilon_s\rho_{\text{C}}\right)}{\partial t} = (\dot{w}_{\text{pyr}} - \dot{w}_{\text{C}}^{\text{H}_2\text{O}} - \dot{w}_{\text{C}}^{\text{CO}_2} - \dot{w}_{\text{C}}^{\text{O}_2})\varepsilon_S. \tag{19}$$

The solid fraction conservation is as follows:

$$\frac{\partial\varepsilon_s}{\partial t} = \left(\frac{-\dot{w}_{\text{C}}^{\text{H}_2\text{O}} - \dot{w}_{\text{C}}^{\text{CO}_2} - \dot{w}_{\text{C}}^{\text{O}_2}}{\rho_s}\right)\varepsilon_s. \tag{20}$$

In order to take into account the bed shrinkage, the following expression is considered:

$$\frac{\partial d_p^3}{\partial t} = \left(\frac{-\dot{w}_{\text{C}}^{\text{H}_2\text{O}} - \dot{w}_{\text{C}}^{\text{CO}_2} - \dot{w}_{\text{C}}^{\text{O}_2}}{\rho_s}\right)d_p^3 \tag{21}$$

while the ash component is assumed to be inert:

$$\frac{\partial\left(\varepsilon_s\rho_a\right)}{\partial t} = 0. \tag{22}$$

In the above conservation equations; $\dot{w}_{\text{moist}}$, $\dot{w}_{\text{pyr}}$, $\dot{w}_{\text{C}}^{\text{H}_2\text{O}}$, $\dot{w}_{\text{C}}^{\text{CO}_2}$ and $\dot{w}_{\text{C}}^{\text{O}_2}$ are the rates of evaporation, pyrolysis, gasification, and combustion of the char, respectively. Accordingly, the total density can be calculated as:

$$\rho_s = Y_{\text{moist}}\rho_{\text{moist}} + Y_{\text{olive}}\rho_{\text{olive}} + Y_{\text{C}}\rho_{\text{C}}. \tag{23}$$

The energy equation is expressed as:

$$\frac{\partial\left(\varepsilon_s C_{p,s}\rho_s T_s\right)}{\partial t} - \frac{\partial}{\partial z}\left(\lambda_{\text{eff},s}\frac{\partial T_s}{\partial z}\right) - \frac{1}{r}\frac{\partial}{\partial r}\left(r\lambda_{\text{eff},s}\frac{\partial T_s}{\partial r}\right) = A_p h_{sg}\left(T_g - T_s\right) + S_s + Q_{\text{rad}}. \tag{24}$$

Here $\lambda_{\text{eff},s}$ is the solid thermal effective conductivity calculated as the sum of the solid phase conductivity and radiation, A_p is the specific surface area, h_{sg} is the convective heat transfer coefficient given in Table 2. S_s and Q_{rad} are two source terms that represent the heat release rate and radiation source, respectively. The latter is modelled as [10,15]:

$$Q_{\text{rad}}(z) = \beta\sigma(\omega_{\text{rad}}T_{\text{wall}}^4 - \omega_s T_s^4) \tag{25}$$

where, β is the absorption coefficient related to the particle diameter and the solid fraction:

$$\beta = -\frac{1}{d_p}\ln(\varepsilon_s). \tag{26}$$

The specific heat of the solid phase C_{ps} is evaluated in terms of the specific heats of its components using:

$$C_{p,s} = Y_{\text{H}_2\text{O}}C_{p,\text{H}_2\text{O}} + Y_C C_{p,C} + Y_{\text{ash}}C_{p,\text{ash}} + Y_{\text{char}}C_{p,\text{char}}. \tag{27}$$

The enthalpy is calculated as:

$$\begin{aligned}\text{H}_s = {} & \dot{w}_{\text{dry}}L_v(T_s) - \dot{w}_{\text{C}}^{\text{O}_2}\Delta_r h_{\text{C}}(T_s) \\ & - \dot{w}_{\text{C}}^{\text{H}_2\text{O}}\Delta_r h_{\text{C}}(T_s) - \dot{w}_{\text{C}}^{\text{CO}_2}\Delta_r h_{\text{C}}(T_s) \\ & - \dot{w}_{\text{dry}}(1-\alpha_{\text{C}})\Delta_r h_{\text{pyr}}(T_s)\end{aligned} \tag{28}$$

and the species conservation is insured by:

$$\frac{\partial}{\partial t}\left(\varepsilon\rho_s Y_{i,s}\right) = S_{i,s}. \tag{29}$$

Here the index i represents, the moisture, the char, and the ash, respectively.

Appendix B. The gas phase governing equations

The continuity equation and the energy conservation in the gas phase are expressed as follows:

$$\frac{\partial\left(\varepsilon_g\rho_g\right)}{\partial t} + \frac{1}{r}\frac{\partial\left(r\rho_g u_{g,r}\right)}{\partial r} + \frac{\partial\left(\rho_g u_{g,z}\right)}{\partial z} = \dot{w}_{\text{moist}} + \dot{w}_{\text{pyr}} + \dot{w}_{\text{char}} \tag{30}$$

$$\begin{aligned}&\frac{\partial}{\partial t}\left(\varepsilon_g C_{p,g}\rho_g T_g\right) + \frac{1}{r}\frac{\partial}{\partial r}\left(r\rho_g C_{p,g}u_{g,z}T_g\right) \\ &\quad + \frac{\partial}{\partial z}(\rho_g C_{p,g}u_{g,z}T_g) + \frac{1}{r}\frac{\partial}{\partial r}\left(r\rho_g\lambda_{\text{eff},g}\frac{\partial T_g}{\partial r}\right) \\ &= \frac{1}{r}\frac{\partial}{\partial r}\left(r\lambda_{\text{eff},g}\frac{\partial T_g}{\partial r}\right) + \frac{\partial}{\partial z}\left(\lambda_{\text{eff},g}\frac{\partial T_g}{\partial z}\right) \\ &\quad + \text{A}_p\text{h}_{\text{gs}}\left(T_{\text{S}} - T_g\right) - \sum_i \dot{w}_i\Delta H_i + \Phi\end{aligned} \tag{31}$$

where

$$\Phi = \sum_i r_{\text{prod},i}\int_{T_g}^{T_s} c_{\text{prod},i}\,\text{d}T. \tag{32}$$

Here, the index i represents the modelled species in the gas phase, CO_2, CH_4, H_2, CO, O_2 and H_2O_g. $\lambda_{\text{eff},g}$ is the gas thermal conductivity and $r_{\text{prod},i}$ is the rate of reaction of gaseous species. $u_{g,r}$ and $u_{g,z}$ are the radial and azimuthal gas velocity components, respectively.

Note that the thermal conductivity, the specific heat and the dynamic viscosity of the gas phase are all temperature and composition dependent. The specific heat is expressed as the weighted sum of the

species' specific heats weighted by their mass fractions of all constituents:

$$c_{p,g}(T) = \sum_i Y_i c_{p,i}(T_g) \tag{33}$$

where Y_i is the ith species mass fraction.

The thermal conductivity and the dynamic viscosity of the gas phase are expressed by [53]:

$$\lambda_g = \sum_i \left(\frac{x_i \lambda_{i,g}}{\sum_j x_i \varphi_{i,j}} \right) \tag{34}$$

$$\mu_g(T_g) = \sum_i \left(\frac{x_i \mu_i(T_g)}{\sum_j x_i \phi_{i,j}} \right). \tag{35}$$

$\varphi_{i,j}$ and ϕ_{ij} were taken directly from the literature [54]. Also, the effective thermal conductivity of the gas inside the reactor is calculated by the following correlation [34]:

$$\lambda_{\text{eff},g} = 0.8\lambda_g + 0.5 d_p c_{p,g} \rho_g \frac{u_g}{\varepsilon}. \tag{36}$$

The momentum equations in the radial and azimuthal directions are expressed by:

$$\begin{aligned}
&\frac{\partial}{\partial t}\left(\varepsilon_g \rho_g u_{g,r}\right) + u_r \frac{\partial}{\partial r}\left(\rho_g u_{g,r}\right) + u_z \frac{\partial}{\partial z}\left(\rho_g u_{g,r}\right) \\
&\quad = -\frac{\partial p}{\partial r} + \mu_e \left(\frac{1}{r}\frac{\partial}{\partial z}\left(r \frac{\partial u_{g,r}}{\partial z} \right) + \frac{1}{r}\frac{\partial}{\partial r}\left(r \frac{\partial u_{g,z}}{\partial r} \right) \right. \\
&\qquad \left. + \frac{\partial^{2u_{g,r}}}{\partial z^2} - 2\frac{u_{g,r}}{r^2} \right) + \mu_e \frac{\partial}{\partial z}\left(\frac{\partial u_{g,r}}{\partial r} \right) \\
&\qquad - \frac{2}{3}\frac{\partial}{\partial r}\left(\mu_e \left(\frac{1}{r}\frac{\partial}{\partial r}\left(r u_{g,r} \right) + \frac{\partial u_{g,z}}{\partial z} \right) + \rho k \right) \\
&\qquad + \varepsilon_g \rho_g g_r + f_r
\end{aligned} \tag{37}$$

with,

$$f_r = \frac{180 \mu_g u_{g,r} (1-\varepsilon_s)}{d^2 p \varepsilon_s^2} + \frac{1.75 \rho_g u_{g,r}^2}{d^2 p \varepsilon_s^2} \tag{38}$$

and

$$\begin{aligned}
&\frac{\partial}{\partial t}\left(\varepsilon_g \rho_g u_z\right) + u_{zr} \frac{\partial}{\partial r}\left(\rho_g u_z\right) + u_z \frac{\partial}{\partial z}\left(\rho_g u_z\right) \\
&\quad = -\frac{\partial p}{\partial z} + \mu_e \left(\frac{1}{r}\frac{\partial}{\partial r}\left(r \frac{\partial u_z}{\partial r} \right) + \frac{1}{r}\frac{\partial}{\partial r}\left(r \frac{\partial u_r}{\partial z} \right) + \frac{\partial^{2u_z}}{\partial z^2} \right) \\
&\qquad - \frac{2}{3}\frac{\partial}{\partial}\left(\frac{1}{r}\frac{\partial}{\partial r}\left(r u_r \right) + \frac{\partial u_z}{\partial z} + \rho k \right) + \varepsilon_g \rho_g g_z + f_r.
\end{aligned} \tag{39}$$

Here, the effective viscosity, μ_e, is expressed as the sum of the molecular dynamic viscosity and the turbulence viscosity.

$$\mu_e = \mu_g + \mu_t. \tag{40}$$

The turbulent viscosity μ_t, is expressed in terms of the turbulence kinetic energy, k, and its dissipation, ϵ, as follows.

$$\mu_t = \rho C_\mu \frac{k^2}{\epsilon} \quad \text{where } C_\mu = 0.09. \tag{41}$$

Here, k and ϵ are modelled using a standard low-Reynolds number $k-\epsilon$ model [55]. The species conservation equations are given by:

$$\begin{aligned}
&\frac{\partial}{\partial t}\left(\varepsilon \rho_g X_{i,g}\right) + \frac{1}{r}\frac{\partial}{\partial r}\left(r \rho_g u_{g,z} X_{i,g}\right) + \frac{\partial}{\partial z}\left(\rho_g u_{g,z} X_{i,g}\right) \\
&\quad = \frac{1}{r}\frac{\partial}{\partial r}\left(r D_{\text{eff},g} \rho_g \frac{\partial X_{i,g}}{\partial r} \right) + \frac{\partial}{\partial z}\left(D_{\text{eff},g} \rho_g \frac{\partial X_{i,g}}{\partial z} \right) + S_i.
\end{aligned} \tag{42}$$

The dispersion coefficient of the gaseous species $D_{\text{eff},g}$ is obtained according to the following correlation [10,56], which accounts for the contribution of mass diffusion and the presence of a packed bed:

$$D_{\text{eff},g} = 0.8 D_{gi,j} + 0.5 \mu_g \frac{d_p}{\varepsilon}. \tag{43}$$

In which $D_{gi,j}$ is the ith species molecular diffusivity. This mixture-averaged diffusion is evaluated using the binary diffusion coefficient, which is modelled using the Chapman–Enskog correlation [56]:

$$D_{gi,j} = 8.380 \frac{\sqrt{\frac{1}{M_i} + \frac{1}{M_i}}}{\sigma_{i,j}^2 \Omega_{i,j}} \left(\frac{T_g}{T_0} \right)^{1.81} \tag{44}$$

where T_0 is a reference temperature. The last term in the right-hand side of (42), S_i, corresponds to the ith species reaction rate.

References

[1] A. Agrifoglio, A. Fichera, A. Gagliano, R. Volpe, *C. R. Chim.*, 2021, **24**, 39-55.

[2] M. A. Gómez, J. Porteiro, D. De la Cuesta, D. Patiño, J. L. Míguez, *Energy Convers. Manage.*, 2017, **140**, 260-272.

[3] C. Yin, L. Rosendahl, S. K. Kær, S. Clausen, S. L. Hvid, T. Hille, *Energy Fuels*, 2008, **22**, 1380-1390.

[4] Y. Menard, "Modélisation de l'incinération sur grille d'ordures ménagères et approche thermodynamique du comportement des métaux lourds", PhD Thesis, Institut National polytechnique de Lorraine-INPL, 2003, Sciences de l'Ingénieur [physics].

[5] R. Mehrabian, A. Shiehnejadhesar, R. Scharler, I. Obernberger, *Fuel*, 2014, **122**, 164-178.

[6] J. Collazo, J. Porteiro, D. Patiño, E. Granada, *Fuel*, 2012, **93**, 149-159.

[7] A. Shiehnejadhesar, R. Scharler, R. Mehrabian, I. Obernberger, *Fuel Process. Technol.*, 2015, **139**, 142-158.

[8] A. Shiehnejadhesar, R. Mehrabian, R. Scharler, G. M. Goldin, I. Obernberger, *Fuel*, 2014, **126**, 177-187.

[9] M. Buchmayr, J. Gruber, M. Hargassner, C. Hochenauer, *Energy Convers. Manage.*, 2016, **115**, 32-42.
[10] N. T. M. Duffy, J. A. Eaton, *Combust. Flame*, 2013, **160**, 2204-2220.
[11] H. Mätzing, H.-J. Gehrmann, H. Seifert, D. Stapf, *Waste Manage.*, 2018, **78**, 686-697.
[12] C. Bruch, B. Peters, T. Nussbaumer, *Fuel*, 2003, **82**, 729-738.
[13] M. A. Gómez, J. Porteiro, D. De la Cuesta, D. Patiño, J. L. Míguez, *Fuel*, 2016, **184**, 987-999.
[14] B. Khiari, F. Marias, F. Zagrouba, J. Vaxelaire, *J. Clean. Prod.*, 2008, **16**, 178-191.
[15] A. Zhou, H. Xu, W. Yang, Y. Tu, M. Xu, W. Yu *et al.*, *Energy Fuels*, 2018, **32**, 9493-9505.
[16] Z. Yu, X. Ma, Y. Liao, *Renew. Energy*, 2010, **35**, 895-903.
[17] C. Galletti, V. Giomo, S. Giorgetti, P. Leoni, L. Tognotti, *Appl. Therm. Eng.*, 2016, **96**, 372-384.
[18] A. Dernbecher, A. Dieguez-Alonso, A. Ortwein, F. Tabet, *Biomass Convers. Biorefin.*, 2019, **9**, 129-182.
[19] Y. Wang, L. Yan, *Int. J. Mol. Sci.*, 2008, **9**, 1108-1130.
[20] B. Rajh, C. Yin, N. Samec, M. Hriberšek, M. Zadravec, *Energy Convers. Manage.*, 2016, **125**, 230-241.
[21] D. Merrick, *Fuel*, 1983, **62**, 534-539.
[22] Y. B. Yang, Y. R. Goh, R. Zakaria, V. Nasserzadeh, J. Swithenbank, *Waste Manage.*, 2002, **22**, 369-380.
[23] A. Anca-Couce, N. Zobel, H. A. Jakobsen, *Fuel*, 2013, **103**, 773-782.
[24] A. H. Mahmoudi, X. Besseron, F. Hoffmann, M. Markovic, B. Peters, *Chem. Eng. Sci.*, 2016, **142**, 32-41.
[25] I. Haberle, Ø. Skreiberg, J. Łazar, N. E. L. Haugen, *Prog. Energy Combust. Sci.*, 2017, **63**, 204-252.
[26] J. K. A. T. Rajika, M. Narayana, *SpringerPlus*, 2016, **5**, article no. 1166.
[27] A. Galgano, C. Di Blasi, A. Horvat, Y. Sinai, *Energy Fuels*, 2006, **20**, 2223-2232.
[28] R. Sun, T. M. Ismail, X. Ren, M. Abd El-Salam, *Waste Manage.*, 2015, **39**, 166-178.
[29] M. A. Mami, H. Mätzing, H.-J. Gehrmann, D. Stapf, R. Bolduan, M. Lajili, *Energies*, 2018, **11**, article no. 1965.
[30] R. Buczyński, R. Weber, A. Szlek, R. Nosek, *Energy Fuels*, 2012, **26**, 4767-4774.
[31] M. A. Gómez, J. Porteiro, D. Patiño, J. L. Míguez, *Fuel*, 2014, **117**, 716-732.
[32] M. Markovic, E. A. Bramer, G. Brem, *Waste Manage.*, 2014, **34**, 49-62.
[33] M. Sreekanth, D. R. Sudhakar, B. V. S. S. S. Prasad, A. K. Kolar, B. Leckner, *Fuel*, 2008, **87**, 2698-2712.
[34] H. Khodaei, Y. M. Al-Abdeli, F. Guzzomi, G. H. Yeoh, *Energy*, 2015, **88**, 946-972.
[35] Y. B. Yang, R. Newman, V. Sharifi, J. Swithenbank, J. Ariss, *Fuel*, 2007, **86**, 129-142.
[36] B. Miljković, I. Pešenjanski, M. Vićević, *Fuel*, 2013, **104**, 351-364.
[37] M. Boutaleb, M. Guiza, S. Román, B. L. Cano, S. Nogales, A. Ouederni, *C. R. Chim.*, 2020, **23**, 607-621.
[38] N. Boukaous, L. Abdelouahed, M. Chikhi, C. Mohabeer, A. H. Meniai, B. Taouk, *C. R. Chim.*, 2020, **23**, 623-634.
[39] A. A. Azzaz, M. Jeguirim, E. A. N. Marks, C. Rad, S. Jellali, M.-L. Goddard, C. M. Ghimbeu, *C. R. Chim.*, 2020, **23**, 635-652.
[40] S. Kordoghli, B. Khiari, M. Paraschiv, F. Zagrouba, M. Tazerout, *Int. J. Hydrog. Energy*, 2019, **44**, 11289-11302.
[41] P. Xu, B. Yu, *Adv. Water Resour.*, 2008, **31**, 74-81.
[42] P. Kaushal, J. Abedi, N. Mahinpey, *Fuel*, 2010, **89**, 3650-3661.
[43] R. Johansson, H. Thunman, B. Leckner, *Combust. Flame*, 2007, **149**, 49-62.
[44] J. Li, M. C. Paul, P. L. Younger, I. Watson, M. Hossain, S. Welch, *Appl. Energy*, 2015, **156**, 749-755.
[45] A. K. Biswas, K. Umeki, *Chem. Eng. J.*, 2015, **274**, 181-191.
[46] A. K. Biswas, M. Rudolfsson, M. Broström, K. Umeki, *Appl. Energy*, 2014, **119**, 79-84.
[47] C. Ryu, Y. B. Yang, A. Khor, N. E. Yates, V. N. Sharifi, J. Swithenbank, *Fuel*, 2006, **85**, 1039-1046.
[48] S. Varunkumar, N. K. S. Rajan, H. S. Mukunda, *Combust. Sci. Technol.*, 2011, **183**, 1147-1163.
[49] H. Thunman, B. Leckner, *Fuel*, 2003, **82**, 275-283.
[50] J. Porterio, D. Patiño, J. L. Miguez, E. Granada, J. Moran, J. Collazo, *Combust. Flame*, 2012, **159**, 1296-1302.
[51] M. A. Mami, M. Lajili, B. Khiari, M. Jeguirim, *Fuel*, 2020, **277**, article no. 118181.
[52] M. A. Gómez, J. Porteiro, D. Patiño, J. L. Míguez, *Fuel*, 2014, **117**, 716-732.
[53] R. B. Bird, W. E. Stewart, E. N. Lightfoot, *Transport Phenomena Revised*, 2nd ed., John Wiley & Sons, New York, 2007.
[54] J. Gosse, *Techniques de l'ingénieur Caractérisation et propriétés de la matière*, 1991.
[55] J.-C. Lezcano-Benítez, D. Correa-Restrepo, A.-A. Amell-Arrieta, F.-J. Cadavid-Sierra, *CT&F - Cienc. Tecnol. Futuro*, 2011, **4**, 89-104.
[56] W. J. Massman, *Atmos. Environ.*, 1998, **32**, 1111-1127.

Comptes Rendus
Chimie
2022, Vol. 25, Special Issue S2, p. 129-143
https://doi.org/10.5802/crchim.136

Sustainable Biomass Resources for Environmental, Agronomic, Biomaterials and Energy Applications 3 / *Ressources de biomasse durables pour des applications environnementales, agronomiques, de biomatériaux et énergétiques 3*

Biohydrogen production by *Thermotoga maritima* from a simplified medium exclusively composed of onion and natural seawater

Lamia Ben Gaida [a], Hana Gannoun [a], Laurence Casalot [b], Sylvain Davidson [b] and Pierre-Pol Liebgott [*, a, b]

[a] Université de Tunis El Manar, Laboratoire des Matériaux et de l'Environnement pour le Développement Durable, ISSBAT, 9 Avenue Zouhaïer Essafi, 1006 Tunis, Tunisia

[b] Aix-Marseille Université, Université de Toulon, IRD, CNRS MIO UM 110, 13288 Marseille, France

E-mails: lamia.bengaida@issbat.utm.tn (L. Ben Gaida), hana.gannoun@issbat.utm.tn (H. Gannoun), laurie.casalot@mio.osupytheas.fr (L. Casalot), sylvain.davidson@mio.osupytheas.fr (S. Davidson), pierre-pol.liebgott@mio.osupytheas.fr (P.-P. Liebgott)

Abstract. Biohydrogen production by the anaerobic hyperthermophilic and halophilic bacterium, *Thermotoga maritima* (TM), was conducted using a mixture of Onion Waste Juice (OWJ) and seawater (SW). The highest production of biohydrogen (H_2) with OWJ, as the exclusive source of carbon and energy, was obtained for an optimum volume of 50% (v/v), with the highest overall productivity of biohydrogen (15.6 mM/h) and a maximum yield of 2.6 (mol_{H_2}/mol_{Hexose}). This was mainly due to the presence of organosulfur compounds and the natural presence of ammonium contained in OWJ. The addition of inorganic nitrogen and iron sources in the mixture of SW and OWJ has improved biohydrogen production, achieving productivity yield (23.0 mM/h for 3.2 mol_{H_2}/mol_{Hexose}) close to the maximum obtained for TM. Above 600 mL, the high concentration of substrate (>30 gCOD/L) led the metabolism to deviate towards lactate production at the expense of H_2 production. A fed-batch culture with the sequential addition of concentrated OWJ mixed with only sea salt was investigated for the prevention of substrate-associated growth inhibition by controlling the nutrient supply. The total cumulative biohydrogen produced was about 300 mM after 30 h of incubation.

Keywords. Biohydrogen, Onion waste juice, Seawater, Dark fermentation, *Thermotoga maritima*, Hyperthermophilic, Bioreactor.
Published online: 7 February 2022

* Corresponding author.

1. Introduction

In the coming years, the increase in world population and in average per capita income would inexorably lead to the growth of fossil fuel demand. However, this heavy dependence on fossil fuels results in a series of environmental problems, e.g., global warming and air pollution, and generates sustainability problems in the face of a continuously increasing demand. Thus, to solve the energy crisis and environmental degradation, exploring clean and renewable energy alternatives is crucial [1,2].

In Tunisia, the vast majority of renewable energy capacity comes nowadays from wind (46%) and solar photovoltaic (42%) sources, which are expected to increase by 2030. With a high percentages of organic waste (nearly 70% of organic waste released in landfills) and only 12% of total energy production expected to come from biomass sources, Tunisia should consider focusing more research on renewable energy recovery from biomass. The biomass resources are often locally available as is waste. Hence, biomass allows not only waste management but also energetic conversion of fermentable waste [3].

Among the organic substrates, onion (*Allium cepa L.*) is the second most commonly cultivated vegetable worldwide, after tomatoes [4]. Its production is witnessing an annual growth given a consumer demand increase (the current annual production of onions is around 93 million tons). Simultaneously, huge amounts of onion waste are produced from different parts and onions processing, affecting the environment in various ways [5]. These onion waste materials are problematic for the industry as they are not suitable as feed for livestock due to their unpleasant smell while the phytopathogenic agents presence makes them also unsuitable as organic fertilizers [6,7]. So far, the main solution for onion waste management was to discharge it in landfills, which has high economic and environmental impacts. However, onion waste consists of a significant amount of functional components as flavonoids, organosulfur and phenolic compounds [8]; its dry weight is composed roughly of 65% of nonstructural/soluble carbohydrates including glucose, fructose, sucrose, and fructooligosaccharides, which are specific functional compounds of onion waste that should be valorized.

Onion valorization is part of some pretreatment methods based on technologies such as organic extraction, supercritical carbon dioxide, supercritical water treatment, microwave, assisted microwave, hydro diffusion, and gravity or high-pressure processing [5]. However, few studies looked into the fermentable potential of onion waste as a renewable raw material for biohydrogen production identified as a clean renewable energy carrier and an ideal candidate to replace fossil fuels [4]. Among the biological processes for waste treatment, anaerobic digestion (AD) is suggested as a truly sustainable process which can handle the contained high organic contents [9].

Dark fermentation (DF) is considered as the simplest process of anaerobic digestion of organic matter, since it is a pollution-free, renewable, and low-cost alternative to conventional processes [10]. Theoretically, in DF processes, the yield of hydrogen production depends on the bacteria involved and acid formation. The various metabolic pathways are influenced by the operating conditions (substrate concentration, pH, temperature, hydraulic retention time, reactor type, and seed sludge). Temperature is one of the most influencing factors since thermophilic conditions are widely used in H_2 production from organic waste [11]. High temperature accelerates reaction rates and offers technical advantages including reduction of viscosity, improvement of mixing efficiency, reduction of the contamination risk, absence of reactor cooling, and enhancement of hydrolysis complex substrates rate [12,13]. The majority of (hyper) thermophilic microbial species producing hydrogen belong to Clostridium, *Caldicellulosiruptor*, *Thermoanaerobacter*, *Thermotoga*, *Thermococcus,* and *Pyrococcus* genus. *Thermotoga maritima* (TM) is one of several hyperthermophilic bacteria (optimal growth temperature around 80 °C), which have received considerable interest recently as potential sources of hydrogen [14]. TM can produce H_2 at levels that approach the Thauer limit (theoretical H_2/C_{6max} = 4; [15]), using a wide range of inexpensive polysaccharide sources, such as cheese whey, molasse, potato starch, or fruit and vegetable waste [16,17]. Nevertheless, it is needed to add inorganic sulfur and nitrogen sources to enhance TM growth. These additions could be replaced by using cost-effective fruits or vegetables providing the whole essential components for its growth. Among the different fruit and vegetable, onion (*Allium cepa L.*)

is a vegetable rich in carbohydrates (structural and nonstructural) being a good source of dietary fiber and fructooligosaccharides [18] as well as organic acids [19]. It also has significant amounts of vitamins, minerals, and trace elements [20]. Moreover, onion represents one of the main sources of bioactive compounds, such as flavonols and organosulfur compounds (e.g., S-alk(en)yl-L-cysteine sulfoxides) [21], and as nitrogen inorganic source in the ammonium form [22].

In the past years, several research studies focused on the production of hydrogen from a variety of waste mixtures in the form of complex substrates, such as lignocellulosic waste, combinations of fruit and vegetable, sewage sludge, and livestock waste. However, a limited number of studies considered the energy recovery of a single waste—as a rich and complete substrate. In this study, we tested the ability of TM to ferment carbohydrates naturally present in onion in a batch stirred tank reactor (STR) supplemented with seawater. The stated objectives were (i) to use a cost-effective simplified medium providing all the needed components for TM growth and biohydrogen production and (ii) to preserve fresh water considered as a scarce resource. Thus, several onion concentrations were tested to evaluate the maximum concentration that TM could tolerate. Thereafter, to optimize biohydrogen production, essential microelements, for the optimal growth of TM, were added in low concentrations in the mixture of seawater and OWJ. Finally, a sequential fed-batch culture was conducted to remove the substrate limitation and optimize the biohydrogen production.

2. Material and methods

2.1. *Strain and culture medium*

T. maritima (TM) strain MSB8 (DSMZ 3109) was cultivated as previously described [23]. The Basal medium contained, per liter: NH_4Cl 0.5 g, K_2HPO_4 0.3 g, KH_2PO_4 0.3 g, $CaCl_2$ 0.1 g, KCl 0.1 g, NaCl 20 g, $MgCl_2$ 0.2 g, yeast extract 2.0 g and glucose 20 mM. Balch trace-mineral-element solution (10 mL) was added [23]. The inoculum was obtained from three bottles of 100 mL each, containing 50 mL of liquid culture.

2.2. *Experimental system and operating conditions*

TM was batch cultivated in a 2L well-mixed double-jacket glass bioreactor (STR) (FairMenTec, France) with a 1.5-L working volume [23]. The pH was controlled at 7.0 ± 0.1 by the addition of sodium hydroxide (NaOH = 0.5 mM) and the temperature was maintained constant at 80 ± 1 °C (Figure 1). The inlet gas stream of N_2 was controlled at 50 standard cubic centimeters per minute (SCCM) via a mass-flow meter (Bronkhorst, range 0–500 SCCM). The online measurements of bioreactor liquid volume, NaOH consumption, CO_2 and H_2 concentrations, were as previously described [23]. The stirring was set to 500 rpm. For each experiment, three successive batches were carried out. Fermentation juice samples were taken every two hours and the kinetics of substrate consumption, metabolite productions, and biohydrogen production were analyzed. The sequential fed-batch operation was carried out after a first batch mode, more precisely after the decrease of the maximal H_2 production rate. The sequential feeding in fed-batch mode was realized using a controlled peristaltic pump connected to a serum bottle containing 1 L of concentrated OWJ supplemented with 30 g/L of sea salt. Each addition was of 10% (v/v) of OWJ about the final volume of the bioreactor. During the experiments, the data of N_2 flow rates and the gas analyses (N_2, H_2, and CO_2) were recorded and used to calculate CO_2 and H_2 flows, which then led to the cumulative amounts of CO_2 and H_2 produced in the bioreactor [23].

2.3. *Culture medium for the bioreactor experiments*

A culture medium was made with natural SW taken directly from the "Bay of Gammarth" located near Tunis (Tunisia). This SW was filtered under vacuum through a 0.45 μm cellulose nitrate filter (Sartorius, Germany). White Onions used in this work came from municipal markets in Tunis. For the OWJ, onions were crushed with an electric juice extractor (OMEGA J8226) fitted with a worm screw system and an Ultem-plastic sieve to filter (0.3 mm) for the filtration and separation of liquid–solid phases. The separated OWJ was directly stored at −20 °C. First, the TM growth was studied in a rich complete medium

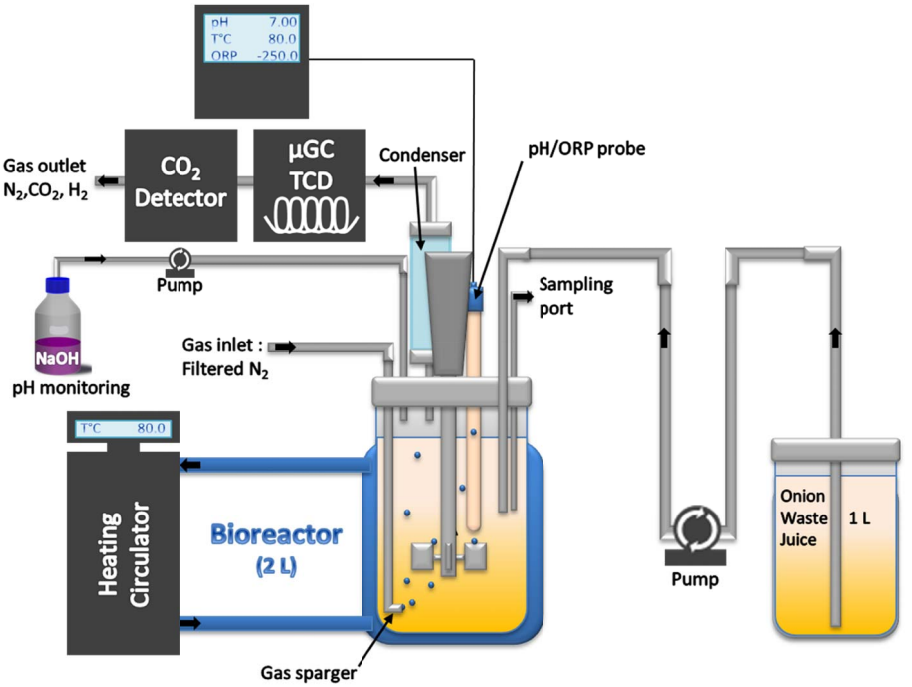

Figure 1. Experimental set-up for batch and fed-batch cultures.

in presence of 17% (v/v) of OWJ (~20 mM of Glucose and 20 mM fructose), 0.5 g/L of NH_4Cl, 0.25 g/L of Cysteine-HCl, 2 g/L of yeast extract, and 1% (v/v) of Balch's oligoelement [24], complemented at 1200 mL with natural seawater (experiment E1), to evaluate the ability of TM to ferment the sugar fraction of OWJ. Thereafter, experiments (E2, E3, E4, E5 and E6) were carried out in bioreactor using 17% of OWJ as a basal medium for biohydrogen production with and without NH_4Cl (0.5 g/L as a source of nitrogen), $FeCl_2$ (10 mg/L as a source of iron) and yeast extract (YE: 2 g/L) to evaluate (i) the efficiency of TM fermentative H_2 production using OWJ as a limiting factor and (ii) the importance of nitrogen, iron and YE in presence of onion. Elsewhere, several experiments (E2, E7, E8, E9 and E10) including respectively different volumes of OWJ (200, 400, 600, 800, and 1000 mL) supplemented with natural seawater (SW) for a final volume of 1200 mL were prepared in order to increase the TM growth and fermentative performance. The fermentability of onion waste under the best conditions was finally tested in a culture medium containing the optimal volume of OWJ.

2.4. *Analytical methods*

The total solids (TS), volatile solids (VS), humidity, chemical oxygen demand (COD) and the pH of the substrates were estimated according to the procedure listed in Standards Methods for the Examination of Water and Wastewater [25]. Glucose, acetate, lactate, and fructose concentrations were determined by HPLC as previously described [23]. Pyruvate was determined with Waters equipment comprising a 1525 pump, a 2996 diode array detector, a Rheodyne injector fitted with a 20 µl loop, a temperature control system, and a degasser. The separation was performed with an Amidex HPX-87H strong cation exchange column (Biorad 300 × 7.8 mm) protected with a pre-column. The column was thermostated at 60 °C and the mobile phase was composed of 0.01 M H_2SO_4 with a flow of 0.5 mL/min. The eluent was monitored at 210 nm. Standard solutions of pyruvate were run from 0.5 to 20 mM. The calibration curve was linear within this range. An injection volume of 20 µl was used for standard and samples. These were harvested immediately after the OWJ was added to the SW. All analyses were performed in triplicate. For

each batch experiment, liquid samples of 2 mL were collected and centrifuged for 5 min at 14,000 g. The supernatants were filtered through Minisart cellulose acetate syringe filters (0.22 μm) and the filtrate (20 μL) was then injected into the column eluted with a sulfuric acid solution (5 mM) with a fixed flow rate of 0.5 mL/min. The data were presented in the Agilent ChemStation software. The analyses were performed in triplicate and the average values were expressed in millimoles per liter corresponding to standard solutions. For total carbohydrate concentration, the anthrone sulfuric acid method was used [26] with modifications. A 0.2% solution of anthrone (w/v) was made up fresh in 75% (v/v) sulfuric acid on the day of measurement. The procedure consists in mixing a 1 mL sample with 2 mL of 75% H_2SO_4 and 4 mL of anthrone reagent by a vortex. Samples were placed on the heating block at 105 °C for 15 min and then cooled down to room temperature. The absorbance of each sample was determined at 625 nm using a UV-visible spectrophotometer. The gas produced during fermentation runs was analyzed continuously with a micro-GC and a CO_2 probe [23]. The micro-GC was dedicated to H_2 and N_2 measurements with temperatures of injector, column, and detector adjusted to 90, 120, and 100 °C, respectively. Argon was used as carrier gas with a pressure of 200 kPa. The gas-analysis frequency was 2 min.

2.5. *Determination of kinetic parameters*

It is important to note that the kinetic parameters reported to compare the efficiency of hydrogenogenic fermentation are: H_2 total production (HP in mM); H_2 production rate or H_2 productivity (HPR in mM/h) and molar H_2/C_6 yield (HY in mol_{H_2}/mol_{Hexose}). All these kinetic parameters have been obtained from experimental data and their processing using part of the models presented in [23,27].

3. Results and discussion

3.1. *Onion composition*

The sugars and pyruvate concentrations were determined in four preparations of OWJ in 1000 mL: 139 ± 14 mM of glucose; 143.2 ± 8.4 mM of fructose; 8.3 ± 2.6 mM of sucrose and 14.8 ± 1.8 mM of pyruvate (equivalent ammonium). None other volatile fatty acids or sugars were detected (Table 1). These values were close to those found in the literature with a difference related to the solubility of sugars essentially present in the juice part [8,28] and the decrease of sucrose after OWJ preparation attributed to sucrose hydrolysis to glucose and fructose due to the acidic pH of 4.0–4.8.

Table 1. Onion waste characterization (g/100 g)

Parameter	Values	Ref.
Humidity	90.3 ± 3.5	This study
Total solids (TS)	6.7 ± 0.5	
Volatile solids (%TS)	90.0 ± 1.0	
Ashes	0.7 ± 0.2	
COD	6.1 ± 0.9	
pH	4.4 ± 0.5	
Total sugars	5.7 ± 1.3	
Glucose	2.5 ± 0.2	
Sucrose	0.3 ± 0.1	
Fructose	2.6 ± 0.4	
Pyruvate/ammonium	0.13 ± 0.03	
Iron, Fe (mg/100 g)	0.21	[15]
Total protein	1.1	
Organic acids	0.17	[5]
Sulfur compounds	0.09	

The carbon to nitrogen ratio (C/N) of the onion was 15.3 [29]; this ratio was considered appropriate for prototroph anaerobic bacteria and therefore no additional nutrients were necessary [9,30].

3.2. *The onion waste juice fermentation*

The fermentative potential of onion indigenous bacterial communities was initially evaluated in anaerobic batch STR reactor with a culture medium containing 200 mL of OWJ mixed with SW in a total volume of 1200 mL (~17% OWJ) without TM (abiotic control). The operating conditions were the same than with TM culture (80 °C, pH 7.0). During these experiments, no production of H_2 nor other compounds (acetate and lactate) was observed. This

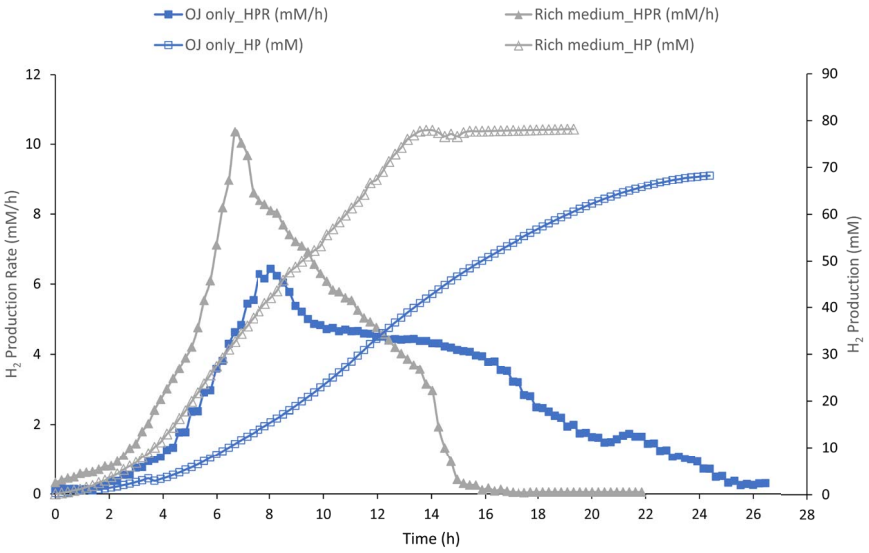

Figure 2. H_2 Production (HP, empty symbol) and H_2 production rate (HPR, full symbol) by *Thermotoga maritima* with 200 mL (17% v/v) onion waste juice (OJ) as the sole carbon and energy source (blue square) and in rich medium in presence of 200 mL onion waste juice (gray triangle).

could be explained by the absence of indigenous extremophilic and/or halotolerant microflora able to produce H_2 by fermentation.

3.2.1. *OWJ fermentation in rich medium*

To evaluate the ability of TM to ferment the sugar fraction of OWJ, rich in inhibiting compounds, the TM growth was studied in a rich complete medium in presence of 17% (v/v) of OWJ. This was considered as a complete medium limited only by the substrate (glucose). The kinetic parameters (HPR and HP) for this experiment (E1) are represented in Figure 2.

The maximal HPR with the rich medium was 10.3 mM/h ± 1.1 with a total HP of 78 mM ± 4.3. The molar H_2 yield (HY) was 2.40 (mM_{H_2}/mM_{Hexose}) (Table 2, E1). Maximal HPR of some *Thermotoga* strains was reported between 2.7 and 12.4 mM/h from equivalent carbohydrate concentrations [31]. In this condition, the H_2 productivity was close to the highest values obtained during other experiments using various biomass-based materials as feedstock [32]. In our conditions, TM was able to ferment sugars, without significant inhibition. Indeed, the onion has been used in biomedicine since antiquity and has long been known to have antibacterial, antifungal, and antiviral effects [33]. The broad-spectrum activity of onion waste juice has been attributed to phytotherapeutic sulfur compounds mainly represented by allicin [34] and by aromatic compounds. However, TM was capable to ferment the soluble sugar present in the liquid fraction of onion waste despite the presence of inhibitory compounds. We could assume that in our conditions these inhibitory compounds did not act on the strain performances. Allicin is a thermolabile compound with a half-life of approximately 17 h at 42 °C [35] which could explain its non-inhibition at 80 °C.

3.2.2. *OWJ as a basal medium for biohydrogen production*

A minimum culture medium containing only 17% of OWJ (200 mL in 1200 mL final) and SW, as a sole micro/macroelement, energy and carbon sources, was inoculated with TM (10% v/v) for a total volume of 1200 mL. The aim was to evaluate the efficiency of TM fermentative H_2 production using OWJ as a limiting factor. The results are presented in Figure 2 and Table 2, E2.

TM produced H_2 with increasing productivity reaching maximum values of 7.4 mM/h ± 0.6. The H_2 total production (or cumulative production) reached the maximum value of 71.8 mM ± 2.3 mM after 24 h of growth. In parallel, simple sugars (glucose and fructose) consumption as well as volatile fatty acids

Table 2. Average results obtained for batch fermentations for experiments in a rich medium, and in presence of only 200 mL of onion juice or supplemented with NH_4Cl, and/or $FeCl_2$ and/or YE. Each experiment was performed in triplicate

OWJ volume (ml or gram) in 1200 mL	E1 200+Rich medium	E2 200	E3 200+NH_4	E4 200+Fe	E5 200 Fe+NH_4	E6 200 Fe+NH_4+YE
Total carbohydrates (mM)	47.4 ± 2.7	44.6 ± 0.8	48.8 ± 2.9	44.0 ± 1.2	44.6 ± 1.6	46.9 ± 2.1
Glucose (mM)	22.6 ± 0.8	23.2 ± 1.2	23.7 ± 1.5	22.5 ± 1.3	21.4 ± 0.6	23.6 ± 1.5
Fructose (mM)	24.8 ± 1.8	21.4 ± 1.5	25.2 ± 3.1	21.6 ± 2.1	23.2 ± 1.3	23.4 ± 1.4
Consumed carbohydrates (mM)	32.5 ± 1.1	32.8 ± 1.7	33.9 ± 0.9	30.8 ± 1.7	31.3 ± 2.3	34.1 ± 1.0
Glucose (mM)	22.6 ± 0.8	23.2 ± 1.2	23.7 ± 1.2	22.5 ± 0.8	21.4 ± 0.7	23.6 ± 0.6
Fructose (mM)	9.9 ± 1.6	11.3 ± 1.3	10.2 ± 0.6	8.3 ± 0.6	9.9 ± 0.5	10.5 ± 0.6
Total volatil fatty acids (mM)	49.7 ± 1.1	47.7 ± 5.6	53.9 ± 4.5	45.32 ± 2.6	48.1 ± 0.8	57.2 ± 0.9
Acetate production (mM)	43.8 ± 1.9	38.6 ± 3.0	43.1 ± 2.1	39.8 ± 1.2	43.2 ± 1.6	52.0 ± 1.8
Lactate production (mM)	5.9 ± 0.5	9.1 ± 3.2	10.8 ± 0.7	5.53 ± 0.8	4.8 ± 0.4	5.2 ± 0.4
Total H_2 production (mM)	78 ± 4.3	71.8 ± 5.3	81.5 ± 5.4	76.1 ± 5.2	86.2 ± 4.6	98.0 ± 3.7
H_2 yield Y_{H_2/C_6}	2.4	2.2	2.4	2.5	2.7	2.9
Maximal H_2 production rate (mM/h)	10.3 ± 0.3	7.4 ± 0.6	7.5 ± 0.9	8.7 ± 0.3	9.4 ± 0.6	9.7 ± 0.3
Produced CO_2 (mM)	35.8 ± 3.2	32.9 ± 4.6	38.6 ± 3.7	33.8 ± 2.5	42.4 ± 2.8	47.6 ± 2.6
NH_4Cl^* (mM)	10.9 ± 0.2	1.9 ± 0.2	2.0 ± 0.2	1.9 ± 0.2	1.9 ± 0.2	1.9 ± 0.2
$Y_{H_2/acetate}$	1.78	1.86	1.89	1.91	1.99	1.88
Y_{VFA/C_6}	1.53	1.46	1.59	1.47	1.54	1.68
$Y_{Glc/Lac}$	0.18	0.28	0.32	0.18	0.15	0.15
Y_{H_2/CO_2}	2.18	2.18	2.11	2.25	2.03	2.06
$Y_{acetate/C_6}$	1.35	1.18	1.27	1.29	1.38	1.52

*NH_4Cl is the concentration equivalent to pyruvate measured.

(acetate and lactate) production by TM during the fermentation was followed by HPLC and represented in Figure 3.

Organic waste has been used for the first time as the sole carbon, oligoelement and energy source for TM growth. Onion has the particularity to contain mainly monosaccharides (glucose and fructose) which are TM choice substrates. During the fermentation (E2), the sugars concentrations gradually decreased in correlation with increasing acetate concentration, reaching a maximum value of 43.8 mM. In fact, TM can ferment soluble sugars present in the OWJ liquid fraction and produce hydrogen following the "acetate" pathway. After 22 h, glucose (22.6 mM ± 0.8), considered as a limiting substrate, was completely consumed by TM which led to growth inhibition and biohydrogen production by directing the metabolism of TM towards the "lactate" pathway. Indeed, fructose is hardly degraded by TM because it does not have a specific fructose transferase system [36].

Although TM was able to grow on onion as a sole oligoelement, carbon and energy sources, kinetic parameters obtained for the experiment with 200 mL of OWJ and SW, were lower than those obtained in complete rich medium. This demonstrated a lack of essential elements in OWJ which limit the dihydrogen production compared to a rich medium. In previous work focusing on H_2 production from organic waste, the medium culture has to contain preferen-

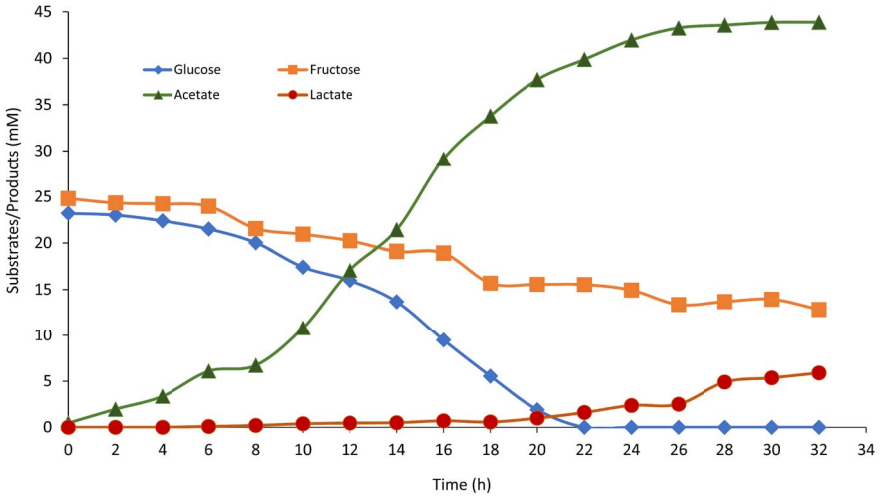

Figure 3. Simple sugar consumption (glucose: blue diamond and fructose: orange square) and volatile fatty acid production (acetate: green triangle and lactate: red circle) over time by *Thermotogamaritima* in presence of 200 mL (17% v/v) onion waste juice as the sole carbon and energy source.

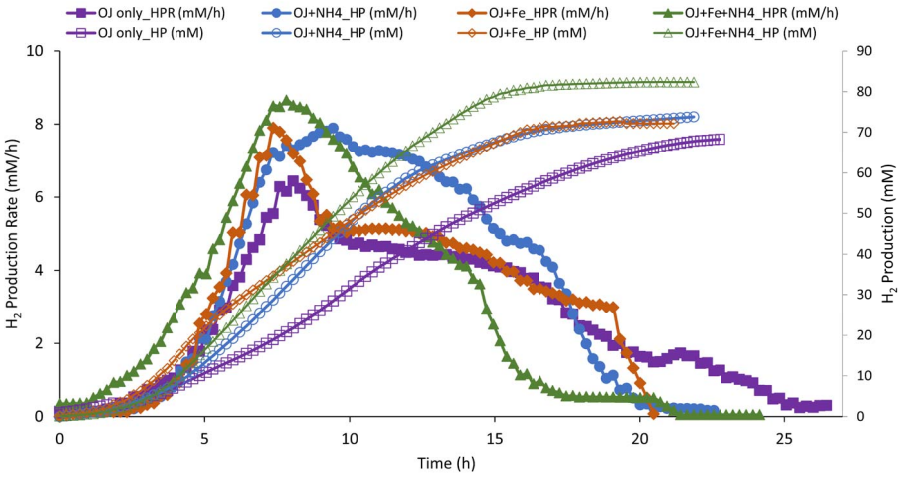

Figure 4. H_2 production (HP; empty symbol) and H_2 production rate (HPR, full symbol) by *Thermotoga maritima* with 200 mL (17% v/v) onion waste juice (OJ) as the sole carbon and energy source (purple square) plus: NH_4Cl (blue circle); $FeCl_2$ (orange diamond); $FeCl_2$+NH_4Cl (green triangle).

tially reduced sulfur compounds, an inorganic nitrogen source and oligoelements especially iron [31]. Since onion is known to be one of the richest vegetables in organsulfur compounds, represented by cysteine derivatives such as S-alk(en)yl-L-cysteine sulfoxides [21], the addition of Cys-HCl did not give any significant difference on the fermentative kinetic parameters, whatever the culture conditions tested (data not shown). In OWJ, the sulfur compounds would bring the organosulfur compounds easily assimilable by TM. Moreover, these sulfur compounds and the antioxidant ones naturally present in onion could protect TM from free radicals produced during oxidative stress. Along the same line, these sul-

fur compounds allow rapid reduction of the medium redox potential, inducing the metabolic activity initiation of TM.

3.3. *Supplied compounds for fermentation optimization*

Results of H_2 productivity and total H_2 production during fermentation from culture mediums containing NH_4Cl and/or $FeCl_2$, as a sources of nitrogen and iron respectively, are represented in Figure 4 and Table 2.

3.3.1. *Nitrogen supply*

To determine if the only ammonium source provided by OWJ was limiting for H_2 production by TM, 0.5 g/L of NH_4Cl (NH_4^+ = 9 mM) was added to 17% of OWJ mixed with SW. Results showed (Figure 4 and Table 2, E3) that HPR (7.52 mM/h ± 0.93), HY (2.41), and THP (81.5 mM ± 7.4) were appreciably equal to those obtained without the addition of nitrogen.

Nitrogen is an essential component of proteins, nucleic acids, and enzymes and thus, of a great importance for hydrogen producers. In previous study, a significant increase in biomass yields was observed with NH_4Cl feed concentrations ranging from 0.5 to 1.0 g/L in continuous culture [33]. In our conditions, OWJ preparation led to pyruvic-acid release accompanied by equimolar ammonium production. Early studies showed that the perceived pungency of fresh onions is correlated with high levels of pyruvate, a byproduct of the enzymatic hydrolysis, catalyzed by allinase, of the alliin (alkyl-cysteine sulphoxide) into allicin, pyruvic acid, and ammonium [28]. After cutting the onion, this enzyme, originally present in the vacuole, is released into the cytoplasm, where is its substrate. Under these conditions, the enzymatic transformation of this major sulfur compound by the alliinase into allicin and pyruvic acid [37] leads to the stoichiometric production of ammonium:

$$2\,\text{Alliin} \xrightarrow{\text{Alliinase}} \text{Allicin} + 2\,\text{pyruvic acid} + 2\,\text{ammonium}\,(NH_4^+)$$

The measured pyruvate concentration (ammonium equivalent) is presented in Table 2. The mix of 200 mL of OWJ and 1000 mL of SW supplied only 2 mM ± 0.2 of ammonium (~0.1 g/L) while the optimum is between 0.5–1 g/L [38].

3.3.2. *Iron supply*

Biohydrogen production requires essential oligoelements for microbial metabolism during fermentation. Among these, iron represents the most important nutrient element to form hydrogenase or other iron proteins required for almost all biohydrogen production [39].

In our conditions, iron concentrations supplied by OWJ (the natural seawater contains between 0.05–2 nM; [40]) did not exceed 0.07 mg/L (0.21 mg/100 g of fresh onion; [20]).

The Fe ion supplementation in fermentative H2 production processes influences them positively and increases the hydrogen activity [35]. Indeed, iron is a major constituent of bifurcating Fe–Fe hydrogenase in TM, the key enzyme involved in pyruvate oxidation to acetyl-CoA and CO_2 and proton reduction to molecular H_2 [41]. The Fe–Fe hydrogenase contains a bimetallic Fe–Fe active center and Fe–S centers and its limitation reduces biohydrogen production by decreasing the TM growth. A previous report revealed that temperature was a governing factor in determining the Fe^{2+} effect on hydrogen production. It was observed that optimum Fe^{2+} concentrations decreased at higher temperatures [42].

Elbeshbishy *et al.* [43] presented a summary of optimal iron concentrations in several hydrogen-producing microorganisms with concentrations ranging from 10 to 1600 mg/L. Laboratory experiments have shown that the optimal iron supply ($FeCl_2$) did not exceed 10 mg/L for an optimal fermentation with TM. Beyond this concentration, the additional iron did not increase the TM fermentative metabolism (data not shown). Thus, 10 mg/L have been supplied in media culture comprising 17% (v/v) of OWJ with SW (Figure 4, Table 2, E4). HPR (8.66 mM/h ± 0.9), HY (2.47 mol_{H_2}/mol_{Hexose}), THP (76.1 mM ± 5.2) were significantly higher than those obtained with only OWJ. Little lactate quantity (5.53 mM ± 0.8) was produced during the fermentation into an iron supply medium comparatively with 200 mL OWJ, with or without NH_4Cl (10.8 and 9.1 mM). Lactate is a byproduct of TM metabolism from the reduction of pyruvate by lactate dehydrogenase when the hydrogenase no longer oxidizes NADH [12]. Lactate levels reported during fermentation by *Thermotoga* species have varied from trace amounts up to levels rivaling that of acetate [44].

Dabrock *et al.* [45] demonstrated that a lactate significant amount was produced during glucose fermentation by *Clostridium pasteurianum* when the iron concentration was limiting. In our case, during growth in NH_4Cl condition, lack of TM iron led to process the pyruvate into acetyl-CoA and shifted its metabolism towards lactate production.

3.3.3. *Iron plus nitrogen supply*

Effect of iron on ammonia-based cultures was further investigated by adding 10 mg/L of $FeCl_2$ and 0.5 g/L of NH_4Cl to OWJ medium mixed with SW (E5). The batch culture in this condition showed a distinct improvement in the fermentation of onion waste by TM (Figure 4). The HPR, HY and THP values with NH_4Cl+$FeCl_2$ were of 9.42 mM/h ± 0.6, 2.76 and 86.2 mM ± 4.6 respectively (Table 2, E5). These values were similar to results obtained in the presence of a rich medium (10.34 mM/h ± 0.3, 2.4, 78 mM ± 4.3). Effect of yeast extract on biohydrogen production was also investigated (Figure 5, Table 2, E6). A comparison was established between H_2 productivities and maximum production rates for a mixture (200 mL OWJ+NH_4+Fe) supplemented or not with yeast extract (E6 and E5). Results showed that HPR, THP, and HY were similar with or without YE (Figure 4 and Table 2). This indicated that OWJ contained amino acids and micro/macronutrients, necessary for TM growth.

These results proved that despite the presence of appropriate materials in OWJ for TM growth, this substrate was not sufficient on its own to ensure optimal growth and H_2 productivity. It is therefore required to provide OWJ with a source of iron and inorganic nitrogen to optimize the TM fermentation performance.

3.4. *Optimization of OWJ concentration*

To increase the TM growth and fermentative performance and confirm whether the H_2 production inhibition was related to a limitation of the OWJ organic load, the experiments using different volumes of OWJ (from 0 to 1000 mL) supplemented with natural seawater (SW) were initially carried out in flasks and then in bioreactor. No production of H_2 or other compounds (acetate and lactate) was observed (data not shown) for the mixture without OWJ (only seawater). The maximum production rate, as well as the total H_2 production, is represented in Figure 6 and Table 3 (E2, E7, E8, E9 and E10) for the different volumes of OWJ (200, 400, 600, 800, and 1000 mL).

The optimum OWJ volume was 600 mL (50% of volume, v/v) (E8) with a corresponding HPR (15.6 mM/h ± 0.7) and THP (156.1 mM ± 7.5), correlated with the greater degradation of sugar (59.1 mM ± 2.5). These values were the highest compared to the other volumes used. Over 600 mL, the onion started to inhibit hydrogen production correlated with a metabolism deviation towards lactate production. The HPR (8.8 mM/h ± 1.6) and HY (2.3) decrease, correlated with high lactate production (31.5 mM ± 4.8) for a volume of 800 mL (E9), could be explained by the high substrate concentrations [11,46]. Most of the batch studies were carried out with initial substrate concentrations of 1–50 gCOD/L and a majority of these studies have suggested that initial substrate concentrations above 20 gCOD/L may decrease H_2/substrate yields via substrate inhibition for both thermophilic and mesophilic bacteria [43,47,48]. The total measured COD in the prepared OWJ was 61.2 g/L ± 9.3. At 800 mL of OWJ, the COD was about 41 gCOD/L whereas for 1000 mL of OWJ no fermentation was performed in these conditions with a COD supply of about 50 gCOD/L.

3.5. *Optimal hydrogen production from 50% OWJ (v/v)*

To evaluate the fermentability of OWJ under the best conditions, we tested the TM fermentation in a culture medium containing 50% v/v of OWJ supplemented with iron (10 mg/L of $FeCl_2$) and ammonium (0.5 g/L of NH_4Cl). This experiment provided a total production of 272.4 mM of biohydrogen. The maximum HPR and HY were also increased to 23 mM/h and 3.2 mol_{H_2}/mol_{Hexose} respectively. These values were close to the highest obtained with TM during a batch culture, under pH and temperature regulation conditions. Interestingly, the addition of YE in the latter condition showed a significant decrease in the kinetic parameters (Figure 7). The addition of YE could lead to a fermentative process limitation due to a COD increase in the culture medium. As beyond about 30 gCOD/L, TM seemed to undergo an inhibition by the substrate. The exact

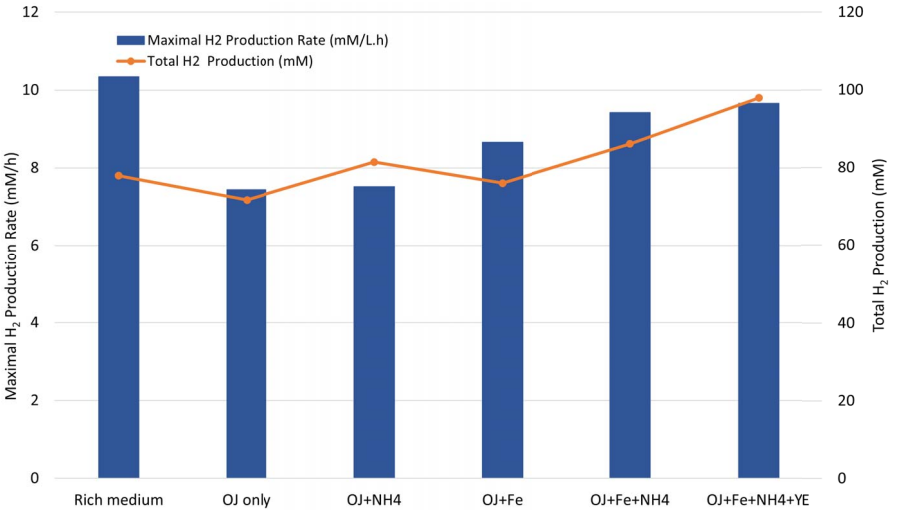

Figure 5. Maximal H_2 production rate (blue bar chart) and total H_2 production (orange curve) by *Thermotoga maritima* with 200 mL (17% v/v) onion waste juice (OJ) as the sole carbon and energy source (OJ only) plus: NH_4Cl (OJ+NH_4); $FeCl_2$ (OJ+Fe); $FeCl_2$+NH_4Cl (OJ+Fe+NH_4); $FeCl_2$+NH_4Cl+YE (OJ+Fe+NH_4+YE).

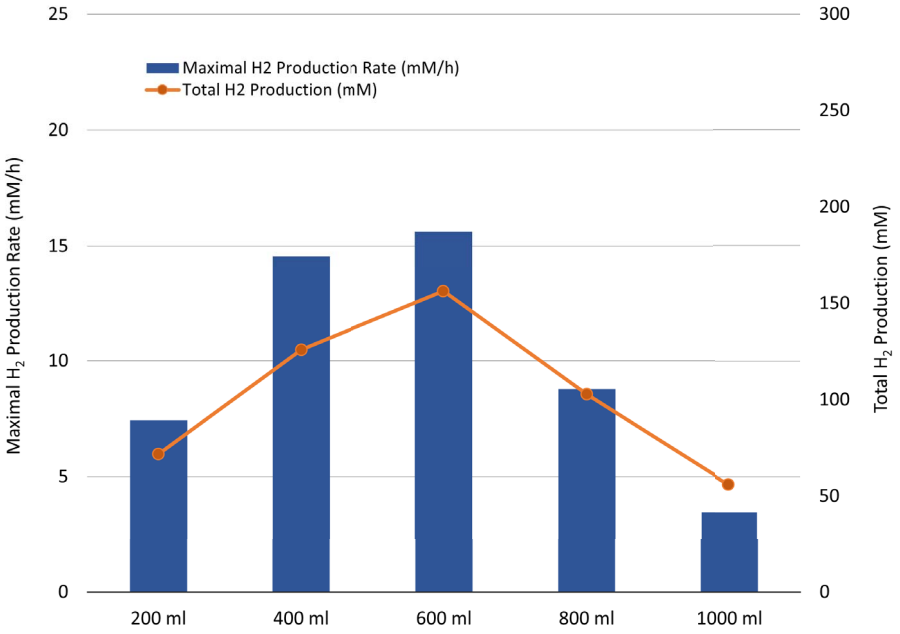

Figure 6. Maximal H_2 production rate (blue bar chart) and total H_2 production (orange curve) by *Thermotoga maritima* with increasing volumes of onion waste juice (OJ) (for 1200 mL final volume: 200; 400; 600; 800 and 1000 mL of onion waste juice).

Table 3. Average results obtained for batch fermentations for experiments in different volumes of onion juice. Each experiment was performed in triplicate, except for the condition with 1000 mL of onion juice performed only in duplicate

OWJ volume (ml or gram) in 1200 mL	E2	E7	E8	E9	E10
	200	400	600	800	1000
Total carbohydrates (mM)	44.6 ± 2.1	93.2 ± 3.9	131.6 ± 5.2	189 ± 6.3	255.6
Glucose (mM)	23.2 ± 1.2	45.4 ± 2.8	71.6 ± 1.2	111.6 ± 1.4	130.2
Fructose (mM)	21.4 ± 1.5	49.8 ± 3.2	61.6 ± 4.9	76.2 ± 9.2	125.4
Consumed carbohydrates (mM)	32.8 ± 1.7	56.3 ± 3.8	59.01 ± 2.5	44.6 ± 1.3	nd
Glucose (mM)	23.2 ± 1.2	35.6 ± 0.8	37.16 ± 0.5	39.26 ± 1.2	nd
Fructose (mM)	11.3 ± 1.3	20.7 ± 1.3	21.85 ± 1.4	5.34 ± 0.8	nd
Total volatil fatty acids (mM)	47.7 ± 5.6	83.3 ± 7.4	97.9 ± 4.8	88.3 ± 3.7	nd
Acetate production (mM)	38.6 ± 6.0	72.6 ± 3.6	82 ± 3.2	56.8 ± 4.6	nd
Lactate production (mM)	9.1 ± 3.2	10.7 ± 2.3	15.9 ± 3.6	31.5 ± 4.8	nd
Total H_2 production (mM)	71.8 ± 5.3	125.7 ± 9.6	156.1 ± 7.5	102.6 ± 10.8	55.9
H_2 yield Y_{H_2/C_6}	2.2	2.2	2.6	2.3	nd
Maximal H_2 production rate (mM/h)	7.4 ± 0.6	14.6 ± 0.9	15.6 ± 0.7	8.8 ± 1.6	1.5
Produced CO_2 (mM)	32.9 ± 4.6	55.6 ± 5.7	70.7 ± 10.3	69.5 ± 5.3	nd
NH_4Cl^* (mM)	1.9 ± 0.2	3.9 ± 0.3	5.9 ± 0.6	7.0 ± 0.7	9.2
$Y_{H_2/acetate}$	1.86	1.73	1.90	1.81	nd
Y_{VFA/C_6}	1.46	1.48	1.66	1.98	nd
$Y_{Glc/Lac}$	0.28	0.19	0.27	0.71	nd
Y_{H_2/CO_2}	2.18	2.26	2.21	1.48	nd
$Y_{acetate/C_6}$	1.18	1.29	1.39	1.27	nd

*NH_4Cl is the concentration equivalent to pyruvate measured. Nd: not defined.

inhibitory substrate concentration requires further experiments in synthetic culture medium in the presence of increasing concentrations of glucose and YE, while following conventional growth kinetic parameters (growth rate, H_2 productivity, total H_2 production ...). However, these results showed that the YE contribution seems unnecessary to improve the OWJ nutritional intake, which consequently would contribute to reducing the synthetic compounds price in feedstocks.

3.6. *Optimization of fermentation mode*

Most of the dark fermentation studies for hydrogen gas production from feedstock substrates were performed by discontinuous cultures. Batch fermentations are usually subject to substrate and product limitations yielding low hydrogen gas productivities. In our conditions, above 50% v/v of OWJ (31 gCOD/L), hydrogen production decreased due to the inhibition by the substrate charge. In this case, the fed-batch operation could have considerable advantages as compared to batch operation and could be used to overcome substrate/product and toxic compound inhibitions encountered at high substrate concentrations. The substrate solution was added with a rate sufficient to support the bacterial community and to eliminate the substrate inhibition with no effluent removal. To develop a larger-scale H_2 production system in overcoming the problem linked to the substrate limitation in batch cultures, fermentation in the fed-batch mode was carried out with OWJ addition in different stages (Figure 8). Each addition of concentrated OWJ mixed with sea salt was performed when the HPR began to decrease. Figure 8

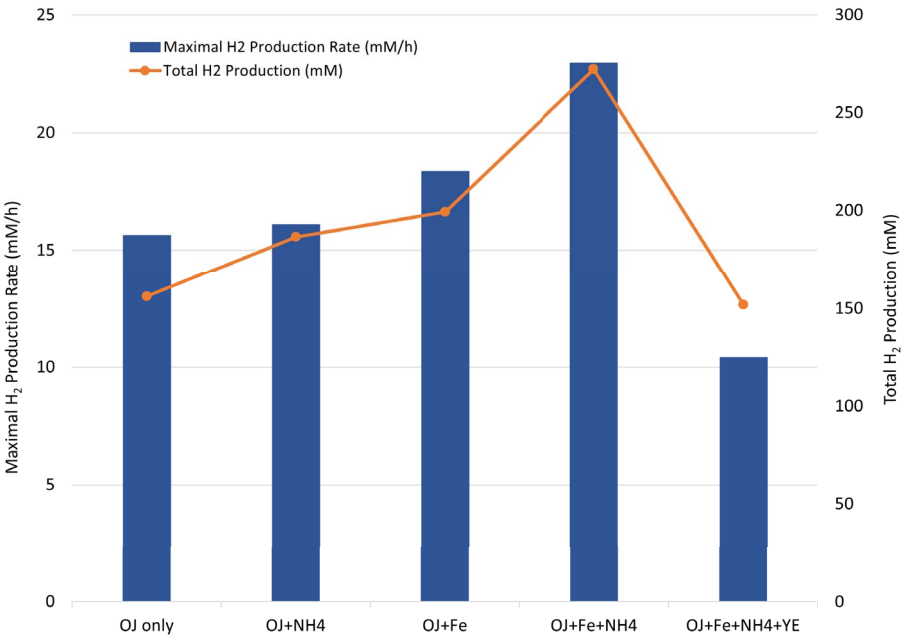

Figure 7. Maximal H_2 production rate (blue bar chart) and total H_2 production (orange curve) by *Thermotoga maritima* with 600 mL (50% v/v) onion waste juice (OJ) as the sole carbon and energy source (OJ only) plus: NH_4Cl (OJ+NH_4); $FeCl_2$ (OJ+Fe); $FeCl_2$+NH_4Cl (OJ+Fe+NH_4); $FeCl_2$+NH_4Cl+YE (OJ+Fe+NH_4+YE).

shows the comparison between batch and fed-batch cultures with 50% OWJ as the only sources of oligoelements, energy and carbon. The first addition of 120 mL of OWJ (10% v/v) in the batch culture condition was made one hour after the HPR was decreased. H_2 production increased again but with a significant decrease in the previous maximum hydrogen production rate (Figure 8). Subsequent additions showed the same effect with an overall decrease in H_2 production. As noted, ammonium and iron are essential for optimal growth. Cell multiplication is dependent on these micro/macro elements. In our Fed-batch experiments, we assumed that the lack of iron and ammonium led to this decrease in hydrogen production combined with a significant COD-increasing effect. However, this experiment showed that it is possible to exceed the limiting concentration of COD in our culture media with TM. After four additions and about 40 h of growth, the maximum H_2 production reached 330 mM. Under optimal conditions with iron and ammonium addition, this H_2 production was doubled (data not shown) showing the efficiency of the fed-batch operation with TM to produce biohydrogen from OWJ.

4. Conclusion

Onion is one of the world's most versatile and traded vegetables (85 million tons) generating a lot of waste at a low cost. These waste materials represent an environmental problem since they are not suitable, in high concentration, for livestock feeding due to onion unpleasant smell and as an inorganic fertilizer given the rapid herbicide and antimicrobial agents development. To date, only few studies focused on the onion waste recycling process for the production of value-added by-products as functional compounds, or of biogas (methane and H_2) by anaerobic digestion [26]. In this work, biohydrogen fermentation by *Thermotoga maritima* (TM) was successfully performed from a mixture of Onion Waste Juice and seawater, in a batch STR system. The presented results indicated that the highest H_2 production parameters were obtained for mixture of OWJ

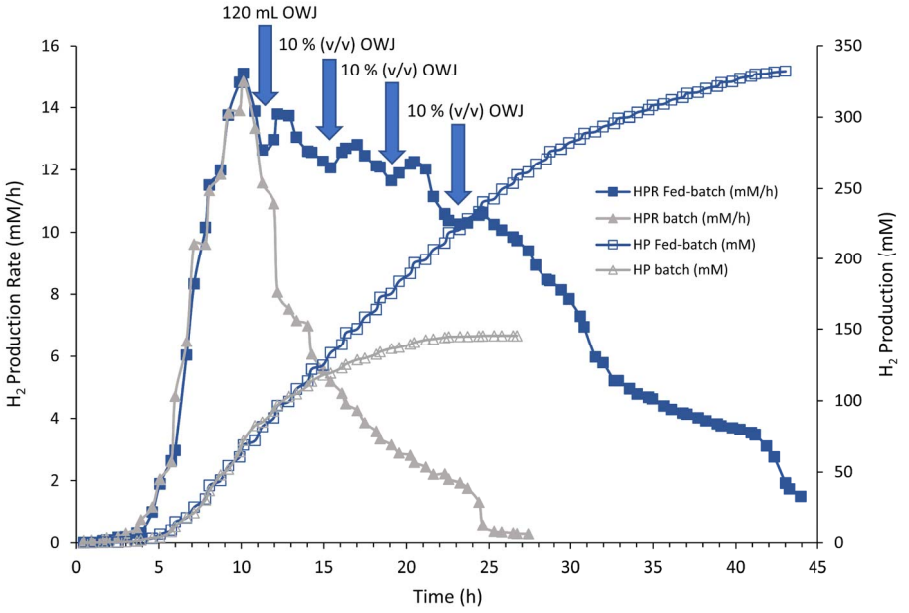

Figure 8. H_2 production (HP; empty symbol) and H_2 production rate (HPR, solid symbol) by *Thermotoga maritima* with 600 ml (50% v/v) onion waste juice (OWJ) as the sole carbon and energy source under batch (gray triangle) and fed-batch (blue square) conditions. In the fed-batch operation, an initial addition of 120 ml of onion waste juice was performed followed by the sequential addition of 10% (v/v) of the initial volume of the culture medium.

with SW and iron/ammonium input. These results were nearly 1.3-fold greater than those in batch cultures without iron/ammonium supply. The fed-batch culture of TM in the 2-L STR bioreactor showed a high production of H_2 despite a COD above 30 gCOD/L. The maximal H_2 production achieved was 330 mM at 40 h. These results could potentially be used in assessing the feasibility of TM use in OWJ conversion into H_2 on an industrial scale.

Conflicts of interest

Authors have no conflict of interest to declare.

Acknowledgements

This work received financial support from the IRD JEAI program (JEAI BIOTECH2). The authors are grateful to Richard Auria, Guillaume Pillot, Yannick Combet-Blanc and Jean Lorquin for their support. Many thanks to the Higher Institute of Applied Biological Sciences of Tunis (ISSBAT) and Tunisian Ministry of Higher Education and Scientific Research for providing their facilities to the research team.

References

[1] N. Boukaous, L. Abdelouahed, M. Chikhi, C. Mohabeer, A. H. Meniai, B. Taouk, *C. R. Chim.*, 2021, **23**, 623-634.
[2] M. Jeguirim, S. Jellali, B. Khiari, *C. R. Chim.*, 2020, **23**, 583-587.
[3] H. Hammani, M. El Achaby, K. El Harfi, M. A. El Mhammedi, A. Aboulkas, *C. R. Chim.*, 2020, **23**, 589-606.
[4] J. S. Sidhu, M. Ali, A. Al-Rashdan, N. Ahmed, *J. Food Sci. Technol.*, 2019, **56**, 1811-1819.
[5] K. Sharma, N. Mahato, S. H. Nile, E. T. Lee, Y. R. Lee, *Food Funct.*, 2016, **7**, 3354-3369.
[6] A. Chorolque, G. Pellejero, M. C. Sosa, J. Palacios, G. Aschkar, C. García-Delgado, R. Jimvénez-Ballesta, *Int. J. Environ. Sci. Technol.*, 2021.
[7] K. Waldron, *Food Sci. Technol. Today*, 2001, **15**, 38-39.
[8] L. Liguori, R. Califano, D. Albanese, F. Raimo, A. Crescitelli, M. Di Matteo, *J. Food Quality*, 2017, **2017**, 1-9.
[9] S. Zara, R. Rihani, W. Blel, F. Bentahar, *C. R. Chim.*, 2021, **24**, 1-15.
[10] A. Tamošiūnas, P. Valatkevičius, V. Valinčius, R. Levinskas, *C. R. Chim.*, 2016, **19**, 433-440.

[11] T. de Vrije, M. A. W. Budde, S. J. Lips, R. R. Bakker, A. E. Mars, P. A. M. Claassen, *Int. J. Hydrog. Energy*, 2010, **35**, 13206-13213.
[12] M. R. A. Verhaart, A. A. M. Bielen, J. van der Oost, A. J. M. Stams, S. W. M. Kengen, *Environ. Technol.*, 2010, **31**, 993-1003.
[13] O. Elsharnouby, H. Hafez, G. Nakhla, M. H. El Naggar, *Int. J. Hydrog. Energy*, 2013, **38**, 4945-4966.
[14] C.-J. Chou, F. E. Jenney, M. W. W. Adams, R. M. Kelly, *Metabol. Eng.*, 2008, **10**, 394-404.
[15] R. Thauer, "Limitation of microbial H_2-formation via fermentation", in *Microbial Energy Conversion* (H. G. Schlegel, J. Barnea, eds.), Pergamon, 1977, 201-204.
[16] M. Cappelletti, G. Bucchi, J. De Sousa Mendes, A. Alberini, S. Fedi, L. Bertin, D. Frascari, *J. Chem. Technol. Biotechnol.*, 2012, **87**, 1291-1301.
[17] R. Saidi, P. P. Liebgott, H. Gannoun, L. Ben Gaida, B. Miladi, M. Hamdi, H. Bouallagui, R. Auria, *Waste Manag.*, 2018, **71**, 474-484.
[18] L. Jaime, E. Mollá, A. Fernández, M. A. Martín-Cabrejas, F. J. López-Andréu, R. M. Esteban, *J. Agric. Food Chem.*, 2002, **50**, 122-128.
[19] B. Rodríguez Galdón, E. M. Rodríguez Rodríguez, C. Díaz Romero, *J. Food Sci.*, 2008, **73**, C599-C605.
[20] S. Pareek, N. A. Sagar, S. Sharma, V. Kumar, "Onion (*Allium cepa* L.)", in *Fruit and Vegetable Phytochemicals* (E. M. Yahia, ed.), John Wiley & Sons, Ltd, Chichester, 2017, 1145-1162.
[21] C. Colina-Coca, B. de Ancos, C. Sánchez-Moreno, *Food Bioproc. Tech.*, 2014, **7**, 289-298.
[22] L. J. W. Shimon, A. Rabinkov, I. Shin, T. Miron, D. Mirelman, M. Wilchek, F. Frolow, *J. Mol. Biol.*, 2007, **366**, 611-625.
[23] C. Boileau, R. Auria, S. Davidson, L. Casalot, P. Christen, P.-P. Liebgott, Y. Combet-Blanc, *Biotechnol. Biofuels*, 2016, **9**, 269-286.
[24] W. E. Balch, G. E. Fox, L. J. Magrum, C. R. Woese, R. S. Wolfe, *Microbiol. Rev.*, 1979, **43**, 260-296.
[25] A.A. WEF, *Standard Methods for the Examination of Water and Wastewater*, 21st ed., American Public Health Association, American Water Works Association, Water Environmental Federation, Washington DC, 2005.
[26] K. Raunkjær, T. Hvitved-Jacobsen, P. H. Nielsen, *Water Res.*, 1994, **28**, 251-262.
[27] R. Auria, C. Boileau, S. Davidson, L. Casalot, P. Christen, P. P. Liebgott, Y. Combet-Blanc, *Biotechnol. Biofuels*, 2016, **9**, article no. 268.
[28] C. J. Clark, M. L. Shaw, K. M. Wright, J. A. McCallum, *J. Sci. Food Agric.*, 2018, **98**, 5525-5533.
[29] J. A. Domínguez-Maldonado, L. Alzate-Gaviria, H. A. Milquez-Sanabria, R. Tapia-Tussell, R. M. Leal-Bautista, E. I. España-Gamboa, *Waste Biomass Valor.*, 2020, **11**, 4181-4194.
[30] R. T. Romano, R. Zhang, *Bioresour. Technol.*, 2008, **99**, 631-637.
[31] M. Lanzilli, N. Esercizio, M. Vastano, Z. Xu, G. Nuzzo, C. Gallo, E. Manzo, A. Fontana, G. d'Ippolito, *Int. J. Mol. Sci.*, 2020, **22**, article no. 341.
[32] N. Esercizio, M. Lanzilli, M. Vastano, S. Landi, Z. Xu, C. Gallo, G. Nuzzo, E. Manzo, A. Fontana, G. d'Ippolito, *Resources*, 2021, **10**, article no. 34.
[33] A. Hannan, T. Humayun, M. B. Hussain, M. Yasir, S. Sikandar, *J. Ayub Med. Coll. Abbottabad*, 2010, **22**, 4.
[34] M. Focke, A. Feld, H. K. Lichtenthaler, *FEBS Lett.*, 1990, **261**, 106-108.
[35] H. Fujisawa, K. Suma, K. Origuchi, T. Seki, T. Ariga, *Biosci. Biotechnol. Biochem.*, 2008, **72**, 2877-2883.
[36] A. D. Frock, S. R. Gray, R. M. Kelly, *Appl. Environ. Microbiol.*, 2012, **78**, 1978-1986.
[37] J. R. Bacon, G. K. Moates, A. Ng, M. J. C. Rhodes, A. C. Smith, K. W. Waldron, *Food Chem.*, 1999, 5.
[38] K. D. Rinker, R. M. Kelly, *Biotechnol. Bioeng.*, 2000, **69**, 537-547.
[39] G. J. Schut, M. W. W. Adams, *J. Bacteriol.*, 2009, **191**, 4451-4457.
[40] E. P. Achterberg, T. W. Holland, A. R. Bowie, R. F. C. Mantoura, P. J. Worsfold, *Anal. Chim. Acta*, 2001, **442**, 1-14.
[41] D.-J. Lee, K.-Y. Show, A. Su, *Bioresour. Technol.*, 2011, **102**, 8393-8402.
[42] Y. Zhang, J. Shen, *Int. J. Hydrog. Energy*, 2006, **31**, 441-446.
[43] E. Elbeshbishy, B. R. Dhar, G. Nakhla, H.-S. Lee, *Renew. Sustain. Energy Rev.*, 2017, **79**, 656-668.
[44] A. D. Frock, J. S. Notey, R. M. Kelly, *Environ. Technol.*, 2010, **31**, 1169-1181.
[45] B. Dabrock, H. Bahl, G. Gottschalk, *Appl. Environ. Microbiol.*, 1992, **58**, 1233-1239.
[46] S.-H. Kim, S.-K. Han, H.-S. Shin, *Process Biochem.*, 2006, **41**, 199-207.
[47] D. Frascari, M. Cappelletti, J. D. S. Mendes, A. Alberini, F. Scimonelli, C. Manfreda, L. Longanesi, D. Zannoni, D. Pinelli, S. Fedi, *Bioresour. Technol.*, 2013, **147**, 553-561.
[48] H. Argun, P. Gokfiliz, I. Karapinar, "Biohydrogen production potential of different biomass sources", in *Biohydrogen Production: Sustainability of Current Technology and Future Perspective* (A. Singh, D. Rathore, eds.), Springer India, New Delhi, 2017, 11-48.

Comptes Rendus
Chimie
2022, Vol. 25, Special Issue S2, p. 145-153
https://doi.org/10.5802/crchim.180

Sustainable Biomass Resources for Environmental, Agronomic, Biomaterials and Energy Applications 3 / *Ressources de biomasse durables pour des applications environnementales, agronomiques, de biomatériaux et énergétiques 3*

Enhanced transesterification of rapeseed oil to biodiesel catalyzed by KCl/CaO

Shuang Tao [a], Zhang Li [a], Fangling Qin [a, b], Shijun Chen [a], Zhou Rui [b] and Ying Tang*, [a]

[a] Shaanxi Province Key Laboratory of Environmental Pollution Control and Reservoir Protection Technology of Oilfields, Xi'an Shiyou University, Xi'an 710065, China

[b] State Key Laboratory of Petroleum Pollution Control, Xi'an Shiyou University, Xi'an 710065, China

E-mails: 2449317972@qq.com (S. Tao), zhangli@xsyu.edu.cn (Z. Li), flqin@xsyu.edu.cn (F. Qin), csjun@xsyu.edu.cn (S. Chen), 1670063100@qq.com (Z. Rui), tangying78@xsyu.edu.cn (Y. Tang)

Abstract. A series of supported solid base catalysts were prepared by impregnation of chloride salts over CaO. The catalytic activity of the prepared catalysts was tested for the transesterification reaction of biodiesel from rapeseed oil and methanol. The KCl/CaO catalyst containing 15% KCl exhibited the highest catalytic activity after calcination at 600 °C for 6 h. A reaction optimization study was carried out using KCl/CaO as catalyst leading to operation conditions for achieving a 98.3% yield of fatty acid methyl ester (FAME) at 2.5 h and 65 °C, a catalyst amount of 10%, and a mole ratio of methanol to rapeseed oil of 15:1. It was found that the highest FAME yield at 2.5 h was faster than that at 6 h for commercial CaO catalysts under the same reaction conditions. The characterization results showed that the pore size of CaO particles was greatly improved by the addition of KCl, which facilitated better access of the reactive molecules to the active sites of the catalyst.

Keywords. Basicity, Biodiesel, Heterogeneous catalysis, KCl/CaO, Rapeseed oil.

Published online: 16 May 2022

1. Introduction

Biodiesel is a promising candidate as an alternative clean fuel due to its distinctive properties such as non-toxicity, low-sulfur content, easy biodegradability, renewable and low harmful gas emissions [1,2]. In recent years, production processes and technologies for biodiesel have been relatively mature and promising [3]. However, it has some disadvantages that hinder its large-scale production, such as high product cost [4], and low reaction rate [5].

Many catalytic systems have been reported for the transesterification reaction of rapeseed oil and methanol, such as acid catalysts, alkali and enzymes [6–8]. In homogeneous acid or alkali catalyzed biodiesel productionss, the catalyst is characterized by high catalytic activity and catalytic rate, but the post-treatment is complicated [9]. Transesterification reactions using enzyme catalysts have been es-

* Corresponding author.

tablished to simplify the separation process of catalysts from products. However, enzyme catalysts are susceptible to poisoning and exhibit low selectivity [10]. Among them, heterogeneous acid base catalysts have attracted much attention because they can overcome the problems posed by other catalysts [11,12]. CaO is a commonly used basic catalyst for transesterification reactions, which is attributed to its cost-effectiveness, high activity, superior basicity, and easy availability of raw materials [13,14]. Liu *et al.* [15] described the transesterification process for the conversion of soybean oil to biodiesel using CaO as a solid catalyst. The reaction was carried out using a 1:12 molar ratio of soybean oil to methanol, a catalyst concentration of 8 wt% (in terms of oil weight) at a temperature of 65 °C within a reaction time of 3 h, and a 95% yield of biodiesel. Tang *et al.* [16] reported that nano-CaO with different particle sizes and crystallinity was prepared by sol–gel method, which exhibited better catalytic performance than commercial CaO for biodiesel production under the same reaction conditions. The best reaction was achieved at 1:1:8 molar ratio of oil to DMC to methanol, 5 wt% nano-CaO catalyst (calcined at 800 °C), and, 65 °C reaction temperature, and the fatty acid methyl ester yield exceeding 4 h was 92%, which is 2 h shorter than that of commercial CaO. Degfie *et al.* [17] prepared nano-CaO via thermal decomposition and used it as a catalyst to valorize waste cooking oil to biodiesel. It was revealed that the highest conversion of 96% was obtained at optimized reaction conditions of 50 °C, methanol/oil ratio of 8, and catalyst dosage of 1 wt% with a reaction time of 90 min. Another notable source of CaO for biodiesel synthesis could be derived from waste shells. Eggshells and aquatic shells have been widely reported as renewable and inexpensive CaO sources to replace rapidly depleting chemicals. Santos *et al.* [18] developed microstructured CaO from chicken eggshells by calcination at 850 °C for 3 h and then used it for biodiesel synthesis from soybean oil. They reported a yield of 84.53% at a catalyst loading of 5 wt%, which is lower than some other studies that used chicken, oyster, duck, or ostrich shells. Apart from this, doped and loaded versions of other modified CaO-based catalyst materials have also been reported. Maryam *et al.* [19] reported the doping of CaO derived from calcined eggshells with Na–K using a wet impregnation method to improve the catalytic activity at low reaction temperatures and to shorten the reaction time. The effect of different Na/K molar ratios was investigated on biodiesel yield from canola oil, and the highest FAME yield of 97.6% was obtained under optimal reaction conditions. Moradi *et al.* [20] described the use of CaO/SiO_2 as a heterogeneous catalyst for biodiesel production from corn oil. The transesterification reaction was carried out in the presence of corn oil, methanol (methanol to oil molar ratio of 16:1) and 6 wt% of catalyst (in terms of oil) at 60 °C for 8 h. The catalyst loading of 70%, calcination temperature of 650 °C and acid to water ratio of 0.5 were optimal values, and the purity and conversion of biodiesel produced were 98.5 and 85.6%, respectively. MacLeod *et al.* [21] evaluated four alkali-doped metal oxide catalysts, $LiNO_3/CaO$, $NaNO_3/CaO$, KNO_3/CaO, and $LiNO_3/MgO$, for biodiesel production from rapeseed oil. The results show that there is a correlation between base strength and catalyst performance, and that the alkali-doped metal oxide catalysts are promising catalysts having short reaction times.

Here we investigated a series of supported solid base catalysts that were prepared by impregnating CaO with different chloride salts, as well as their catalytic applications in the transesterification of rapeseed oil for biodiesel production. The influence of various process parameters, such as. kinds of active components, reaction temperature, catalyst dosage, and reaction time, were investigated in detail.

2. Experimental

2.1. *Materials*

Refined rapeseed oil was purchased from JianXing Agriculture Technology Group Co., Ltd. (Xi'an, Shaanxi) Calcium oxide was purchased from Sinopharm Chemical Reagent Co., Ltd. Kalium chloratum, methanol, cyclohexane, were purchased from TianLi Chemical Reagent Ltd. (Tianjin) Methyl heptadecanoate was purchased from Sigma. All chemicals were of analytical reagent grade were used without pretreatment.

2.2. *Catalyst preparation*

The supported solid base catalysts were prepared using a well-known immersion method based on the supporter CaO. The CaO support was pretreated into

a muffle furnace for calcination at 600 °C for 6 h according to the previous results as suggested by Mohammed's [22], and then impregnated with the prepared solutions of different chloride salts at room temperature. After 12 h, the resulting pre-catalyst was immediately dried in an oven at 110 °C for 5 h and then calcined under a specified time and temperature conditions.

2.3. *Catalytic testing*

Amount of rapeseed oil and methanol were added in a three-necked round-bottomed flask equipped with a reflux condenser and a thermometer, and the catalyst was added under stirring. Then the mixture was heated to refluxing temperature of methanol (65 °C) under stirring. The catalytic performance was evaluated by analyzing the sample taken out from the reaction mixture every 1 h. All samples were treated by centrifugation for the separation of catalysts, and the excess methanol in the samples was distilled off under vacuum.

2.4. *Characterization of catalysts*

The particle sizes and shapes of the prepared catalysts were examined using SEM (JSM-6390A, HI2TACHI). Adsorption isotherms of nitrogen on the prepared catalysts were obtained using an automated volumetric adsorption apparatus (ASAP2010, Micromeritics). Samples were evacuated at 300 °C for 2 h before exposure to nitrogen gas at 77 K. The BET surface areas were calculated using the Brunauer–Emmett–Teller equation. Temperature programmed desorption (TPD) of carbon dioxide was carried out using ChemiSorb2750 instrument (Micromeritics). The temperature of the sample was increased to 850 °C at a ramping rate of 10 °C/min and the desorbed carbon dioxide was detected using a thermal conductivity detector.

2.5. *Pretreatment of biodiesel*

If vegetable oil contains free fatty acid (FFA), it will react with homogenous base catalysts to form soap and water [23]. NaOH was used to remove free fatty acid from raw rapeseed oil. After multiple washings with water, then cyclohexane was used to remove remain water and the refined rapeseed oil was obtained.

The transesterification reaction was carried out in a 100 mL flask with a three-necked, round-bottomed, and thermometer. Rapeseed oil and methanol were first mixed under magnetic stirring and then heated to the reflux temperature of methanol in a water bath. The reaction occurs after adding the amount of catalyst into the mixture. After the desired time, the catalyst was separated by centrifugation and unreacted methanol was separated from the supernatant by vacuum distillation. Then the purified samples were collected for analysis.

2.6. *Analyses*

Samples, 1 μL, were analyzed by gas chromatography equipped with HP-INNOWAX (30 m × 0.15 mm) column with a flame-ionization detector and N_2 as carrier gas. The column was maintained at 100 °C for 1 min, then increased at 20 °C/min to 240 °C and maintained for 1 min. Detector and injection temperature were 280 °C and 320 °C, respectively. The yield of biodiesel was calculated by the flowing equation given by Leung and Guo [24].

$$\text{Yield (\%)} = 100 \times \frac{\text{weight of biodiesel}}{\text{weight of oil}}.$$

3. Results and discussion

3.1. *Transesterification of rapeseed oil to biodiesel*

3.1.1. *The catalytic performance of different catalysts*

According to previous studies, it was observed that the introduction of Cl^- not only increased the number of base sites, but also significantly changed its base strength [25]. In our study, biodiesel was prepared by the catalysis of CaO supported with different active components, namely KCl, $AlCl_3$, NH_4Cl, $FeCl_3$, and LiCl. The results are shown in Figure 1. As shown, all supported catalysts catalyzed the transesterification reaction of rapeseed oil. Among them, KCl/CaO showed the best catalytic activity under the same reaction conditions. The optimal performance was obtained when KCl/CaO was used as a catalyst, with 98.4% of yield to biodiesel, which was 15.1% higher than commercial CaO. However, Reyero *et al.* [26] studied the heterogenization of biodiesel synthesis over CaO catalysts and found that

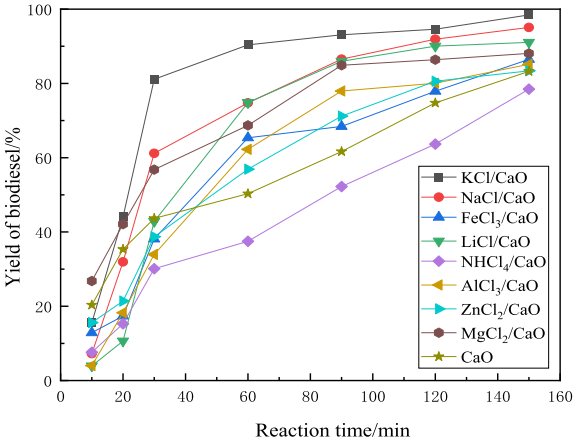

Figure 1. Comparison of biodiesel yield over different catalysts.

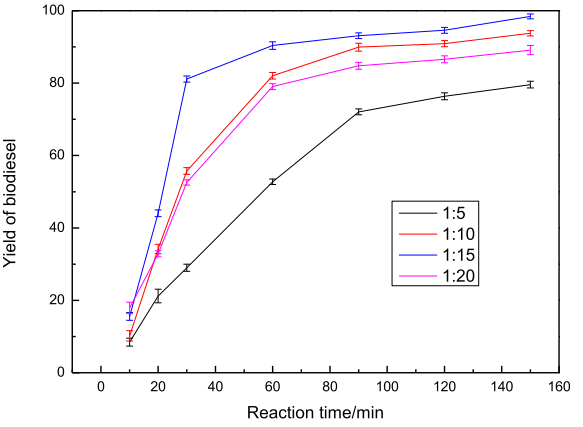

Figure 2. Effect of molar ratio on yield of biodiesel.

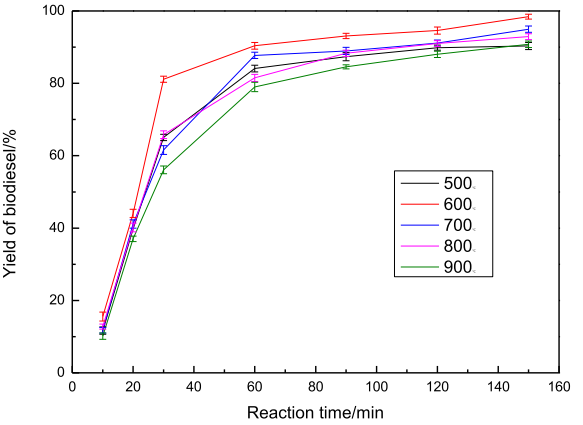

Figure 3. Effect of calcination temperature on yield of biodiesel.

Ca-glyceroxide possessed appreciable basicity and could increase the yield of biodiesel to about 83.4% within 2 h reaction time. The results suggest that active components have an important influence on the catalysis of CaO. The performance of the catalyst was significantly improved with the addition of KCl, which could appropriately modify the pore structure and inner surface area of CaO. The specific reason for this needs to be further studied and will be explained in detail later. Based on the results, KCl/CaO was used for further experiments.

3.1.2. *The influence of molar ratio*

One of the most important parameters affecting the transesterification process is the molar ratio of the reactants [27]. Theoretically, the biodiesel yield can reach a maximum when the molar ratio of methanol to rapeseed oil at 3:1. However, more methanol was introduced to keep the equation shifted to biodiesel production. The effect of the molar ratio of methanol to rapeseed oil was examined and the results are shown in Figure 2. The biodiesel yield tended to increase with increasing amount of methanol, and reached a maximum of 98.4% when the molar ratio of methanol to oil was 15:1. In contrast to Huang's study [28], the biodiesel yield reached only 97.8% at the same molar ratio of methanol to oil. It was also observed that when the molar ratio of oil to methanol was increased to 20:1, the yield of biodiesel decreased remarkably due to dilution effect. Hence, the optimum operating ratio for conversion will be 15:1.

3.1.3. *The influence of calcination temperature*

Calcination temperature was found to be of great importance in the preparation of catalysts with high catalytic activity [29]. The effect of calcination temperature on biodiesel yield is depicted in Figure 3. Increasing the calcination temperature leads to an increase in biodiesel yield due to the appearance of active sites derived from the decomposition of chloride salts at higher temperatures. The most favorable yield of biodiesel at 2.5 h was 98.3% when the reaction was carried out by calcination of the catalyst at 600 °C. However, when the catalyst was calcined above 600 °C, the excessively high temperature led to

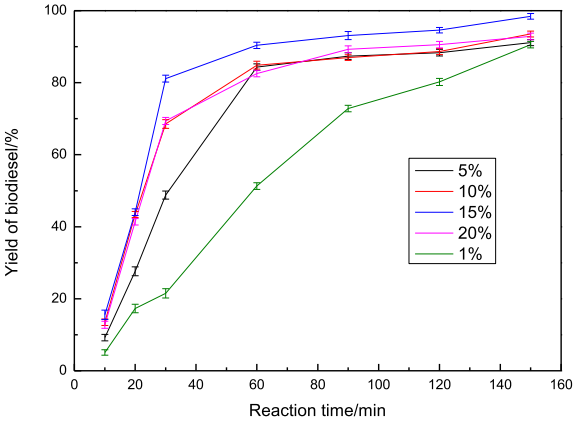

Figure 4. Effect of KCl addition on yield of biodiesel.

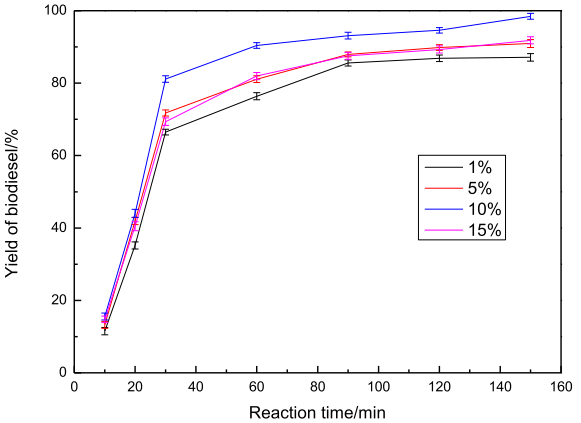

Figure 5. The effect of catalyst amount on yield of biodiesel.

CaO sintering, resulting in a decrease in the biodiesel yield. These results indicate that the catalyst activities strongly depend on the calcination temperature [30] and that a suitable calcination temperature is beneficial to the performance of the in terms of flavor and appearance. The optimal calcination temperature was set at 600 °C. In a similar study, Chen *et al.* [31] reported a biodiesel yield of about 90% using $CaO/MgO/Fe_3O_4$ calcined at 600 °C as a catalyst.

3.1.4. *The influence of loading amount of KCl*

Considering that the highest catalytic performance was exhibited over KCl/CaO, the loading amount of KCl was further considered for evaluating the reaction parameters. As illustrated in Figure 4, the catalytic activity was increased by increasing the amount of KCl from 1% to 15%. While increasing the amount of KCl further, the yield of biodiesel did not increase but decreased significantly due to the excess of KCl covering the active sites on the CaO surface. Therefore, the optimum amount of KCl in this reaction is 15% by weight of CaO. In contrast to Tang's study [25], it was found that KCl/CaO impregnated in a 15% KCl solution for 12 h and calcined at 600 °C gave the best performance with the highest yield of 96.4%, where there was an appropriate dispersion of CaO particles with strong basic sites.

3.1.5. *The influence of catalyst amount*

The influence of catalyst amount on the catalytic performance of rapeseed oil transesterification to biodiesel was investigated from 1% to 15%, and the results are shown in Figure 5. From the results, it can be seen that the yield of biodiesel gradually increased with an increase in catalyst weight, and reached the highest value of 98.4% at 10% catalyst usage. Oliveira *et al.* [32] reported that the obtained catalysts were tested at the following reaction parameters: 20:1 methanol:oil molar ratio; 10% of catalyst amount; 60 °C temperature for 5 h, with the highest yield (92.2%) to be obtained. Whereas the yield of biodiesel decreased to some extent as the catalyst amount was increased to 15%. The results clearly indicate that a sufficient number of basic sites are required to catalyze the completion of the reaction [33]. This decreasing trend was attributed to the formation of soap in the presence of large amounts of catalyst, which increased the viscosity of the reactants and lowered the yield of esters [34].

3.1.6. *The influence of reaction time*

Figure 6 illustrates the influence of reaction time on the yield of biodiesel, which varies in time from 10 to 180 min at reflux temperature. From the results, it can be found that the yield of biodiesel initially increases with increasing reaction time [35], with a maximum yield of 98.3% at the time when the reaction was carried out at reflux temperature for 2.5 h. Whereas, in Wen's study [36], they prepared the KF/CaO nanocatalyst by impregnation method and used it to convert Chinese tallow seed oil to biodiesel. The optimum reaction conditions were 12:1 alcohol to oil molar ratio, 4 wt% catalyst loading /w of oil, 65 °C reaction temperature, and 2.5 h reaction time

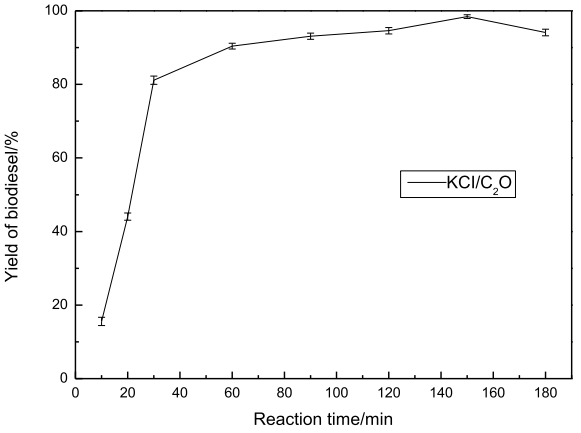

Figure 6. Effect of reaction time on the yield of biodiesel.

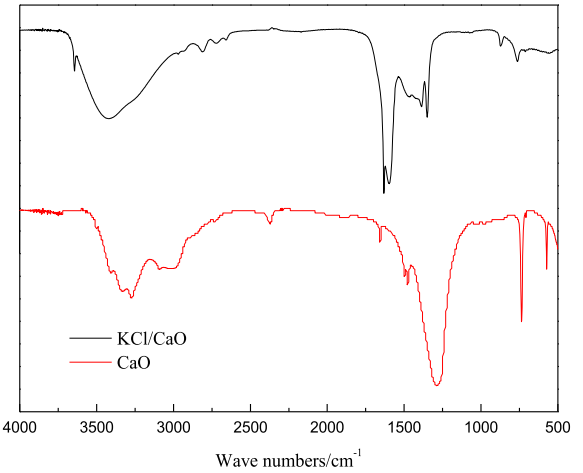

Figure 7. IR spectra of different catalysts.

resulting in 96.8% biodiesel yield. Further extension of the time to 4 h did not result in an increase in biodiesel yield, but indicated a slight decline in the stage of side reactions that appeared, such as the decomposition of glycerides.

3.2. *Catalyst characterization*

3.2.1. *FT-IR spectrum of different catalysts*

FT-IR patterns of the KCl/CaO catalyst and CaO are shown in Figure 7. The broadband in the 3200–3600 cm^{-1} region is attributed to the –OH stretching vibrations of the surface hydroxyl groups. The peaks observed at 1625, 1450, and 876 cm^{-1} could be due to CO_3^{2-} vibrations. The main reason for the formation of –OH and CO_3^{2-} is the absorption of CO_2 and water from the air by the catalyst [37]. The presence of KCl obviously reduces the intensity of –OH, which indicates that the formation of KCl/CaO not only enhances the stability of CaO in air, but also makes it well active.

3.2.2. *SEM results*

The morphologies of CaO before and after support were studied using SEM images. As shown in Figure 8, the surface morphology of CaO particles changed greatly after being supported, and their morphology changed from flocculent particles to spherical granules. The results indicated that the active components could be dispersed on the surface of the catalyst [38]. After loading with KCl, the catalysts were larger in size, with good particle dispersion and exhibited excellent catalytic performance. The EDX analysis of the surface (inserted in b) confirms the composition of the materials. From the results, the amount of KCl over KCl/CaO was found to be lower than the supporting amount, thus indicating the leaching of KCl during the catalyst preparation process.

3.2.3. *N_2 physisorption*

The structural properties of the catalysts were determined by N_2 adsorption–desorption. As can be seen in Figure 9, the isotherms are typically type II, presenting upward at first and slightly concave upward later in the curve. The curve for CaO seems to overlap, and it may have a cylindrical hole but closed at one end. In contrast, KCl/CaO may have a cylindrical hole open at both ends, or possibly in the shape of an ink bottle. A comparison of the two hysteresis curves of the catalyst suggests that KCl/CaO may exhibit a regular and orderly structure. The unique structure of KCl/CaO may help to improve the catalytic activity.

The textural structure and basicity of the samples are summarized in Table 1. It can be found that the surface area and total pore volume of CaO and KCl/CaO gradually decreased from 37.69 to 28.9567 m^2/g, respectively. However, the pore size of CaO particles improved greatly from 61.584 to 126.7323 nm upon the addition of KCl. These results indicate that the higher the activity of the catalyst,

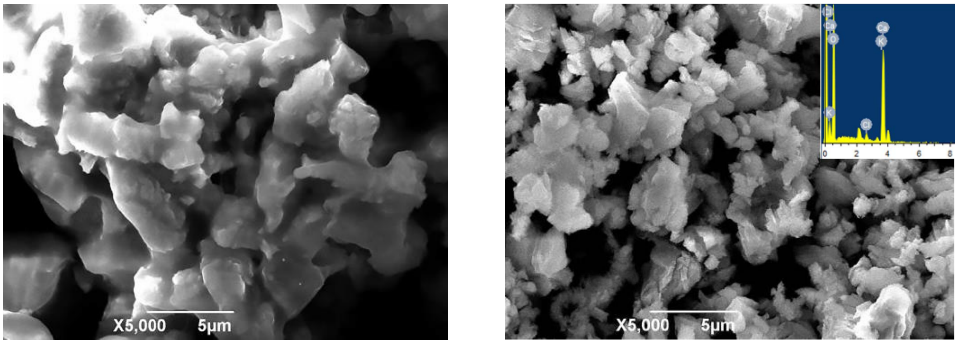

（a）KCl/CaO （b）CaO

Figure 8. Scanning electron micrograph of different catalysts.

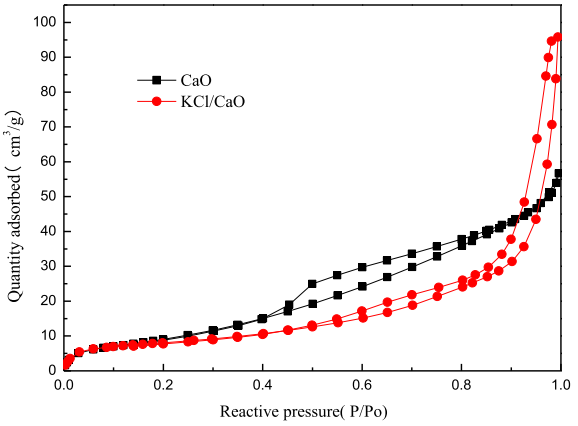

Figure 9. Nitrogen adsorption–desorption curves of different catalysts.

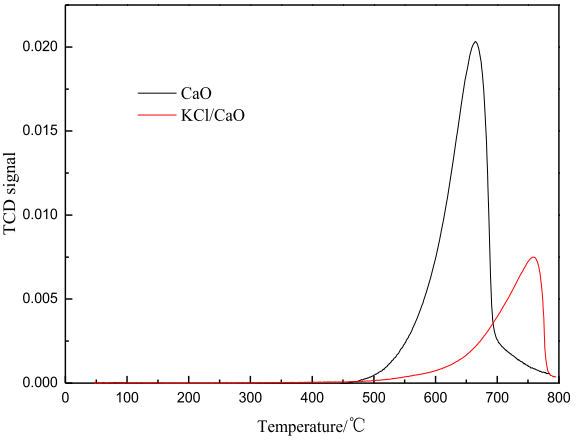

Figure 10. CO_2-TPD curves of different catalysts.

the larger the average pore diameter of the catalyst. This suggests that the average aperture increases obviously with the addition of KCl, which may be beneficial for the reactive molecules to better access the active sites of the catalysts.

3.2.4. *Basic properties*

Solid base catalysts have better catalytic activity for the transesterification of rapeseed oil to biodiesel if they have strong basicity and more basic sites [35]. The improvement of catalyst performance should contribute to the formation of methoxyl on the active basic sites of solid catalysts. To find out the basic strength and the number of basic sites, TPD was performed on the calcined catalysts, and the results are shown in Figure 10. No desorption peaks were observed below 200 °C, indicating that both samples are not weakly basic. The desorption peaks appeared in the high temperature range from 600 to 800 °C, attributed to strong basic sites, and the peaks shifted to the high temperature range over KCl/CaO, indicating that the suggested that KCl modified CaO has stronger basic sites, with the CO_2 desorption peak appearing at 758 °C. This fact would confirm the presence of strong basic sites in KCl/CaO as well as explain the high catalytic activity observed when it was used as a catalyst for the transesterification of rapeseed oil. Under the same reaction conditions, CaO exhibited a FAME yield of 61.2%, whereas the yield of FAME relative to KCl/CaO was more than 98%.

Table 1. Pore structure properties of different supported catalysts

	BET surface area (m^2/g)	Total pore volume ($cm^3/g \times 10^2$)	Average pore diameter (nm)
CaO	37.6900	8.8013	61.5840
15%KCl/CaO	28.9567	9.1744	126.7323

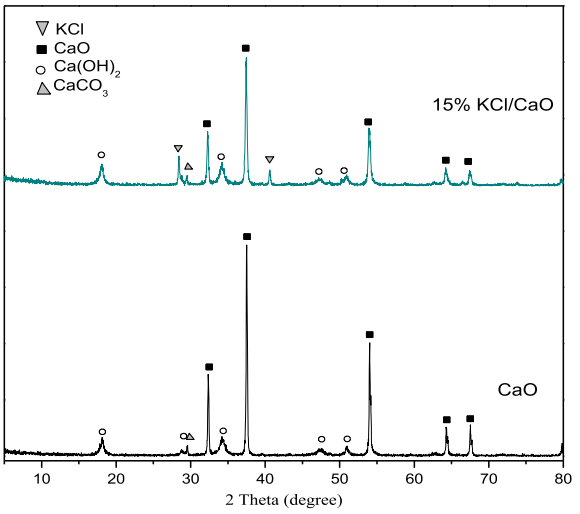

Figure 11. XRD patterns of CaO and KCl/CaO.

3.2.5. *XRD results*

The XRD patterns associated with KCl/CaO and CaO are shown in Figure 11. The characteristic XRD lines of CaO appeared with relatively low intensity, while a significant KCl crystallographic diffraction intensity was observed after modification with KCl, indicating that the presence of KCl limits the sintering of CaO particles. Since CaO is known to have a very high basicity, it is considered to be the main basic site responsible for transesterification. The more dispersed the CaO particles are, the higher the amount of FAME yield. Furthermore, weak peaks of $CaCO_3$ could be detected, indicating the presence of amorphous carbonates and a slower carbonation process of CaO compared to rapid hydration. The results are in agreement with the data reported by Granados [39].

4. Conclusions

The transesterification reaction of rapeseed oil with methanol was carried out using modified CaO with various chloride salts. Improvements were made by adding alkali metals to eggshell-derived CaO, and these catalysts typically require almost longer reaction times and high temperature, which can result in spending more time, energy, and cost. The influence of metal types has been investigated and the greater activity of KCl/CaO relative to other modified CaO can be explained by the presence of CaO with a higher concentration of super-basic sites not present in CaO. The novel solid basic catalysts showed high activities for biodiesel production with yields exceeding 98%. The structural properties and performance of these catalysts in biodiesel production from rapeseed oil were investigated and the reaction conditions were optimized to see if biodiesel could be produced under milder conditions (i.e., at a lower price) in the presence of these catalysts. Finally, the stability of the catalysts with the highest yields was also examined. CaO was found to possess the advantages of high basicity, high pore volume and good dispersion.

Conflicts of interest

The authors confirm that this article content has no conflict of interest.

Acknowledgments

This work was supported financially by National Science Foundation of China (21763030) and Youth Innovation Team of Shaanxi University. We also thank the Center of Advanced Analysis and Testing at Xi'an Shiyou University for their work.

References

[1] Y. Tang, Q. Cheng, H. Cao, L. Zhang, J. Zhang, H. Li, *C. R. Chim.*, 2015, **18**, 1328-1334.
[2] Y. Tang, L. Li, S. Wang, Q. Cheng, J. Zhang, *Environ. Prog.*, 2016, **35**, 257-262.
[3] A. E. I. Gharbawy, *J. Pet. Min. Eng.*, 2021, **23**, 98-103.
[4] N. E. Rodriguez, M. A. Martinello, *Fuel*, 2021, **296**, 120597-120608.

[5] J. M. Encinar, S. N. Delgado, N. Sanchez, *Arab. J. Chem.*, 2021, **14**, 103048-103063.
[6] S. N. Gebrenariam, J. M. Marchetti, *Biofuel. Bioprod. Biorefin.*, 2021, **15**, 815-824.
[7] Y. Tang, F. Chang, R. Zhou, B. Shen, Q. Cheng, *Russ. J. Appl. Chem.*, 2016, **89**, 2066-2071.
[8] A. Wang, P. Sudarsanam, Y. Xu, H. Zhang, H. Li, S. Yang, *Green Chem.*, 2021, **22**, 2977-3012.
[9] S. Zabala, I. Reyero, I. Campo, G. Arzamendi, L. M. Gandia, *Energies*, 2021, **14**, 4192-4207.
[10] A. S. Adekunle, J. Adekunle, I. Oduwale, O. S. Oluwafemi, *Energy Rep.*, 2020, **6**, 2861-2871.
[11] D. Bojaraj, S. B. A. V. S. Lakshmi, M. S. B. K. Mohamed, A. Narayanan, *Environ. Prog. Sustain. Energy*, 2021, **2**, 1-8.
[12] J. Cheng, H. Guo, X. Yang, Y. Mao, W. Yang, *Energy Convers. Manag.*, 2021, **232**, 113872-113883.
[13] Y. Tang, T. Yan, B. Shen, H. Li, J. Ayodeji, *Can. J. Chem. Eng.*, 2016, **94**, 1466-1471.
[14] Y. Tang, S. Li, J. Dong, M. Meng, J. Zhang, *J. Am. Oil Chem. Soc.*, 2018, **95**, 1487-1496.
[15] X. Liu, H. He, Y. Wang, S. Zhu, X. Piao, *Fuel*, 2008, **87**, 216-221.
[16] Y. Tang, Y. Yang, H. Liu, T. L. Yan, Z. F. Zhang, *Inorg. Nano-Met. Chem.*, 2020, **50**, 501-507.
[17] T. A. Degfie, T. T. Mamo, Y. S. Mekonnen, *Sci. Rep.*, 2019, **9**, 1-8.
[18] S. Santos, L. Nobre, J. Gomes, J. Puna, R. Quinta-Ferreira, J. Bordado, *Energies*, 2019, **12**, 1-10.
[19] K. Maryam, K. Farhad, L. Afsanehsadat, *Renew. Energy*, 2021, **163**, 1626-1636.
[20] G. Moradi, M. Mohadesi, Z. Hojabri, *React. Kinet. Mech. Catal.*, 2014, **113**, 169-186.
[21] C. S. MacLeod, A. P. Harvey, A. F. Lee, K. Wilson, *Chem. Eng. J.*, 2008, **135**, 63-70.
[22] Y. A. Mohammed, C. Chen, R. K. Afshar, *Agron. J.*, 2016, **109**, 309-316.
[23] Y. Tang, Y. Xue, T. Yan, R. Zhou, *J. Saudi Chem. Soc.*, 2019, **23**, 494-502.
[24] D. Y. C. Leung, Y. Guo, *Fuel Process. Technol.*, 2006, **87**, 883-890.
[25] Y. Tang, H. Liu, H. Ren, Q. Cheng, Y. Cui, J. Zhang, *Environ. Prog.*, 2019, **38**, 647-653.
[26] I. Reyero, G. Arzamendi, L. M. Gandía, *Chem. Eng. Res. Des.*, 2014, **92**, 1519-1530.
[27] Y. Tang, H. Ren, F. Chang, X. Gu, J. Zhang, *RSC Adv.*, 2017, **7**, 5694-5700.
[28] J. Huang, Y. Zou, M. Yaseen, H. Y. Qu, R. N. He, Z. F. Tong, *Fuel*, 2021, **290**, 119799-119810.
[29] M. A. Davoodbasha, A. Pugazhendhi, J. W. Kim, S. Y. Lee, T. Nooruddin, *Fuel*, 2021, **300**, 121018-121030.
[30] Z. Cui, S. Huang, M. Wang, K. Nie, T. Yan, *Renew. Energy*, 2021, **170**, 5-6.
[31] Y. Chen, D. Chen, Y. Xie, X. L. Leng, L. J. Cheng, *J. Fuel Chem. Technol.*, 2010, **38**, 415-421.
[32] T. P. Oliveira, M. F. V. D. Santos, A. C. D. M. Batista, A. M. D. M. Araujo, A. D. Gondim, *J. Therm. Anal. Calorim.*, 2021, **146**, 1-13.
[33] Z. Zhu, Y. Liu, W. Cong, X. Zhao, Z. Fang, *Ind. Crops Prod.*, 2021, **166**, 113479-113495.
[34] J. Nowicki, J. Lach, M. Organek, E. Sabura, *Appl. Catal. A*, 2016, **524**, 17-24.
[35] U. Kumar, P. Gupta, *React. Kinet. Mech. Catal.*, 2020, **130**, 875-901.
[36] L. Wen, Y. Wang, D. Lu, S. Hu, H. Han, *Fuel*, 2010, **89**, 2267-2271.
[37] N. Mansir, H. Siow, M. N. A. Teo, T. Y. Yun, *Catal. Commun.*, 2021, **149**, 160201-160209.
[38] P. Zhang, X. Chan, Y. Leng, Y. Dong, M. Fan, *Fuel*, 2020, **272**, 117680-117693.
[39] M. L. Granados, M. D. Poves, D. M. Alonso, R. Mariscal, F. C. Galisteo, R. Moreno, J. Santamaría, J. L. G. Fierro, *Appl. Catal. B*, 2007, **73**, 317-326.

Comptes Rendus
Chimie
2022, Vol. 25, Special Issue S2, p. 155-167
https://doi.org/10.5802/crchim.192

Sustainable Biomass Resources for Environmental, Agronomic, Biomaterials and Energy Applications 3 / *Ressources de biomasse durables pour des applications environnementales, agronomiques, de biomatériaux et énergétiques 3*

H_2-rich syngas production by sorption enhanced steam gasification of palm empty fruit bunch

Nabila Aprianti [a, b], **Muhammad Faizal** [*, b], **Muhammad Said** [b] **and Subriyer Nasir** [b]

[a] Doctoral Program of Environmental Science, Graduate School, Universitas Sriwijaya, Palembang 30139, South Sumatra, Indonesia

[b] Chemical Engineering Department, Faculty of Engineering, Universitas Sriwijaya, Ogan Ilir 30662, South Sumatra, Indonesia

E-mails: nabilaaprianti5@gmail.com (N. Aprianti), muhammadfaizal@unsri.ac.id (M. Faizal), m.said@unsri.ac.id (M. Said), subriyer@unsri.ac.id (S. Nasir)

Abstract. Hydrogen-rich syngas from palm empty fruit bunch has been produced using CaO and bentonite as absorbent and catalyst. The gasification process is carried out at 550–750 °C at atmospheric pressure in the fixed bed gasifier with steam to biomass ratio (S/B) of 0–2.5 and Ca/C ratio of 0–2. The results showed that CaO only acts as CO_2 absorbent during the process. Increasing the ratio of Ca/C and S/B has increased the concentration of H_2 and absorption of CO_2 in the syngas. The addition of CaO did not significantly increase the production of CH_4 and CO in the syngas. The H_2 concentration reaches about 78.16 vol% at 700 °C and Ca/C 2.

Keywords. H_2 purity, Palm waste, Steam gasification, Catalytic gasification, CO_2 absorption.
Published online: 6 July 2022

1. Introduction

Global warming is a serious environmental problem that threatens the survival of all living beings. Global warming is mainly caused by the accumulation of carbon dioxide in the atmosphere. CO_2 is responsible for at least 76% of all greenhouse gas (GHG) emissions, with 65% arising from fossil fuel combustion and industrial usage [1–3]. In addition, fossil energy reserves continue to decline, accompanied by rising crude oil prices. The use of renewable energy to substitute fossil fuels is one way to reduce CO_2 emissions. As the prime renewable carbon source with neutral carbon, biomass is an alternative energy source that can be utilized side by side with fossil fuels.

Biomass is a renewable energy source that is compatible with fossil energy. Knowledge in developing biomass conversion technology and filling gaps needs to be deepened. Agricultural and plantation waste that is not competitive in the food sector is a suitable energy source. Being the largest palm oil exporter, Indonesia produced and exported nearly 45 million tons of palm oil and 26 million tons in 2020. For every ton of crude palm oil produced, there are around 1.5–2 tons of palm empty fruit bunch

* Corresponding author.

(PEFB), or 22% of the whole process [4–7]. PEFB is a by-product of sterilizing and stripping oil palm fruit from fresh fruit bunches [8,9]. PEFB is occasionally allowed to decompose on the discharge side, creating anaerobic conditions with strong greenhouse gas (GHG) emissions of methane [10]. The current practice of PEFB disposal is by burning to produce steam to generate electricity in palm oil mills [11] or used as organic fertilizer [12]. Direct combustion of PEFB as biomass has several disadvantages: low calorific value, high moisture content, corrosion problems, wide particle size distribution, and low homogeneity [13–15]. However, since PEFB mainly comprises cellulose, hemicellulose, and lignin, processing wastes such as anaerobic digestion without pre-treatment will be complex [13,16,17].

To improve the properties of biomass fuels, many conversion processes have been applied to obtain high-quality fuels from biomasses. Biomass conversion can be carried out by various processes such as thermochemical, bioprocesses, and various physical and chemical processes [18–20]. Gasification as thermochemical conversion technology can effectively convert biomass into syngas consisting of H_2 and CO. Utilization of biomass becomes real and valuable through gasification, which produces high purity H_2. However, there are still limitations in increasing the added value of biomass. Carbonaceous gases such as CO, CH_4, and CO_2 are also present in the syngas, which dilutes the H_2 concentration. Sorption enhanced steam gasification (SESG) is a simple and novel technology to produce H_2 rich syngas from biomass. CaO is used as an absorbent in the process to remove CO_2, which is formed directly during the gasification process. This increases the concentration of H_2 in the syngas. The optimal temperature based on literature studies is 500–750 °C under atmospheric pressure [21–25]. This is related to CO_2 absorption so that syngas rich in H_2 and low in CO_2 concentration is obtained.

Research on SESG using CaO has been carried out on several biomasses. Martinez *et al.* [26] used wood and wheat straw as feedstock in the steam gasification process with absorption focused on tar formation. Inayat *et al.* [27] obtained 75 vol% H_2 from EFB at 700 °C. In addition to the steam ratio, temperature also affects the gasification process by absorption. At 750 °C, CaO only acts as the catalyst to increase the carbon conversion rate. The maximum CO_2 absorbed by CaO was 189.88 mL/g in the gasification of cellulose by Mbeugang *et al.* [28]. Sufficiently high H_2 concentrations were also obtained for sugarcane leaves by the same process using CaO/MgO at 600 °C [29]. Dong *et al.* [30] also confirmed that the addition of CaO to biochar increased H_2 at 700 °C. Detchusananard *et al.* [31] stated that the ratio of S/C and gasification temperature were the parameters that most influenced the gasification of wood residue. However, the carbon conversion and gasification efficiency of the SESG process are pretty low at the existing gasification temperature range. Gasification of biomass at lower temperatures will produce high tar. Although CaO has been shown to catalyze cracking or reformation, tar is still formed during the gasification process. There are two main ways to increase H_2 yield further and reduce tar from the current SESG process. One method adds pressure to the process to raise the reaction temperature [32–34]. Under pressure, a higher gasification temperature can be achieved to increase the CO_2 absorption rate. Meanwhile, in such a case, the gasification efficiency and the conversion rate of biomass carbon will be greatly improved, significantly increasing the yield of high-purity H_2. The key problems in this method are the pressurized system's great complexity and difficulty of the operation and the high capital and operational expenditure. Another option is to include a catalyst in the process to speed up the gasification reaction [27,35,36].

Bentonite has been widely used as an absorbent and catalyst in several waste treatment processes [37–40] and energy conversion, especially pyrolysis [41–45]. In our previous study [46,47], the application of bentonite was shown to increase H_2 in conventional gasification at low temperatures. In addition, bentonite can reduce tar during the gasification process [48] and increase the heating value of the gas as an adsorbent [49]. To the best of our knowledge, there is very limited literature discussing catalytic sorption enhanced steam gasification of PEFB to obtain high H_2 concentrations in syngas. Moreover, a bentonite catalyst has never been applied to this process. This study aims to produce H_2-rich syngas from PEFB through the SESG catalytic process. Parameters evaluated were the effect of temperature, steam to biomass ratio, and Ca/C ratio on syngas composition, H_2 increase, and CO_2 reduction, as well as calorific value and gasification

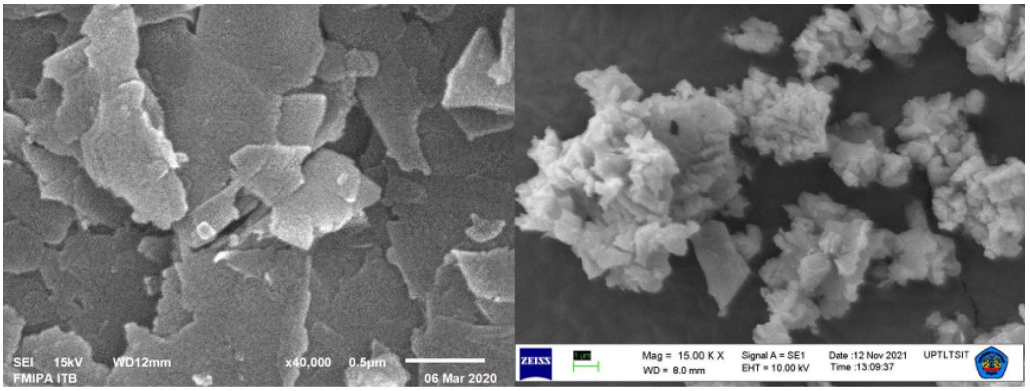

Figure 1. SEM image of (a) bentonite and (b) CaO.

efficiency.

2. Materials and methods

2.1. *Feedstock*

Palm empty fruit bunch in this study was obtained from the local crude palm oil industry in South Sumatra, Indonesia. The analysis and results of proximate and ultimate PEFB and bentonite as a catalyst in this study were reported in our earlier studies [46,47]. The absorbents used in this study consist of 96.23% CaO, and 1.75% MgO, and the rest are Fe_2O_3, SiO_2, K_2O_3, as well as Al_2O_3, each of which are less than 1% as determined by XRF analysis. The morphology of CaO and bentonite is seen from Scanning Electron Microscope (SEM) images (Figure 1). SEM microscopy was performed using SEM JEOL-JSM-6510 LA. As seen, calcined bentonite has a simple structure while calcined CaO possesses a loose structure, and the active surface is quite porous and rough, which is suitable for CO_2 uptake.

2.2. *Experiments*

The gasification apparatus shown in Figure 2 consists of a gasifier (OD 230 mm and height 670 mm), a cleaning system, a biomass hopper, and a cooling system. The gasifier was made of stainless-steel pipe with a thickness of 15 mm and was heated by three electrical heaters to reach reaction temperature (550–750 °C). The gasification process was carried out in a fixed bed gasifier, with steam serving as the gasification agent and being injected into the bottom of the gasifier. At the beginning of the process, the CaO is placed in the bed that is upper from feedstock and catalyst. The gasification products passed through the cooling system. Tar was separated after cooled and collected in the storage tank. Gas chromatograph (Perkin Elmer Clarus 680) was used to evaluate the syngas composition after being collected in the gas bag. Steam gasification of PEFB with bentonite catalyst was performed at temperatures between 550 °C to 750 °C, and the ratio of steam to biomass (S/B) varied from 0 to 2.5. The Ca/C revealed the CaO and carbon ratio in PEFB varied from 0 to 2.

3. Results and discussion

3.1. *Effect of variation of catalytic gasification temperature on* $S/B = 1$

Syngas yield and syngas composition from palm empty fruit bunch (PEFB) catalytic gasification at different temperatures are shown in Figure 3. Syngas yield increased gradually with increasing temperature. At 750 °C, the syngas yield reached 1.03 m^3/kg. These results indicated the potential of PEFB to produce syngas. This finding aligns with SESG results from other feedstocks, which show that higher temperatures favor carbon conversion, resulting in higher syngas yields [28,50,51].

The concentration of H_2 increased with increasing temperature, while, the opposite trend was found

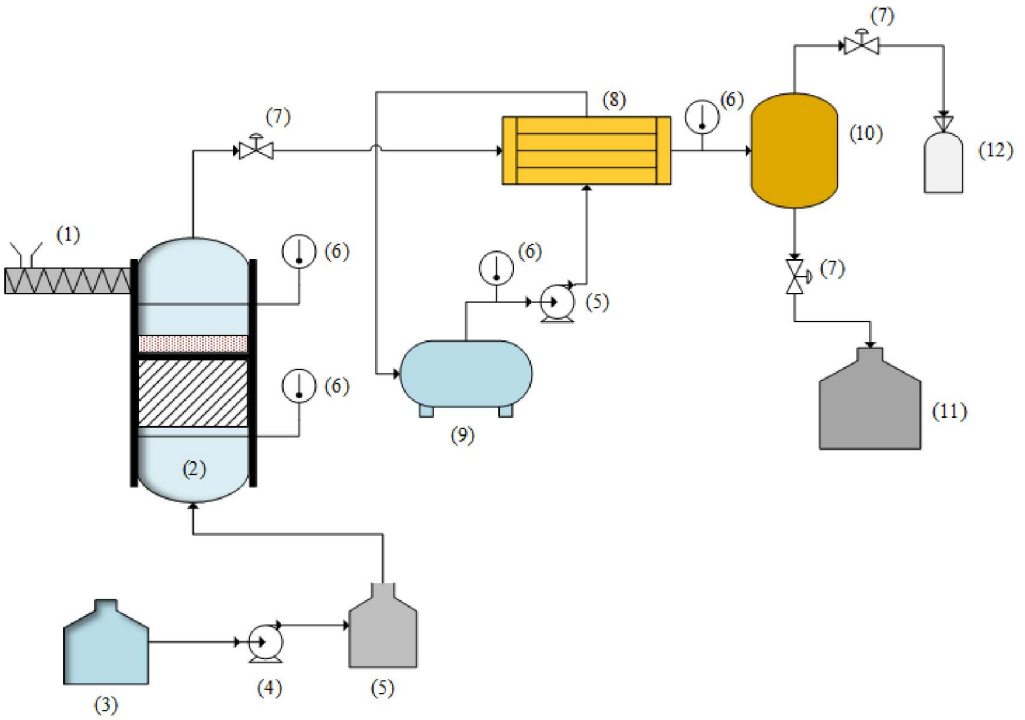

Figure 2. Illustration of the experimental setup for SESG of PEFB. (1) Biomass hopper; (2) gasifier; (3) water tank; (4) pump; (5) steam generator; (6) temperature controller; (7) valve; (8) heat exchanger; (9) cooling water tank; (10) separator; (11) liquid storage; (12) gas bag.

for CO. Kinetically, the increasing temperature is suitable for the water gas shift (WGS) reaction to produce H_2 to a certain extent. Gasification can take place at low temperatures, such as in this study, with a temperature range of 550–750 °C. It is still necessary to support the absorption process and a catalyst to optimize the gasification reaction in PEFB. With increasing temperature, the concentration of H_2 increases rapidly so that the H_2 in the syngas reaches 42.15 vol%. The increase in H_2 is also influenced by the bentonite catalyst used. Our previous work revealed that H_2 increased after bentonite was applied [46]. The concentration of CH_4 is marginally increased due to the breaking of the branching of the volatile molecule. CO was also generated during the cracking and reforming processes, although it was insignificant. If there is a quick increase in H_2 and CH_4 concentrations, the WGS reaction will consume some of the CO, resulting in a continual reduction in CO concentration. The concentration of CO, which was initially high at 40.12 vol%, decreased to 31.24 vol% at 750 °C. With increasing gasification temperature, the concentration of CO_2, which was initially reduced and then increased, obtained a minimum value of 13.26 vol% at a temperature of 650 °C. CO_2 is formed from the primary cracking of the C=O functional group in the PEFB biomass molecule, steam reforming from volatile pyrolysis, and the WGS reaction.

The cracking and reformation of the volatiles are generally sufficient around 650–750 °C. During the PEFB steam gasification process, the WGS reaction rate increases and becomes the dominant reaction. As the temperature rises from 650 to 750 °C, the reaction rate of the WGS reaction increases, causing the CO content to drop progressively and the concentrations of H_2 and CO_2 to rise. In addition, steam reforming of CH_4 occurs significantly at higher temperatures, leading to a decrease in its concentration. According to Figure 3, the concentration of H_2 in the syngas is relatively low (29.65–42.15 vol%) because a substantial amount of carbon gas (CO, CH_4, and CO_2)

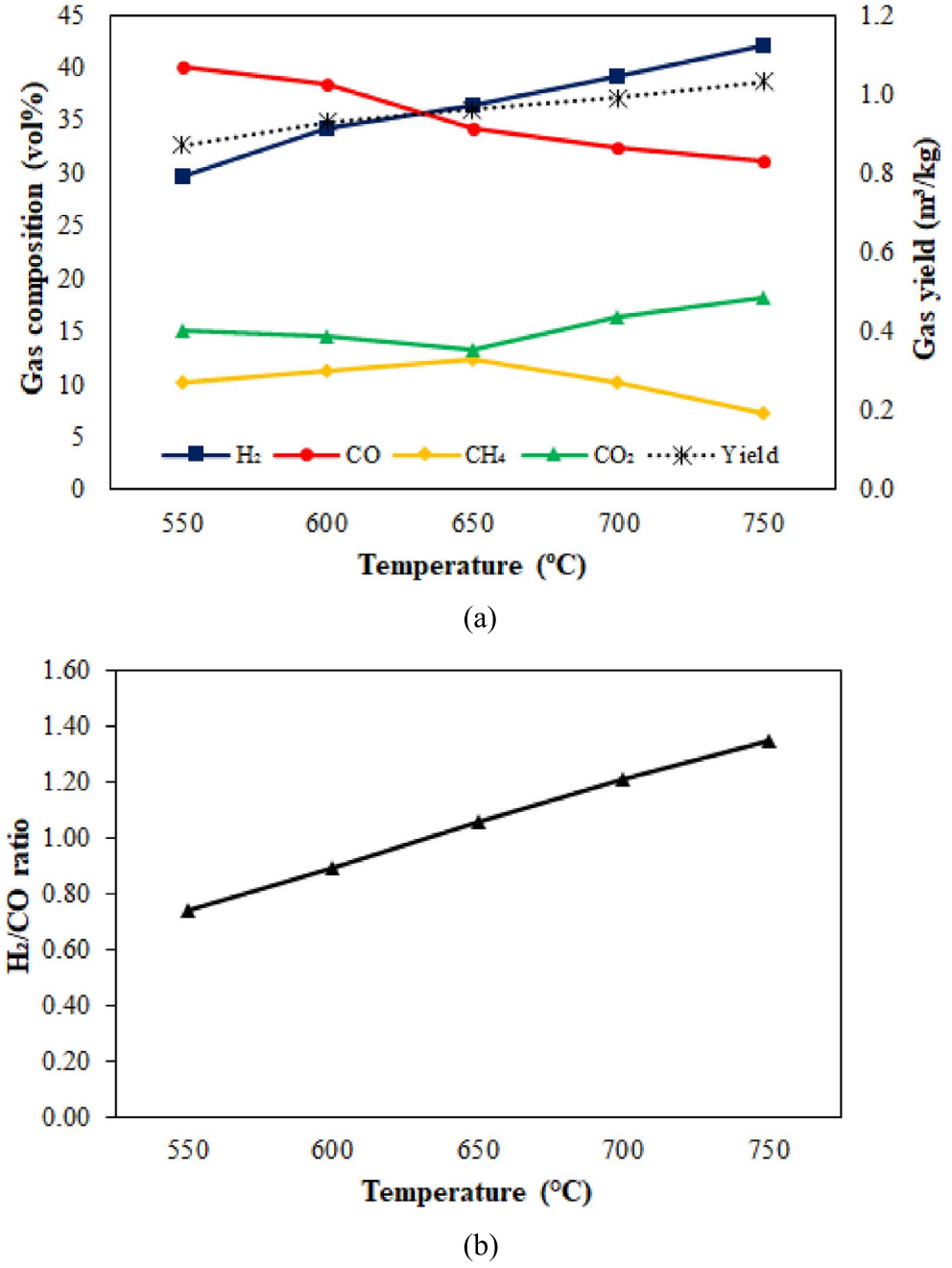

Figure 3. Effect of gasification temperature on (a) syngas composition and yield, (b) H_2/CO ratio at S/B = 1.

is still present, diluting the H_2 concentration. A major portion of carbon-containing components may be transformed to H_2 by steam reforming and the WGS reaction, and CO_2 can be decreased further from the resulting gas, higher yields of high-purity H_2 are expected. Temperatures above >650 °C do increase H_2, but CO_2 increases 5 vol%. From the PEFB gasification process with S/B = 1, the maximum H_2 was achieved

at 700 °C.

The H_2/CO ratio is a benchmark for classifying the use of advanced fuels. In Figure 3b, the ratio of H_2/CO at various gasification temperatures is presented. At 550 °C and 600 °C, the H_2/CO ratio obtained is relatively low because it is deluded by the high CO content. In this condition, the effect of the catalyst is powerful to produce CO through the Boudouard reaction, water gas reaction, and steam methane reforming. The H_2/CO ratios at 550 °C and 600 °C were 0.74 and 0.89, respectively, suitable for ethanol production [52]. The high CO concentration causes the H_2/CO ratio to be less than two. The syngas produced at this stage is only suitable for producing aldehydes and alcohols. Therefore, improving the quality of H_2 to achieve a higher H_2/CO ratio is carried out at a later stage.

3.2. *Effect of S/B variation on syngas composition from PEFB*

In the previous catalytic steam gasification process, a high concentration of H_2 was produced at 700 °C with S/B = 1. Therefore, gasification was continued by varying the S/B, focusing on increasing H_2. An increase in H_2 volume indicates success in quality improvement. The addition of steam is beneficial for the re-formation of methane (methane reforming reaction). For gasification at atmospheric pressure, as in the present study, more steam is needed to enrich the H_2 content and provide adequate mixing to encourage the reaction to completion. Steam is used to enrich the volume fraction H_2 in the final product. The steam to biomass (S/B) ratio is calculated by dividing the steam flow rate by the biomass mass flow rate on a dry basis.

Figure 4 shows the syngas composition and yield from PEFB steam gasification with variation steam to biomass (S/B). As expected, the steam injection in the process increased in the total syngas yield and volume fraction of H_2. An increase in S/B from 0.5 to 2.5 indicates a gradual increase in gas yield and H_2 concentration from 0.99 m^3/kg to 1.36 m^3/kg and 39.21 vol% to 49.26 vol%. This is due to the rise in S/B ratio increasing the partial pressure of steam in the gasification system, thereby increasing the gasification of volatile steam and char, and the WGS reaction to produce more H_2. However, because the S/B ratio exceeded 1.5, the concentration of H_2 and the ratio of H_2/CO had decreased and increased slowly (Figure 4b). This indicates that additional steam is large enough for the steam gasification process. A significant excess of steam will also increase the system's overall energy consumption. Thereupon, the S/B ratio should not be too high during the gasification process.

The volume of H_2 increased as the S/B ratio increased, while the volume of CO and CH_4 decreased. The addition of steam to the gasification process raises the partial pressure of steam in the gasifier, which aids the reaction of water–gas shift and steam reforming, resulting in increased H_2 generation [53]. The volume of H_2 increased by 13.69% after steam was injected at 550 °C, while the volume of CO decreased by 10.90%. The presence of steam in the gas phase reaction results in the decomposition of hydrocarbons and an increase in the content of H_2 and CO_2 as reaction products. These results are supported by research conducted by Lei and Zhou [54], who found a significant increase in H_2 while CO decreased drastically.

Low heating value (LHV) decreased with an increase in the S/B ratio from 11.94 to 8.61 MJ/N·m^3. The principal contributors to LHV are H_2, CO, and CH_4. The decrease in LHV gas was caused by the reduced content of CH_4 and CO because they have a more significant contribution to LHV gas. This system works well in calorific value, as seen from the slight decrease in calorific content. A reduction in the calorific value of gases for steam gasification was also investigated by Rupesh *et al.* [55]. The decline in calorific value was caused by a decrease in the high energy content of the gas (CH_4 and CO) at an S/B ratio higher than 1. The drop in CO and CH_4 levels was seen to be greater than the rise in H_2 content. The lower calorific value of the biomass and product gas determines the efficiency of the cold gas to evaluate the performance of the gasification system.

Figure 5 depicts the effect of S/B ratio changes on carbon conversion (CCE) and cold gas efficiency (CGE). The carbon conversion and cold gas efficiencies are higher at S/B ratio of 0 and decrease with increasing S/B ratio. The reduction of efficiencies was driven by descending the CH_4, CO, and CO_2 concentrations. Meanwhile, the CGE decreased due to the increase in the S/B ratio from 95.14% to 80.14% because it was related to the LHV gas, which de-

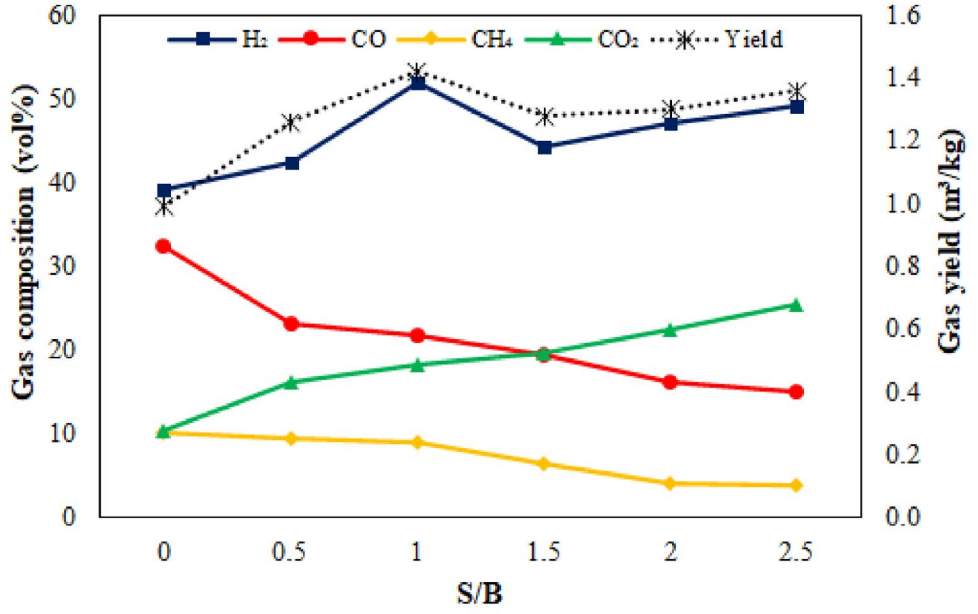

(a)

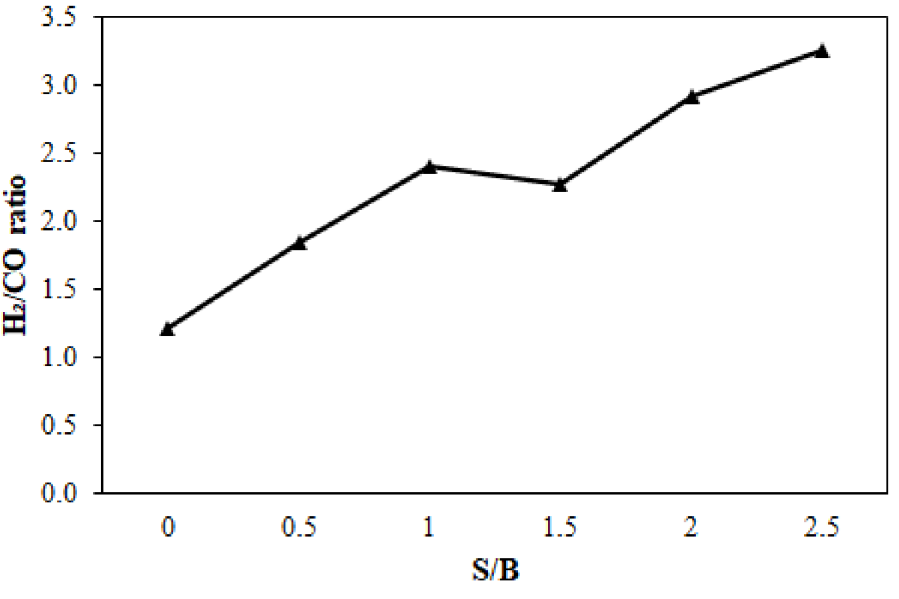

(b)

Figure 4. Effect of S/B variation on (a) syngas composition and yield and (b) H_2/CO ratio of PEFB catalytic gasification.

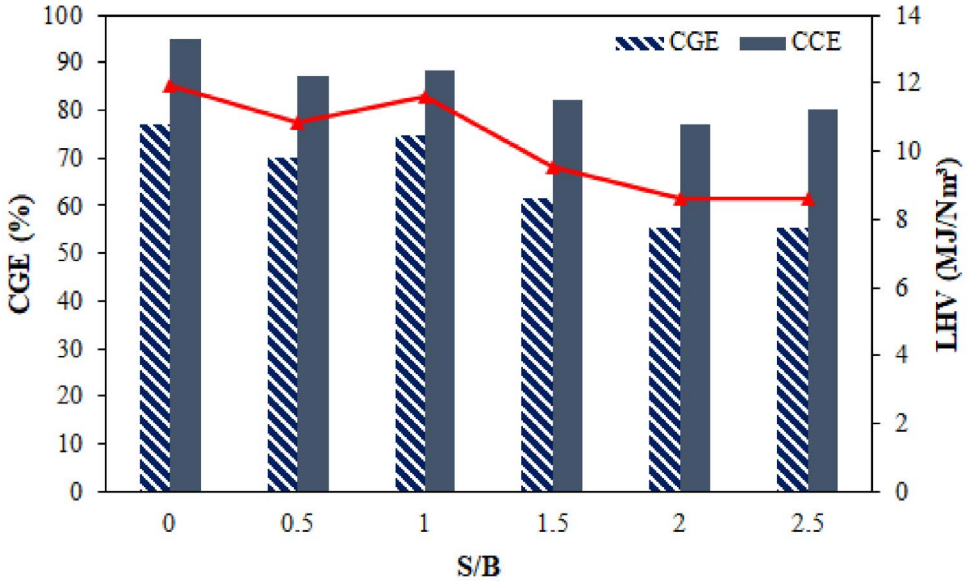

Figure 5. Effect of S/B ratio on cold gas efficiency and LHV syngas.

creased with the increase in the S/B ratio. Shahbaz *et al.* [56] and Tavares *et al.* [57] also reported a similar trend.

3.3. *Effect of variation of CaO/PEFB ratio (wt/wt) on syngas quality*

The PEFB gasification process with absorption was carried out at different variations of CaO. In addition, after the temperature was increased by more than 700 °C on steam gasification, the CO_2 concentration continued to increase, and the WGS reaction was active under these conditions. It prevented the reverse carbonation reaction [58]. Figure 6 shows the syngas composition and yield from PEFB steam gasification with various ratios of CaO/PEFB. The total syngas yield and the concentration of H_2 in syngas increase with increasing the Ca/C ratio. Syngas yield increased from 1.52 m^3/kg to 1.83 m^3/kg, rising Ca/C from 0 to 2. The concentration of H_2 in the produced gas also increased from 52.05 vol% to 68.16 vol%, while decreasing the concentration of CO from 21.57 to 9.15 vol%. The same trend also occurred in the CO_2 concentration, which dropped slightly from 17.26 vol% to 9.64 vol%. The fundamental reason for this is that the in-situ CaO absorbs the CO_2 produced during the gasification process, causing the chemical balance of the WGS reaction to shift with more H_2 being produced. CO_2 absorbed by CaO through the carbonation reaction causes WGS to be more dominant to produce H_2 than the Boudouard reaction because CO_2 as a reactant has been reduced.

The concentration of CH_4 did not show a significant increase with the addition of CaO, which was still maintained at a relatively high concentration. Li *et al.* [59] also stated that steam could activate CaO, thereby increasing the reactivity of CO_2 absorption by CaO and increasing H_2 concentration. S/B variations were not carried out in gasification using CaO because, based on the previous literature, there was a decrease in the partial pressure of CO_2 in the product gas, which reduced the ability of CaO to absorb CO_2. This can weaken the effect of increasing the addition of CaO in the H_2 production process. As for the CH_4 concentration, its contents remained stable, indicating that CaO has little impact on CH_4 reforming under the experimental conditions of this study. The H_2/CO ratio is a quality indicator for syngas. As shown in Figure 6, the H_2/CO ratio increased significantly along with the increase in CaO. The highest increase mainly occurred when the Ca/C was increased from 1.5 to 2. When CaO was not added, the H_2/CO

ratio was only 2.41 but then increased to 7.45 with the maximum addition of CaO. According to Guzman *et al.* [60], syngas with H_2/CO ratio > 2 are suitable for fuel, Fischer–Tropsch synthesis, and methanol.

Figure 7 shows that CO_2 absorption by CaO increased significantly as Ca/C increased from 0.5 to 1 and continued to increase at a consistent pace when Ca/C grew from 1.5 to 2. The percentage of CaO absorbed was 61.53%. Increasing the Ca/C thickens the bed to prolong the residence time of tar vapours and gases such as CO and CO_2 in the absorbent layer. Thus, the cracking reaction of the tar compound on the surface of the CaO particles and the WGS reaction became more intense as more CO_2 was absorbed by the high absorbent, resulting in more CO being transformed into H_2. The increase in H_2 almost doubled after the S/B = 1 and Ca/C = 2 ratios were applied. It becomes a reactive condition of CaO in the carbonation reaction, and an increase in H_2 occurs through the WGS reaction. The synergistic effect of the two materials has a favorable impact on improving the quality of the syngas.

The low heating value decreased from 11.58 to 10.73 MJ/N·m^3 with an increase in the Ca/C ratio from 0 to 2.5 due to a decrease in the content of CH_4, CO, and CO_2, as shown in Figure 8, while a slight increase in LHV gas was observed when the Ca/C ratio was further improved. Carbon conversion and cold gas efficiency decreased to 51.85% and 69.15%, respectively, with a ratio of 2. The carbon conversion efficiency value was lower than the cold gas efficiency because it was measured based on the carbon content in syngas. The same trend has been described in the literature [61].

3.4. *Correlation analysis between the operating condition of PEFB gasification*

Analysis of variance (ANOVA) was used to test the significance level of individual research variables. Table 1 displays the results of the analysis of variance (ANOVA). From the results of ANOVA analysis, it was found that the coefficient of determination (R^2) and the value of determination adjustment (Adj. R^2) were high for Ca/C and temperature, which explained that these two variables significantly affected the gasification process. The p-value < 0.05 has also determined that the variable is significant. Of the three experimental variables, Ca/C was the most significant in increasing the concentration of H_2 with a p-value of 0.00095, followed by temperature with a p-value of 0.00277. Nevertheless, the steam to biomass ratio did not support the production of H_2 because it only has an effect of 12%, and the p-value > 0.05, so it is considered insignificant. It can be concluded that the Ca/C ratio and temperature are the most important parameters in producing H_2-rich syngas in PEFB gasification.

Principal component analysis (PCA) was performed to analyze the correlation between gasification operating variables [62]. Figure 9 shows the direction of the eigenvectors of temperature, S/B, and Ca/C for the syngas composition, where a1–a5 corresponds to the temperature of 550–750 °C, ab1–ab5 corresponds to the S/B ratio of 0.5–2.5, and ac1–ac5 corresponds to Ca/C ratio of 0–2. PCA chart shows the part of each parameter that affects the production of H_2. Almost all research variables except temperature of 550 °C have eigenvectors with the same direction and small angle. They are positively correlated with H_2 concentration, which is also confirmed by the results of the Pareto chart (Figure 10). Meanwhile, the eigenvectors with opposite directions show that the research variables are inversely correlated with CH_4 and CO_2.

The steam gasification process enhanced by absorption using CaO in other studies is presented in Table 2 to compare research results. It is worth noting that, PEFB has also been exploited with a similar process by Inayat *et al.* [27], which uses zeolite as a catalyst. The maximum H_2 concentration produced is 75 vol%. In general, the characteristics of the PEFB used were similar when viewed from the proximate and ultimate analysis, but the concentration of H_2 in this study was higher. Besides PEFB, waste from the CPO industry that has been utilized is palm kernel shell (PKS). Shahbaz *et al.* [36,56] investigated simulated and experimental PKS gasification that obtained high H_2 concentrations for both studies (79.32 and 79.77 vol%). Coal bottom ash is used as a catalyst to increase H_2. The higher H_2 concentration in PKS was influenced by the higher volatile matter and carbon content than PEFB in this study. This is also consistent with other studies using different biomass, which got different H_2 due to different volatile matter and carbon content [23]. In addition, the steam ratio used in this study is higher so that the energy input is more. Comparing the results with

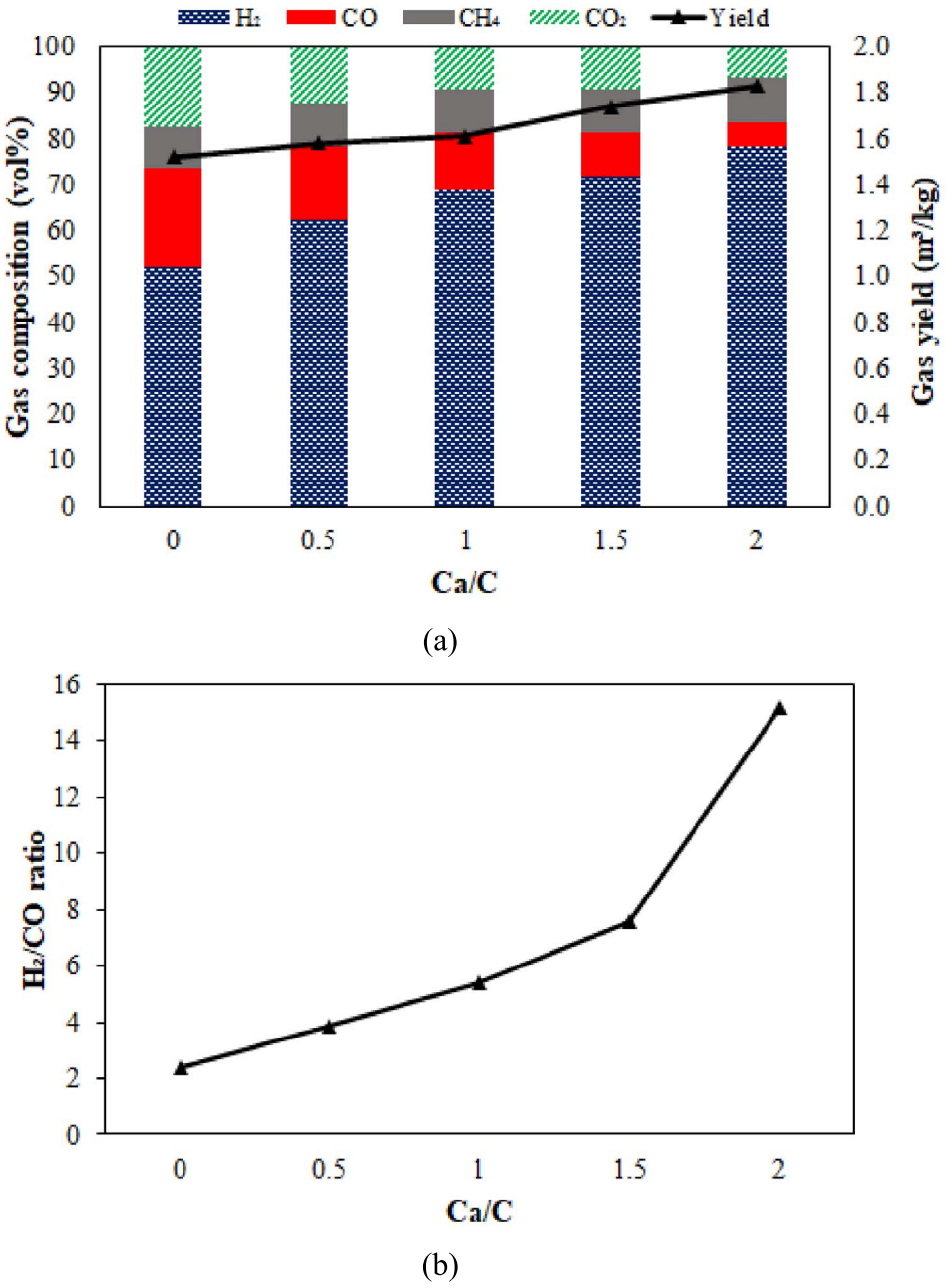

Figure 6. Effect of Ca/C ratio on (a) the syngas composition and yield and (b) H_2/CO ratio of PEFB sorption steam gasification.

published literature shows that the gasification process in this study makes it possible to generate large amounts of hydrogen from PEFB waste and compete.

4. Conclusion

Steam gasification enhanced by absorption in palm empty fruit bunch was carried out in a fixed bed reactor. The effect of gasification temperature, steam to biomass ratio, and Ca/C ratio on hydrogen-rich

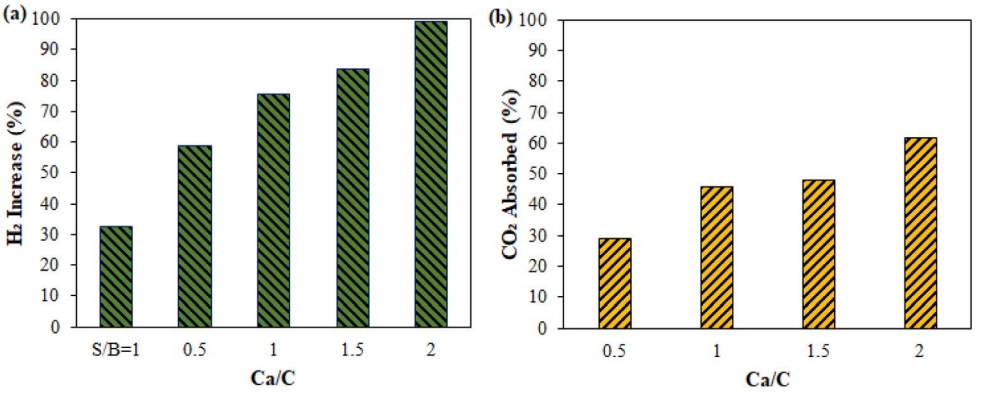

Figure 7. Effect of Ca/C ratio on the percentage increase in H_2 and CO_2 absorption in the catalytic gasification of PEFB.

Table 1. Statistical analysis of parameters affecting H_2 production

Parameter	*F*-value	*P*-value	R^2	Adj. R^2
Temperature (°C)	83.46527	0.00277	0.96530	0.95374
S/B	0.43218	0.55786	0.12592	−0.16544
Ca/C	172.85330	0.00095	0.98294	0.97725

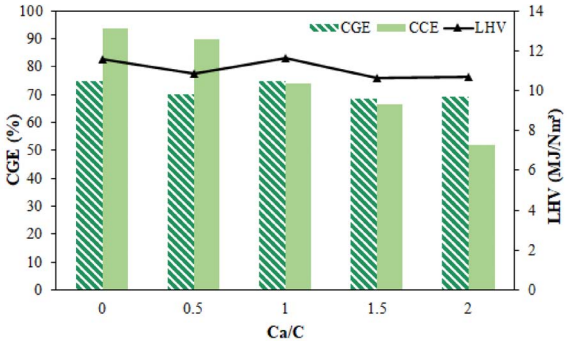

Figure 8. Effect of Ca/C ratio on cold gas efficiency and LHV syngas.

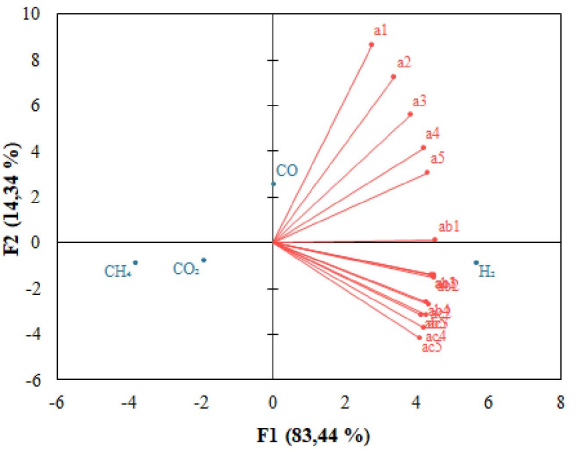

Figure 9. PCA plot of operating variables on syngas composition.

syngas production was investigated. CaO plays the role of an absorbent in the gasification process, characterized by the absorption rate of CO_2 reaching 61.53%. The addition of CaO makes the water gas-shift reaction dominant to produce more hydrogen. At 700 °C, S/B ratio of 1 and Ca/C ratio of 2, the maximum syngas yield and H_2 concentrations obtained were 1.83 m^3/kg and 78.16 vol%, respectively. Based on statistical analyses, the temperature and Ca/C ratio are variables that affect H_2 production significantly. The absorption process in steam gasification of palm empty fruit bunch has succeeded in producing quality syngas rich in hydrogen.

Conflicts of interest

Authors have no conflicts of interest to declare.

Table 2. Summary of syngas production via the sorption enhanced steam gasification of biomass reported in the literature

Feedstock	H_2 (%)	Operation condition	References
PEFB	78.16	T = 700 °C S/B = 1 Ca/C = 2	Present study
PEFB	75	T = 700 °C S/B = 2 Ca/C = 1	[27]
PKS	79.77	T = 692 °C S/B = 1.5 Ca/C = 1.42	[36]
PKS	79.32	T = 700 °C S/B = 1.5 Ca/C = 1.42 Simulation	[56]
Pine sawdust	76	T = 650 °C Ca/C = 2	[63]
Corn stalks Rice straw Wheat Straw Peanut shell	61.23 60.28 58.69 60.84	T = 650 °C S/B = 1 Ca/C = 1	[23]

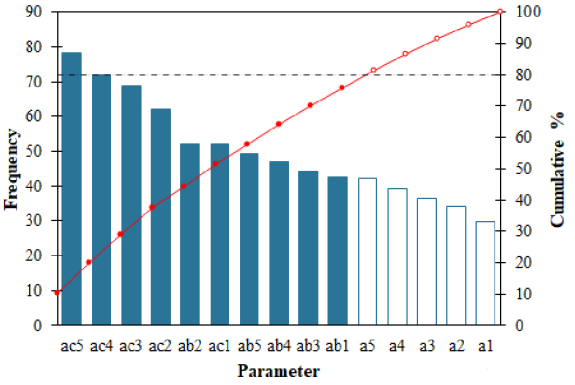

Figure 10. Pareto chart of PEFB gasification parameters for H_2 production.

Acknowledgments

This research was supported by Ministry of Education, Culture, Research, and Technology of the Republic of Indonesia through PMDSU scheme (Grant Number: 054/E4.1/AK/04.PT/2021 and 0163/UN9/SB3.LP2M.PT/2021).

References

[1] I. S. Farouq, N. Umar Sambo, A. U. Ahmad, A. H. Jakada, I. A. Danmaraya, *Quant. Financ. Econ.*, 2021, **5**, 247-263.
[2] E. Billig, M. Decker, W. Benzinger, F. Ketelsen, P. Pfeifer, R. Peters, D. Stolten, D. Thrän, *J. CO2 Util.*, 2019, **30**, 130-141.
[3] E. Lindstad, B. Lagemann, A. Rialland, G. M. Gamlem, A. Valland, *Transp. Res. D Transp. Environ.*, 2021, **101**, article no. 103075.
[4] H. M. Yoo, S. W. Park, Y. C. Seo, K. H. Kim, *J. Environ. Manage.*, 2019, **234**, 1-7.
[5] S. X. Chin, C. H. Chia, S. Zakaria, Z. Fang, S. Ahmad, *J. Taiwan Inst. Chem. Eng.*, 2015, **52**, 85-92.
[6] S. K. Loh, *Energy Convers. Manag.*, 2017, **141**, 285-298.
[7] J. A. Garcia-nunez, D. Tatiana, C. Andr, N. Elizabeth, E. Eduardo, S. Lora, C. Stuart, C. Stockle, J. Amonette, M. Garcia-perez, *Biomass Bioenerg*, 2016, **95**, 310-329.
[8] V. Subramaniam, S. K. Loh, A. A. Aziz, *Sustain. Prod. Consum.*, 2021, **28**, 1552-1564.

[9] F. B. Ahmad, Z. Zhang, W. O. S. Doherty, I. M. O. Hara, *Renew. Sust. Energy Rev.*, 2019, **109**, 386-411.

[10] Y. Krishnan, C. P. C. Bong, N. F. Azman, Z. Zakaria, N. Othman, N. Abdullah, C. S. Ho, C. T. Lee, S. B. Hansen, H. Hara, *J. Clean. Prod.*, 2017, **146**, 94-100.

[11] S. Y. Lee, T. Alam, J. H. Kim, J. C. Lee, S. W. Park, *Biomass Convers. Biorefin.*, 2021, 1-10.

[12] L. J. Hau, R. Shamsuddin, A. K. A. May, A. Saenong, A. M. Lazim, M. Narasimha, A. Low, *Waste Biomass Valorization*, 2020, **11**, 5539-5548.

[13] P. Zhao, Y. Shen, S. Ge, Z. Chen, K. Yoshikawa, *Appl. Energy.*, 2014, **131**, 345-367.

[14] W. H. Chen, B. J. Lin, Y. Y. Lin, Y. S. Chu, A. T. Ubando, P. L. Show, H. C. Ong, J. S. Chang, S. H. Ho, A. B. Culaba, A. Pétrissans, M. Pétrissans, *Prog. Energy Combust. Sci.*, 2021, **82**, article no. 100887.

[15] H. C. Ong, K. L. Yu, W. H. Chen, M. K. Pillejera, X. Bi, K. Q. Tran, A. Pétrissans, M. Pétrissans, *Renew. Sust. Energy Rev.*, 2021, **152**, article no. 111698.

[16] S. S. Qureshi, S. Nizamuddin, H. A. Baloch, M. T. H. Siddiqui, N. M. Mubarak, G. J. Griffin, *Biomass Convers. Biorefin.*, 2019, **9**, 827-841.

[17] P. M. Abdul, J. Jahim, S. Harun, M. Markom, N. A. Lutpi, O. Hassan, V. Balan, B. E. Dale, M. Tusirin, M. Nor, *Bioresour. Technol.*, 2016, **211**, 200-208.

[18] G. Kumar, J. Dharmaraja, S. Arvindnarayan, S. Shoban, *Fuel*, 2019, **251**, 352-367.

[19] H. Hammani, M. El Achaby, K. El Harfi, M. A. El Mhammedi, A. Aboulkas, *C. R. Chim.*, 2016, **15**, 1-12.

[20] A. Agrifoglio, A. Fichera, A. Gagliano, R. Volpe, *C. R. Chim.*, 2016, **15**, 1-12.

[21] R. Y. Chein, W. H. Hsu, *Renew. Energy*, 2020, **153**, 117-129.

[22] Z. Khan, S. Yusup, M. Aslam, A. Inayat, M. Shahbaz, S. Raza Naqvi, R. Farooq, I. Watson, *J. Clean. Prod.*, 2019, **236**, article no. 117636.

[23] B. Li, H. Yang, L. Wei, J. Shao, X. Wang, H. Chen, *Int. J. Hydrog. Energy*, 2017, **42**, 4832-4839.

[24] B. Li, C. Fabrice Magoua Mbeugang, D. Liu, S. Zhang, S. Wang, Q. Wang, Z. Xu, X. Hu, *Int. J. Hydrog. Energy*, 2020, **45**, 26855-26864.

[25] S. A. Salaudeen, B. Acharya, M. Heidari, S. M. Al-Salem, A. Dutta, *Energy Fuels*, 2020, **34**, 4828-4836.

[26] I. Martínez, M. S. Callén, G. Grasa, J. M. López, R. Murillo, *Fuel Process. Technol.*, 2022, **226**, article no. 107074.

[27] A. Inayat, Z. Khan, M. Aslam, M. Shahbaz, M. M. Ahmad, M. I. Abdul Mutalib, S. Yusup, *Int. J. Hydrog. Energy*, 2020, **46**, 30581-30591.

[28] C. F. M. Mbeugang, B. Li, D. Lin, X. Xie, S. Wang, S. Wang, S. Zhang, Y. Huang, D. Liu, Q. Wang, *Energy*, 2021, **228**, article no. 120659.

[29] T. Bunma, P. Kuchonthara, *Process Saf. Environ. Prot.*, 2018, **118**, 188-194.

[30] J. Dong, A. Nzihou, Y. Chi, E. Weiss-Hortala, M. Ni, N. Lyczko, Y. Tang, M. Ducousso, *Waste Biomass Valorization*, 2017, **8**, 2735-2746.

[31] T. Detchusananard, K. Im-orb, F. Maréchal, A. Arpornwichanop, *Energy*, 2020, **207**, article no. 118190.

[32] X. Zhou, X. Yang, J. Li, J. Zhao, C. Li, M. Du, Z. Yu, Y. Fang, *Energy Convers. Manag.*, 2019, **198**, article no. 111899.

[33] X. Zhou, J. Zhao, S. Guo, J. Li, Z. Yu, S. S. Song, J. Li, Y. Fang, *Int. J. Hydrog. Energy*, 2018, **43**, 17091-17099.

[34] K. Kumabe, Y. Hasegawa, H. Moritomi, *ACS Omega*, 2020, **5**, 236-242.

[35] B. Li, H. Yang, L. Wei, J. Shao, X. Wang, H. Chen, *Int. J. Hydrog. Energy*, 2017, **42**, 5840-5848.

[36] M. Shahbaz, S. Yusup, A. Inayat, D. O. Patrick, M. Ammar, A. Pratama, *Energy Fuels*, 2017, **31**, 13824-13833.

[37] S. Pandey, *J. Mol. Liq.*, 2017, **241**, 1091-1113.

[38] X. Chen, L. Wu, F. Liu, P. Luo, X. Zhuang, J. Wu, Z. Zhu, S. Xu, G. Xie, *Environ. Sci. Pollut. Res.*, 2018, **25**, 15980-15989.

[39] S. Barakan, V. Aghazadeh, *Environ. Sci. Pollut. Res.*, 2021, **28**, 2572-2599.

[40] A. Mateus, J. Torres, W. Marimon-Bolivar, L. Pulgarín, *Water Resour. Ind.*, 2021, **26**, article no. 100154.

[41] G. Dou, J. L. Goldfarb, *Fuel*, 2017, **195**, 273-283.

[42] A. M. Elfadly, I. F. Zeid, F. Z. Yehia, M. M. Abouelela, A. M. Rabie, *Fuel Process. Technol.*, 2017, **163**, 1-7.

[43] Y. Kar, *Biomass Bioenergy*, 2018, **119**, 473-479.

[44] B. A. Mohamed, N. Ellis, C. S. Kim, X. Bi, *Renew. Energy*, 2019, **142**, 304-315.

[45] D. D. Sewu, D. S. Lee, H. N. Tran, S. H. Woo, *J. Taiwan Inst. Chem. Eng.*, 2019, **104**, 106-113.

[46] N. Aprianti, M. Faizal, M. Said, S. Nasir, *J. Appl. Eng. Sci.*, 2021, **19**, 334-343.

[47] M. Faizal, N. Aprianti, M. Said, S. Nasir, *J. Appl. Eng. Sci.*, 2021, **19**, 934-941.

[48] S. D. S. Murti, Y. Sudo, S. Yan, Adiarso, R. Noda, *IOP Conf. Ser. Earth Environ. Sci.*, 2018, **105**, article no. 012105.

[49] M. Lasich, *ACS Omega*, 2020, **5**, 11068-11074.

[50] S. Chen, Z. Zhao, A. Soomro, S. Ma, M. Wu, Z. Sun, W. Xiang, *Biomass Bioenergy*, 2020, **138**, article no. 105607.

[51] A. M. Parvez, S. Hafner, M. Hornberger, M. Schmid, G. Scheffknecht, *Renew. Sustain. Energy Rev.*, 2021, **141**, article no. 110756.

[52] S. Hernández, M. A. Farkhondehfal, F. Sastre, M. Makkee, G. Saracco, N. Russo, *Green Chem.*, 2017, **19**, 2326-2346.

[53] K. Jin, D. Ji, Q. Xie, Y. Nie, F. Yu, J. Ji, *Int. J. Hydrog. Energy*, 2019, **44**, 22919-22925.

[54] Y. Lei, R. Zhou, *Util. Environ. Eff.*, 2019, 1-7.

[55] S. Rupesh, C. Muraleedharan, P. Arun, *Resour. Technol.*, 2016, **2**, 94-103.

[56] M. Shahbaz, S. Yusup, A. Inayat, M. Ammar, D. O. Patrick, A. Pratama, S. R. Naqvi, *Energy Fuels*, 2017, **31**, 12350-12357.

[57] R. Tavares, E. Monteiro, F. Tabet, A. Rouboa, *Renew. Energy*, 2020, **146**, 1309-1314.

[58] M. Shahbaz, S. Yusup, A. Inayat, D. O. Patrick, A. Pratama, M. Ammar, *Bioresour. Technol.*, 2017, **241**, 284-295.

[59] Z. Li, Y. Wang, Z. Li, G. Luo, S. Lin, H. Yao, *Fuel*, 2016, **184**, 409-417.

[60] H. Guzman, D. Roldan, A. Sacco, M. Castellino, M. Fontana, N. Russo, S. Hernandez, *Nanomaterials*, 2021, **11**, article no. 3052.

[61] P. Kumari, B. Mohanty, *Int. J. Energy Res.*, 2020, **44**, 6927-6938.

[62] S. A. A. Al-Muraisy, L. A. Soares, S. Chuayboon, S. Bin Ismail, S. Abanades, J. B. van Lier, R. E. F. Lindeboom, *Fuel Process. Technol.*, 2022, **227**, article no. 107118.

[63] C. Li, R. Liu, J. Zheng, Z. Wang, Y. Zhang, *Int. J. Hydrog. Energy*, 2021, **46**, 24956-24964.

Comptes Rendus

Chimie

Objet de la revue

Les *Comptes Rendus Chimie* sont une revue électronique évaluée par les pairs de niveau international, qui couvre l'ensemble des domaines de la discipline. Ils publient principalement des numéros thématiques, mais également des articles originaux de recherche, des annonces préliminaires, des articles de revue, des mises en perspective historiques, des textes à visée pédagogique ou encore des actes de colloque, sans limite de longueur, en anglais ou en français. Les *Comptes Rendus Chimie* sont diffusés selon une politique vertueuse de libre accès diamant, gratuit pour les auteurs (pas de frais de publications) comme pour les lecteurs (libre accès immédiat et pérenne).

À propos de la revue

Toutes les informations concernant la revue, y compris le texte des articles publiés qui est en accès libre intégral, figurent sur le site https://comptes-rendus.academie-sciences.fr/chimie/.

Informations à l'attention des auteurs

Pour toute question relative à la soumission des articles, les auteurs peuvent consulter le site https://comptes-rendus.academie-sciences.fr/chimie/.

Contact

Académie des sciences
23, quai de Conti, 75006 Paris, France
Tél. : (+33) (0)1 44 41 43 72
CR-Chimie@academie-sciences.fr

Comptes Rendus
de l'Académie des sciences

Chimie

Volume 25, nº S2, 2022

Special issue / *Numéro thématique*

Sustainable Biomass Resources for Environmental, Agronomic, Biomaterials and Energy Applications 3 / *Ressources de biomasse durables pour des applications environnementales, agronomiques, de biomatériaux et énergétiques 3*

Guest editors / *Rédacteurs en chef invités*

Mejdi Jeguirim (Université de Haute-Alsace, Institut de Sciences des Matériaux de Mulhouse, France), Salah Jellali (Sultan Qaboos University, Oman)
Besma Khiari (Centre of Water Researches and Technologies, Tunisia)

1878-1543 (electronic)

Académie des sciences — Paris

COMPTES RENDUS
DE L'ACADÉMIE DES SCIENCES

Chimie

Volume 25, nº S2, 2022